TREND-2

Trapped Radiation Environment Model Development

Final Report

ESTEC/Contract No. 9828/92/NL/FM[1]

J. Lemaire (IASB), Project Manager
A.D. Johnstone (MSSL)
D. Heynderickx (BIRA)
D.J. Rodgers (MSSL)
S. Szita (MSSL)
V. Pierrard (IASB)

February 1995

[1]ESA Technical Management: E.J. Daly (ESTEC/WMA)

European Space Agency

Contract Report

The work described in this report was done under ESA contract. Responsibility for the contents resides in the author or organisation that prepared it.

APPENDIX 4

ESA STUDY CONTRACT REPORT

No ESA Study Contract Report will be accepted unless this sheet is inserted at the beginning of each volume of the Report.

ESA CONTRACT NO:	SUBJECT:	NAME OF CONTRACTOR
9828/92/NL/FM	Trapped Radiation Environment Model Development	BIRA/IASB MSSL

* ESA CR( ) No:	* STAR CODE	No. of Volumes 1 This is Volume No: 1	CONTRACTOR'S REFERENCE:

ABSTRACT:

This document is the final report of the *TRapped Radiation ENvironment model Development* (TREND) study by the *Belgian Institute for Space Aeronomy* and the *Mullard Space Science Laboratory*.

Trapped radiation belt models based on the NASA models AP-8 and AE-8 and on data from Soviet satellites have been produced in the Soviet Union. The Soviet models have been evaluated and compared to the NASA models.

The UNIRAD software package has been extended and upgraded. A new external magnetic field model has been added and pitch angle dependence has been implemented. New trapped proton and electron models based on CRRES data have been added and new user interfaces have been written. The calculation of (B, L) coordinates has been hardwired into TREP to assure that the correct geomagnetic field models are used to access the trapped particle models. A study was made of the secular motion of the South Atlantic Anomaly and a correction for this effect was added to TREP.

A comprehensive and detailed description of the CRRES satellite, its payload and the data base formats has been compiled. The AZUR data base has been obtained from NSSDC.

The limitations of the (B, L) coordinate system at low altitudes already were noted in the previous TREND study. We found that a weighted average of the atmospheric density over a drift shell is much more effective to order trapped proton fluxes at low altitudes and may account for solar cycle variations of these fluxes. A program to calculate the density average, developed by A. Hassitt at UCSD, has been upgraded and extended. It has been applied to the flux distribution in the AP-8 models.

A statistical survey of the geostationary Meteosat-3 SEM-2 electron flux data was made. Average fluxes, energy spectra, anisotropies and flux level probabilities have been determined as a function of local time and geomagnetic activity indices. A wavelet analysis suggests a minimum repeat period of 3 hours for injection events.

The local time distribution of LANL geosynchronous electron fluxes and of electron data from the MEA and HEEF instruments on CRRES has been compared to the distribution of the Meteosat-3 SEM-2 electron measurements. There is good agreement between the HEEF and MEA data and between the MEA and SEM-2 data, but there are significant differences with the LANL data. The agreement between the MEA, HEEF and SEM-2 data marks them as valuable databases for new radiation belt models.

Electron pitch angle distributions were obtained from the MEA data. Different coordinate systems have been used to map the observed fluxes and their standard deviation. A new electron flux model in the (α_0, L) coordinate system has been produced.

The geostationary GOES-7 energetic particle data were correlated with the Meteosat-3 SEM-2 electron data. Correlation coefficients between K_p and the GOES-7 electron flux have been determined. Periods of 27 and 13 days appear in the electron data, and a period of 22 days in the proton data. The GOES-7 data revealed that the SEM-2 electron flux at high energy contains a substorm component.

Names of authors:

D. LEMAIRE, A.D. JOHNSTONE, D. HEYNDERICKX, D.J. RODGERS, S. SZITA, V. PIERRARD

** NAME OF ESA STUDY MANAGER E.J. DALY DIV: WMA DIRECTORATE	** ESA BUDGET HEADING 61(TRP)	

* Sections to be completed by ESA

** Information to be provided by ESA Study Manager

TREND-2

Trapped Radiation Environment Model Development

Final Report

ESTEC/Contract No. 9828/92/NL/FM[1]

J. Lemaire (IASB), Project Manager
A.D. Johnstone (MSSL)
D. Heynderickx (BIRA)
D.J. Rodgers (MSSL)
S. Szita (MSSL)
V. Pierrard (IASB)

February 1995

[1]ESA Technical Management: E.J. Daly (ESTEC/WMA)

Contents

List of Figures

List of Tables

Preface

This Final Report contains the main results obtained and the recommendations made by the TREND-2 team during the study *TRapped Radiation ENvironment model Development.*

The TREND study was initiated and funded by ESA under ESTEC Contract No. 8011/88/NL/MAC. It has been followed by this TREND-2 study, which started on March 1, 1992 under ESA Contract No. ESTEC/9828/92/NL/FM and a Rider. This contract had a duration of 30 months.

The institutes participating in TREND-2 are the *Belgisch Instituut voor Ruimte-Aëronomie / Institut d'Aéronomie Spatiale de Belgique* (BIRA/IASB) and the *Mullard Space Science Laboratory* (MSSL). The team members are:

- BIRA/IASB
  - J. Lemaire (Project Manager)
  - D. Heynderickx
  - V. Pierrard
  - L. Bossy
  - L. Fedullo
- MSSL
  - A.D. Johnstone
  - D.J. Rodgers
  - S. Szita
  - A. Coates
  - R. Liu
  - M. Birdseye
  - N. Flowers

During a visit to BIRA/IASB, A.A. Beliaev of the *Institute for Nuclear Physics, Moscow State University* (INP/MSU) participated in the Rider activities. A.L. Vampola of *Consulting Aerospace Environment* acted as consultant.

The TREND-2 study was divided into nine components. BIRA/IASB was in charge of:

- Project Management (WP 0);
- Low-Altitude Coordinates and Particle Flux (WP 1);
- Evaluation of CRRES Databases (WP 2);
- Evaluation of Russian Models (Rider WP 2.1);
- AZUR Data Analysis (Rider WP 2.2).

MSSL was in charge of:

- Higher Altitude Environments (WP 3);
- Substorm Analysis (Rider WP 1.1);
- Wavelet Analysis (Rider WP 1.2);
- GOES Data Analysis (Rider WP 1.3).

During the course of the TREND-2 study a number of interesting extensions were identified. This resulted in a new ESTEC contract No. 10725/94/NL/JG, which has been called TREND-3.

TREND-2 analysed satellite data from the two main regions in the trapped radiation belts:

1. high altitude orbits, with CRRES, METEOSAT and GOES data;
2. intermediate and low L values, with CRRES and AZUR data.

A number of additional data sets for the TREND-3 study were identified, i.e. DMSP/F7 and ISEE-2. By reviving data sets archived by the *National Space Science Data Center* (NSSDC), TREND-2 provided an opportunity to cross-fertilize these older data with the very recent results of CRRES and METEOSAT.

Acknowledgements

During the TREND-2 study, the ESA Technical Manager E.J. Daly has closely followed the progress of the data analysis and model development. His experience and collaboration have been very stimulating and greatly appreciated by the team members. We also benefited from H. Evans' assistance and support.

T. Cayton (LANL) is acknowledged for providing the detectors used in the SEM-2 on Meteosat-3. Ph. Guilleman (Centre Nationale de Recherche Scientifique, Marseille, France) has written the wavelet software `ONDELET3` and J.-L. Modave and F. Collin (Koninklijke Sterrenwacht van België/Observatoire Royale de Belgique) have adapted it.

We would like to thank J.H. King, director of NSSDC, for making the archived AZUR and DMSP/F7 data available to ESTEC and BIRA/IASB. We also thank H. Sauer at the *National Oceanic and Atmospheric Administration* (NOAA) for providing the GOES data and for his assistance in interpreting it. C. Tranquille (ESTEC) also contributed to the data analysis. D. Hovestadt of the *Max Planck Institut für Physik und Astrophysik* provided the necessary documentation for the analysis of the AZUR data and granted the permission to use this data set. *Los Alamos National Laboratory* (LANL) is acknowledged for providing the LANL data.

A.L. Vampola has kindly released the CRRES/MEA data and assisted with its analysis. He participated in a TREND-2 Progress Meeting where he presented his activities in the areas of data processing and modelling the Earth's trapped radiation environment. He also provided a copy of his software package `RADMODLS`.

We are indebted to E.G. Mullen and S.M. Gussenhoven of *Phillips Laboratory Geophysics Directorate* (PLGD) for providing the CRRES Science Summary Data Base, parts of the CRRES/PROTEL and CRRES/HEEF databases, the models CRRESRAD and CRRESPRO, and their assistance with the data analysis.

The involvement of A.A. Beliaev in the TREND-2 study has been made possible by M.I. Panasyuk, director of INP/MSU, who also provided BIRA/IASB with the Russian trapped radiation models.

C.E. McIlwain has kindly provided BIRA/IASB with a revised copy of a software code developed by A. Hassitt at *University of California San Diego* (UCSD), La Jolla,

to compute atmospheric densities averaged over drift shells.

A. Konradi has sent a copy of the directional AP-8 model block data sets to BIRA/IASB. D. Bilitza has transferred the original versions of the AP-8 trapped particle models and the MSIS and IRI software to BIRA/IASB.

S. Szita acknowledges a studentship from University College London.

We acknowledge the Director of BIRA/IASB, Baron M. Ackerman, who gave full support to the TREND-2 study and its realisation. A. Simon and the administrative staff at BIRA/IASB and MSSL have provided a most efficient assistance to the project manager of TREND-2. They are all deeply acknowledged for their cooperation.

Chapter 1

General overview and background

In the introduction to this chapter (Sect. 1.1), a general description of the radiation belts and the physical processes active within them is presented. Parts of this description follow a recent review paper by Van Allen (1991). In Sect. 1.2 we recall the coordinate systems used to map radiation belt fluxes and the concept of drift shell. Section 1.3 contains a description of the NASA trapped radiation models. In Sects. 1.4–1.14 we outline the objectives and content of each of the following chapters in this final report. Each chapter corresponds to a work package of the TREND-2 study.

1.1 Introduction

The Earth's magnetosphere extends about 10 Earth radii toward the Sun and hundreds of times that far in the direction away from the Sun. Its outer boundaries and much of its physical dynamics are attributed to the solar wind—the tenuous, ionized, magnetized gas (plasma) that flows outward from the solar corona through interplanetary space. The solar wind does not readily penetrate the geomagnetic field but compresses and confines the field around the Earth. The sunward boundary is located where the external pressure of the flowing solar wind equals the internal pressure of the geomagnetic field. A complex process of interconnection of the solar wind's magnetic field and the geomagnetic field stretches out the magnetic field in the direction away from the Sun, creating the long magnetotail.

A radiation belt is an interior feature of a magnetosphere and comprises a population of energetic, electrically charged particles (electrons, protons, and heavier atomic ions) durably trapped in the magnetic field of the planet. In this context the

term energetic conventionally means kinetic energies $E \geq 30\,\mathrm{keV}$. A radiation belt is toroidally shaped, encircles the planet, and its axis of rotational symmetry coincides with the magnetic dipolar axis of the planet. To a first approximation, each particle therein moves with constant energy and independently of all other particles along a helical path encircling a magnetic field line. This motion is subject only to the Lorentz force of a static magnetic field on a moving electrically charged particle, namely $q(\boldsymbol{v} \times \boldsymbol{B})$, where q is the particle's electrical charge, $\boldsymbol{v}$ its velocity, and $\boldsymbol{B}$ the local magnetic field intensity. The angle between $\boldsymbol{v}$ and $\boldsymbol{B}$ (the pitch angle of the helix) tends toward either 0° or 180° at the magnetic equator during each latitudinal excursion and becomes 90° at mirror or reflection points in the northern and southern hemispheres as the particle penetrates into the stronger magnetic field near the planet. The helix drifts slowly in longitude, westward for $q > 0$ (protons and other ions) and eastward for $q < 0$ (electrons), so as to generate the overall toroidal shape of the trapping region. The drift velocity is proportional to the particles' kinetic energy.

In this simplified, idealized case of motion in a vacuum in a dipolar magnetic field, each particle has an infinite residence time. All of this was shown theoretically in 1907 by Størmer. The Størmerian approach is usually supplanted by characterizing a particle's motion with three adiabatic invariants, corresponding to the three cyclic components of motion having widely different periods, namely, gyration around $\boldsymbol{B}$ (~milliseconds), latitudinal oscillation (~seconds), and longitudinal drift (~hours).

The magnetospheric properties are an essential part of its gross phenomenological character. They define the external environment and reflect the internal properties of the planet. The energetic particle population places important constraints on the practicality of in situ measurements and on the survival of electronic and optical equipment, human flight crews, animals, and other life forms flown therein. The particle population of the Earth's radiation belts makes it dangerous for humans without massive shielding to do more than quickly pass through them.

The diverse particle phenomena in the Earth's magnetic field have been studied intensively, both observationally and theoretically, since Van Allen's discovery of their existence in 1958. In addition, a series of artificial radiation belts were produced by the United States and the Soviet Union in 1958 and 1962. The energetic particles (principally electrons) in these artificial belts were the decay products of radioactive fission nuclei injected into the magnetic field by nuclear bomb bursts at high altitudes. Other temporary radiation belts are formed naturally deep in the magnetosphere by spectacular injection events like that of 24 March 1991.

The physical mechanisms for the creation of magnetospheric phenomena are of an electromagnetic nature. Within the solar system, the minimum condition for the existence of a planetary radiation belt is that the planet's dipole magnetic moment be sufficiently great that the flow of the solar wind is arrested before it reaches the

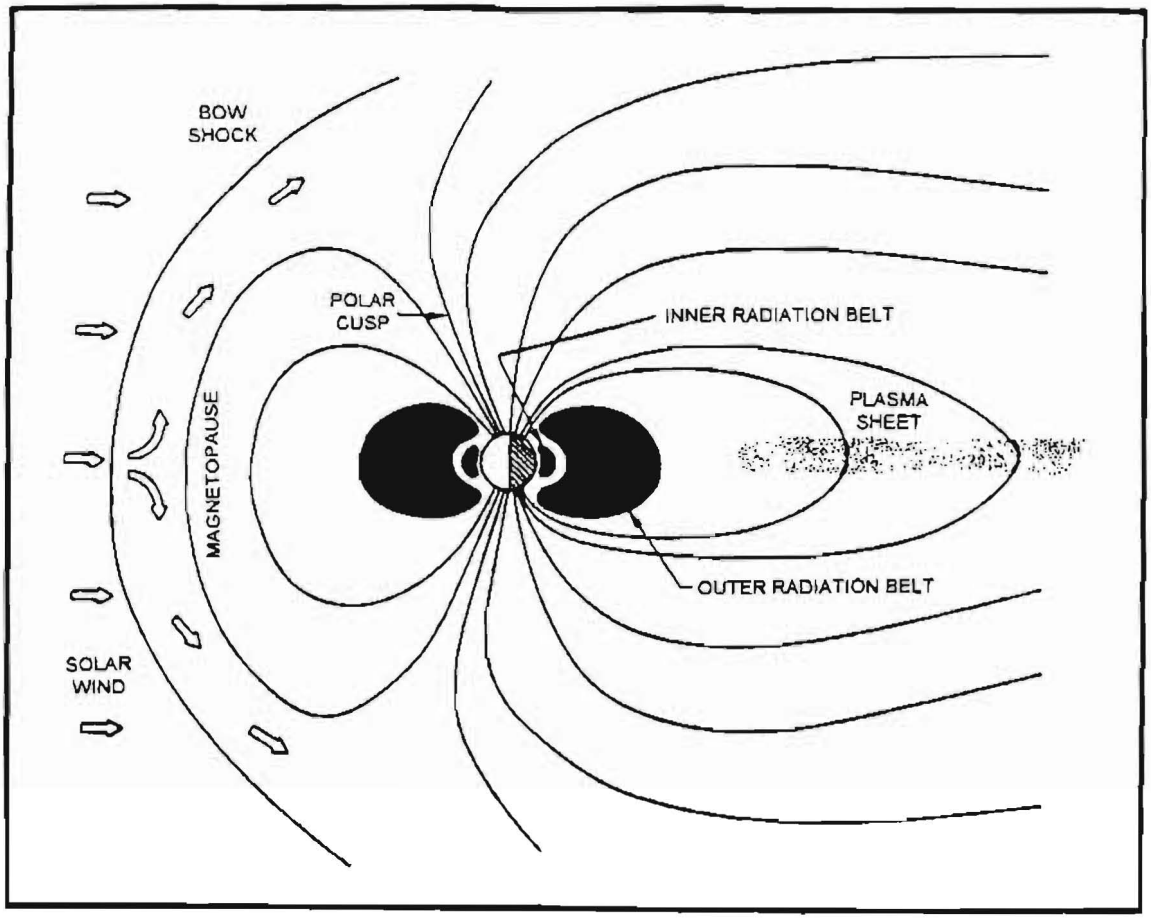

Figure 1.1. Principal features of the Earth's magnetosphere to approximate scale in the noon-midnight meridian plane cross section

top of the appreciable atmosphere or the surface of the planet. Durable trapping of charged particles is possible only if this condition is met. Otherwise, particles are lost quickly by collisions with atmospheric gas or the solid body of the planet. But even when the foregoing condition is not met, important plasma physical phenomena still occur.

The radiation belts and other features of the Earth's magnetosphere are shown to approximate scale in the noon-midnight meridian plane cross section of Fig. 1.1. The inner and outer radiation belts are two distinct features, defined by the intensity of particles capable of penetrating a specific shield ($\sim 1\,\mathrm{g\,cm^{-2}}$ of aluminium). In a generalized sense, there are as many different radiation belts as there are different species of particles and energy ranges that one wishes to distinguish. The principal sources of particles for the outer belt are the solar wind and the ionosphere; for the inner belt, sources are electrons and protons from the in-flight radioactive decay of

neutrons from nuclear reactions produced by galactic cosmic rays and solar energetic particles in the tenuous gas of the upper atmosphere. The eventual fate of magnetospheric particles is to become part of the atmosphere, to collide with satellites or particulate matter or to escape into space. The first two sources of particles are responsible for most of the gross geophysical manifestations of the magnetosphere (aurorae, geomagnetic storms, and heating of the upper atmosphere). The third is responsible for the relatively stable population of very energetic protons and some of the energetic electrons in the inner radiation belt. It is noted that this third source would produce a radiation belt around a magnetized planet even if the solar wind did not exist.

The residence times of individual particles in the radiation belts of Earth, controlled by ionization losses in the atmosphere near the Earth (altitudes of < 400 km), increase rapidly to the order of years at a radial distance of about 8,000 km (1.25 Earth radii), then decline in a complex and time-variable way to values of the order of weeks, days, and minutes in the outer fringes. There are quite low intensities of radiation belt particles within a spherical shell of about 400 km thickness around Earth. This is the region of space flight that is relatively safe from the radiation point of view. The inner radiation belt extends from this lower boundary to an equatorial radial distance of about 12,000 km and the outer radiation belt from this point outward to about 60,000 km. There is considerable overlap of the two principal belts and a complex and time-variable structure in the outer one. Some sample omnidirectional intensities are $J = 2 \times 10^4\,\mathrm{cm^{-2}s^{-1}}$ of protons $E_\mathrm{p} > 30$ MeV in the most intense region of the inner belt; and $J = 3 \times 10^8\,\mathrm{cm^{-2}s^{-1}}$ of protons $E_\mathrm{p} > 0.1$ MeV, $J = 2 \times 10^8\,\mathrm{cm^{-2}s^{-1}}$ of electrons $E_\mathrm{e} > 0.04$ MeV, and $J = 1 \times 10^4\,\mathrm{cm^{-2}s^{-1}}$ of electrons $E_\mathrm{e} > 1.6$ MeV in the most intense region of the outer belt.

1.2 Mapping of radiation belt fluxes

Radiation belt fluxes usually are mapped in a geomagnetic coordinate system (B, L) introduced by McIlwain (1961). B is the magnetic field intensity at the point of measurement and L is a parameter defining the drift shell (B, L) of a trapped particle with pitch angle equal to 90° at the point of observation. For particles mirroring at this point B and L are adiabatic invariants, uniquely determined in terms of the first and second adiabatic invariants of motion μ and I (McIlwain 1961). For a particle not mirroring at the point of observation, i.e. having a pitch angle $\alpha \neq 90°$, the magnetic field intensity at the mirror point is $B_\mathrm{m} \equiv B/\sin^2\alpha$, and L_m is the L value determined by I_m, which in turn is obtained by tracing the field line passing through the point of observation down to the conjugate mirror points. Both B_m and L_m are adiabatic invariants.

Another drift shell parameter L^* was introduced by Roederer (1970). This pa-

rameter is determined by the third adiabatic invariant, i.e. the magnetic flux through the surface subtended by a drift shell. The parameter L^* also uniquely defines a drift shell. However, the calculation of L^* involves integrating over a whole drift shell, while for L it is sufficient to integrate over just one field line segment that is part of the drift shell. In addition, the conservation of the third adiabatic invariant is much more easily violated than the conservation of the first and second invariants. For these reasons, the (B, L) coordinate system introduced by McIlwain (1961) is more practical and the most commonly used one.

L is often associated with the equatorial distance of a magnetic field line. This notion is misleading for two reasons. Firstly, L is not constant along magnetic field lines, except in the case of a pure dipole field. Secondly, during its azimuthal drift motion a trapped particle moves over adjacent field lines, whose equatorial distance changes with longitude. The shape and radial extent of the magnetic field lines "visited" by a particle during its azimuthal drift motion may vary strongly with longitude. For instance, when passing from the midnight sector to the dayside sector the equatorial distance may decrease by as much as one Earth radius. This effect has led to the term "drift shell splitting", by which it was attempted to visualize the breakdown of the axial symmetry of the surface on which a particle is trapped[1]. Particles with different pitch angles on the same magnetic field line at a given longitude or local time drift in azimuth on different magnetic field lines with different equatorial distances. Their drift shells are characterized by different L^* and (B_m, L_m) values. The shape and position of a drift shell of a trapped particle are determined by the geomagnetic field distribution and the pitch angle at the point of observation and are described without any ambiguity by the coordinate pair (B_m, L_m). From now on, we will drop the subscript "m" and assume that the mirror point instead of the point of observation is considered in the calculation of (B, L).

The geomagnetic field distribution undergoes changes on widely different time scales, from less than 1 s to more than 10^5 year. Hence, the (B, L) values for a fixed point in space will change with epoch. For L values below about 3, the main effect is the slow secular variation, consisting of a decrease in the geomagnetic dipole moment (0.5% per decade), a change in tilt angle of the geomagnetic axis (6.5 arcmin per decade), an increase of the eccentric distance of the centre of the Earth's dipole (2.5 km per year), and similar secular variations of all higher order moments (Fraser-Smith 1987). The ensuing secular variation of the (B, L) coordinates has important consequences for the mapping of trapped particle fluxes at low altitudes, i.e. below about 2000 km.

[1] In a pure dipole field, the magnetic field and hence particle drift shells are axially symmetric with respect to the geomagnetic axis. As a consequence, the distance of closest approach of a particle remains constant during its azimuthal drift in a pure dipole field.

1.3 The NASA trapped radiation models

The distribution of the omnidirectional flux of protons and electrons has been measured since 1958 by different types of particle detectors flown in all regions of the magnetosphere.

The first empirical models of the radiation environment were designed at Aerospace Corporation and later on at NASA by J.I. Vette and colleagues (see Vette 1991b and Spjeldvik & Rothwell 1985 for comprehensive reviews). The latest versions of the NASA electron models are called AE-8 MIN and AE-8 MAX (Vette 1991a). These models refer to conditions of minimum and maximum solar activity, respectively. The corresponding proton models are AP-8 MIN and AP-8 MAX (Sawyer & Vette 1976). The E, L, B dependence of the omnidirectional proton and electron fluxes is stored as a three dimensional array in the models (Vette 1991a; see also the final report of the TREND study, Lemaire et al. 1991). Compressed versions of the proton models, called AP-8 MIC and AP-8 MAC, also have been released by NSSDC for use on computers with limited memory capacity. All the NASA models are in the public domain and available from NSSDC by FTP (Bilitza 1992).

The AP-8 and AE-8 models are distributed widely and will probably remain standards for some time yet, until new or updated models of the radiation environment are produced. Because of the secular variation of the geomagnetic field distribution which was mentioned earlier, some care should be taken when applying the NASA models for contemporary flux calculations, especially for low altitude missions. The first TREND study recommended to use exactly the same geomagnetic field models to calculate (B, L) as were used to build the trapped particle models. According to Vette (1991a and private communications), the Jensen & Cain (1962) model has been used to produce AP-8 MIN, AE-8 MIN and AE-8 MAX, and the GSFC 12/66 model (Cain et al. 1967), updated to 1970, to generate AP-8 MAX (Heynderickx et al. 1995). Consequently, the `UNIRAD` software has been adapted to accomodate these magnetic field models for flux calculations based on the empirical NASA models.

Since the NASA models were built more than twenty years ago, the location of the SAA has shifted considerably to the West compared to its location predicted by the old magnetic field models, due to the secular variation of the geomagnetic field distribution. The effect of this drift can be compensated by applying an eastward rotation to the geographic coordinates of the points where the flux is to be estimated (Heynderickx 1995). This feature has been implemented in `UNIRAD` as well. These improvements to the `UNIRAD` software have been described in Technical Note 1 and are summarised in Chapter 3.

1.4 Comparison of NASA and INP models

Trapped radiation belt models based on the NASA models AP-8 and AE-8 and on data from Soviet satellites have been produced in the Soviet Union to evaluate fluences and radiation doses on future space missions. Although the format of the Russian models is not basically different from the format of the NASA models, some differences remain and the fluxes predicted by the respective models differ somewhat.

As part of the Rider of the TREND-2 study, we have evaluated the models developed at the Institute for Nuclear Physics of the Moscow State University (INP/MSU). The INP models have been compared to the NASA models in Technical Note A. The results of this comparison will be submitted to *Journal of Spacecraft and Rockets* by Beliaev, Lemaire & Panasyuk, and are summarised in Chapter 2.

1.5 Improvements to UNIRAD

ESTEC has developed the software package UNIRAD to estimate radiation fluences and doses accumulated over specified orbits.

The ensemble of software routines in UNIRAD has been extended and upgraded at BIRA/IASB in the framework of the TREND-2 contract. A detailed description of the modifications is given in Technical Note 1 and in the latest version of the UNIRAD user manual. The new features are briefly outlined in Sects. 1.5.1–1.5.6 and described in some more detail in Chapter 3.

1.5.1 Correction of an error in AP-8 MIN

During the comparison of the NASA and INP models, D. Heynderickx and A.A. Beliaev have identified and corrected an error in the AP-8 MIN block data file originally distributed by NSSDC. It was found that two statements were out of sequence in the block data file for this particular model. This error did not exist in the compressed version AP-8 MIC which is used by most laboratories and space agencies for flux and dose calculations. The error was corrected and a copy of the updated file was sent to NSSDC, who will re-implement AP-8 MIN/MAX in their distribution.

1.5.2 Implementation of the Olson-Pfitzer dynamic magnetic field model

Originally, the UNIRAD software package made use of the routine SHELLG to convert geographic coordinates of the point of observation into (B, L) coordinates. SHELLG

uses a special transformation of coordinate systems that improves the speed of calculation of the second adiabatic invariant I from which L is derived. However, this coordinate transformation is only appropriate for geomagnetic field models with no external component. Therefore, SHELLG does not allow the inclusion of external magnetic field models.

In order to extend UNIRAD to be able to work with external magnetic field models, new software, called BLXTRA, has been developed at BIRA/IASB in the framework of the first TREND study. With the new routine (B, L) coordinates can be calculated for a combination of internal and external field models. The implementation of this extension meant that the main algorithm of SHELLG had to be abandoned and a new field line tracing algorithm had to be developed for BLXTRA.

The TREND team implemented five external magnetic field models: the model developed by Mead & Fairfield (1975), Tsyganenko's three models (Tsyganenko 1987, 1989; Tsyganenko & Usmanov 1982), and Olson & Pfitzer's (1977) tilt dependent model. TREND-2 added one more field model, i.e. Olson & Pfitzer's dynamic model (Pfitzer et al. 1988), which may be useful to map satellite observations for drift shells with L >3–4, where the magnetic field distribution is highly dependent on the solar wind conditions and on the intensity of the ring current.

The Olson & Pfitzer dynamic model and its implementation in BLXTRA are described in Sect. 3.1. Comparisons of (B, L) coordinates obtained with this model and with the other external field models, for quiet and disturbed magnetic conditions, also are presented in Sect. 3.1 and in Technical Note 1. The magnetic field strength obtained with the different external models is compared to magnetic field measurements made by the CRRES satellite.

1.5.3 New file formats and NAMELIST parameters

The program flow of the UNIRAD program suite has been optimized and documented by BIRA/IASB in the TREND-2 study. The format of the common interface file used by SAPRE, BLXTRA and TREP, and the format of the interface file generated by TREP for use in SHIELDOSE, EQFRUX and EQFRUXGA have been modified accordingly.

A complete description of the latest version of UNIRAD is provided in the user manual. The manual includes tables with the revised sets of NAMELIST parameters, descriptions of file formats and flow diagrams.

1.5.4 Implementation of pitch angle dependence

The (B, L) coordinates corresponding to a geographical position P define the drift shell of particles whose mirror point coincides with P, i.e. particles with local pitch angle $\alpha_P = 90°$. As emphasized in Sect. 1.2, particles moving through P with

$\alpha_P \neq 90°$ will mirror at another point Q further down on the field line passing through P. The drift shell for these particles is determined by a different pair of coordinates (B_m, L_m). This means that particles measured at this point generally are on different drift shells. When these particles drift around the Earth, they do not remain on common field lines unless the geomagnetic field distribution is axially symmetric. This effect has been called "drift shell splitting" by Roederer (1967) who consequently introduced a different characterisation of drift shells based on the parameter L^* (Roederer 1970), which is defined in terms of the third adiabatic invariant (the magnetic flux invariant Φ) instead of the second adiabatic invariant I on which McIlwain's (1961) L parameter is based.

According to McIlwain's (1961) definition the L parameter alone does not fully determine a drift shell since L is not constant on magnetic field lines (except for a pure dipole field). A drift shell is uniquely determined by the coordinate pair (B_m, L_m) as a surface formed by segments of magnetic field lines between conjugate mirror points. Therefore, drift shells which are tangent to one another or cut one another at a given longitude or local time where they have a common segment of field line, generally are separate from one another at a different longitude or local time—in Roederer's terms these drift shells "split". But since these drift shells are different entitities from the outset, there is no real need to infer a notion of splitting.

The confusion about "shell splitting" arises from the fact that it has become common practice to identify a whole magnetic field line by "its" L value, which approximately corresponds to its equatorial radial distance. This correspondence is exact only in the case of an axially symmetric geomagnetic field distribution such as a pure dipole field. It is confusing for all other geomagnetic field distributions. The correct use of the (B, L) coordinates (instead of L alone) to characterise a drift shell avoids all possible confusion, even when local time dependent magnetic field models are considered.

The field line tracing algorithm has been modified in BLXTRA so that it is now possible to calculate (B_m, L_m) coordinates. These coordinates depend not only on the geographic position of the point of observation but also on the pitch angle α. A pitch angle α can now be stored in the common interface file generated by SAPRE and used to calculate (B_m, L_m). The subscript "m" will be dropped from now on.

TREP has been modified so that it calculates (B, L) independently of BLXTRA with the correct magnetic field models and with pitch angle values specified on the common interface file. The directional versions of the AP-8 trapped radiation models have been added to TREP.

The new features of BLXTRA and TREP are most useful to calculate the (B, L) coordinates of particles entering a detector at a pitch angle $\alpha \neq 90°$. It enables one to map unidirectional fluxes measured at different pitch angles into different bins of (B, L) space, while with the previous versions of BLXTRA and TREP all these

measurements were mapped into one bin of (B, L) space. The improvements to BLXTRA and TREP have been applied to unidirectional proton flux measurements made by the CRRES/PROTEL proton telescope and to measurements made by the CRRES/MEA electron spectrometer. The results are presented in Sects. 3.2.3 and 9.2 and in Technical Notes 1 and 10.

1.5.5 Implementation of new environment models

New empirical flux models of the trapped radiation belts have been built on the basis of measurements made by the CRRES satellite. A trapped proton model called CRRESPRO (Meffert & Gussenhoven 1994) has been produced at PLGD. It has been modified by BIRA/IASB for implementation in TREP and is described in Technical Note 3 and Chapter 5. A new electron model MEA1 was developed by MSSL and also implemented in TREP by BIRA/IASB.

1.5.6 Other modifications

The field line tracing algorithm used in the first version of BLXTRA has been replaced by a more efficient and accurate algorithm developed by Pfitzer (1991) and further modified by BIRA/IASB.

As indicated in Sect. 1.3, the NASA trapped radiation models AP-8 and AE-8 should only be accessed with (B, L) values obtained respectively with the Jensen & Cain (1962) or the GSFC 12/66 model (Cain et al. 1967), updated to 1970 (Heynderickx et al. 1995). The modified TREP software now calculates (B, L) coordinates with these magnetic field models, bypassing BLXTRA, so that improper use of the AP-8 and AE-8 models is now impossible. In addition, it is possible to request a correction for the Westward drift of the SAA, as described in Sect. 1.3 and by Heynderickx (1995).

A new user manual for UNIRAD has been written by BIRA/IASB.

1.6 Access to the CRRES database and its evaluation

The TREND study identified specific weaknesses in the existing trapped radiation models and identified suitable satellite data sets for updating the models. TREND recommended the use of the results of the *Combined Release and Radiation Effects Satellite* (CRRES) mission, in combination with archived data sets, as input for a new modelling effort.

The Combined Release and Radiation Effects Satellite (CRRES) Program is a joint National Aeronautics and Space Administration (NASA) and U.S. Department of Defense (DOD) undertaking to study the near-Earth space environment and the effects of the Earth's radiation environment on state-of-the-art microelectronic components and other spacecraft components.

To perform these studies, CRRES was launched with a complex array of scientific payloads. Among the experiments supported by the CRRES Program, the Phillips Laboratory Geophysics Directorate (formerly AFGL, now PLGD) Space Radiation Effects Program (SPACERAD) is of particular relevance to the TREND-2 study. One of the aims of the SPACERAD Program is to update the static models of the Earth's radiation belts and develop dynamic models of the high-energy particle populations in the near-Earth environment. In addition, radiation-induced single event upsets (SEUs) and total dose degradation of state-of-the-art microelectronics devices are measured in a known space environment.

CRRES was launched on July 25, 1990 at 19h21 UT, into a Geosynchronous Transfer Orbit (GTO) with perigee at 350 km, apogee at 33,500 km, and an inclination of 18.1°. This orbit crosses both the inner and outer radiation belts. The orbital period is 9^h52^m, and the spin rate is 2 rpm. The spacecraft spin axis is maintained such that the angle between the solar direction and the normal to the top surface, containing solar panels, is always between 5° and 15°.

The spacecraft was designed for a one year mission duration with a goal of 3 years. Unfortunately, due to a battery failure, the mission was aborted on October 9, 1991, after 15 months of operation.

There are three primary mission objectives:

1. to study the effects of the natural radiation environment on microelectronic components and on high-efficiency gallium arsenide solar cells, and to map this environment;

2. to conduct Low-Altitude Satellite Studies of Ionospheric Irregularities (LASSII);

3. to conduct a series of chemical release experiments in the ionosphere and magnetosphere.

A description of all experiments has been compiled in Technical Note 4.

The CRRES instruments relevant for the TREND-2 study are:

1. PROton TELescope (PROTEL);

2. Medium Electron Analyser (MEA);

3. High Energy Electron Fluxmeter (HEEF);

4. fluxgate magnetometer.

The channel characteristics of the first three instruments are given in Technical Note 4.

At the start of the TREND-2 study, the telemetry data were still being processed, so that only preliminary descriptions of final data formats could be given. By that time, however, PLGD had released a Science Summary Data Base (SSDB) which contains one-minute averages of tentatively calibrated data from selected instrument channels. The SSDB was implemented at BIRA/IASB, together with new ephemeris files for all CRRES orbits.

A new interpolation routine for determining intermediate positions from the ephemeris files was developed and replaces the routine written by Heck (1992). The data format of the SSDB and a preliminary assessment of the data are presented in Chapter 6 and in Technical Note 4.

E.G. Mullen and S.M. Gussenhoven of PLGD have provided ten orbits of PROTEL data to E.J. Daly, who has forwarded them to BIRA/IASB. These data have been plotted in different coordinate systems to assess the feasability of using them for the creation of a new low-altitude trapped proton model. It became apparent that there are problems with background contamination at low altitude, which was confirmed by PLGD. There currently is no straightforward way to evaluate the background contamination and to subtract it from the data. For this reason, PLGD did not find it opportune to use the low altitude PROTEL database for the purpose of a modelling effort nor to let BIRA/IASB access the whole PROTEL database. Instead, E.G. Mullen sent BIRA/IASB a copy of the CRRESPRO trapped proton model developed from the PROTEL database, which is valid for $L > 1.4$. This model has been implemented in TREP, as described in Chapter 5 and in Technical Note 3.

1.7 AZUR data analysis

WP 2.2 of the Rider to TREND-2 involves the implementation of the AZUR database at BIRA/IASB. The AZUR satellite was launched in November 1969 in a polar orbit. It had two particle telescopes and two omnidirectional detectors for protons and electrons on board. High quality data were collected for about seven months.

BIRA/IASB has acquired the database from NSSDC and installed it. A routine has been written to convert the raw counts in the data files to physical units. Plots have been produced of the first days of data, in various coordinate systems. It appears that background contamination is negligible and that the data provide

excellent coverage of the loss cone. Thus, they will prove very useful in a follow-up study of the low altitude environment. It should be noted that the directional proton measurements made by AZUR constituted the database used to implement solar cycle dependence to the AP-8 MIN model, resulting in the creation of AP-8 MAX. Nevertheless, this excellent data set has not been fully exploited and could be used in a further study to build a new directional proton flux model.

1.8 Implementation of a new proton model

As the low altitude part of the full PROTEL database has not been released by PLGD, TREND-2 has been unable to produce a new proton model as expected in the proposal. Therefore, it has been decided instead to implement PLGD's CRRESPRO model (Meffert & Gussenhoven 1994) into TREP. To this effect, the model files were transformed into the AP-8 model format by applying fit functions to the pitch angle distribution, since the source code of the pitch angle interpolation routines was not available. The resulting model files, one for quiet magnetic activity conditions and one for active conditions, have been added to TREP. The models are accessible through new NAMELIST parameters and are valid above $L = 1.4$.

The implementation of the CRRESPRO model in TREP has been used to calculate the proton flux along three types of orbit: GTO, LEO and polar. The proton flux distributions and energy spectra have been compared to those obtained with AP-8 MAX for the same orbits. The results for the GTO orbit also were compared to results published in the CRRESPRO documentation (Meffert & Gussenhoven 1994).

This part of the study is documented in Chapter 5 and in Technical Note 3. We plan to extend this work by applying more appropriate fit functions to the pitch angle distribution in the model files to account for the steep flux decrease in the loss cone, which is neglected with the fit functions suggested by PLGD. In a future study it would be appropriate to regenerate the low altitude part of the model with better coverage of the loss cone. This should be undertaken in close collaboration with PLGD.

1.9 Atmospheric cut-off

McIlwain's (1961) (B, L) coordinates have been very useful to map fluxes of protons and electrons averaged over drift shells. These coordinates depend only on the geomagnetic field model. Energetic proton and electron fluxes trapped in the magnetosphere above 1000–2000 km altitude are well organised in terms of the geomagnetic coordinates (B, L). At lower altitudes, however, the Earth's atmosphere erodes the inner edge of the radiation belts. Between 100 km and 1000 km altitude

the flux of energetic particles has a steep gradient which is directly controlled by the density distribution of the atmosphere and of the ionosphere, but not by the distribution of the magnetic field intensity B as it is at higher altitudes. Furthermore, the variation in the magnetic field intensity B is relatively small (a few percent) for a change in altitude of 1000 km over which the atmospheric density and the intensity of energetic protons and electrons decrease by several orders of magnitude. This indicates that B is not a very appropriate variable to map the low altitude flux distribution of Van Allen belt particles.

The limitations of the (B, L) coordinate system at low altitudes already have been noted by McIlwain (1990, personal communication) in the previous TREND study, where it has been recommended to use at low altitude a coordinate depending on the atmospheric density distribution. In the TREND-2 study we have examined this question in detail and have considered several alternative coordinates which are discussed in Chapter 4 and in Technical Note 2.

The equatorial pitch angle α_0 is the first alternative coordinate that has been suggested to replace B or B/B_0. The second alternative is the angle $\varphi = \arcsin[(B - B_0)/(B_c - B_0)]$ introduced by Daly & Evans (1993). When B varies from B_0 to B_c, φ varies from 0° to 90°.

The third option is an average of the atmospheric density over a drift shell. To calculate this average density we have adapted a program developed by A. Hassitt at UCSD. A revised copy of this program has kindly been sent to J. Lemaire by C.E. McIlwain. As part of the TREND-2 study we replaced the old Anderson & Francis (1964) atmospheric model by the MSIS model developed by Hedin (1987) and added the IRI ionospheric model and the plasmaspheric extension of Carpenter & Anderson (1992). We also added the IGRF and GSFC 12/66 (Cain et al. 1967) geomagnetic field models to the Jensen & Cain (1962) model already implemented in Hassitt's software.

The atmospheric densities are weighted by the energy dependent collision cross sections of incident particles with the major atmospheric atoms and molecules and ionospheric and plasmaspheric ions, by means of a routine that takes into account all relevant collision processes with atmospheric and ionospheric constituents.

The distribution of the AP-8 MIN and AP-8 MAX fluxes has been plotted versus the shell averaged density n_s. It has been found that the distribution of proton fluxes versus n_s along magnetic field lines is almost identical for minimum and maximum solar activity conditions for $L < L_{max}$, where L_{max} is a threshold value that depends on the energy of the incident particle (for $E_p = 1$ MeV $L_{max} \simeq 1.7$). This new finding corroborates a result obtained by Pfitzer (1990) that at low altitudes (350–500 km) the distribution of the fluxes of AP-8 MIN and AP-8 MAX is determined by the atmospheric density distribution corresponding to minimum and maximum solar activity conditions.

Our results have lead us to recommend the use of $\log n_s$ as a coordinate to map future proton models for $L < L_{max}$. For higher L values atmospheric scattering is not the major process determining the distribution of particle fluxes along magnetic field lines. In this case, cross-L and pitch angle diffusion due to electric and magnetic fluctuations are the dominant processes.

This work is documented in Chapter 4 and in Technical Note 2. Further extensions of this study could be envisaged in a future study to include the effect of pitch angle diffusion and cross-L diffusion averaged over drift shells.

1.10 Geosynchronous environment

WP 3.1 was devoted to the statistical study of the electron flux at geostationary orbit. To this purpose the Meteosat-3 SEM-2 electron flux data have been used to make a statistical survey. Average fluxes, energy spectra, anisotropies and probabilities of occurence of fluxes exceeding certain levels have been determined as a function of local time and geomagnetic activity indices.

The median fluxes and threshold fluxes for 95% and 5% occurrence have been determined during substorm injection events as well as for quiet conditions. The spectral index of the differential energy spectra have also been calculated and plotted. Fourier analysis of the SEM-2 data also has been performed. Significant peaks at the periods of 12 hours and 24 hours have been identified as well known local time variations.

Furthermore, the loss rate of 42–300 keV electrons at geostationary orbit is of the order of 40% per day, in the absence of new injection events. High energy (200–300 keV) electron flux enhancements lag behind low energy (43–60 keV) enhancements by one day. This is consistent with the recirculation model of Fujimoto & Nishida (1990).

The results of the correlation analysis and superposed epoch analysis have been presented in Chapter 7 and Technical Note 6-7.

1.11 Wavelet analysis

As part of the Rider WP 1.2, MSSL has re-examined the SEM-2 data from the standpoint of wavelet analysis using the program ONDELET-3, developed at the Université Catholique de Louvain (UCL), and which has been supplied to MSSL by BIRA/IASB.

This study suggests the existence of a minimum repeat period of 3 hours for injection events. The results are described in Sect. 7.5 and in Technical Note 6.

1.12 Comparison of SEM-2, LANL and CRRES data

As part of WP 3.1, MSSL acquired electron data from the *Los Alamos National Laboratory* (LANL). These geosynchronous data have been interfaced with the MSSL software system. Similarly, data from the MEA and HEEF instruments on CRRES were acquired and processed by MSSL for the period of July 1990 to October 1991.

The local time distribution of the electron fluxes obtained by these two satellites has been compared to that of the MeteoSat SEM-2 electron measurements. Large differences in the measurements for the different satellites are observed at low energies as well as at high energies. Furthermore, a comparison of the SEM-2 data to the AE-8 models indicates that the NASA models underestimate the electron flux at lower L values and overestimate it at higher L values.

There is however good agreement between the CRRES HEEF and MEA instruments. The MEA data agree well with the SEM-2 data, using the L parameter to compare data taken at different positions. There are however significant differences with the LANL data by a factor of up to 15. Because of the unresolved calibration problem with the LANL data, TREND-2 does not recommend to use them in the creation of new trapped radiation belt models. On the other hand, the good agreement between MEA, HEEF and SEM-2 data leads us to consider them as valuable databases in the creation of new radiation environment models.

This work is reported in Chapter 8 and in Technical Note 8.

1.13 Study of the CRRES outer electron belt

WP 3.2 was devoted to the statistical study of CRRES/MEA data for electrons of energy in the range 110–1633 keV. These data have been made available and transferred to MSSL by A.L. Vampola. The data have been analysed in close collaboration with A.L. Vampola who visited MSSL and attended a TREND Progress Meeting at BIRA/IASB in June 1994.

Electron pitch angle distributions were obtained from the MEA data. Different coordinate systems have been used to map the observed fluxes: (B, L), $(B/B_0, L)$, (LT, L), $(B_\mathrm{m}/B_0, L)$, $[\log(B_\mathrm{m}/B_0), L|$ and (α_0, L) (B_m and L_m were calculated with BLXTRA which allows the calculation of these quantities for $\alpha \neq 90°$, as indicated above). The standard deviation was also calculated and binned in the different coordinate systems.

This work is reported in Chapter 9 and in Technical Note 9, where it is concluded that the $[\log(B_\mathrm{m}/B_0), L]$ and (α_0, L) coordinates provided good coverage

and produced systematic variations and acceptable standard deviations in the outer radiation belt. However, since the (α_0, L) coordinate system is much simpler to visualize and does not exaggerate the data resolution in the loss cone, this pair of coordinates is strongly recommended by TREND-2 for future modelling of the outer radiation belt. A first attempt at such a model has been described in Technical Note 10 and is reported in Chapter 9.

1.14 Analysis of GOES-7 electron and proton data

The energetic particle data from the GOES-7 geostationary satellite have been transferred to MSSL. The analysis software developed for SEM-2 has been adapted to analyse this new data source. These tasks and a comparison of GOES-7 and SEM-2 data constitute WP 1.3 of the Rider to TREND-2.

Autocorrelation of both data sets has been performed. Local time distributions of the GOES-7 data have been summed into daily averages. Correlation coefficients between K_p and the electron flux of GOES-7 have been determined as a function of time offset for electron energies > 2 MeV. From this analysis it could be concluded that periods of 27 and 13 days appear in the electron data. A 22 day period is seen in the proton data.

The GOES-7 data revealed that the SEM-2 electron flux at high energy (202–300 keV) contained some substorm component. The changes in 43–60 keV electron flux, 202–300 keV flux and > 2 MeV flux when K_p is enhanced, occur in sequence (i.e. the flux of the lower energy electrons is enhanced earlier than the flux of the higher energy electrons), with a total elapsed time of 3 days. This is in support of the recirculation model of Fujimoto & Nishida (1990), i.e. for a process of heating ambient magnetospheric plasma up to radiation belt energies over a time scale of the order of 3 days.

This work has been described in Chapter 10 and in WP Report 3.

Chapter 2

Evaluation of the INP radiation belt models

2.1 Introduction

In the sixties and seventies NASA has developed a series of empirical trapped radiation belt models for proton and electron fluxes (Vette 1991b). The last versions are AP-8 MIN and AP-8 MAX for protons (Sawyer & Vette 1976) and AE-8 MIN and AE-8 MAX for electrons (Vette 1991a), where MIN, MAX refer to conditions of minimum and maximum solar activity, respectively. In addition, NSSDC released compressed versions of the two AP-8 models, i.e. AP-8 MIC and AP-8 MAC, which contain only part of the full model grid and were released for computer systems with limited memory capacity. It is recommended to use the full versions since they cover the region occupied by the radiation belts with a much finer grid than the compressed models, thus minimizing interpolation errors.

It should be pointed out that during the TREND-2 study an error has been found in the AP-8 MIN block data file (Heynderickx & Beliaev 1995). D. Bilitza at NSSDC was informed of this error and a copy of the corrected block data file was sent to him.

Following the long-term effort of NASA to produce a series of radiation environment models, the Soviet Union has developed in parallel its own models and software to determine the fluences and radiation doses on future satellite missions. INP/MSU has been most active in the U.S.S.R. and C.I.S. in developing trapped radiation environment models similar to those of NASA. Their most recent models have been developed by E.D. Tolstaya, G.I. Pugacheva and A.A. Gusev under the direction of M. Panasyuk, director of INP/MSU.

In order to assess the similarities and differences between both sets of models and

to put in a new perspective the modelling efforts in the C.I.S., TREND-2 has undertaken to compare in a systematic way the NASA and INP empirical models. The structure (format, gridding and file organisation) of both sets of models is compared in Sect. 2.2. Comparison of flux, energy spectra and fluences for different orbits and solar activity conditions are reported in Sect. 2.3. The computer programs used for this study have been developed by A. Beliaev in collaboration with J. Lemaire and D. Heynderickx.

A more detailed description of the results and the new software is given in Technical Note A and in the User Requirement Document (URD), Software Requirement Document (SRD), Architectural Design Document (ADD) and Detailed Design Document (DDD). This work constitutes WP 2.1 of the Rider to TREND-2.

2.2 Comparison of model structure and organisation

A description of the NASA and INP trapped radiation models is given below. Both sets of models are organised as a three-dimensional array: E, L, B for the INP models and $E, L, B/B_0$ for the NASA models. The differences resulting from the choice of different coordinate systems and from the interpolation methods are described.

2.2.1 Description of the NASA trapped radiation models

Several models of the trapped radiation environment were developed by NASA during the period 1964–1991 (Vette 1991b). The latest in the series of NASA models, AP-8 for protons and AE-8 for electrons, are described by Sawyer & Vette (1976) and Vette (1991a), respectively.

The AE-8 and AP-8 models are static representations of the trapped radiation environment, with local time dependence averaged out. There are four models, called AP-8 MIN, AP-8 MAX, AE-8 MIN, and AE-8 MAX. They correspond to conditions of solar minimum (MIN) and solar maximum (MAX).

The NASA models use the $(B/B_0, L)$ coordinate system. B/B_0 is used to locate the position along the field line and is defined as the ratio of the magnetic field strength at the point of observation to B_0, the minimal value of the magnetic field strength along the given magnetic field line[1]. B/B_0 ranges from 1 to some maximum value B_c/B_0 which corresponds to the relative geomagnetic field strength in the region where particles are absorbed by the upper atmosphere.

[1]For the NASA models, the value $B_0 = 0.311653/L^3$ is used. With this definition, B_0 is an adiabatic invariant since it depends only on L.

For a set of values of the particle energy E, covering the whole energy spectrum of trapped electrons and protons, the models provide the omnidirectional integral flux as $\log J(> E, B/B_0 = 1)$ for a series of discrete values of L, followed by scaled increments in B/B_0 corresponding to fixed decrements in $\log J(> E, B/B_0)$.

The subroutines TRARA1 and TRARA2 are used to interpolate in $(E, L, B/B_0)$ space. Interpolation problems with these subroutines were reported by Daly & Evans (1993). In order to improve the interpolation procedure, they suggested to replace B/B_0 by a new coordinate φ defined as

$$\varphi = \arcsin \frac{B - B_0}{B_c - B_0} . \tag{2.1}$$

The interpolation in (E, L, φ) space is done with a new subroutine TRARAP. Daly & Evans (1993) have shown that the ripples found in flux contour lines derived with the TRARA1 and TRARA2 subroutines, disappear almost completely when TRARAP is used.

Due to the fact that the original AP-8 MIN data sets were too large to fit in the memory of computers commonly used at the time of the release of this model, "compressed" versions of AP-8 MIN and AP-8 MAX were released by NSSDC. These compressed versions of the AP-8 models are described by Vette (1977) and are referred to as AP-8 MIC and AP-8 MAC.

To model the fluctuations of the electron flux in the outer radiation belt, the statistical standard deviation of the electron flux was introduced in AE-8. It is defined for the whole energy range of the model and for $3 < L < 11$ in the form of a discrete function (Vette 1991a), giving the standard deviation of $\log J(> E)$ as a function of L and E.

Table 2.1. Characteristics of the NASA trapped radiation models

Characteristic	AP-8	AE-8
Energy range (MeV)	0.1–400	0.04–7
L range	1.15–6.6	1.2–11
Epoch	1964/1970	1964/1970
Date of publication	1976	1983 (documented in 1991)
Number of satellites	24	24
Number of instruments	29	26
Number of data channels used	101	95
Channel-months of data	264	1303

The main characteristics of the AP-8 and AE-8 models are presented in Table 2.1, which is compiled from Vette (1991b) and Gaffey & Bilitza (1994).

2.2.2 Description of the INP trapped radiation models

Since the 1970s, INP/MSU is developing various models of the space environment. The first trapped radiation belt models developed at INP were published under the name Cosmos Model-82. The most recent models are described by Getselev et al. (1991). These models will be called "INP" models.

The NASA models were used as base models to produce reference spectra. More recent satellite observations were then compared to those reference spectra. The new data were collected with ISEE-1 (Williams & Frank 1984), SCATHA (Fennell 1982), GORISONT (Grafodatsky et al. 1989), COSMOS-900 (Goriainov et al. 1983, Vlasova et al. 1984), and INTERCOSMOS-19 (Volkov et al. 1985). Theoretical considerations based on low altitude satellite data (Savun & Yushkov 1985) have been used to update the flux values in a limited region of (E, L, B) space. Earlier versions of these models have been adopted as USSR State Standards (GOST 1986).

The INP models are a static representation of the trapped radiation flux, with local time dependencies averaged out as in the NASA models. There are four models, two for protons and two for electrons, one of each for solar minimum and for solar maximum, to be called INP-PROTMIN, INP-PROTMAX, INP-ELECMIN, INP-ELECMAX. These names correspond to data file names.

Unlike the NASA models, the INP models use a (B, L) grid instead of a $(B/B_0, L)$ grid. For each L value, equatorial flux values and a number of off-equator flux values are provided for a series of energies and for a set of tabulated values of B. The magnetic field models used to calculate B and L are assumed to be the same as those used for the NASA models, i.e. the Jensen & Cain (1962) model for both electron models and for the solar minimum proton model and the GSFC 12/66 model (Cain et al. 1967), updated to 1970, for the solar maximum proton model (Heynderickx et al. 1995). The more recent data used to update the Russian model did however use magnetic field models of later epoch.

2.2.3 Model ranges and limits

The ranges and limits of AE-8/AP-8 and of the INP models are briefly summarised in Table 2.2. The computer programs originally provided with the models issue warnings in case the fluxes are lower than a given threshold. The values of these thresholds are given as flux limits in Table 2.2.

Table 2.2. Limits of the NASA and INP trapped radiation models

Type of limit	AE-8/AP-8 Model Limits	INP Model Limits
Energy range	protons: 0.1–400 MeV electrons: 0.04–7 MeV	protons: 0.1–400 MeV electrons: 0.04–7 MeV
L range	protons: 1.15–6.6 electrons: 1.2–11	protons: 1.2–6.6 electrons: 1.2–7.0
B/B_0 range	empirical atmospheric cut-off	not applicable
B range	not applicable	empirical atmospheric cut-off
Flux range	$\geq 10\,\mathrm{cm}^{-2}\,\mathrm{s}^{-1}$	$\geq 1\,\mathrm{cm}^{-2}\,\mathrm{s}^{-1}$

2.2.4 Data file organisation and internal data representation

The NASA model data sets are stored as arrays of integers, with common scale factors stored at the beginning of each file. This structure limits the round-off errors and needs less storage space. The structure of the database is the same in the file and in computer memory, thus simplifying the process of loading the data.

Since the computerised version of the INP models was developed only for Intel-based PC compatible computers, binary format was used to store the database. However, for the present study, the original ASCII data files were used to provide platform-independence. The database itself consists of a set of two-dimensional tables, each showing the (B, L) dependence of particle fluxes for a given energy. The files consist of a header of variable length, followed by a variable number of tables. The header contains the number of energy levels for each table in the file and the set of corresponding energy values. Each table begins with a one-line header, the L value for this table and the number of lines in this table. Each line of the table contains a B value followed by a set of flux values. In order to simplify the table look-up procedure, the routine `INPINIT` has been written to transform the sequence of tables into a more appropriate form (a source code listing of `INPINIT` is given in Technical Note A).

The (E, L, B) grid of the NASA models is denser than the grid of the INP models. For the proton models the INP grid is quite comparable to that used in the compressed NASA models AP-8 MAC and AP-8 MIC. The equatorial grid points for both sets of models are plotted in Figs. 2.1 and 2.2.

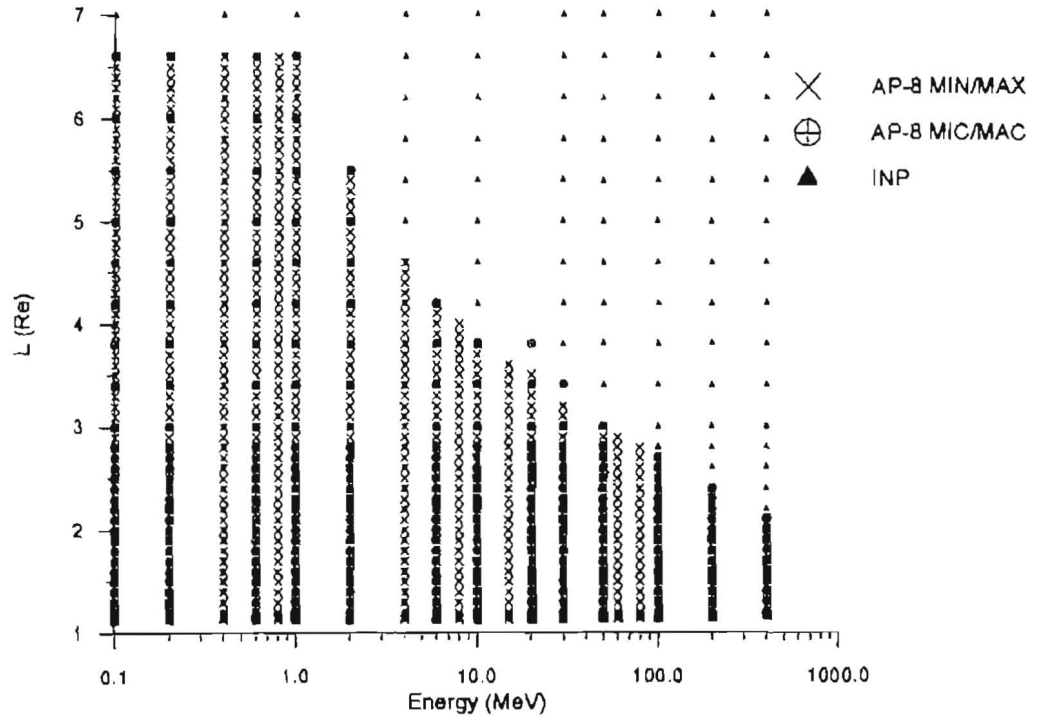

Figure 2.1. (E, L) grid of NASA and INP proton models

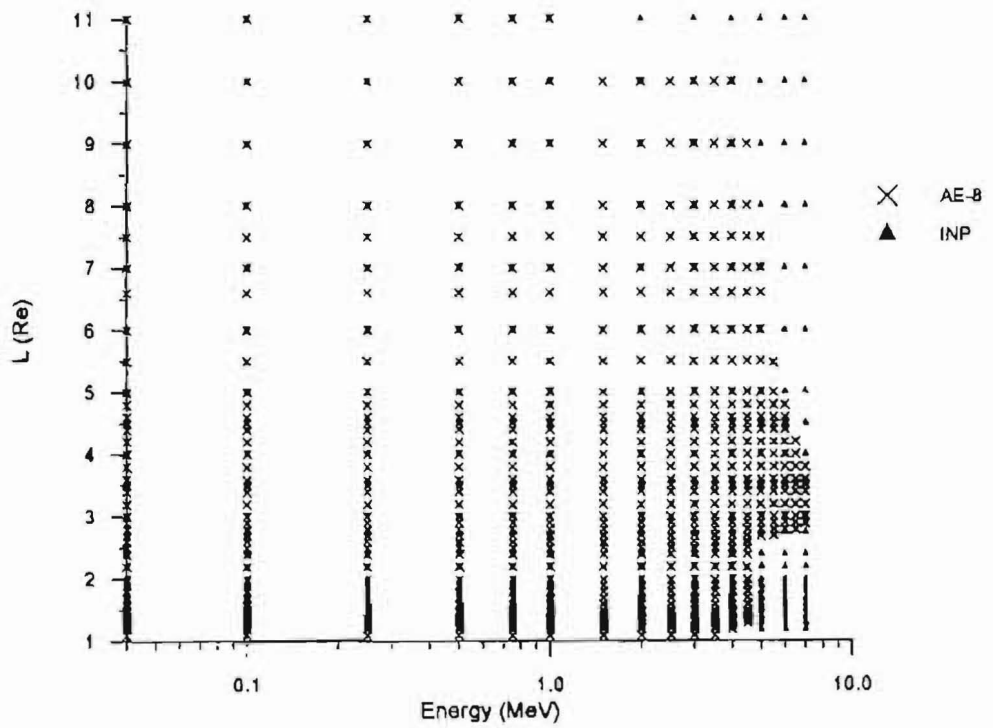

Figure 2.2. (E, L) grid of NASA and INP electron models

2.2.5 Interpolation methods

To interpolate between grid points in the AP-8 and AE-8 models the FORTRAN programs TRARA1 and TRARA2 are generally used. TRARA1 performs a linear interpolation of $\log J$ in energy space, while TRARA2 performs a linear interpolation of $\log J$ in $(B/B_0, L)$ space. The interpolation algorithm used in TRARA2 is described by Vette (1991a). An alternative method of interpolation was introduced recently by Daly & Evans (1993)—see Sect. 2.2.1—and is implemented in the subroutine TRARAP.

The interpolation method used with the INP models is less sophisticated and more straightforward compared to that used with the NASA models. Linear interpolation is performed for B and L, while logarithmic interpolation is performed for E. The interpolation subroutine used in the INP models is called FINTL1.

2.3 Flux comparisons

To compare the fluxes obtained with the two sets of models, the ratio $J_{\mathrm{INP}}/J_{\mathrm{NASA}}$ was calculated for each pair of corresponding models. The logarithm of the ratios is plotted as a colour map (in this document the colour maps are represented in grey scale; the original colour maps are given in Technical Note A). The TRARAP subroutine was used to interpolate between grid points in the NASA models. For the interpolation in the INP models, the FORTRAN subroutine FINTL1BO was written. Solid contour lines correspond to the flux values of the second model in the comparison. Points of the maps for which one or both models return fluxes below their respective thresholds were shaded with gray. It should be noted that for each map the colour palette was scaled differently, so that the colour range covers the whole range of values. Therefore, when comparing different figures, attention should be paid to the values shown in the colour legend of the map.

Vette (1991b) estimates that the errors in the NASA models are "about a factor of two". He also noted that "the greatest error should be expected where steep gradients in spatial or spectral distributions exist". Therefore, we will also consider here that when the fluxes of the INP and NASA models agree to within a factor of two the models are in satisfactory agreement with each other.

The comparison between the full and "compressed" NASA models can also be made with the software developed during this study. Comparisons of results obtained with TRARA2 and TRARAP for the same model are also possible with the same software.

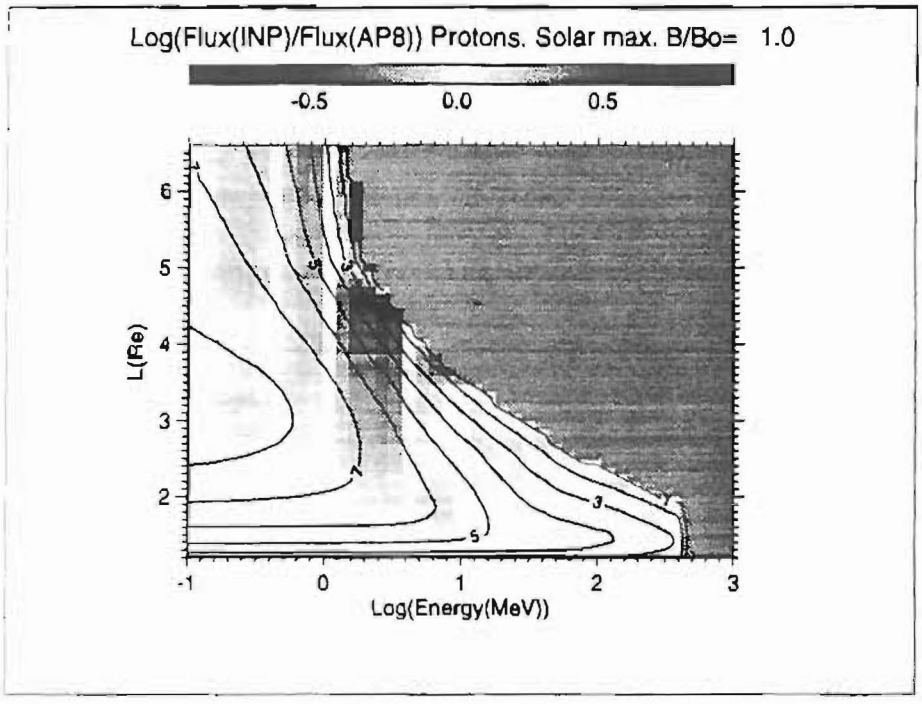

Figure 2.3. Comparison of equatorial proton fluxes for solar maximum

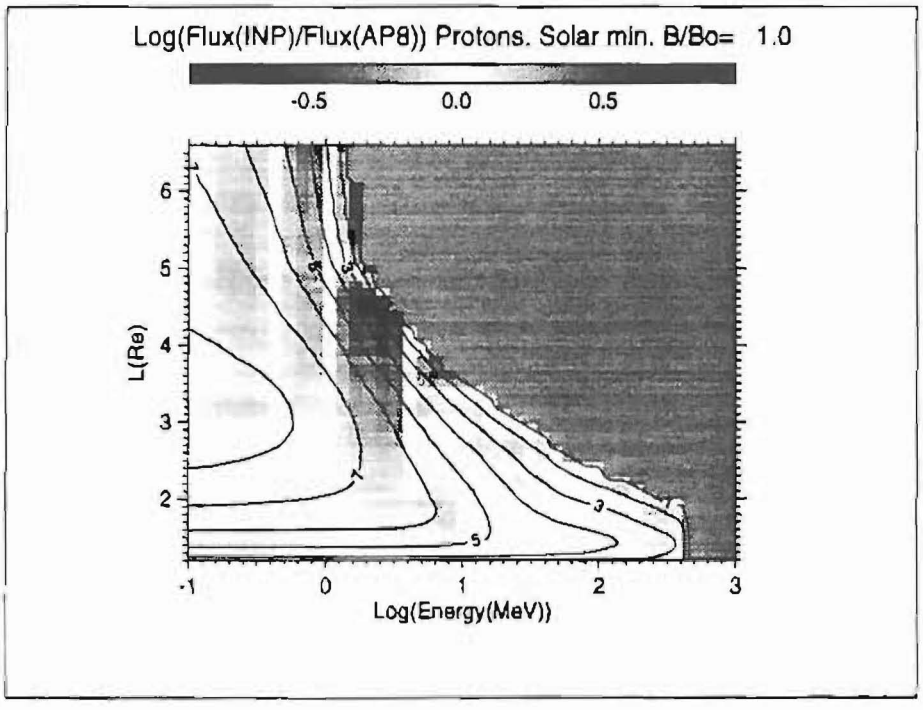

Figure 2.4. Comparison of equatorial proton fluxes for solar minimum

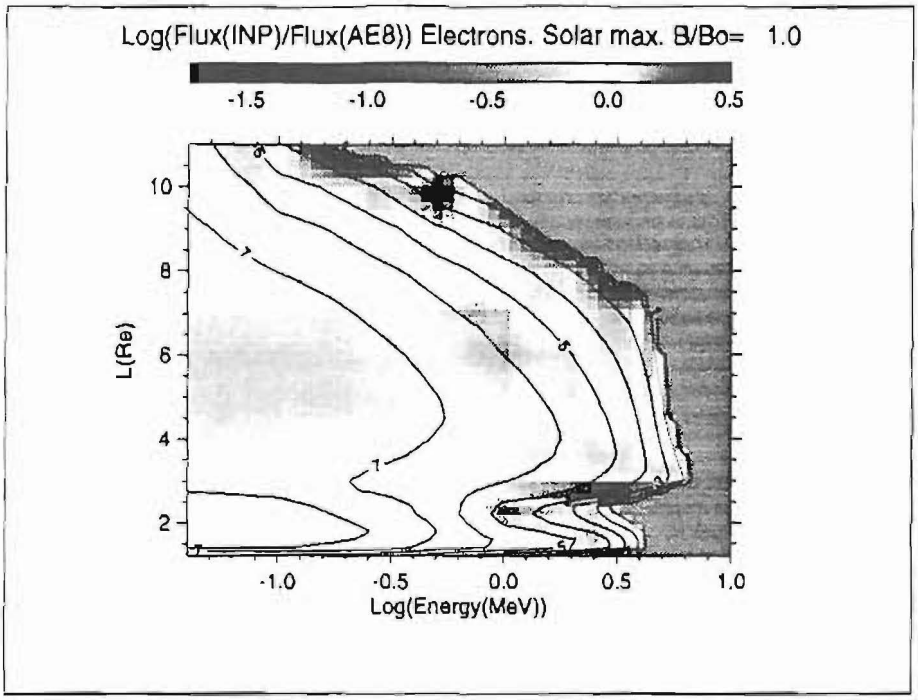

Figure 2.5. Comparison of equatorial electron fluxes for solar maximum

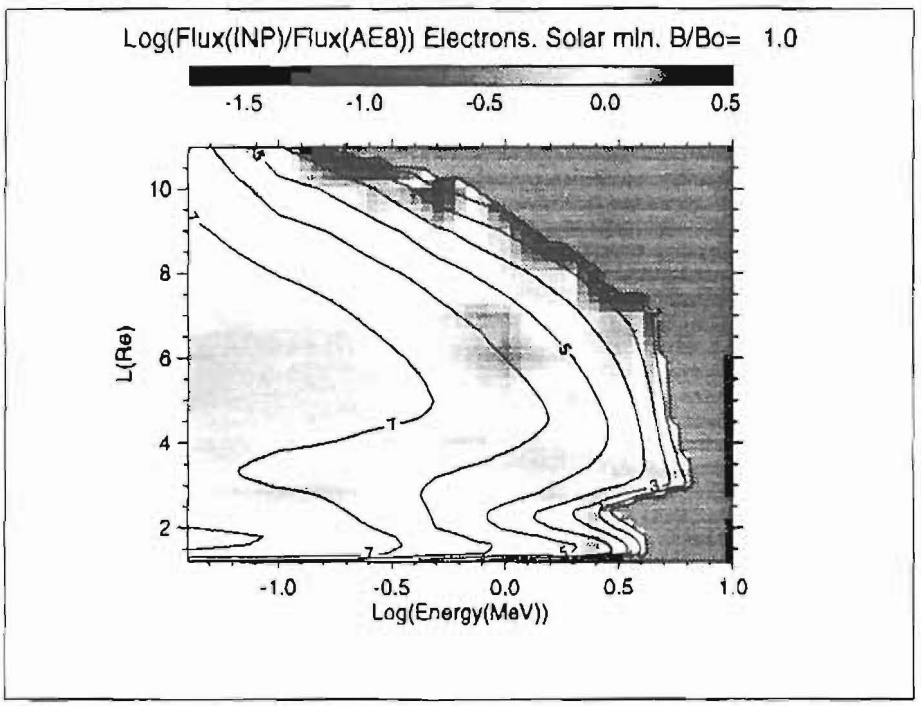

Figure 2.6. Comparison of electron equatorial fluxes for solar minimum

2.3.1 Equatorial fluxes

Figures 2.3 and 2.4 compare the equatorial proton fluxes obtained with the INP and NASA proton models for solar maximum and solar minimum, respectively. These figures illustrate the relatively good agreement between INP and AP-8 models. For most of the (E, L) space the difference is less then a factor of two. However, a difference of more than one order of magnitude is observed in the region of steep gradients close to the outer border of the radiation belt at the energy values 0.4, 1, 4 and 10 MeV, which are part of the grids of both the NASA and the INP models. This difference indicates that larger discrepancies between the models are present in the regions where the grid is sparser in the INP model because of the different interpolation methods used.

Over most of the (E, L) space the difference between the equatorial electron fluxes obtained with the NASA and INP models, shown in Figs. 2.5 and 2.6, does not exceed 0.1 in logarithm. There are larger differences, however, in the region of steep gradients. In most cases the INP models underestimate the fluxes compared to the AE-8 models, except for a small region around $E = 500$ keV and $L = 10$, where the INP model fluxes are half an order of magnitude higher than the AE-8 fluxes. These discrepancies occur in the proximity of the boundary of applicability of AE-8 where the accuracy of AE-8 itself is about an order of magnitude. It can therefore be concluded that both models give consistent results in the region where the flux is large enough and where the gradients are not too steep.

It can be concluded that near the geomagnetic equator both models produce comparable results. The largest discrepancies are found in the region of steep gradients where different methods of interpolation and different networks of grid points lead to differences in the interpolated fluxes. The limited number of observations in some regions of the magnetosphere as well as the fact that the observed flux at high altitudes is rather variable in time probably are the reasons for most of the discrepancies. Furthermore, since no external magnetic field is used to determine (B, L) in any of these models, the $(B/B_0, L)$ coordinate system becomes inadequate at $L > 6$.

2.3.2 Off-equator fluxes

To compare the models away from the geomagnetic equator colour maps were produced for protons of 2 MeV and 100 MeV and for electrons of 0.5 MeV and 2 MeV. The plots for 2 MeV protons and 0.5 MeV electrons for solar minimum are shown in Figs. 2.7 and 2.8. The low-L border where the particle flux decreases rapidly to zero corresponds to the atmospheric cut-off. Both models have similar cut-off values.

The differences between the two sets of models are much larger at lower energies

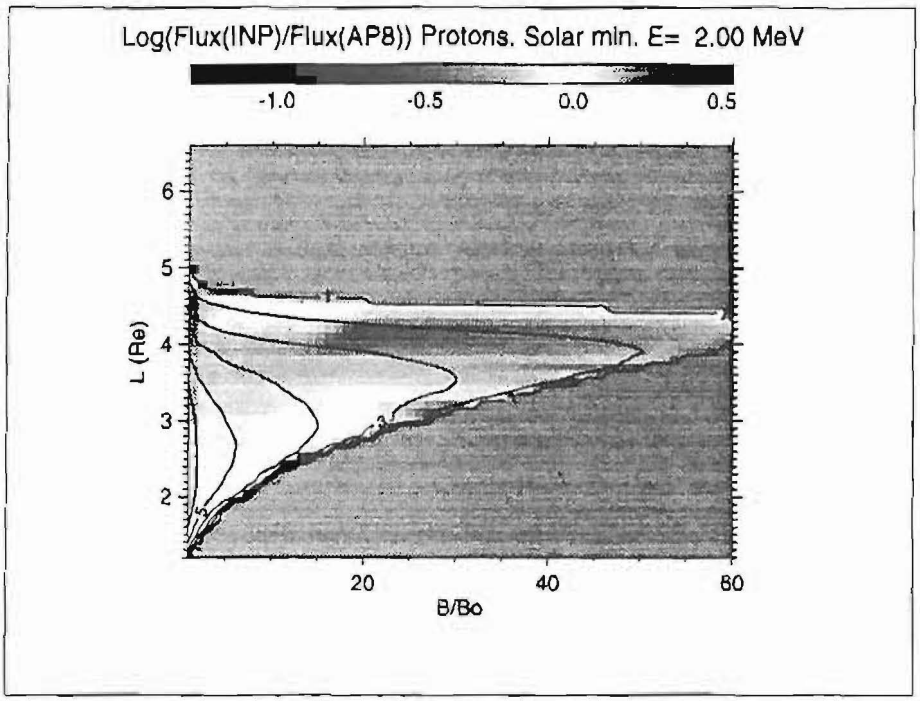

Figure 2.7. Comparison of 2 MeV proton fluxes for solar minimum

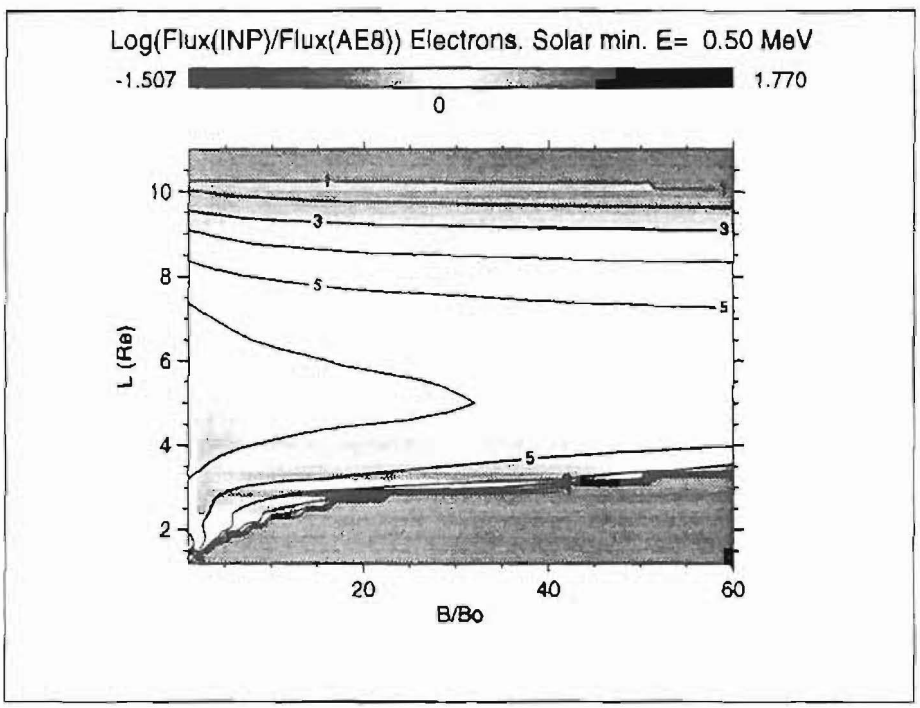

Figure 2.8. Comparison of 0.5 MeV electron fluxes for solar minimum

than at higher energies. For example, for 2 MeV protons the INP models underestimate the fluxes compared with the NASA models in most of the radiation belts. For 100 MeV protons the comparison gives agreement well below a factor of two difference, except in the region of atmospheric cut-off.

The comparison of electron fluxes in Fig. 2.8 shows that much better agreement is found in the region of the inner electron belt ($L < 2.5$) than in the region of the outer electron belt. Again a poor agreement is observed at the edges of the radiation belts, where the flux gradients are largest. Note that both sets of models differ significantly between $L = 2.5$ and $L = 3$. The largest discrepancies are found for solar maximum conditions. For solar maximum, the INP model electron flux in this region is an order of magnitude lower than the AE-8 MAX flux.

Colour maps of the flux ratio versus E and B/B_0 have also been produced for a constant value $L = 6.6$. These maps for proton and electron fluxes are shown in Figs. 2.9 and 2.10, respectively, for solar minimum. In Fig. 2.9 bright vertical stripes are seen at the energy values where the energy grid points of the INP models coincide with those of the NASA models. For other energies larger differences are observed. This shows again the importance of the interpolation methods used in retrieving fluxes from tabulated empirical models.

Figure 2.10 shows that small corrections (less then a factor of two) were introduced in the INP electron models at $L = 6.6$ and energies 0.5–1 MeV. The discrepancies in this region cannot be explained by interpolation artefacts, since both models have a similar grid spacing in this region. However, the corrections in the INP are small and the differences with the NASA models mostly are well inside the range of uncertainty of the NASA model.

It can be concluded that although some differences between the NASA and INP electron models exist in limited regions of E, L, and B/B_0, on the whole the models show reasonable agreement with each other.

2.3.3 Solar cycle variations

To compare the influence of the solar cycle on both sets of models, colour maps were produced for $\log(J_{\mathrm{MAX}}/J_{\mathrm{MIN}})$, for both the NASA and the INP models.

The AP-8 models for protons have the same equatorial fluxes for solar minimum and maximum, except in a narrow region near the atmospheric cut-off where the fluxes are lower for the AP-8 MAX model. The INP proton flux models show the same feature. Additional small flux variations over the solar cycle across the whole trapped radiation belt region are present in the INP models. This can be explained by the fact that the fluxes in the INP models are given to only three digits. Round-off errors together with interpolation errors can produce the small flux variations.

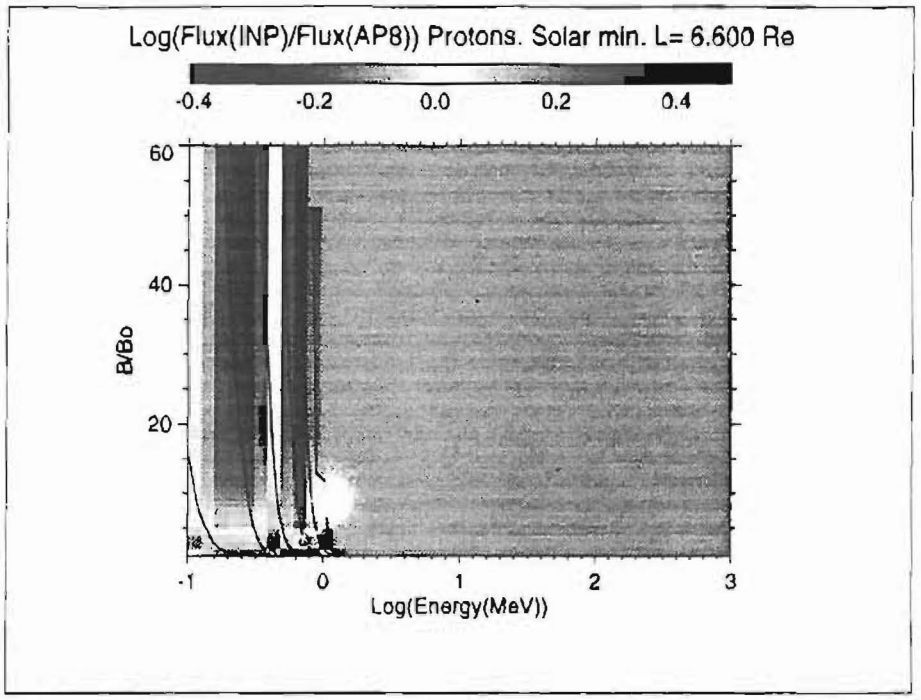

Figure 2.9. Comparison of proton fluxes for $L = 6.6$ for solar minimum

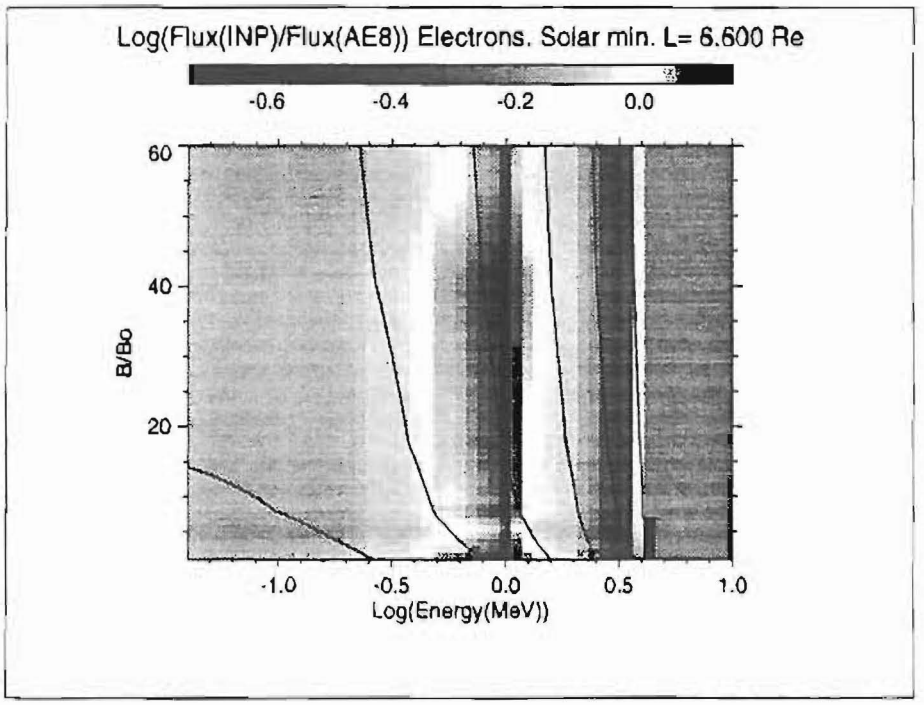

Figure 2.10. Comparison of electron fluxes for $L = 6.6$ for solar minimum

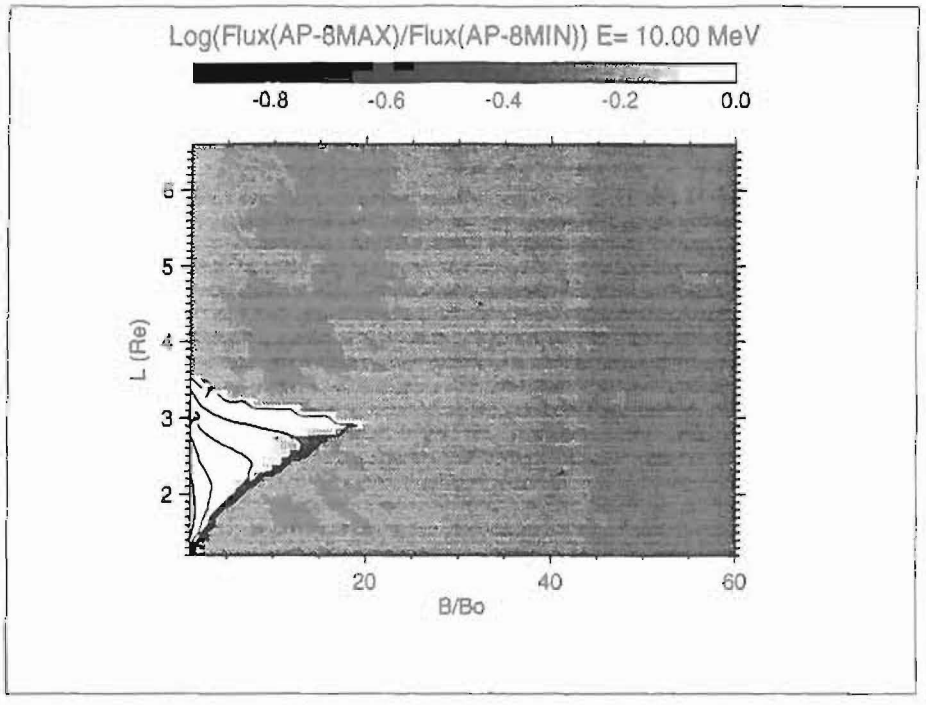

Figure 2.11. Solar cycle variations of the AP-8 model fluxes for 10 MeV protons

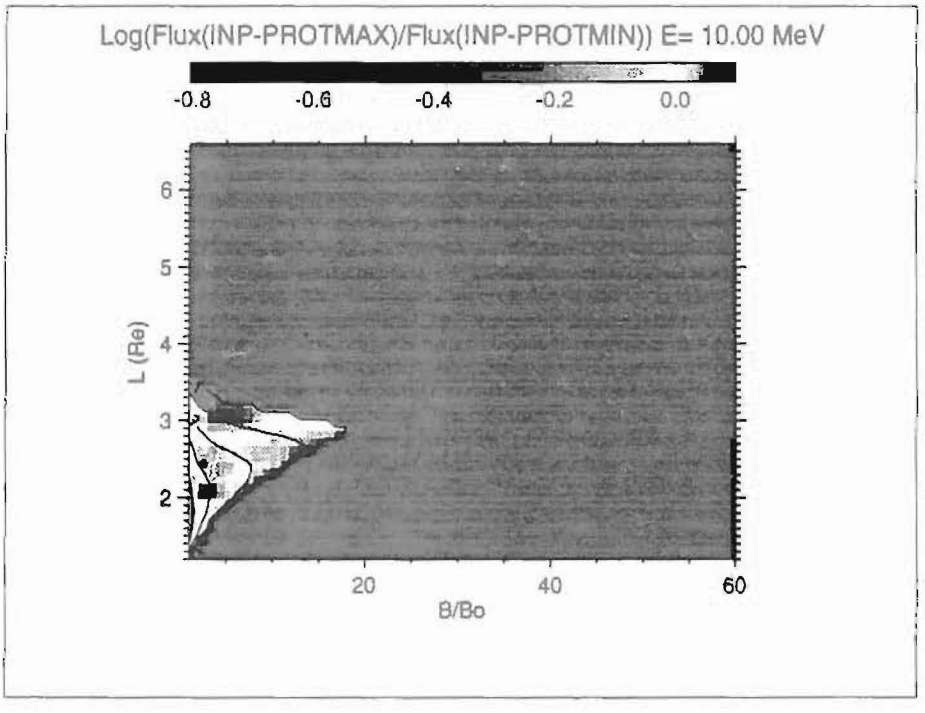

Figure 2.12. Solar cycle variations of the INP model fluxes for 10 MeV protons

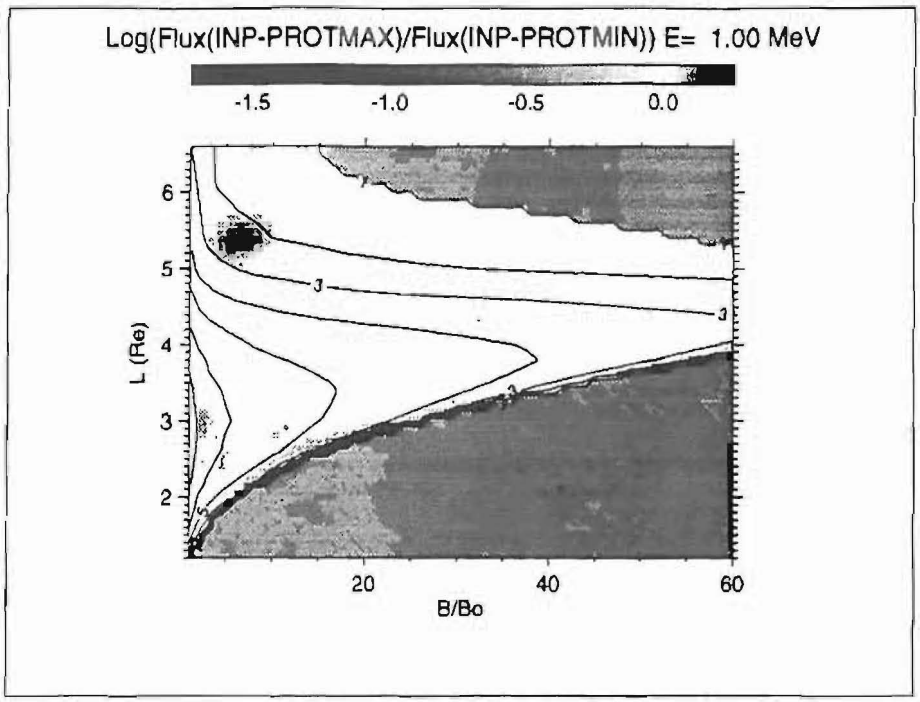

Figure 2.13. Solar cycle variations of the INP model fluxes for 1 MeV protons

The comparison for the electron models showed that for $L < 5$ the NASA and INP models produce similar flux variations over the solar cycle. For most energies in this region the flux during solar maximum is about a factor of 6 larger than during solar minimum. The flux in the region of $L > 5$ remains constant in AE-8 while it shows small variations in the INP models, similar to the variations in the INP proton models.

Figures 2.11 and 2.12 were produced for proton energy $E = 10\,\text{MeV}$. These figures illustrate that both the INP and the NASA models have solar cycle flux variations at all points along magnetic field lines. Figure 2.13 shows the ratio of the INP proton fluxes at 1 MeV between solar maximum and solar minimum. The red spot around $L = 5.5$ and $B/B_0 = 5$–10 is due to the fact that additional satellite data has been used in this region to update one of the INP models. However, this difference is rather small (a factor of 2 at most).

Figures 2.14 and 2.15 are obtained for electrons of 2 MeV. The electron fluxes in both models have similar field line dependences. Again one can clearly see small discrepancies, which we attribute to round-off errors.

The colour map in Fig. 2.16 shows the ratio of the INP electron fluxes at solar maximum and minimum for $L = 6.6$. We explain the observed pattern as the result of the interpolation. This serves as a good illustration of the disadvantages of the method of interpolation selected for the INP models.

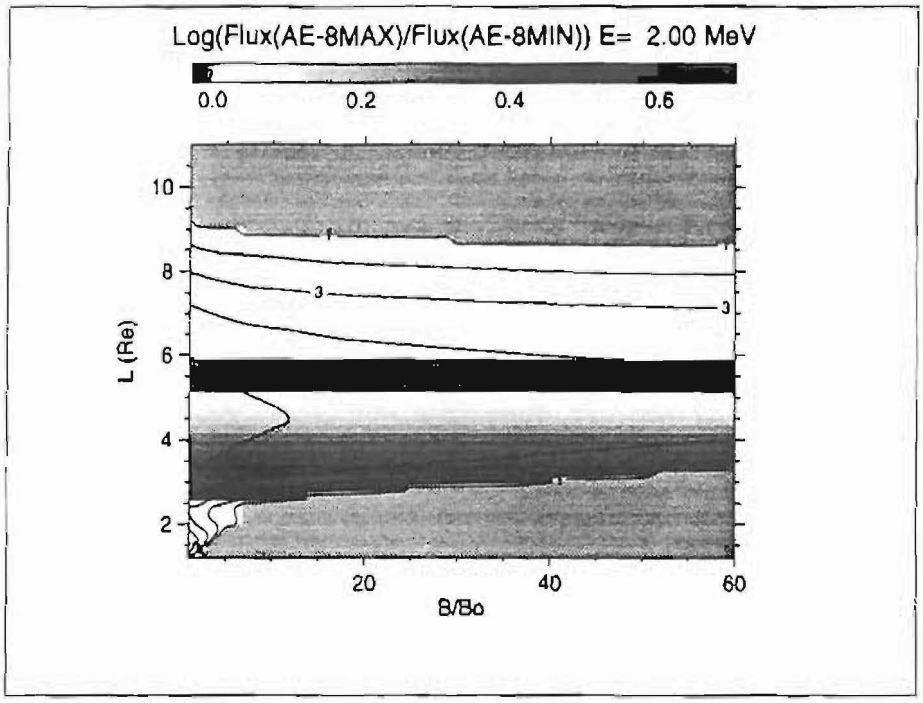

Figure 2.14. Solar cycle variations of the AE-8 model fluxes for 2 MeV electrons

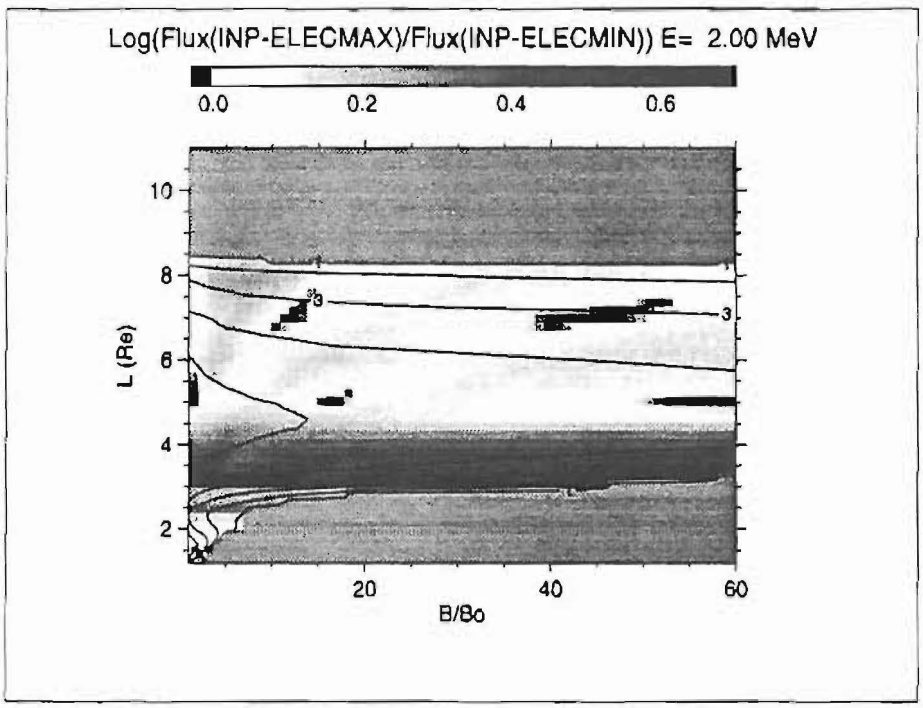

Figure 2.15. Solar cycle variations of the INP model fluxes for 2 MeV electrons

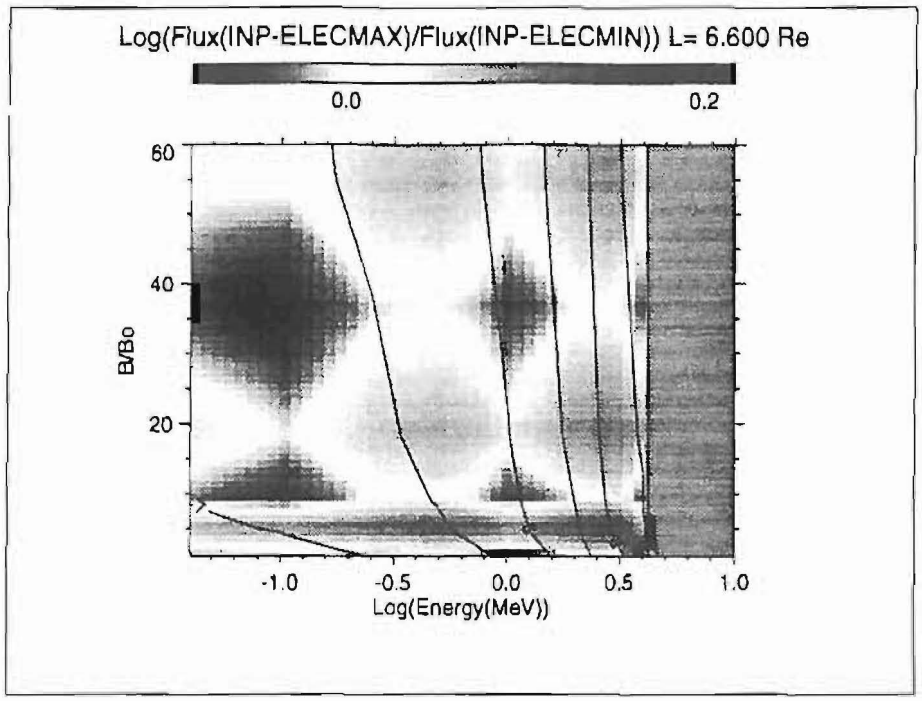

Figure 2.16. Solar cycle variations of the INP model electron flux at $L = 6.6$

2.4 Fluence comparisons

To study the differences in the NASA and INP models, daily particle fluences for a LEO orbit were calculated using both models. The fluence calculations were made for a circular orbit with altitude 500 km and inclination 51.6° (one of the possible orbits for a Shuttle-Mir mission). Spacecraft positions in geographical and (B, L) coordinates were calculated with UNIRAD for 30 second intervals during 24 hours. The Jensen and Cain (1962) magnetic field model and the GSFC 12/66 model (Cain et al. 1967), updated to 1970, were used to calculate (B, L) coordinates for electrons and protons respectively, as recommended by Heynderickx et al. (1995). Daily fluences for a set of energy values were then calculated for the (B, L) coordinates using both the NASA and INP models for solar maximum. The resulting fluences for protons and electrons are shown in Figs. 2.17 and 2.18, respectively. The results show good agreement between daily fluences calculated with the INP and NASA models. It should be noted that most of the LEO orbit is located close to the atmospheric cut-off in the region of steep flux gradients. However, the averaging along the orbit produces fluences which differ at most by a factor of two.

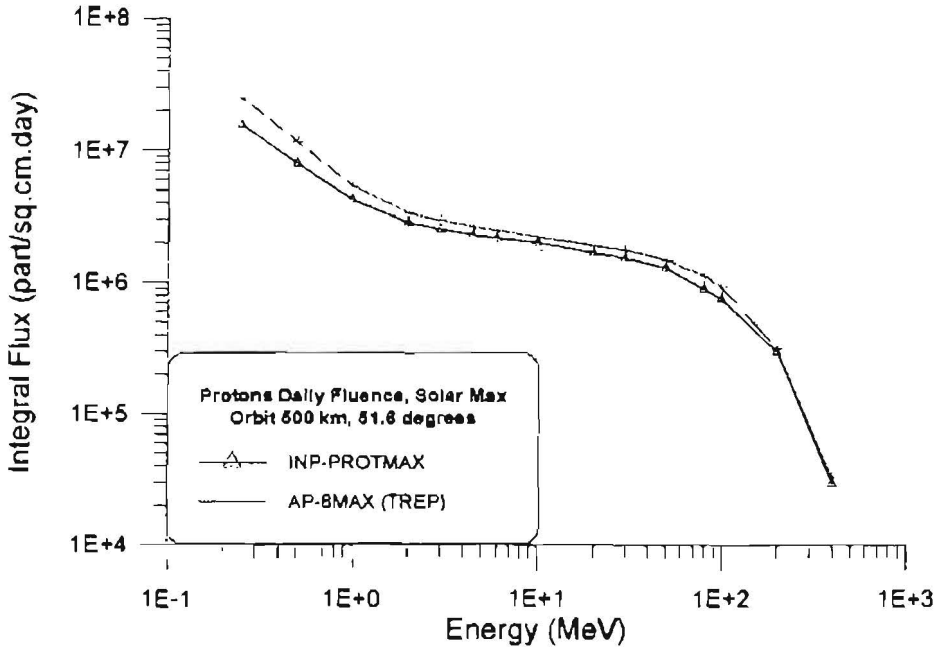

Figure 2.17. Daily proton fluence according to the NASA and INP models

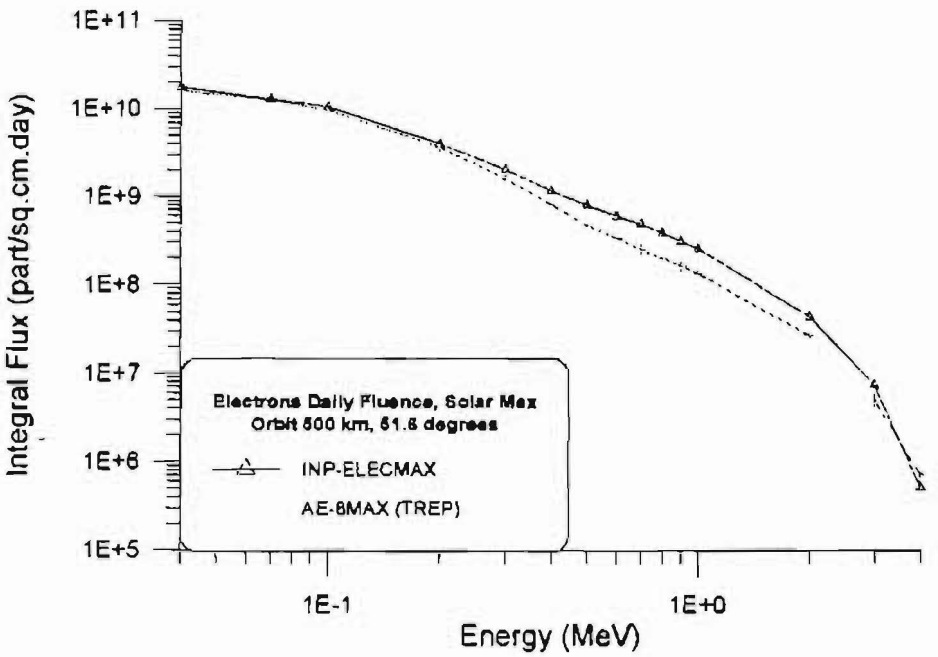

Figure 2.18. Daily electron fluence according to the NASA and INP models

2.5 Conclusions

The trapped radiation models developed at INP/MSU and at NASA use different interpolation methods and different grids of points to store the data. However, it can be concluded from the comparisons made in the present study that both the NASA and INP trapped radiation models produce similar fluxes in the bulk of the Earth's radiation belts where the largest fluxes are observed and where the gradients are not too large. There are differences between the models in limited ranges of L, E, and B/B_0, such as for electron fluxes during solar maximum for $L = 2.5$–3.

There are significant differences between the models in the regions of steep gradients. One of the reasons for this discrepancy is the different choice of the B or B/B_0 coordinate to organise the INP and the NASA models, respectively. Future trapped radiation models should be organised in another coordinate such as φ (Daly & Evans 1993) or the drift shell averaged atmospheric density n_s (Hassitt 1965b).

The present study also showed that there is a need for "standardizing" the models, i.e. specifying the methods of storing and accessing models values. This may simplify future use of the models and reduce the impact of different storage and interpolation methods on the flux values. It should be also taken into account that the methods currently used in the NASA models were developed 20 years ago and that modern computers can easily handle much more extensive calculations and finer grids.

Chapter 3

Improvements to UNIRAD

In this chapter we describe the changes made to the UNIRAD software routines BLXTRA and TREP.

After careful study of the program structure, we were able to significantly simplify the program flow and to eliminate several subroutines which were never called. In addition, a few minor errors were detected and corrected.

In Sect. 3.1, we document the addition of an external geomagnetic field model to BLXTRA, i.e. Olson & Pfitzer's dynamic model (Pfitzer et al. 1988).

In order to study directional particle flux measurements, pitch angle dependence had to be implemented in the software. This is described in Sect. 3.2. First, we replaced McIlwain's field line tracing algorithm INVAR in BLXTRA with an algorithm developed by Pfitzer (1991). The common interface file for SAPRE, BLXTRA, and TREP was modified so that the pitch angle is one of the input parameters for the latter two programs. The field line tracing now extends beyond the geographical location to the location of the mirror points determined by the pitch angle. In TREP, the mirror point magnetic field value is used to access AP-8 and AE-8 instead of the magnetic field value at the point of measurement (these points coincide for pitch angle 90°). In addition, a unidirectional version of the AP-8 proton models has been implemented. The differences between the coordinates (B_m, L_m) and (B, L) are discussed and illustrated.

The modified routines have been extensively tested. In particular, Pfitzer's (1991) field line tracing algorithm provides for better coverage of a field line than INVAR. The new software has been applied to CRRES measurements to illustrate the effects of the inclusion of pitch angle dependence.

As a result of continuing interaction with J. Vette, the question of which geomagnetic field models were used to construct AP-8 and AE-8 was finally resolved. It appears that AE-8 MIN, AP-8 MIN, and AE-8 MAX were built with the Jensen & Cain (1962) time-independent model with epoch 1960, while for the solar maximum

model AP-8 MAX the GSFC 12/66 model (Cain et al. 1967), updated to epoch 1970, was used. Consequently, these magnetic field models should be used also when the NASA flux models are accessed.

A disadvantage of this approach is that when the field models for these earlier epochs are used, the secular drift of the *South Atlantic Anomaly (SAA)* is not taken into account. Hence, we made a study of methods to correct for this effect. Three methods were compared in Technical Note 1, based on different ways of determining the position of the SAA. We found that a time-dependent eastward correction of the satellite position is in best agreement with observational data on the secular drift of the SAA. We studied the effect of this correction on a low-Earth orbit.

The new record structure of the common interface file and the new `NAMELIST` parameters for `BLXTRA` and `TREP` are described in the user manual for `UNIRAD`.

3.1 Implementation of the Olson & Pfitzer dynamic field model

The software package `BLXTRA` performs the conversion of geodetic coordinates to the magnetic coordinates (B, L) (McIlwain 1961) in the `UNIRAD` package. `BLXTRA` uses both internal and external geomagnetic field models. Recently, we added Olson and Pfitzer's dynamic external model (Pfitzer et al. 1988) to `BLXTRA`. In this section, we describe this model and its inclusion in `BLXTRA`.

3.1.1 The Olson-Pfitzer dynamic field model

Olson & Pfitzer's (Pfitzer et al. 1988) dynamic model for the external geomagnetic field was developed for event studies in the NASA *Coordinated Data Analysis Workshops (CDAW)*. It extends the Olson & Pfitzer (1974) tilt averaged and the Olson & Pfitzer (1977) tilt dependent models by modelling the variation of the strength and size of the major magnetospheric current systems in response to their interplanetary sources. The model is capable of accurately representing the dayside magnetic field at geosynchronous orbit for all magnetic conditions and the nightside field for non-substorm conditions. The model does not accurately represent the magnetic field in the inner tail region during storm conditions, because it does not include the extension of the Birkeland currents into the magnetosphere.

The dynamic model can be used to represent any set of magnetic conditions. In the model, the pressure of the solar wind is used to determine the scale and strength of the magnetopause currents. The ring current is driven by a modified D_{st} index in which the contribution of the magnetopause currents has been removed. At present, the tail currents are scaled in the same way as the magnetopause currents.

On the daylight side of the Earth, the model is able to predict the strength of the magnetic field at synchronous orbit to within 5 nT for magnetopause standoff distances between 7 and 11 R_E. Since the model does not yet include the effects of the asymmetric ring and Birkeland currents, it is not as accurate on the night side of the Earth.

In the following sections, we present the Olson & Pfitzer (1974) tilt averaged and the Olson & Pfitzer (1977) tilt dependent models, and we describe the scale factors used for each current system in the Olson & Pfitzer dynamic model (Pfitzer et al. 1988).

The Olson-Pfitzer tilt averaged model

The contribution of the external magnetic field is represented by the sum of two terms in Olson & Pfitzer's (1974) tilt-averaged model. The first term describes the magnetic field $\boldsymbol{B}_M$ produced by the magnetopause currents. The second term represents the field associated with the distributed currents, i.e. the ring current field $\boldsymbol{B}_R$ and the tail current field $\boldsymbol{B}_T$.

For the magnetopause field, Olson's (1969) model is used, which determines the magnetopause shape and currents self-consistently, using the pressure balance condition. The distributed currents are represented by wire loops (Olson 1974). They include the effects of both the quiet time ring current and the tail current.

The external magnetic field contributions in the *Solar Magnetic (SM)* (Russell 1971) coordinate system (x, y, z) are expressed as sums of terms of the form

$$\left.\begin{aligned} B_x &= \sum_{i=0}^{6}\sum_{j=0}^{3}\sum_{k=0}^{3}\left[a_{ijk} + b_{ijk}\exp(-0.015\,r^2)\right] x^i y^{2j} z^{2k+1}\,, \\ B_y &= \sum_{i=0}^{6}\sum_{j=0}^{3}\sum_{k=0}^{3}\left[c_{ijk} + d_{ijk}\exp(-0.015\,r^2)\right] x^i y^{2j+1} z^{2k+1}\,, \\ B_z &= \sum_{i=0}^{6}\sum_{j=0}^{3}\sum_{k=0}^{3}\left[e_{ijk} + f_{ijk}\exp(-0.03\,r^2)\right] x^i y^{2j} z^{2k}\,, \end{aligned}\right\} \tag{3.1}$$

$$\left.\begin{aligned} a_{ijk} = b_{ijk} &= 0 \quad \text{for} \quad i+2j+2k > 6\,, \\ c_{ijk} = d_{ijk} &= 0 \quad \text{for} \quad i+2j+2k > 5\,, \\ e_{ijk} = f_{ijk} &= 0 \quad \text{for} \quad i+2j+2k > 7\,, \end{aligned}\right\} \tag{3.2}$$

where

$$r = \sqrt{x^2 + y^2 + z^2}\,. \tag{3.3}$$

The coefficients in these expansions are given in tables by Olson & Pfitzer (1974) for $\boldsymbol{B}_M$ and $\boldsymbol{B}_R + \boldsymbol{B}_T$.

The model is based on quiet time data and should not be used to study storm time conditions. Since many of the input data were averaged over the dipole tilt angle ψ, defined as the complement of the angle between the north magnetic dipole direction and the Earth-Sun line (positive when the north magnetic pole is tilted towards the Sun), the model represents only the symmetric magnetospheric field configuration with the solar wind direction perpendicular to the geomagnetic dipole axis.

The Olson-Pfitzer tilt dependent model

The Olson & Pfitzer (1977) tilt dependent model is a revision of the Olson & Pitzer (1974) tilt averaged model. The revision was made because the tilt averaged model does not adequately represent the case $\psi = 0$, primarily at large distances on the midnight equator.

The SM components of the external magnetic field are represented as sums of terms of the form

$$\left.\begin{aligned} B_x &= \sum_{i=1}^{5}\sum_{j=1}^{3}\sum_{k=1}^{5}\left[A_{ijk} + B_{ijk}\exp(-0.06\,r^2)\right] x^{i-1}y^{2j-2}z^{k-1}\,, \\ &\qquad i+2j+k \le 9\,, \\ B_y &= \sum_{i=1}^{5}\sum_{j=1}^{3}\sum_{k=1}^{5}\left[C_{ijk} + D_{ijk}\exp(-0.06\,r^2)\right] x^{i-1}y^{2j-1}z^{k-1}\,, \\ &\qquad i+2j+k \le 9\,, \\ B_z &= \sum_{i=1}^{5}\sum_{j=1}^{3}\sum_{k=1}^{5}\left[E_{ijk} + F_{ijk}\exp(-0.06\,r^2)\right] x^{i-1}y^{2j-2}z^{k-1}\,, \\ &\qquad i+2j+k \le 9\,. \end{aligned}\right\} \qquad (3.4)$$

The coefficients in these expansions are themselves linear or quadratic expansions in terms of the dipole tilt angle ψ. The values of the coefficients are tabulated in Olson & Pfitzer (1977).

The Olson-Pfitzer dynamic model

The principal feature of the Olson & Pfitzer dynamic model (Pfitzer et al. 1988) is the introduction of variable strength factors multiplying the quiet models of the fields of the three current systems. The SM components of the magnetic fields are represented as expansions in the SM coordinates (x, y, z). The scaling of the three magnetic field contributions is described in the following sections (cfr. Olson & Pfitzer 1982).

Magnetopause currents The strength and size of the magnetopause currents are determined by means of a pressure balance equation that relates the kinetic pressure of the solar wind to the magnetic energy density of the magnetic field inside the magnetopause. The stand-off distance R_s, i.e. the distance from the centre of the Earth along the Sun-Earth line to the location of the magnetopause, is represented empirically in terms of the solar wind pressure ρV^2 as

$$R_s = \frac{98}{(\rho V^2)^{1/6}}\,, \tag{3.5}$$

where R_s is expressed in units of R_E, and ρ and V are the density and velocity of the solar wind, in units of particles/cm^3 and km/s, respectively.

The pressure balance formalism also provides a direct relation between the strength of the magnetopause currents and the solar wind pressure. The variation in the strength of the magnetopause currents is approximated by

$$S_M = \left(\frac{10.5}{R_s}\right)^3\,, \tag{3.6}$$

where 10.5 is the quiet time magnetopause stand-off distance used in the Olson & Pfitzer (1974) model.

Since the relative shape of the magnetopause remains unchanged for all values of the solar wind pressure, the magnetic field vector $\boldsymbol{B}_m(\boldsymbol{r})$ associated with the magnetopause currents can be expressed in terms of the field expansion for quiet times $\boldsymbol{B}_{Mq}$ at the point $\boldsymbol{r}'$ as

$$\boldsymbol{B}_M(\boldsymbol{r}) = S_M\,\boldsymbol{B}_{Mq}(\boldsymbol{r}')\,, \tag{3.7}$$

where

$$\boldsymbol{r}' = \frac{10.5}{R_s}\,\boldsymbol{r}\,. \tag{3.8}$$

Ring current The ring current system is scaled in terms of a modified D_{st} index, defined as

$$D_{st,m} \equiv D_{st} - 15\,(S_M - 1)\,, \tag{3.9}$$

with D_{st} given in nT. The scale factor quantifying the strength of the ring current is given as

$$S_R = 1 - 0.03\,D_{st,m}\,. \tag{3.10}$$

When the magnetopause is compressed, only the outer edges of the ring are compressed. Since the largest contributions of the ring are near L-values of 3 or 4, the size of the ring is not scaled, so that

$$\boldsymbol{B}_R = S_R\,\boldsymbol{B}_{Rq}\,. \tag{3.11}$$

The error introduced by this approximation is assumed to be small enough so that the representation of the storm time ring current system is reasonable.

Tail currents The contribution to the magnetic field due to the tail current system is scaled in the same way as the magnetopause contribution, both in strength and geometry:

$$\boldsymbol{B}_{\mathrm{T}}(\boldsymbol{r}) = S_{\mathrm{M}}\, \boldsymbol{B}_{\mathrm{Tq}}(\boldsymbol{r}')\,. \tag{3.12}$$

There is no apparent justification for this procedure, except that a suitable alternative has not been found.

3.1.2 Implementation in BLXTRA

The implementation of the dynamic field model in `BLXTRA` is based on Pfitzer's release of 13 May 1988. It is accessed by specifying `OUTER=6` in the `NAMELIST BLXTRA` used with UNIRAD.

Pfitzer provides the following default values for the input parameters:

$$\left.\begin{aligned} V &= 300\,\mathrm{km/s}\,, \\ \rho &= 25\,\mathrm{particles/cm^3}\,, \\ D_{\mathrm{st}} &= -30\,\mathrm{nT}\,. \end{aligned}\right\} \tag{3.13}$$

Other values for these parameters can be specified in the `NAMELIST BLXTRA` with the variables `VEL`, `DEN`, and `DST` for V, ρ, and D_{st}, respectively.

Values for the input parameters can be found in NSSDC's OMNITAPE data base or in the *Solar-Geophysical Data prompt reports*, published by NOAA, U.S. Dept. Commerce.

3.1.3 Application to CRRES SSDB orbits

In order to check the implementation of the external field models in `BLXTRA`, we calculated the model field values for two CRRES *Science Summary Data Base (SSDB)* orbits. The SSDB has been described in Technical Note 4.

The SSDB contains model values for B and L, calculated with the IGRF 85 model, updated to 1991, and Olson & Pfitzer's (1977) tilt dependent model (Kerns & Gussenhoven 1992). We illustrate the influence of the input parameters for the external magnetic field routines for two orbits, one during quiet magnetic conditions (orbit 251), and one during very disturbed conditions (orbit 588). We used the IGRF 90 model field, updated to 1991 for the internal field contribution. For the calculation of L, we made the assumption that the location of a measurement is a mirror point, i.e. the local pitch angle was set to 90°.

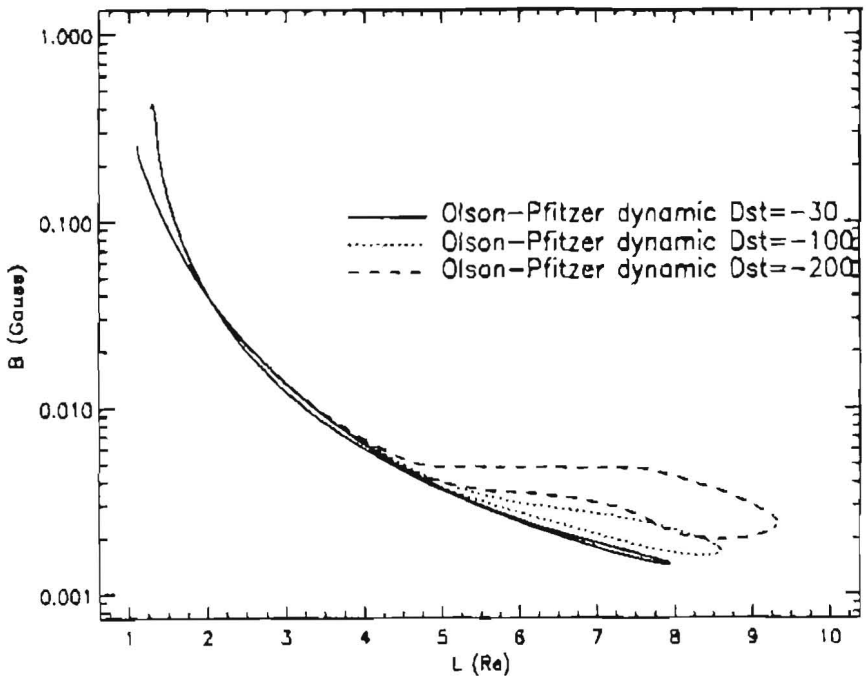

Figure 3.1. Influence of the D_{st} parameter on the magnetic field calculated with the Olson & Pfitzer dynamic magnetic field model (Pfitzer et al. 1988) for CRRES orbit 251. For both curves, $V = 300\,\mathrm{km/s}$ and $\rho = 25\,\mathrm{particles/cm^3}$.

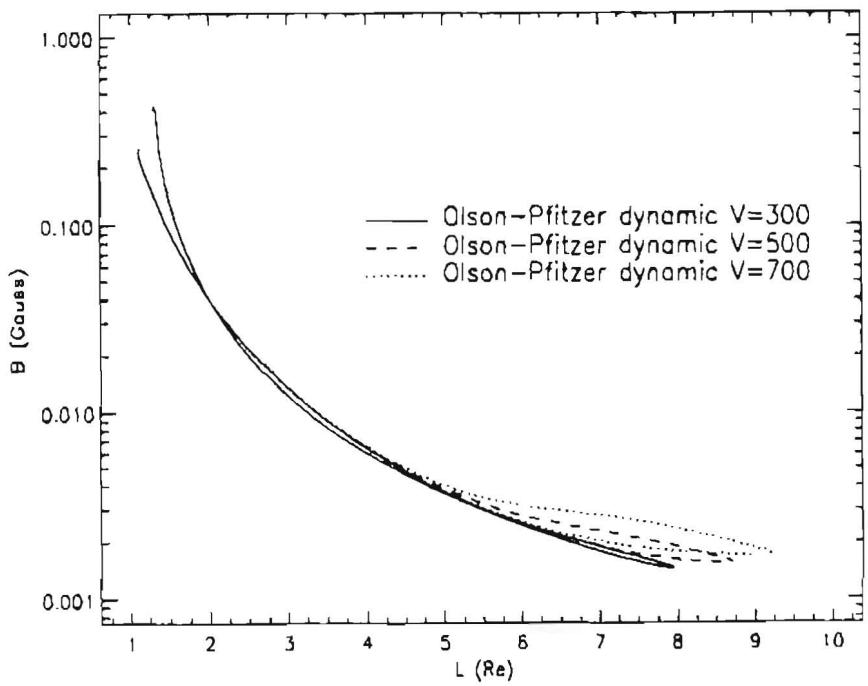

Figure 3.2. Influence of the value of V on the magnetic field calculated with the Olson & Pfitzer dynamic magnetic field model (Pfitzer et al. 1988) for CRRES orbit 251. For both curves, $D_{st} = -30\,\mathrm{nT}$ and $\rho = 25\,\mathrm{particles/cm^3}$.

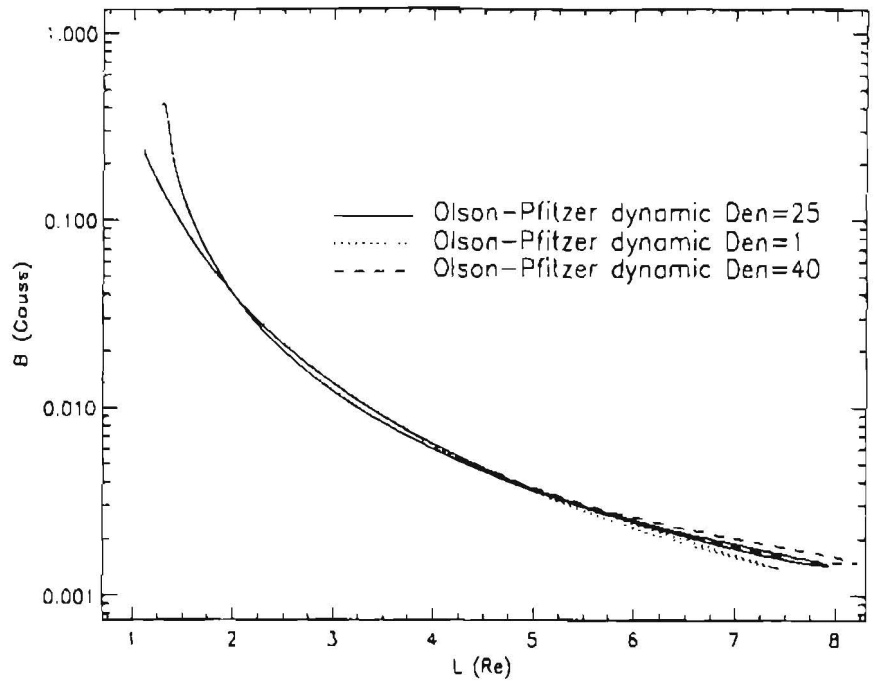

Figure 3.3. Influence of the value of ρ on the magnetic field calculated with the Olson & Pfitzer dynamic magnetic field model (Pfitzer et al. 1988) for CRRES orbit 251. For both curves, $V = 300\,\mathrm{km/s}$ and $D_{st} = -30\,\mathrm{nT}$.

Magnetically quiet conditions

The influence of changing the input parameters D_{st}, ρ, and V in the Olson & Pfitzer (1988) dynamic model is shown in Figs. 3.1 to 3.3. In each of these graphs, the (B, L) diagram obtained with Pfitzer's default values, given in Eq. (3.13), is shown for comparison.

The (B, L) diagrams obtained by setting $D_{st} = -100\,\mathrm{nT}$ and $D_{st} = -200\,\mathrm{nT}$, while keeping V and ρ constant, are shown in Fig. 3.1. The influence of this change is much greater than the influence of K_p on the Tsyganenko (1989) model. From Fig. 3.2 it appears that increasing V to 500 km/s, and even to 700 km/s, has a smaller effect. Finally, Fig. 3.3 illustrates that the effect of substantially lowering or raising ρ, to 1 particle/cm^3 and 40 particles/cm^3, respectively, is minor.

Magnetically disturbed conditions

Orbit 588 covers the period of the onset of the magnetic storm on March 24 1991. Figure 3.4 represents the one-minute averages of the magnetic field measurements in the SSDB file for orbit 588 as a function of altitude. We superimposed the field values obtained with the Olson & Pfitzer (1977) tilt dependent model, the Olson & Pfitzer dynamic model (Pfitzer et al. 1988), and the Tsyganenko (1989) model,

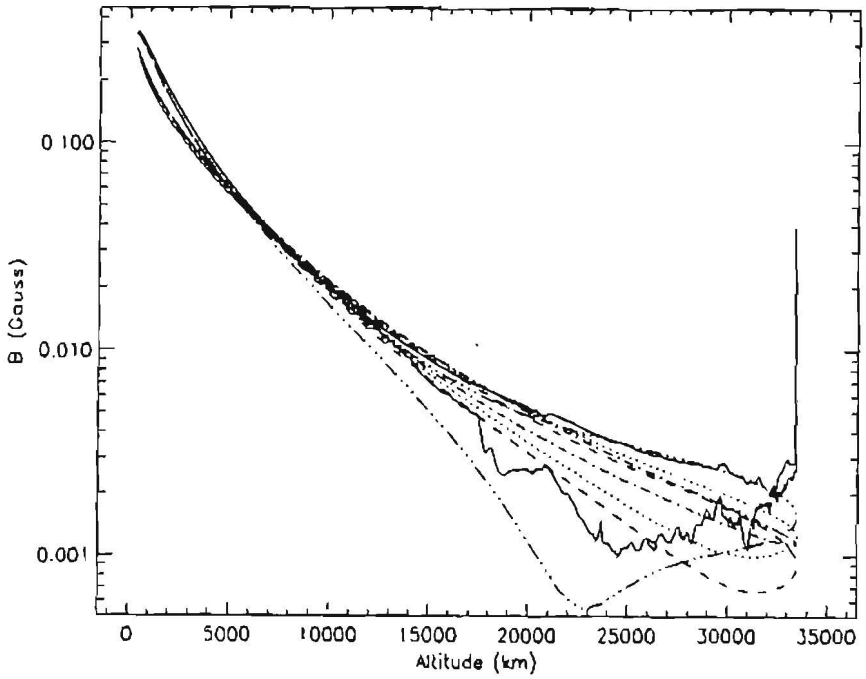

Figure 3.4. Measured and modelled magnetic field for CRRES orbit 588. The solid line represents the one-minute magnetometer averages in the SSDB. The Olson & Pfitzer (1977) tilt dependent model values are represented by the dash-dot line, the Olson & Pfitzer dynamic model (Pfitzer et al. 1988) values by the dashed and dash-triple-dot lines for the first and second set of parameters in the text, respectively, and the Tsyganenko (1989) model values for $K_p = 5$ by the dotted line.

combined with the IGRF 90 model updated to 1991. For the model parameters, we used the values given in the *Solar-Geophysical Data Prompt Reports* for the period covered by the orbit: $K_p = 7$, $D_{st} = -70\,\mathrm{nT}$, $V = 528\,\mathrm{km/s}$, $\rho = 8.02\,\mathrm{particles/cm^3}$.

None of the three external models reproduces the measured field over the whole orbit. The Olson-Pfitzer tilt dependent model gives an adequate average of the high-altitude field. The Olson-Pfitzer dynamic model accounts for part of the disturbance in the field on the ascending part of the orbit, but understimates the field on the descending part. We also calculated the Olson-Pfitzer dynamic model for a second set of parameters for the whole orbit, corresponding to the conditions on 25 March 1991: $D_{st} = -270\,\mathrm{nT}$, $V = 613\,\mathrm{km/s}$, $\rho = 13.7\,\mathrm{particles/cm^3}$. With these values, the magnetic field is very well fitted on the descending part of the orbit, but not on the ascending part. It may be possible to obtain good coverage over the whole orbit by suitably varying the parameters D_{st}, ρ, V in the Olson-Pfitzer dynamic model.

The Tsyganenko (1989) model depends only on ψ and K_p. On both 24 and 25 March, $K_p \geq 5$, which means that the most disturbed version of the Tsyganenko model is used throughout this period. Even using this version, the disturbances are

underestimated throughout the orbit.

3.2 Implementation of pitch angle dependence in UNIRAD

The standard software routines used for calculating (B, L) coordinates for a point in space implicitly make the assumption that this point is the mirror point of a particle on the geomagnetic field line passing through it. This approach was adopted for use with older trapped particle models, since these generally are given in terms of omnidirectional fluxes.

More modern measurements, however, include flux measurements with high directional resolution. Therefore, in order to make use of this additional information, pitch angle dependence has to be implemented in the calculation of B and L. In this section, we describe the changes made to BLXTRA and TREP in this respect.

3.2.1 (B, L) coordinates for particles with $\alpha \neq 90°$

McIlwain's (1961) L-parameter is defined in terms of the integral I:

$$I = \int_A^{A'} \sqrt{1 - \frac{B(s)}{B_m}}\, ds\,, \tag{3.14}$$

where A and A' represent the locations of two magnetically conjugate points, and B and ds are the magnetic field intensity and the line element along the field line. A corresponds to the point for which the value of L is sought. B_m is the magnetic field intensity at the points A and A'. Due to the conservation of the first adiabatic invariant μ and of the particle energy E, B_m is an adiabatic invariant of motion for all particles mirroring at A and A'. Due to the conservation of the second invariant of motion J, I also is an adiabatic invariant for all particles mirroring at A and A'.

These properties have led to the introduction of the (B_m, I) coordinates to map perpendicular integral fluxes J and differential fluxes j of energetic particles mirroring at A, i.e. with velocities perpendicular to the magnetic field vector $\boldsymbol{B}$ and thus with pitch angles $\alpha = 90°$. The coordinate pair (B_m, I) uniquely defines the drift shell of all particles mirroring at A. A drift shell is the surface formed by the segments of the magnetic field lines bounded by the intersections of the surfaces $B = B_m$ and $I = \text{cst}$. It is important to realise that drift shells do not correspond to magnetic shells which are surfaces formed by the magnetic field lines with $B_{eq} = \text{cst}$ (B_{eq} is the magnetic field intensity on the magnetic equator) and extend down to the surface of the Earth (see Fig. 3.5).

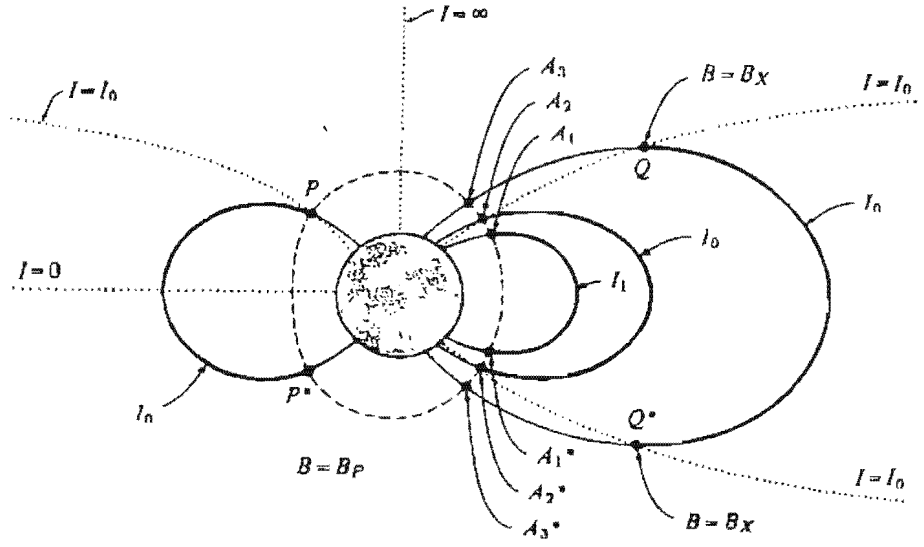

Figure 3.5. Projection of surfaces of constant B_m and of constant I. Contours of constant B_m and of constant I are represented by dashed and dotted lines, respectively. The thick solid lines are the projections of drift shells. Magnetic shells are defined by extension along the magnetic field line to the surface of the Earth, as indicated by the thin solid lines. [Taken from Hess (1968)].

In a pure dipole magnetic field, the magnetic field distribution is axisymmetric with respect to the magnetic axis, and thus drift shells are axisymmetric as well. On the basis of this property, McIlwain (1961) found it more convenient and appealing to introduce a more geometrically meaningful parameter L_m, which corresponds to the equatorial radius of a drift shell in the case of a dipole field. McIlwain extended this definition to non-dipole field distributions, such as the geomagnetic field, by applying the functional relation between L_m, B_m, and I, derived for a dipole field, to non-dipole field distributions. L_m is unambiguously determined for each point on a closed magnetic field line, using (B_m, I) computed with a model magnetic field distribution (including external field models). Consequently, the coordinate pair (B_m, L_m) is equivalent to the coordinate pair (B_m, I). Usually, the index "m" is dropped and the McIlwain coordinates are denoted by (B, L).

For particles with pitch angles $\alpha \neq 90°$, A and A' are not mirror points. Consequently, neither B, nor I, nor L then are invariants of motion, and, although it has become common usage, it is not appropriate to map $J(\alpha \neq 90°)$ or $j(\alpha \neq 90°)$, measured by a directional detector, in (B, L) coordinates.

The mirror point M of a particle with pitch angle $\alpha \neq 90°$, measured at A, does not coincide with A. The magnetic field intensity B_m at M is given by

$$B_m = \frac{B}{\sin^2\alpha}. \tag{3.15}$$

The adiabatic invariant I is then obtained by substituting A and A' by M and M' in Eq. (3.14). L_m is obtained from (B_m, I) using McIlwain's (1961) or Hilton's (1971) algorithm. The coordinates (B_m, L_m) calculated in this way label the drift shell of particles measured at A with pitch angle α. These pitch angle dependent coordinates have been implemented in the latest version of BLXTRA and will be used to map measurements of CRRES and other satellites.

Particles measured at A with different pitch angles will move on different drift shells, which are uniquely defined by (B_m, L_m) (see Fig. 3.6). This phenomenon is usually called—erroneously—"drift shell splitting". This term is misleading since it suggests that a particle is forced onto different drift shells during its longitudinal drift motion, which is not the case. In fact, a given particle always remains on the same drift shell (which is not the same as a magnetic shell!), for any magnetic field configuration in which adiabatic conditions are maintained. Magnetic shells may split, but not drift shells. The dependence on longitude of the radial extent of a drift shell in a non-dipole field causes the well-established effect that a particle's equatorial radial distance changes with local time. Therefore, as was emphasized by McIlwain (1966), L_m should not be identified with a fixed distance, but should merely be considered as a label to identify drift shells. Since L_m is not constant along a field line in a non-dipole magnetic field, it is incorrect to label magnetic field lines with McIlwain's L_m. The proper way to identify a field line is with (B_{eq}, ϕ_{eq}), where ϕ_{eq} is the longitude of the point where the field line intersects the magnetic equator.

Instead of (B_m, L_m), the coordinate pair (α_0, L_m) may be used, where α_0 is the equatorial pitch angle determined as

$$\sin^2\alpha_0 = \sin^2\alpha \frac{B_0}{B} = \frac{B_0}{B_m}, \tag{3.16}$$

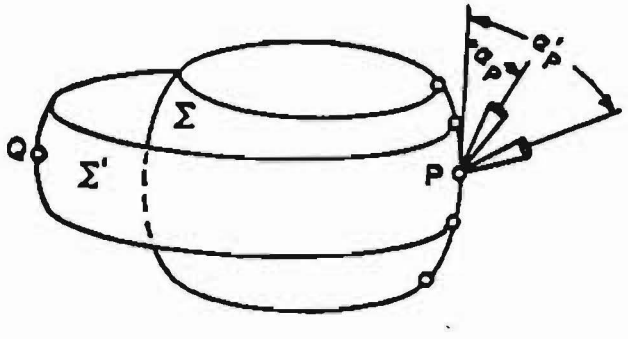

Figure 3.6. Illustration of the different drift shells for two particles measured at the same point with different pitch angles [from Roederer (1970)]

where B_0 is defined as

$$B_0 = \frac{0.311653}{L_m^3} \tag{3.17}$$

and 0.311653 is the value of the geomagnetic moment implemented in McIlwain's software. This expression for B_0 was used in the building of NASA's trapped radiation models (Sawyer and Vette 1976, p. 8; Singley and Vette 1972, p. 10).

3.2.2 Pitch angle dependence in TREP

The NASA trapped radiation models AP-8 and AE-8 are distributed as tables of omnidirectional fluxes. However, there also exists a version of the AP-8 models in terms of perpendicular fluxes (Vette, unpublished report), which has been sent to BIRA/IASB by A. Konradi. In the following sections, we describe the organisation and implementation of these models.

Conversion between omnidirectional and unidirectional fluxes

The knowledge of the omnidirectional flux everywhere along a magnetic field line is equivalent to the knowledge of the unidirectional flux everywhere along the same field line (Ray 1960, Lenchek et al. 1961).

The unidirectional flux at a point on a magnetic field line can be described by a function $j(\alpha, \varphi, p, B, L_m)$, where φ is the phase angle around the magnetic field vector $\boldsymbol{B}$, and p the momentum of the particle. For nearly all practical situations, j is independent of φ, except at low altitudes. For a magnetic field distribution that is constant in time, p is constant along the particle's trajectory. In this special case, Liouville's theorem implies that $j(\alpha, B, L_m)$ (where we have dropped the dependence on φ and p) is constant along a field line.

For a given pitch angle α, one can then write the following relation between the unidirectional flux at the point of measurement on a field line and the perpendicular flux at the mirror point associated with α on the same field line:

$$j(\alpha, B, L'_m) = j(90°, B_m, L_m)\,, \tag{3.18}$$

where B_m is given by Eq. (3.15). The notation for the perpendicular flux will be simplified to $j_\perp(B_m, L_m)$. We will also drop the dependence on L_m from the notation, since L_m was assumed to be constant along field lines in the construction of the NASA trapped radiation models.

The perpendicular flux can also be related to the unidirectional flux at the equator:

$$j(\alpha_0, B_0) = j_\perp(B_m)\,. \tag{3.19}$$

The omnidirectional flux $J(B)$ is given by

$$J(B) = 2 \int_0^{\pi/2} j(\alpha, B)\, 2\pi \sin\alpha \, d\alpha \,. \tag{3.20}$$

The factor two in front of the integral takes into account particles moving in opposite directions on a field line. In terms of the equatorial pitch angle distribution, the omnidirectional flux becomes

$$J(B) = 4\pi \frac{B}{B_0} \int_0^{\arcsin\sqrt{B_0/B}} j(\alpha_0, B_0) \sin\alpha_0 \frac{\sqrt{1-\sin^2\alpha_0}}{\sqrt{1-(B/B_0)\sin^2\alpha_0}} \, d\alpha_0 \,. \tag{3.21}$$

In principle, this integral can be inverted to yield $j(\alpha, B)$ or $j(\alpha_0, B_0)$ in terms of $J(B)$. However, this inversion is not unique since an integral of any function $h(\alpha, B)$ for which

$$0 = \int_0^{\arcsin\sqrt{B_0/B}} h(\alpha_0, B_0) \sin\alpha_0 \frac{\sqrt{1-\sin^2\alpha_0}}{\sqrt{1-(B/B_0)\sin^2\alpha_0}} \, d\alpha_0 \tag{3.22}$$

can be added to the right hand side of Eq. (3.21) without affecting the left hand side. In addition, the integration in Eq. (3.21) can only be carried out in closed form for a limited number of functions $j(\alpha_0, B_0)$ (examples are given by Roberts [1965]). Lenchek et al. (1961) and Roberts (1965) describe an inversion method consisting of approximating the flux distribution by a discrete function.

Parker (1957) proved that, for particles performing adiabatic motion, the pitch angle distribution is of the form

$$j(\alpha, B) = \begin{cases} f\left(\dfrac{\sin^2\alpha}{B}\right) & \alpha \geq \alpha_L \\ g(\alpha) & \alpha \leq \alpha_L \end{cases} \tag{3.23}$$

where α_L is the loss cone angle. α_L is related to the characteristic magnetic field intensity B_c in the region of atmospheric cut-off by

$$\sin^2\alpha_L = \frac{B}{B_c} \,. \tag{3.24}$$

Several functions f and g have been proposed by different authors. We give two examples, converted to equatorial pitch angles:

$$j(\alpha_0, B_0) = \begin{cases} K\, B_0^{n/2} \left(\dfrac{\sin\alpha_0}{\sqrt{B_0}} - \dfrac{1}{\sqrt{B_c}}\right)^n & \alpha_0 \geq \alpha_{0L} \\ 0 & \alpha_0 \leq \alpha_{0L} \end{cases} \tag{3.25}$$

(Valot & Engelmann 1973), and

$$j(\alpha_0, B_0) = \begin{cases} K\left(\frac{\sin\alpha_0}{\sqrt{B_0}} - \frac{1}{\sqrt{B_c}}\right) \exp\left[-\beta\left(\frac{\sin\alpha_0}{\sqrt{B_0}} - \frac{1}{\sqrt{B_c}}\right)\right] & \alpha_0 \geq \alpha_{0L} \\ 0 & \alpha_0 \leq \alpha_{0L} \end{cases} \tag{3.26}$$

(Badhwar & Konradi 1990). We have transformed the unidirectional version of the AP-8 MAX model into equatorial pitch angle distributions by means of Eqs. (3.19) and (3.16). We then fitted the functions in Eqs. (3.25) and (3.26) to the transformed proton flux models and determined the fitting parameters K, β, and n by means of the least-squares method. For B_c, we used the expression given by Vette (1991a):

$$\frac{B_c}{B_0} = 0.6572\, L^{3.452}. \tag{3.27}$$

Figure 3.7 represents the two fitted functions for the case $E = 0.1$ MeV and $L = 2.0$. It appears that the fit function of Badhwar & Konradi (1990) is closest to the AP-8 MAX model values. This is the case for the whole range of L and E, both for AP-8 MAX and AP-8 MIN.

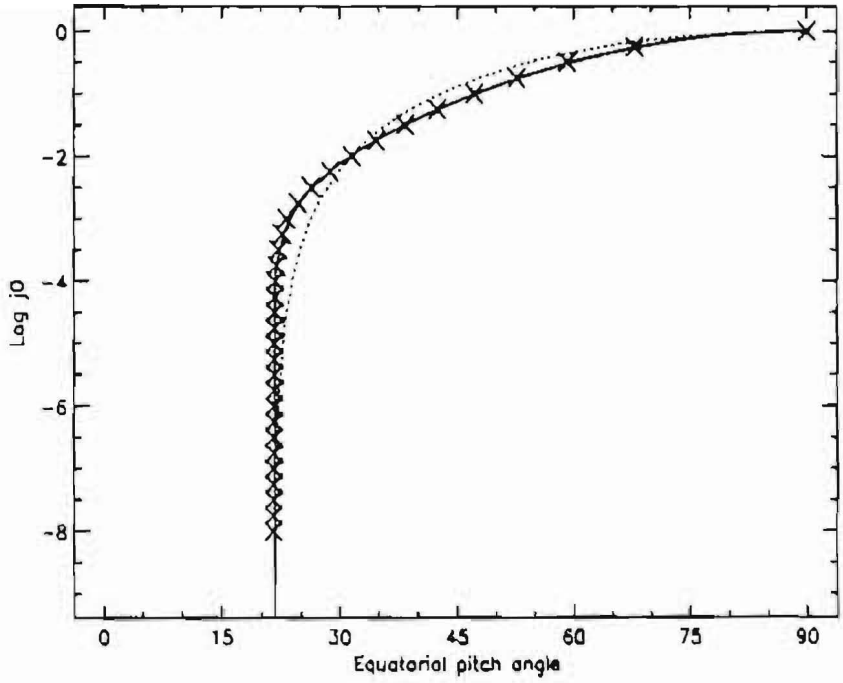

Figure 3.7. AP-8 MAX equatorial flux distribution for $L = 2\,R_E$, $E = 0.1$ MeV. The symbols × represent the model values converted from perpendicular to equatorial flux, the solid and dotted lines are the fit functions defined by Eqs. (3.26) and (3.25), respectively.

Implementation in TREP

Originally, TREP read geodetic coordinates as well as (B, L) values, calculated by SHELLG or BLXTRA, from the common interface file. TREP has since been modified so that it calculates (B_m, L_m) independently, with the appropriate magnetic field models: Jensen & Cain (1962) for AE-8 MIN, AP-8 MIN, and AE-8 MAX, and GSFC 12/66 (Cain et al. 1967) updated to epoch 1970 for AP-8 MAX.

The magnetic coordinates are written to the common interface file by TREP and are to be interpreted as (B, L_m), i.e. the magnetic field intensity at the point of measurement and the L-value obtained by tracing the field line to the mirror point. With the value of α, which now is included in the interface file, B_m can be obtained by means of Eq. (3.15).

For protons, the user can choose between the calculation of omnidirectional or unidirectional fluxes by means of the NAMELIST parameter OMNI. With OMNI=1 (the default), omnidirectional fluxes are calculated, OMNI=0 results in unidirectional fluxes.

3.2.3 Application to a CRRES orbit

CRRES PROTEL data for ten orbits in January 1991, i.e. orbits 411–420, are available at BIRA/IASB. The data files contain the time of measurement, values for B and L (calculated at PLGD), the PROTEL HEH pitch angle, and the counts for the 16 HEH PROTEL channels, at a time resolution of 1.024 s. The available data are limited to the low altitude parts of the orbits, i.e. below 1.5 R_E.

As a test of the new version of BLXTRA, we calculated (B, L) with the IGRF 90 model, updated to 1991, for all points in our data file for orbit 411, by setting all pitch angles equal to 90°. Next, we determined (B_m, L_m) with the values of the pitch angles in the PROTEL data file. Figures 3.8 and 3.9 show the outbound and inbound low-altitude parts of orbit 411 in (B, L) space as a solid line. The (B_m, L_m) coordinates—which depend on α—are superimposed on these graphs with the symbol $\times$. The difference between (B, L) and (B_m, L_m) coordinates is clearly illustrated in these figures. When pitch angles are taken into account, the particles measured by CRRES are distributed over a family of drift shells covering a large area in the (B, L) plane.

The scatter in mirror points is mainly due to the large variation of B_m in function of α. The difference between L and L_m is small (less than 1%).

The values of the proton fluxes measured in PROTEL channel HEH-8 are shown in Fig. 3.10 as a function of CRRES altitude along the orbit. The uniform scatter of points in this graph is due to the fact that at a given altitude many pitch angles are sampled by the spinning spacecraft. For the outbound part of the orbit, the

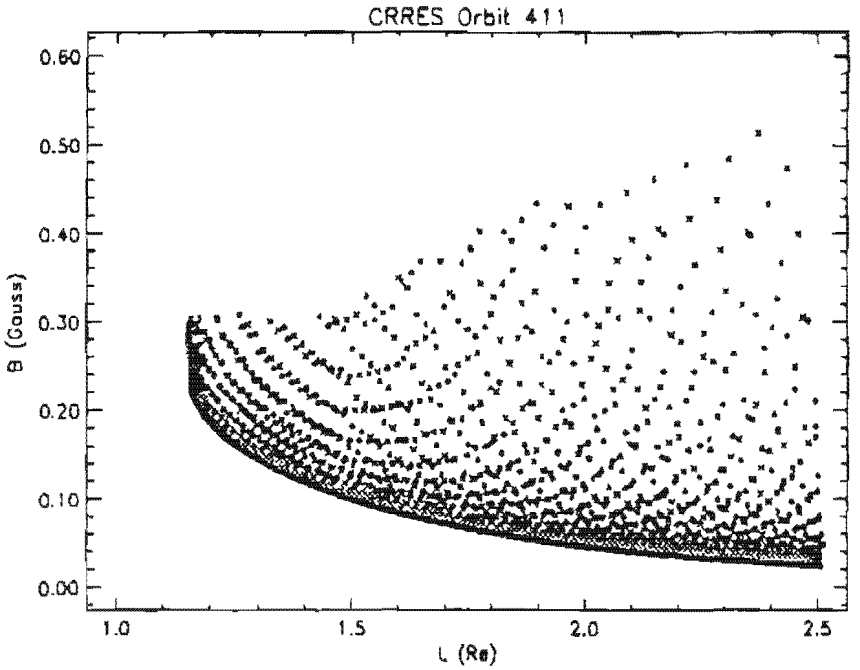

Figure 3.8. (B, L) (solid line) and (B_m, L_m) (×) coordinates for the outbound part of CRRES orbit 411

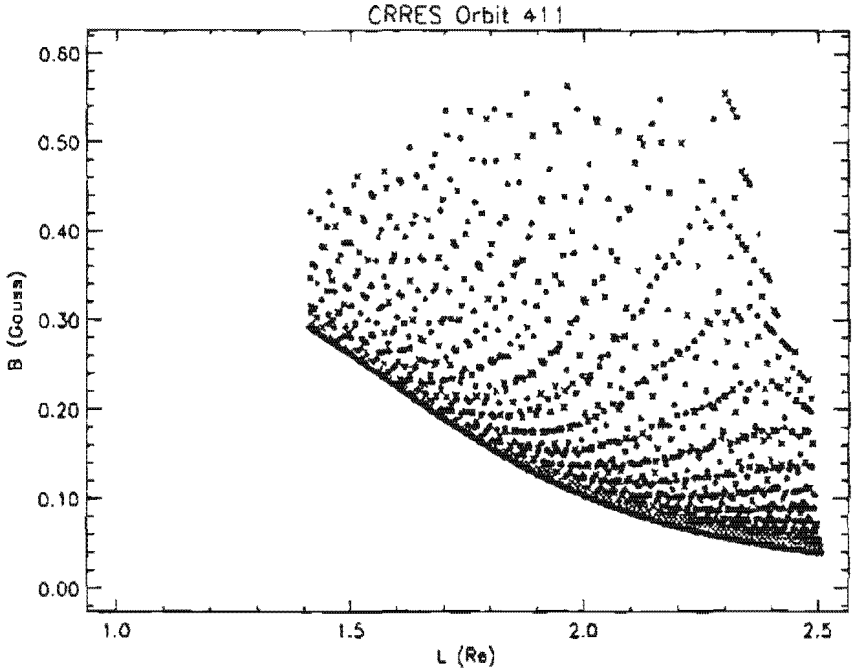

Figure 3.9. (B, L) (solid line) and (B_m, L_m) (×) coordinates for the inbound part of CRRES orbit 411

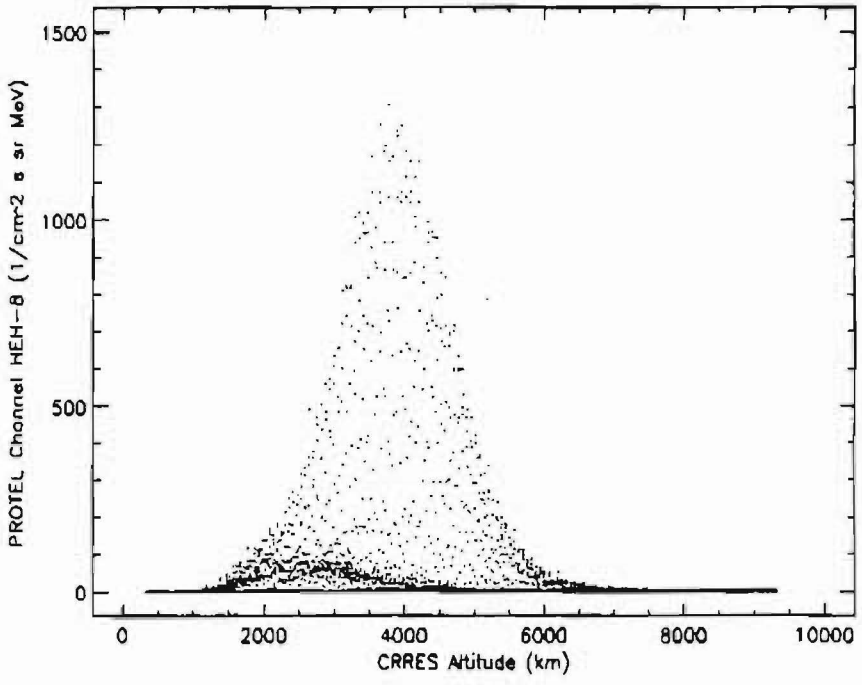

Figure 3.10. Differential proton flux measured in PROTEL channel HEH-8 for a partial CRRES orbit, as a function of CRRES altitude

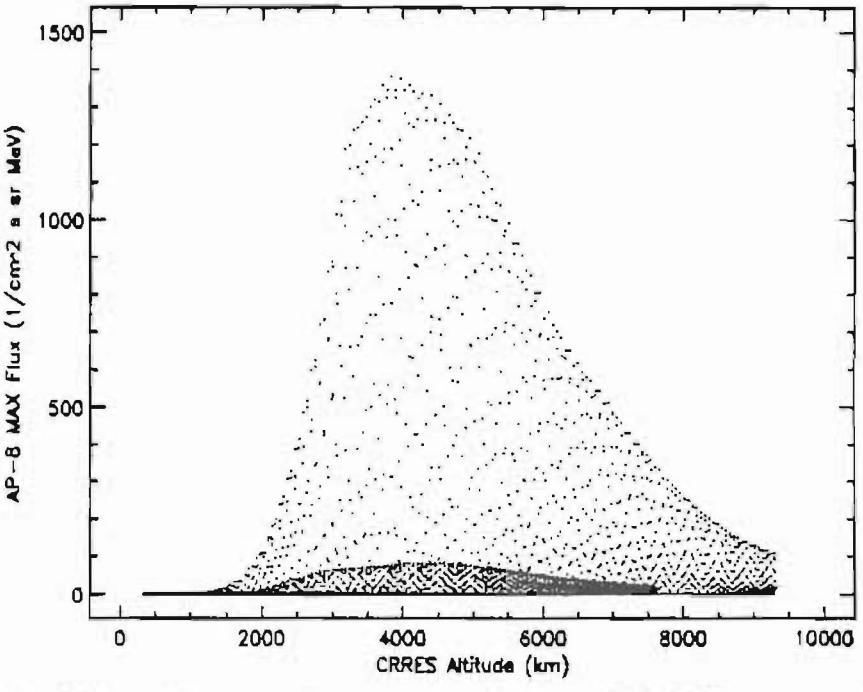

Figure 3.11. Differential proton flux calculated with AP-8 MAX for a partial CRRES orbit, as a function of CRRES altitude

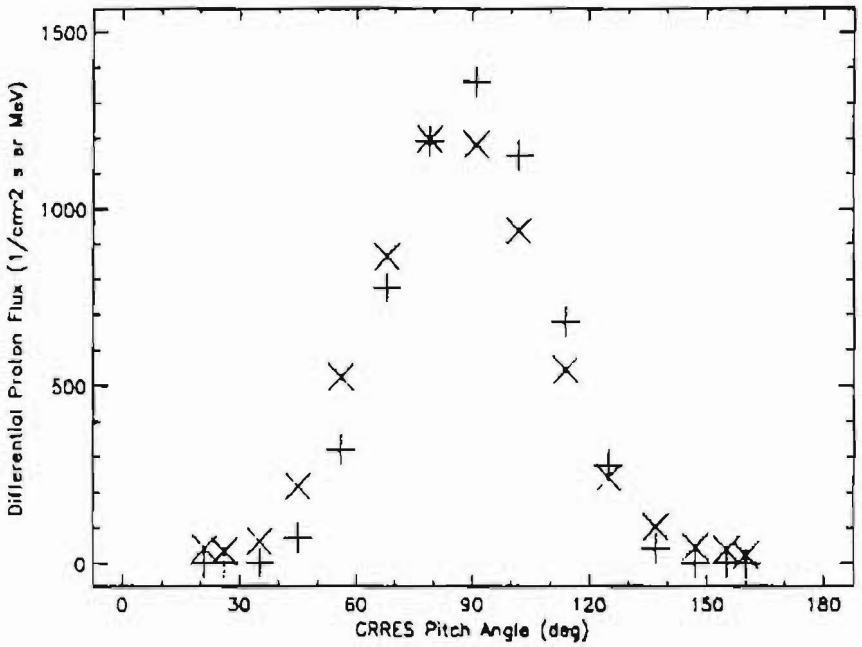

Figure 3.12. Proton flux measured in PROTEL channel HEH-8 (×) and calculated with AP-8 MAX (+) as a function of PROTEL pitch angle for half a spacecraft spin rotation in the outbound part of a partial CRRES orbit

maximum flux is reached around altitude 3800 km, where CRRES traverses the maximum of the proton belt corresponding to the energy range of channel HEH-8 (18.0–20.8 MeV). For the inbound part of the orbit, the flux maximum is observed around 2600 km.

In order to compare AP-8 MAX model fluxes to the PROTEL data, the differential flux in the PROTEL HEH-8 channel was modelled as

$$\frac{j(20) - j(17)}{3}, \tag{3.28}$$

where j represents the unidirectional AP-8 MAX integral flux obtained with (B_m, L_m) above a threshold given in MeV. The AP-8 MAX fluxes were calculated with the pitch angle values taken from the PROTEL data file. Figure 3.11 shows the fluxes thus obtained with AP-8 MAX in the same format as Fig. 3.10. The outer envelopes of the scatter diagrams correspond to the fluxes obtained by means of (B, L) coordinates, i.e. assuming that $\alpha = 90°$. As in Fig. 3.10, the data points below the envelopes correspond to pitch angles $\alpha \neq 90°$.

From the comparison of Figs. 3.10 and 3.11, it follows that the flux maximum predicted by the AP-8 MAX model is comparable to the maximum of the flux measured by PROTEL. However, the half-width of the envelopes obtained with AP-8 MAX

is much larger than that of the PROTEL envelopes. The low-altitude profiles of the envelopes in Figs. 3.10 and 3.11 are similar, but the high-altitude profiles differ significantly, indicating that the extent of the proton radiation belt is smaller in the CRRES data than in the AP-8 MAX model.

Figure 3.12 represents the PROTEL HEH-8 proton flux as a function of measured pitch angle during one half of a CRRES spin period, as an illustration of the time resolution of the PROTEL measurements. The differential fluxes obtained with the unidirectional version of AP-8 MAX are superimposed.

3.3 Secular drift of the South Atlantic Anomaly

The main portion of the radiation flux encountered by a satellite in a *low-Earth orbit (LEO)* is concentrated in the SAA. The existence of the SAA is related to the distribution of the geomagnetic field. It has been well established (Merrill & McElhinny 1983) that the surface features of the geomagnetic field experience a secular westward drift.

The displacement of the field distribution has important consequences for particles trapped at low altitudes. Their drift shells are displaced with respect to the Earth's surface so that they penetrate deeper into the atmosphere in a region just east of the Atlantic coast of South America. Trapped particles that penetrate the atmosphere in this region are lost due to absorption and scattering. This enhanced loss constitutes a longitudinal asymmetry in the distribution of particles trapped at low altitudes.

The NASA models AP-8 and AE-8 that describe the trapped radiation environment were constructed in the sixties and seventies (Vette 1991b). Consequently, they should be accessed with values of B/B_0 and L computed for the geomagnetic field models used at that time. A drawback of this procedure is that the location of the SAA predicted by the old field models does not coincide with the current location of the SAA. In this section, we present a method to compensate for the secular motion of the SAA. Once the relative positions of the SAA for both epochs are known, a suitable coordinate transformation will position the satellite trajectory correctly with respect to the location of the SAA for the epoch of the NASA model used.

3.3.1 Determination of the location of the SAA

According to the different definitions of the SAA, three methods are available to determine the location of the centre of the SAA. One can approximate the location of the centre of the SAA as the mirror point of the geographic location of the centre

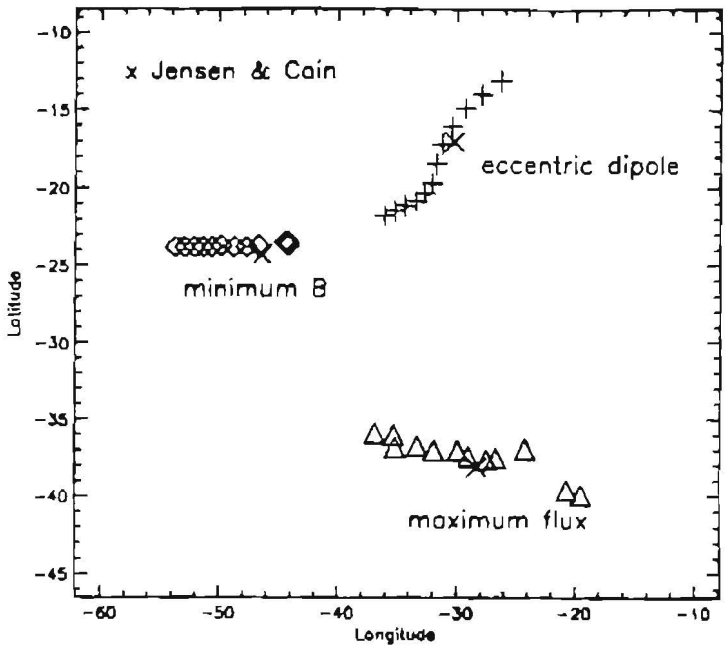

Figure 3.13. Location of the SAA as a function of epoch

of the eccentric dipole approximation to the geomagnetic field. More accurately, the centre of the SAA is identified as the locus of the local minimum of the geomagnetic field at a fixed altitude in the region of the South Atlantic. Alternatively, one can associate the centre of the SAA with the empirically determined local particle flux maximum. In Technical Note 1 each method is described in detail.

Evaluation of the three methods

In Fig. 3.13 we represent the geographic longitude and latitude of the SAA derived with the three methods described in Technical Note 1, as a function of time. The respective locations obtained with the three methods for a given epoch differ substantially.

The location and extent of the particle SAA is dependent on the energy of the particles. The higher the energy, the closer the flux maximum lies to the point where the minimum of the geomagnetic field is situated. The locus of the flux maximum also depends on the model of the trapped radiation environment.

The mirror point of the eccentric dipole position is only a first-order approximation to the location of the SAA. According to Roederer (1972), higher-order terms influence the location and extent of the SAA.

The determination of the location of the magnetic SAA does not depend on particle energy, nor on approximations introduced by truncating the spherical harmonic

expansion of the magnetic field potential. Even though the point where the geomagnetic field has a local minimum does not coincide with the locus of the maximum particle flux, even at high energies, the secular motion of the particle SAA should be linked to the secular motion of the locus of the field minimum.

From Fig. 3.13, it appears that the secular motion of the magnetic SAA has no transversal component. The particle SAA seems to move slightly northward as well as westward. However, the loci corresponding to epochs before 1960 were derived with geomagnetic field models that were constructed without satellite measurements. Therefore, the three corresponding loci cannot be very accurately determined. If we consider only epochs later than 1960, the secular motion of the particle SAA is mainly longitudinal. Consequently, we assume that the secular motion of the particle SAA in time is westward only.

The rate of the westward drift of the magnetic SAA and the particle SAA can then be estimated with a linear regression fit to the longitudes in Fig. 3.13, excluding the value for the Jensen & Cain (1962) field model and the DGRF values with epochs earlier than 1960. Epochs later than 1990 are also excluded since the associated results are based on extrapolations of the IGRF 90 model. The rate of the westward drift resulting from the regression analysis is 0.18°/year for the magnetic SAA and 0.29°/year for the particle SAA, respectively.

Konradi et al. (1992) have estimated the westward drift of the SAA by comparing Space Shuttle dose measurements with dose calculations based on AP-8. They report a yearly drift of 0.34°/year, which is in satisfactory agreement with the value we found.

The difference between the drift rate of the magnetic SAA and the particle SAA may be ascribed to the fact that the secular change in the geomagnetic field is more complex than just a westward drift. Merrill and McElhinny (1983) describe the separation of the Earth's non-dipole field into drifting and standing parts. The standing and drifting parts of the none-dipole field are of approximately the same size and intensity. The drifting field consists mainly of low harmonics ($l \leq 3$) whereas the standing field has a more complicated distribution. The drifting part of the non-dipole field moves westward at a rate slightly greater than 0.3°/year. The inclusion of the standing part of the non-dipole field in the drift rate lowers the average rate to near 0.2°/year, which value corresponds to the value we found for the westward drift rate of the magnetic SAA.

In order to correct a satellite trajectory for the westward drift of the particle SAA, we apply an eastward shift $\delta\phi$ to the geographic satellite longitude, so that the corrected longitude becomes $\phi + \delta\phi$. $\delta\phi$ is a function of the time t for which the satellite trajectory is calculated and is defined as

$$\delta\phi(t) = 0.3^\circ\,(t - \mathrm{EPOCH})\,. \tag{3.29}$$

EPOCH is the reference epoch associated with the magnetic field models used to construct AP-8 and AE-8. According to Vette (1991b), most of the data used for constructing the NASA models were ordered by means of the Jensen & Cain (1962) geomagnetic field model. However, after further investigation (Vette, private communication), it turned out that AP-8 MAX was built with the GSFC 12/66 model (Cain et al. 1967), updated to 1970. Consequently, EPOCH is set to 1970 for AP-8 MAX and to 1960 for the other models.

Application to a LEO trajectory

The correct prediction of the location of the SAA is crucial for the planning of EVA's for vehicles like the Space Shuttle. When the uncorrected AP-8 models are used to map particle flux distributions, the predicted encounter with the SAA occurs about one orbit later than is actually measured.

We illustrate the influence of the westward drift of the SAA on a typical LEO trajectory represented in Fig. 3.14. The orbit altitude is 350 km, the inclination is 28.5°. We considered only three orbits, in order not to average out the longitude effects.

For this trajectory, we calculated the integral proton flux above 5 MeV, 20 MeV, and 100 MeV for the Jensen & Cain (1962) geomagnetic field model without correcting for the westward drift of the SAA. We then repeated the calculations, with the same magnetic field model, applying the longitude correction given by Eq. (3.29) for five-year intervals starting in 1945. The resulting time dependence of the proton flux corrected for the westward drift of 0.3°/year is shown in Fig. 3.15. The proton flux increases strongly with time, as expected.

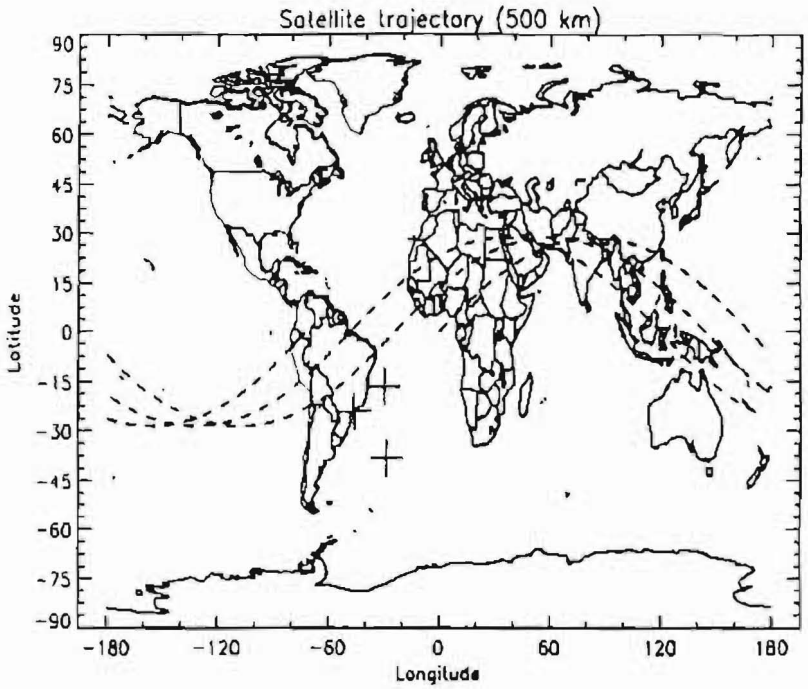

Figure 3.14. Representation of the LEO satellite trajectory used for the flux calculations described in the text. The three loci of the SAA for the Jensen & Cain (1962) model are represented by the symbols +.

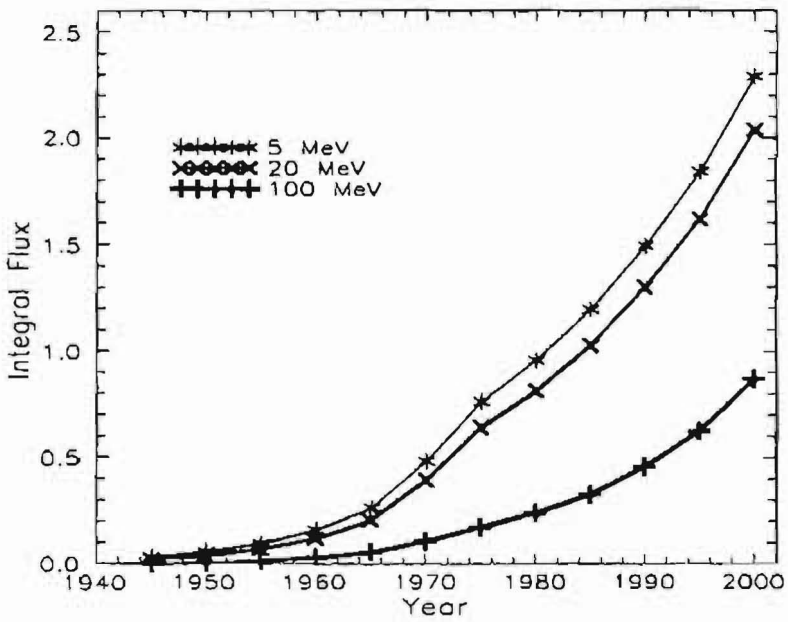

Figure 3.15. Time dependence of the integral proton flux corrected for the westward drift of the SAA

Chapter 4

Atmospheric cut-off

In this chapter we describe a coordinate that can be used instead of B/B_0 to map trapped radiation fluxes in combination with L. This alternative coordinate is the atmospheric density averaged over a drift shell (B, L).

In Sect. 4.1 we review different coordinate systems that may be used to map trapped radiation fluxes. These coordinates work well over most of the region covered by the Van Allen belts, but are less suitable in the low altitude region where the Earth's upper atmosphere interacts with the trapped particle population. The concept of atmospheric cut-off also is introduced in this section.

At low altitudes, the main loss process for trapped particles is scattering by the Earth's atmosphere. The probability that a particle is scattered along its longitudinal drift path is proportional to the amount of material traversed and to the (energy dependent) collisional cross sections with the atmospheric constituents. For this reason, the atmospheric density averaged over drift shells and weighted with the atmospheric cross sections should be a good parameter to represent trapped particle distributions at low altitude.

An average density along the bounce motion of particles between their mirror points and along their drift shells can be determined by means of a computer code designed by Hassitt (1964) and kindly provided to J. Lemaire by C.E. McIlwain. This code has been updated and improved. The implementation of the code for this project is described in Sect. 4.2, which contains the definition of the drift shell averaged density and a description of the calculation method.

In order to calculate drift shell averaged densities, one needs models of the density distribution in the neutral atmosphere and in the ionosphere. We describe the models used in this study in Sect. 4.2, and in more detail in Technical Note 2.

Finally, in order to determine the penetration depths and the trapping life time of protons and electrons we need estimates of the collision cross sections for these particles as a function of energy. A compilation of the relevant collision processes

and the associated cross sections is given in Technical Note 2.

The software is applied to the proton flux distribution given by the AP-8 model in Sect. 4.3. It will be used to map DMSP and AZUR data in the future. Greyscale plots of the averaged density over the Earth's surface are presented as well.

4.1 Coordinate systems for low altitudes

Trapped particle fluxes usually are mapped in the (B, L) coordinate system (McIlwain 1961). While these coordinates have proved very suitable for most of the region covered by the Van Allen belts, they are not very well suited for the low-altitude regions where the Earth's atmosphere interacts with the trapped particle population. The concept of atmospheric cut-off is defined in Sect. 4.1.1. An alternative coordinate has been proposed by Daly & Evans (1993) to take into account the steep flux gradients in the region of the upper atmosphere. This coordinate is discussed in Sect. 4.1.2.

It is well known from previous studies that the cosmic ray intensity observed within the atmosphere depends on the quantity of absorbing material traversed before observation. Besides the magnetic rigidity effect, the barometric pressure has an appreciable effect on the measured cosmic ray intensity. This is why cosmic ray fluxes usually are reported in terms of atmospheric depth, i.e. the mass of air per unit area above the point of observation, or air pressure at the point of observation.

The same concept should also be applied to identify an equivalent atmospheric penetration depth of Van Allen belt particles. Evidence that the flux of Van Allen belt particles depends on the atmospheric density distribution has been forwarded by Pfitzer (1990), who found that the atmospheric density at space station altitudes is a better variable than B/B_0 to organise the AP-8 MIN and AP-8 MAX fluxes.

In order to estimate the influence of the Earth's atmosphere on the distribution of trapped particles, the effects of the atmosphere have to be averaged over the particle's orbit. Ray (1960) and Lenchek & Singer (1962) derived expressions for the atmospheric density averaged over the orbit of a particle trapped in a dipole field. Newkirk & Walt (1964) determined the average density for a realistic representation of the geomagnetic field. Hassitt (1965b) simplified considerably the procedure of Newkirk & Walt (1964), while maintaining the same accuracy. In Sect. 4.2 we describe Hassitt's (1965b) method and its application to the study of low-altitude coordinate systems.

4.1.1 Definition of atmospheric cut-off

Trapped ions and electrons whose pitch angle is scattered into the loss cone, either by wave-particle interaction at high altitude or Coulomb collisions with ions and electrons in the ionosphere, are dumped in the atmosphere where they lose their energy.

Some of these energetic particles are backscattered and re-enter the magnetosphere with a different energy. The penetration depth of the primaries into the atmosphere depends on their energy. Calculations of penetration depths have been given by Bailey (1959), Rees (1963) and Kamiyama (1966).

Electrons of 2 keV, vertically incident, penetrate down to 120 km altitude. When their energy is 1 MeV, they can penetrate down to 60 km altitude. Protons of 20 keV and 20 MeV penetrate down to 120 km and 60 km, respectively. Of course, particles with pitch angles not equal to zero penetrate with a larger angle of incidence in the atmosphere, spiral over larger distances in the atmosphere and consequently dissipate their energy at higher altitudes.

The range of cut-off altitudes over which primary Van Allen belt particles are interacting most strongly with the neutral atmosphere is rather narrow (from 50 to 200 km) compared to the length of their drift path within the magnetosphere. Over this small altitude range the magnetic field intensity varies only slightly: an altitude variation corresponding to one atmospheric scale height[1] of 50 km corresponds to a change of only a few percent in the value of B but of orders of magnitude in the energetic particle flux. This indicates how sensitive flux values provided by environment models are to even small inaccuracies and imprecisions in the value of B or B/B_0 (where B_0 is defined as $B_0 = 0.311653/L^3$) at low altitudes[2].

The equatorial loss cone is very narrow at medium and high latitudes. As a direct consequence, the distribution of atmospheric density between 60 km and 200 km will mostly influence the equatorial pitch angle distribution of particles in only the very narrow loss cone angle around $\alpha_0 = 0°$ and $\alpha_0 = 180°$.

Figure 4.1 shows the relative magnetic field intensity B/B_0 as a function of altitude in the meridian plane through the heart of the SAA, for different latitudes. An altitude variation corresponding to one atmospheric scale height of 50 km corresponds to a change of only 2.3% in the value of B/B_0. This indicates again how sensitive flux values provided by environment models may be to small inaccuracies in the value of B or B/B_0 at low altitudes in the atmosphere.

The locus of points of deepest penetration for trapped particles can be described

[1]The atmospheric scale height is defined as $H = kT/\overline{m}g$, where k is the Boltzmann constant, T the atmospheric temperature, and $\overline{m}g$ the gravitational force on atmospheric particles of mean mass m.

[2]Note that with the above definition, B_0 is an invariant of motion.

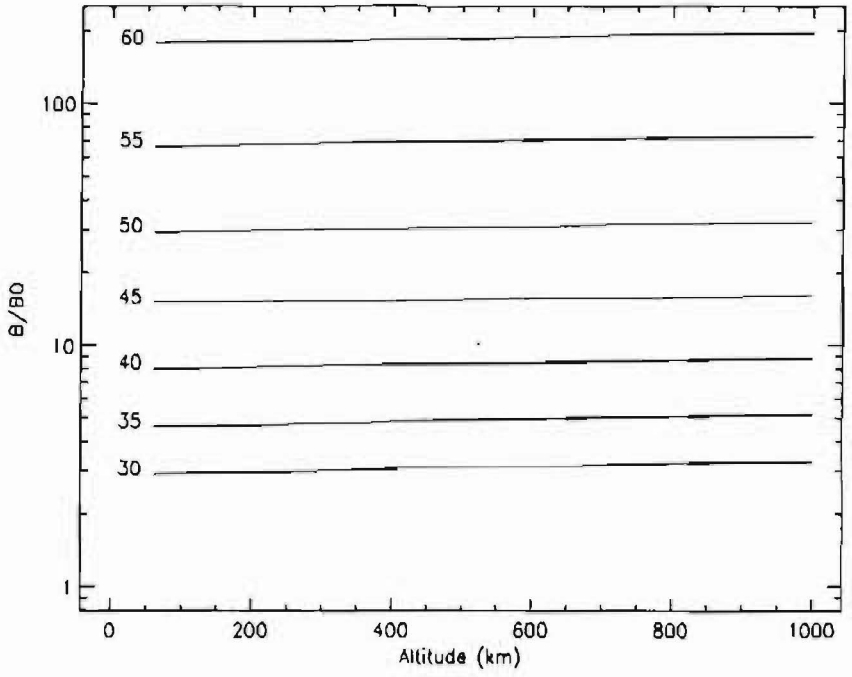

Figure 4.1. Relative magnetic field intensity B/B_0 as a function of altitude in the meridian plane passing through the SAA, for the latitudes given by the line labels

by the magnetic cut-off field intensity $B_c(L)$. Among the family of drift shells (B, L), for a given L, B_c is the highest B value for which all particles on the drift shell (B, L) are trapped. Particles on drift shells (B, L) with $B > B_c$ are precipitating or quasi-trapped particles. Since the separation between trapped and quasi-trapped particles is determined by the neutral atmosphere, B_c must be a function of the parameters influencing the density distribution of the atmosphere, such as A_p or K_p and mainly the solar radio flux $F_{10.7}$, which controls the heating of the upper atmosphere. In addition, B_c also depends on the particle energy E.

The thin atmospheric layer where the precipitated particles lose their energy can be considered as a rather abrupt absorbing wall. In the AP-8 (Sawyer & Vette 1976) and AE-8 (Vette 1991a) trapped particle models, the omnidirectional integral flux $J(E, L, B/B_0)$ drops to zero for $B_c/B_0 = 0.6572\,L^{3.452}$, an empirical formula derived by Vette (1991a) (note that with this definition B_c/B_0 also is an adiabatic invariant since it only depends on L). In the family of drift shells (B, L), the drift shell (B_c, L) is the one where the lowest altitude reached by a particle moving on this shell is 100 km. Whether the atmospheric cut-off is located at 100 km or 200 km altitude will not change significantly the equatorial loss cone angle $\alpha_{0c} = \arcsin\sqrt{B_0/B_c}$. Similarly, the equatorial pitch angle distribution $J(E, L, \alpha_0)$ will only depend significantly on B_c near $\alpha_0 = \alpha_{0c}$ and not at all near $\alpha_0 = 90°$.

Because of the very small variation of the magnetic field over the limited alti-

tude range where the trapped particle flux decreases by several orders of magnitude, neither B, B/B_0, nor α_0 are appropriate coordinates to map omnidirectional or directional particle fluxes at low altitudes. Indeed, small inaccuracies in the determination of B or α_0 will result in large errors on the atmospheric cut-off altitude. To illustrate this point, we show in Fig. 4.2 the integral proton flux $J(> 10\,\mathrm{MeV})$ in the AP-8 models (Sawyer & Vette 1976) as a function of B/B_0, for five values of L. The solid lines correspond to proton fluxes for minimum solar activity, the symbols to fluxes for solar maximum. For L values below 3 the flux decreases almost vertically when B/B_0 approaches B_c/B_0. This steep gradient of J clearly makes an accurate determination of the particle flux by interpolation in B/B_0 difficult and coarse near the atmospheric cut-off. The dependence of the particle flux J on the equatorial pitch angle α_0 is equally steep near the loss cone angle α_{0c} and equally difficult to interpolate.

4.1.2 Alternative coordinates

A useful alternative to B/B_0 has been proposed by Daly & Evans (1993). While B/B_0 varies from a value close to 1 at the geomagnetic equator to a large value near the Earth's surface, the angle φ defined as

$$\varphi = \arcsin\left(\frac{B - B_0}{B_c - B_0}\right) \tag{4.1}$$

varies from a value close to 0° at the equator to 90° at the atmospheric cut-off where $B = B_c$. The advantage of φ is that low-altitude variations in flux are spread over a larger range of variation of φ, so that interpolation between flux values becomes less difficult. This effect is illustrated in Fig. 4.3, which shows the dependence of the AP-8 MIN (solid line) and AP-8 MAX (symbols) fluxes on φ, for the same values of E and L as in Fig. 4.2.

However, it remains that the determination of the coordinate φ by means of Eq. (4.1) requires a magnetic field model with a very high accuracy and precision. In particular, near the cut-off region the coordinate φ becomes very sensitive to the value chosen for B_c. It should be emphasized that the altitude corresponding to B_c depends on the energy of the particle and ranges between 50 and 200 km.

Daly & Evans (1993) used the following values for B_c/B_0:

$$\frac{B_c}{B_0} = \begin{cases} 0.66\,L^{3.452} & \text{for AP-8 MIN} \\ 0.65\,L^{3.452} & \text{for AP-8 MAX}, \end{cases} \tag{4.2}$$

which they obtained by fitting the maximum B/B_0 values in AP-8. Figure 4.4 shows the invariant altitude corresponding to the last value of B/B_0 of the L blocks in the

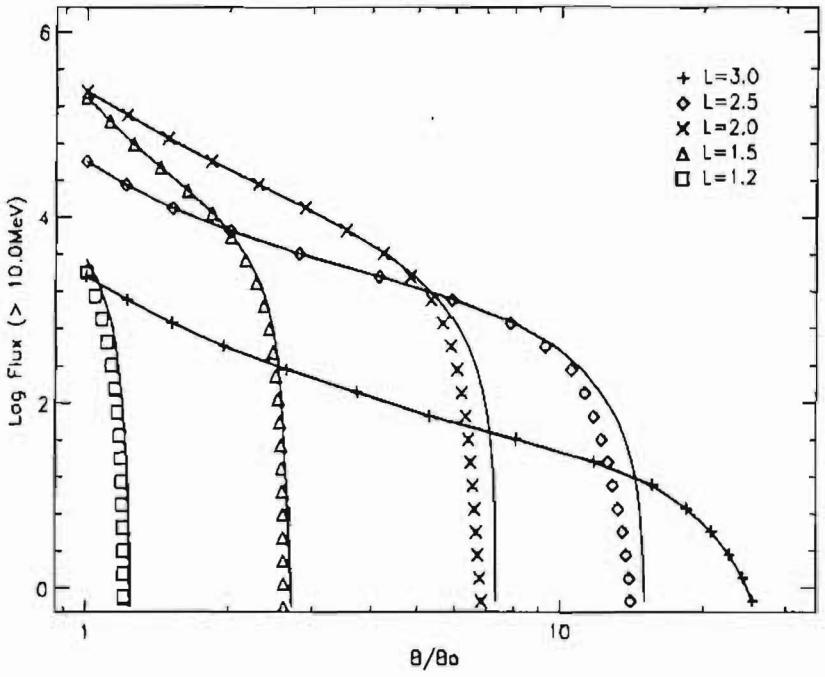

Figure 4.2. Integral AP-8 MIN/MAX proton flux above 10 MeV as a function of B/B_0 for selected L values. The symbols denote AP-8 MAX values, the AP-8 MIN values are represented by the solid lines.

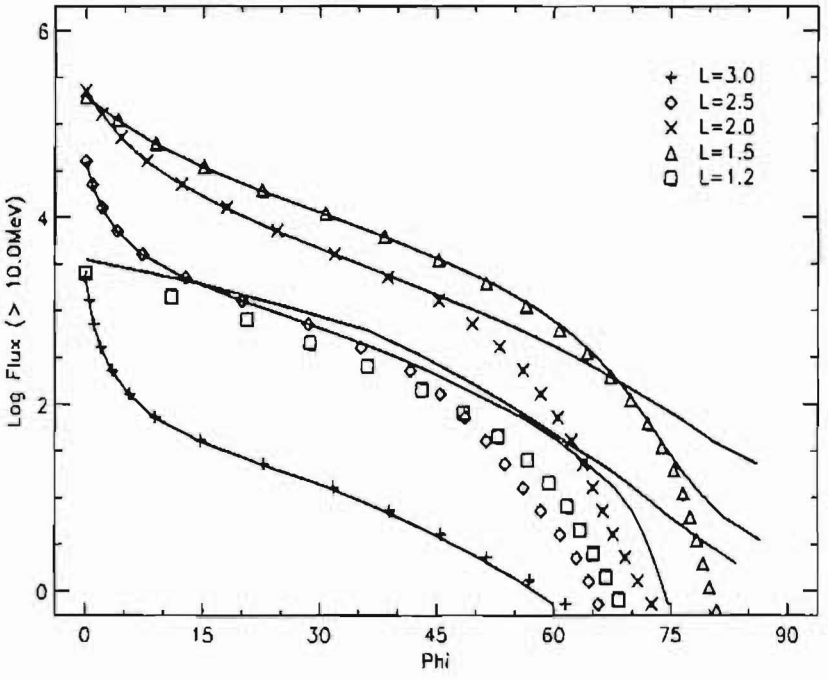

Figure 4.3. Integral AP-8 MIN/MAX proton flux above 10 MeV as a function of φ for selected L values. The symbols and lines have the same meaning as in Fig. 4.2.

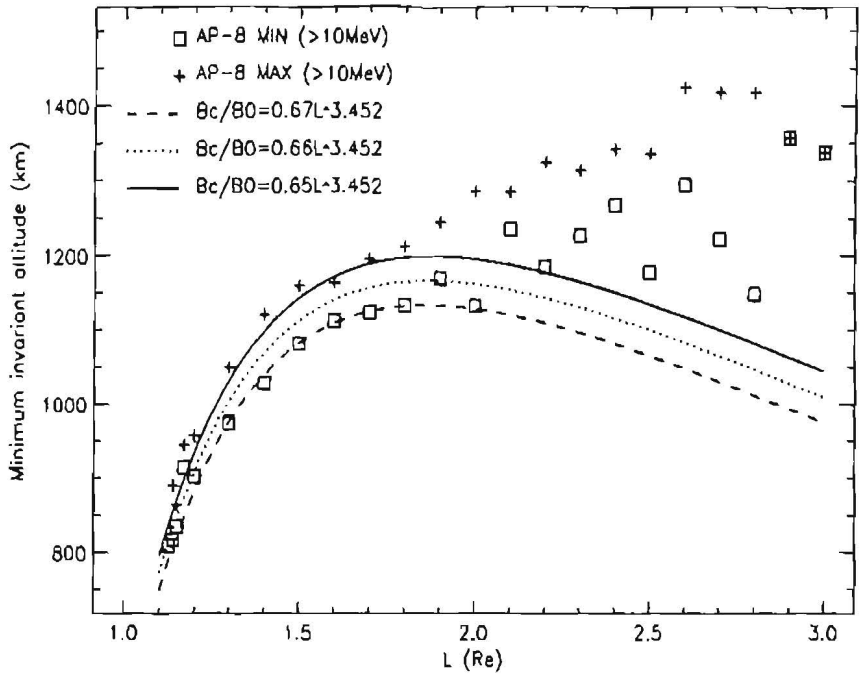

Figure 4.4. Invariant altitudes corresponding to the last B/B_0 value of the L blocks in AP-8 MAX (+) and AP-8 MIN (□), for $E > 10\,\mathrm{MeV}$. The lines show the invariant altitude corresponding to three fits of B_c/B_0.

AP-8 models, for $E > 10\,\mathrm{MeV}$, as a function of L. The dotted and solid lines in this figure represent the invariant altitude for B_c as given by Eqs. (4.2). It can be seen that for $L \leq 2$ the invariant altitude corresponding to B_c for the solar minimum model lies above the minimum invariant altitudes of the model points, which means that the B_c values are too low. A better agreement is found by raising the coefficient in the fit function from 0.66 to 0.67 (we have used the coefficient 0.67 for Fig. 4.3). The corresponding invariant altitude is shown by the dashed line in Fig. 4.4. Below $L \simeq 2$ the field line segments in AP-8 terminate very close to or on the fitted B_c values. Above $L \simeq 2$ the proton flux in the models drops to zero before the cut-off region is reached.

4.1.3 Drift shell average of atmospheric density

Although the use of the coordinate φ makes the interpolation of low altitude fluxes more accurate, Def. (4.1) is a functional dependence chosen solely for its benefit of improving the numerical accuracy of the interpolation and has no physical grounds. Similarly, Def. (4.2) is an empirical relation that was found to fit the AP-8 model data.

It has already been pointed out by Pfitzer (1990) that the atmospheric density

is a better coordinate to organise AP-8 proton fluxes at Space Station altitudes. He found that the AP-8 MIN and AP-8 MAX proton fluxes for Space Station altitudes (350–500 km) fall on almost the same curve when plotted as a function of the atmospheric densities for minimum and maximum solar activity conditions, respectively. Pfitzer's (1990) study confirms that at low altitudes the atmospheric density distribution governs the flux distribution of trapped protons. Note that the limited altitude range considered by Pfitzer corresponds to a restricted range of atmospheric density of 10^{-16}–$10^{-14}\,\mathrm{g\,cm^{-3}}$. Our study covers the full range of atmospheric densities and altitudes.

The atmospheric density $\rho(h_1)$ at a given altitude h_1 does not determine, however, the total mass of material traversed by a particle detected at the altitude h_1. In an atmosphere where the density decreases exponentially with a constant scale height H, i.e.

$$\rho(h) = \rho(h_0)\,\exp\left(-\frac{h-h_0}{H}\right), \tag{4.3}$$

the total mass of material per unit area above the point of observation at altitude h_1 is given by

$$\begin{aligned} M(h_1) &= \int_{h_1}^{\infty} \rho(h)\,dh \\ &= \rho(h_1)\,H\,. \end{aligned} \tag{4.4}$$

The atmospheric pressure scale height H is defined as

$$H = \frac{kT}{\overline{m}g}\,. \tag{4.5}$$

H is proportional to the thermospheric temperature T which is larger during solar maximum conditions than during solar minimum conditions. Therefore, the total mass $M(h_1)$ encountered by a precipitated particle is not only proportional to $\rho(h_1)$, but to $\rho(h_1)\,H$, where both $\rho(h_1)$ and H depend on solar activity conditions. Consequently, it is expected that the low altitude observations of precipitated fluxes should be better organized in terms of $M(h_1)$ than in $\rho(h_1)$.

Instead, one should consider an average of the atmospheric density over an azimuthal drift path of particles of a given species and with a given energy. Hassitt (1965b) has developed a computer code at UCSD Physics Department which calculates the number density of atoms, ions, and molecules given by appropriate atmospheric and ionospheric models over a drift shell (B, L). A weighted average density $n_s(B, L)$ is then determined by multiplying the resulting number densities with the collision cross section σ_i of the trapped particles with the constituents i, summing over i and integrating the sum over the drift shell (B, L). C.E. McIlwain has kindly provided J. Lemaire with a revised version of Hassitt's original program,

which we have modified further. A detailed description of the software package is given by Hassitt (1964).

The final output of Hassitt's code is the shell height $H_s(B, L)$, the altitude where the drift shell mean density is equal to the density in a conventional one-dimensional atmospheric model. In order to obtain a meaningful correspondence between H_s and real altitudes, it is useful (but not necessary) to adopt a reasonable density profile of the upper atmosphere.

Hassitt's code also provides the minimum altitude reached while tracing the drift shell and the atmospheric density averaged over the mirror points.

In Sect. 4.2 we describe the algorithm developed by Hassitt (1964) and the improvements we made to it.

4.2 The drift shell averaged density

In order to estimate the influence of the Earth's atmosphere on the distribution of trapped particles, the effects of the atmosphere have to be averaged over the particle's orbit. Ray (1960) and Lenchek & Singer (1962) have derived expressions for the atmospheric density averaged over the orbit of a particle trapped in a dipole field. Newkirk & Walt (1964) have determined the average density for a realistic representation of the geomagnetic field. Hassitt (1965b) has simplified considerably the procedure of Newkirk & Walt (1964), while maintaining the same accuracy. In the following sections, we will describe Hassitt's (1965b) method and it's application to the study of low-altitude coordinate systems.

4.2.1 Definition of the average

The guiding centre of a trapped particle moves along a field line with velocity

$$v_p = v\sqrt{1 - \frac{B}{B_m}}, \tag{4.6}$$

where v is the total velocity of the particle, B is the local magnetic field intensity, and B_m is the magnetic field intensity in the mirror points. The guiding centre also follows a longitudinal drift motion perpendicular to the field line. The average perpendicular drift velocity is

$$v_d = \frac{c}{qB^2T}\nabla J \times \nabla B, \tag{4.7}$$

where c is the velocity of light and q is the charge of the particle (Roederer 1970). T is the bounce time for one oscillation between the conjugate mirror points M and

M':

$$T = \int_{M'}^{M} \frac{ds}{v_p}, \tag{4.8}$$

where ds denotes an element of length along the field line. J is the second adiabatic invariant

$$J = \int_{M'}^{M} v_p \, ds \,. \tag{4.9}$$

In the absence of external forces v is constant and

$$I \equiv \frac{J}{v} \tag{4.10}$$

also is an invariant of the motion.

The adiabatic motion of a trapped particle is determined by the invariants B_m and L_m [McIwain's (1961) L obtained by tracing to the conjugate mirror points; from here on, we will drop the index "m"]. During the drift motion of a trapped particle, its guiding centre moves on a surface formed by segments of field lines determined by the conditions B=cst and L=cst. This surface is called a drift shell and is defined by the coordinate pair (B, L) (not just by L). The average atmospheric density—or the average of any quantity $f(\boldsymbol{r})$—encountered by a trapped particle is obtained by averaging $f(\boldsymbol{r})$ over the particle's drift shell.

Consider particles of energy E trapped on a drift shell (B, L). At a point P on the drift shell with geocentric coordinate vector $\boldsymbol{r}$, the number density $n_i(\boldsymbol{r})$ of atmospheric or ionospheric constituent i can be determined from suitable atmospheric and ionospheric models. We define a local weighted average density $n(\boldsymbol{r})$ as

$$n(\boldsymbol{r}) = \frac{\sum_i \sigma_i(E)\, n_i(\boldsymbol{r})}{\sigma_0}, \tag{4.11}$$

where $\sigma_0 = 10^{-15}\mathrm{cm}^2$ is a normalization factor of the order of magnitude of the collision cross sections for trapped protons with atmospheric particles. The summation in Eq. (4.11) extends over all atmospheric, ionospheric and plasmaspheric constituents that interact with trapped particles. Note that originally Hassitt's (1964) code used constant values for the cross sections, while we implemented energy dependent cross sections.

The field aligned velocity component v_p of the trapped particles depends on their local pitch angle, being zero at the mirror points and reaching its maximum on the geomagnetic equator. Consequently, the particles spend more time in the high density region around their mirror points than closer to the equator. To account for this effect when integrating the local average density n over the drift shell, we apply as a weight factor the time needed for the particles to move to a neighbouring point on the same field line during their bounce motion. The azimuthal drift velocity also

is position dependent, so that a second weight factor, namely the time needed to drift to a neighbouring field line on the azimuthal drift motion, has to be used.

Let dx and dy denote elements of length along a field line and along the direction of azimuthal drift, respectively, and v_p and v_d the corresponding local drift velocities. A drift shell averaged atmospheric density n_s then can be defined as

$$n_s(B, L) = \frac{S(n, B, L)}{S(1, B, L)}, \tag{4.12}$$

with

$$S(n, B, L) = \iint n(\boldsymbol{r}) \frac{dx}{v_p} \frac{dy}{v_d}, \tag{4.13}$$

where the denominator in Eq. (4.12) serves as a normalisation factor and the integration in Eq. (4.13) extends over the whole drift shell.

Equation (4.13) can be written in an alternative way. Let $\dot{\phi}$ be the projection of v_d along the ϕ axis in polar coordinates (r, θ, ϕ). One then has that

$$\frac{dy}{v_d} = \frac{d\phi}{\dot{\phi}}, \tag{4.14}$$

so that S can be defined in terms of $d\phi/\dot{\phi}$ rather than dy/v_d.

4.2.2 Calculation of the average

The calculation of $\dot{\phi}$ is a difficult and time consuming numerical process. Hassitt (1965a) has shown that $d\phi/\dot{\phi}$ is independent of s, s being the distance along the field line measured from the equator. The distance between two neighbouring field lines varies with s, as does $\dot{\phi}$, but $d\phi/\dot{\phi}$—which represents the time needed to drift from one field line to the other—is independent of s, as a first approximation. Consequently, Eq. (4.13) can be written as

$$S(n, L, B) = \int U(n, L, B, \phi_0) \frac{d\phi}{\dot{\phi}}, \tag{4.15}$$

where

$$U(n, L, B, \phi_0) = \int n(\boldsymbol{r}) \frac{ds}{v_p}, \tag{4.16}$$

and ϕ_0 is the azimuth of the point where the field line intersects the equator. The quantity $d\phi/\dot{\phi}$ can be evaluated at any point on the field line, but the simplest way is to choose the point of intersection with the magnetic equator plane. By using Eqs. (4.15) and (4.16), the two-dimensional integration over the drift shell is decomposed into two one-dimensional integrations. In addition, $\dot{\phi}$ has to be evaluated at one point only for each field line. Note that it follows from Eq. (4.8) that $U(1, L, B, \phi_0) = T$, where T is the bounce time between mirror points.

4.2.3 The computer program

Hassitt (1964) has written a computer code to evaluate n_s. It uses the Jensen & Cain (1962) geomagnetic field model and the now obsolete atmosphere model of Anderson & Francis (1964). In Hassitt's program, $n = n(r)$ is a function of the geodetic altitude only and does not depend on latitude or longitude, which is a severe limitation.

Hassitt's (1964) program makes use of two additional approximations, which could have been avoided at the expense of (significantly) increased computing time. The first approximation is that $\dot{\phi}$ is approximated by the value of $\dot{\phi}$ for a particle mirroring at the equator. In this case, the following expression can be used:

$$v_d = mcv^2 \frac{|\nabla B|}{2qB^2} \tag{4.17}$$

(see, for instance, Lew 1961). $\dot{\phi}$ is a function of B_m, but Hassitt (1965a) has shown that for two mirror points on the same field line the ratio $\dot{\phi}(B_1)/\dot{\phi}(B_2)$ depends only weakly on ϕ.

The second approximation in the program is that a drift shell is defined as a shell of constant B_0. In other words, L is assumed to be constant along field lines, which is—although only true for a dipole field—a reasonable approximation in the near-Earth geomagnetic field where the dipole is the dominant term. Hassitt (1965b) argues that by averaging over the longitudinal drift, the resulting errors are virtually cancelled out. The major advantage of identifying a shell by B_0 is that it is much easier to locate it than if one has to calculate L in a series of points along the field line. In addition, for a given value of ϕ_0 and a series of values of B, it is sufficient to trace one field line, while otherwise it would be necessary to retrace the field line for each value of B.

4.2.4 Definition of a shell height

The drift shell averaging program provides the weighted average density of a number of atmospheric and ionospheric constituents encountered by a trapped particle during one full drift motion around the Earth. In order to visualize better the result of the calculations, Hassitt (1965b) introduced an average height related to the average density.

Hassitt's definition

Originally, Hassitt (1965b) made use of a simple exponential atmosphere model to relate a shell height to the average density. In this model, the density of the neutral

constituents of the atmosphere varies as

$$n(h) = A\,\mathrm{e}^{-\mu h^*}\,, \tag{4.18}$$

where

$$h^* = \frac{h}{R_\mathrm{E} + h} \tag{4.19}$$

is the reduced height and $R_\mathrm{E} = 6371.2\,\mathrm{km}$ is the radius of the Earth. Given an average density $n_\mathrm{s}(L, B_\mathrm{m})$, the corresponding reduced average height is defined as

$$h^*_\mathrm{av} = -\frac{\ln\left(\frac{n_\mathrm{s}}{A}\right)}{\mu}\,, \tag{4.20}$$

and the average height as

$$h_\mathrm{av} = \frac{h^*_\mathrm{av}}{1 - h^*_\mathrm{av}}\,R_\mathrm{E}\,. \tag{4.21}$$

Hassitt (1965b) has fitted the Anderson & Francis (1964) model with Expression (4.18) and determined A and μ for the various atmospheric constituents.

McIlwain's definition

In the software BIRA/IASB received from C. McIlwain, the shell height is computed in a different way. For a given value of the shell-averaged density, the subroutine EQAT determines the altitude at which the average density is equal to the density given by the Anderson & Francis (1964) model. This approach has the disadvantage that the shell height depends on the choice of the atmosphere model used to calculate the average density, so that solar cycle effects and other influences are largely cancelled out.

New approach

We opted for a simpler approach, in which we make use of a very basic average atmosphere model. Allen (1985) provides a table with average atmosphere and ionosphere number densities as a function of altitude. We fitted this distribution with an exponential distribution below 100 km and with two linear functions between 100 and 1000 km and above 1000 km. The tabulated points and the fit functions are shown in Fig. 4.5. Depending on the input density, the appropriate fit function is inverted to yield the shell height.

The advantage of this approach is that the shell height does not depend on the atmosphere model used to calculate the shell-averaged density. In addition, the inversion procedure is very simple and does not involve a numerical procedure for location of zero points.

Table 4.1. NAMELIST parameters for the shell height program

Parameter	Data Type	Default	Function
		SHELL	
MODEL	INTEGER	0	Chooses the geomagnetic model: 0: DGRF/IGRF 1: Jensen & Cain (1962) 2: GSFC 12/66 (Cain et al. 1967)
BLTIME	REAL*8	1990.0	Epoch for geomagnetic field model
		ATMOS	
ATMMOD	CHARACTER*2	MI	Chooses the atmosphere model: AF: Anderson & Francis (1964) MI: MSISE-90, IRI-90, Carpenter & Anderson (1992) MD: MDAC (Pfitzer 1990) NO: No atmosphere model
DAY	INTEGER	1	Day of year
UT	REAL*8	0.0	Universal time (hrs)
TL	REAL*8	0.0	Local time (hrs)
F107	REAL*8	100.0	Daily $F_{10.7}$ flux for previous day
F107M	REAL*8	100.0	3 Month average of $F_{10.7}$ flux
AP	REAL*8(7)	7*0.0	Magnetic index A_p: AP(1): daily A_p AP(2): 3 hr A_p index for current time AP(3): 3 hr A_p index for 3 hrs. before current time AP(4): 3 hr A_p index for 6 hrs. before current time AP(5): 3 hr A_p index for 9 hrs. before current time AP(6): average of eight 3 hr A_p indices from 12 to 33 hrs. prior to current time AP(7): average of eight 3 hr A_p indices from 36 to 59 hrs. prior to current time

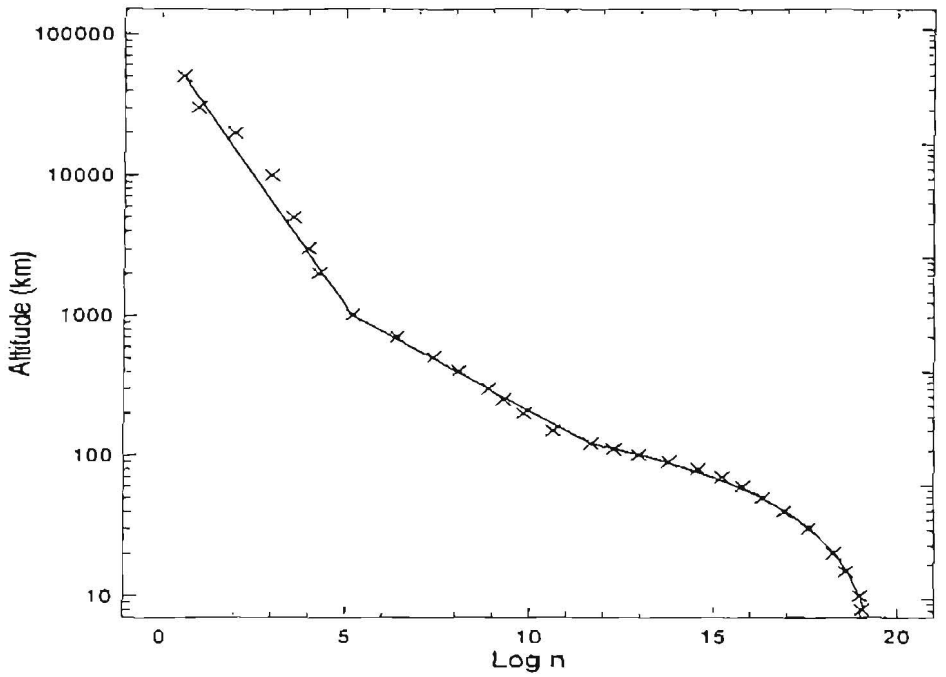

Figure 4.5. Density distribution (from Allen [1985]) used in the new definition of the shell height. The solid line represents the fit functions used for different altitude ranges.

Table 4.1. (continued)

Parameter	Data Type	Default	Function
			SWI(9) $\neq -1$: only daily A_p is used.
SWI	REAL*8(25)	25*1.0	Selects variation on 25 parameters: 0: main effects off, cross terms off 1: main effects on, cross terms on 2: main effects on, cross terms off
		ATMOS	
RZ	REAL*8	100.0	Zürich solar sunspot number
KPMAX	REAL*8	1.0	Maximum K_p value for Carpenter & Anderson (1992) model
CROSS	INTEGER	1	0: Hassitt's cross sections $\neq$ 0: cross section obtained with CROSS

Table 4.2. NAMELIST parameters for the shell height program, for conditions of solar minimum and solar maximum

Parameter	Solar minimum	Solar maximum
F107	50.0	300
F107M	60.0	200.0
AP	7*0.0	300.0, 6*0.0
SWI	25*1.0	25*1.0
RZ	50.0	250.0
KPMAX	1.0	6.0

4.2.5 Modifications of Hassitt's software

This section gives an overview of the modifications that were made to Hassitt's (1964) original software:

1. The DGRF/IGRF and GSFC 12/66 (Cain et al. 1967) geomagnetic field models were added.

2. The MSIS and IRI models and the model of Carpenter & Anderson (1992) were added for a better description of the upper atmosphere, the ionosphere, and the plasmasphere. The atmosphere model developed by McDonnell Douglas Astronautics Co. (MDAC), used by Pfitzer (1990), also was included. The subroutine ATMO was added to calculate or set up appropriate parameters depending on the choice of atmosphere model. It is also possible to run the code without an atmospheric model.

3. The input parameters are read from two NAMELISTs, SHELL and ATMOS. The parameters are listed in Table 4.1. The values of the NAMELIST parameters we adopted for solar minimum and solar maximum conditions in the next sections are listed in Table 4.2.

4. The subroutine that calculates the shell height was replaced.

In addition, the structure of the original program was modified and simplified. The old Fortran code was updated to the FORTRAN-77 standard. Comments have been inserted where significant modifications were made.

The implementation of MSIS, MDAC, IRI and the plasmaspheric extension are discussed briefly in the following sections and in more detail in Technical Note 2.

The MSIS atmosphere models

The Mass-Spectrometer-Incoherent-Scatter (MSIS) neutral atmosphere model describes the neutral temperature and the densities of He, O, N_2, O_2, Ar, H, and N. The MSIS model is based on the extensive data compilation and analysis of A.E. Hedin and his collaborators. The model version used for TREND is MSISE-90 (Hedin 1991).

Data sources for the model MSISE-90 include temperature and density measurements from several rockets, satellites (OGO 6, San Marco 3, Aeros-A, AE-C, AE-D, AE-E, ESRO 4, DE 2) and incoherent scatter radars (Millstone Hill, St. Santin, Arecibo, Jicamarca, Malvern). Since the MSIS-83 model, terms were added or changed to better represent seasonal variations in the polar regions under both quiet and magnetically disturbed conditions and local time variations in the magnetic activity effect. In addition, a new species, atomic N, was added to the list of species covered by the model.

The model expects as input: year, day of year, universal time, geodetic altitude, latitude and longitude, local apparent solar time, solar $F_{10.7}$ flux (for previous day and three-month average), and magnetic A_p index (daily A_p or A_p history for last 59 hours). For these conditions, the following output parameters are calculated: number density of He, O, N_2, O_2, Ar, H and N, total mass density, neutral temperature, and exospheric temperature. The source code is equipped with 25 flags `SWI` to turn on or off variations due to seasonal, diurnal, semidiurnal, terdiurnal, ... changes.

The input parameters for MSISE-90 are supplied in the `NAMELIST ATMOS`. Table 4.1 lists the `NAMELIST` parameters, together with their data type, default values, and a brief description. The main MSIS routine is called from the subroutine `ATMO` with the appropriate input parameters. The values returned are the neutral and the exospheric temperature, the number density of all constituents, and the total mass density.

The `NAMELIST` parameters for MSISE-90 are: `DAYNR`, `UT`, `F107`, `F107M`, `AP`, `SWI`. The 25 flags `SWI` allow one to disable all longitudinal and temporal variations in the calculation of the MSIS densities. We set the default `SWI` values to one.

The MDAC atmosphere model

McDonnell Douglas Astronautics Co. under contract to the Air Force Office of Scientific Research developed an atmospheric density model (*Response of the Magnetosphere and Atmosphere to the Solar Wind*, Final MDAC Scientific Report for Contract F44620-72-C-0084 for the Air Force Office of Scientific Research, December 1975).

This model has the advantage of simplicity. The altitude dependent term is

Table 4.3. Limiting values for the input parameters in IRI-90

Parameter	Lower (Day/Night)	Upper
Altitude for electron density	60/80 km	1000 km
Altitude for temperatures	120 km	3000 km
Altitude for ion densities	100 km	1000 km
Solar sunspot number	0	250

a global average term and thus can be used directly in this study. The average atmospheric density d is given as

$$d = d_0 \exp\left(-\frac{z-120}{A\sqrt{z-103}}\right), \tag{4.22}$$

where d is the density in $\mathrm{g\,cm^{-3}}$, $d_0 = 2.7 \times 10^{-11}\mathrm{g\,cm^{-3}}$, z is the altitude in km, and A is the solar cycle term:

$$A = 0.99 + 0.518\sqrt{\frac{F_{10.7} + F_{10.7M}}{110}}. \tag{4.23}$$

The IRI ionosphere models

The International Refererence Ionosphere (IRI) is the standard ionospheric model established and updated by a joint working group of URSI and COSPAR. Based on a large volume of ground and space data, IRI describes monthly averages of electron density, electron temperature, ion temperature, ion composition and ion drift in the altitude range from 50 km to 1000 km for magnetically quiet conditions in the non-auroral ionosphere. The auroral region is beyond the L values corresponding to the trapped radiation belts.

The latest version of IRI is IRI-90 (Bilitza 1990). The most recent version of the IRI computer program (No. 12) was released in November 1991. It includes the most recent COSPAR International Reference Atmosphere (CIRA) for the neutral temperature. We obtained this version from NSSDC and implemented it in Hassitt's software. The input parameters for IRI-90 are day of year, U.T., and the Zürich solar sunspot number R_Z. The data types and default values for these parameters are given in Table 4.1. The limiting values for the altitude and for R_Z are listed in Table 4.3.

The input parameters for the main subroutine `IRIS12.FOR` in IRI-90 are geodetic or geomagnetic latitude and longitude, geodetic altitude, Zürich sunspot number

(twelve-month running mean), day of year, local or universal time, and a series of logical variables. The output consists of: electron density, normalised electron density (to F2 peak density), neutral temperature (CIRA-86), electron and ion temperature, electron to ion temperature ratio, and relative percentage densities of O^+, H^+, He^+, NO^+, and O_2^+. The altitude limits are given in Table 4.3.

Plasmaspheric extensions

Since the IRI-90 model is limited to the altitudes given in Table 4.3, an extension of the ionization density in the magnetosphere is required to account for the small loss from pitch angle scattering experienced by the trapped ions and electrons forming the radiation belts. It is usually held that pitch angle scattering of trapped particles is due to wave-particle interactions. In this study, we only considered the effects of collisions.

Several three dimensional models have been proposed to describe the equatorial and field-aligned ionization density in the plasmasphere and plasmatrough. We used the model of Carpenter & Anderson (1992), which is described below.

The model of Carpenter & Anderson (1992) of the equatorial density is based on

1. electron density profiles derived from sweep frequency receiver radio measurements made along near-equatorial ISEE 1 satellite orbits,

2. results from whistlers.

The model describes, in piecewise fashion, the "saturated plasmasphere", i.e. the region of steep plasmapause gradients, and the plasmatrough (Carpenter & Anderson 1992).

The plasmapause inner limit L_{ppi} is a function of the magnetic activity index $K_{\mathrm{p_{max}}}$:

$$L_{\mathrm{ppi}} = 5.6 - 0.46\, K_{\mathrm{p_{max}}}\,, \tag{4.24}$$

where $K_{\mathrm{p_{max}}}$ is the maximum K_{p} value of the preceding 24 hours. There are three exceptions: for L_{ppi} in the magnetic local time (MLT) intervals 06–09, 09–12, and 12–15, omit the one, two, or three immediately preceding K_{p} values, respectively, in the determination of $K_{\mathrm{p_{max}}}$.

The density of the saturated plasmasphere element for $2.25 \le L \le L_{\mathrm{ppi}}$ is given by

$$\log n_{\mathrm{e}} = (-0.3145\, L + 3.9043) + \left\{ 0.15 \left[\cos \frac{2\pi(d+9)}{365} - 0.5 \cos \frac{4\pi(d+9)}{365} \right] + 0.00127 R_Z - 0.0635 \right\} \mathrm{e}^{-(L-2)/1.5}\,, \tag{4.25}$$

where R_Z is the 13 month average sunspot number and d the day number. This expression gives the electron density in the equatorial plane.

In order to determine the thermal plasma densities at non-equatorial latitudes along magnetic flux tubes, the hydrostatic equations should in principle be integrated as in Angerami & Thomas (1964), or a more complex kinetic (exospheric) model should be used as in Lemaire (1989), Chiu et al. (1978), or Rycroft & Jones (1985, 1987). Even more sophisticated dynamical models are now developed by using Monte Carlo simulation methods (Wilson 1992).

In this study, we used the following procedure. For points beyond the plasmapause, i.e. when the geocentric distance $r > L_{\mathrm{ppi}}$, we set $n_e = n_{H^+} = 10\,\mathrm{cm}^{-3}$ and $T_e = T_{H^+} = 4000\,\mathrm{K}$. The densities of the other ions are neglected and set to zero.

The field-aligned electron density in a point P below the plasmapause, with geodetic coordinates (r, λ, ϕ), is approximated by

$$n_e(r, \lambda, \phi) = n_{CA}(L)\, e^{-CR_E/r}\,, \tag{4.26}$$

where n_{CA} is the Carpenter & Anderson (1992) equatorial electron density on the dipole field line passing through P. For a centred dipole geomagnetic field model, the corresponding L value is given by

$$LR_E = \frac{r}{\cos^2 \lambda_1}\,, \tag{4.27}$$

where λ_1 is the geomagnetic latitude of P. C is determined by the IRI-90 electron density in the point Q on the same field line (and thus with the same geomagnetic longitude ϕ_1 in the centred dipole model) at altitude 1000 km (the limiting altitude of IRI-90). The geomagnetic latitude of Q is

$$\lambda_m \equiv \arccos \sqrt{\frac{R_E + 1000}{LR_E}}\,. \tag{4.28}$$

Applying the coordinate transformation from geomagnetic to geocentric coordinates yields the geocentric latitude and longitude λ_c, ϕ_c of Q, which are used as input to IRI-90 to determine n_{1000}, the electron density at 1000 km altitude. From Eq. (4.26) it then follows that

$$C = -\left(1 + \frac{1000}{R_E}\right) \ln \frac{n_e(R_E + 1000, \lambda_c, \phi_c)}{n_{CA}(L)}\,. \tag{4.29}$$

In order to determine the ion densities, we assume that the plasmaspheric density of a plasma constituent i can be approximated by using the condition of isothermal diffusive equilibrium, i.e.

$$n_i(r, \lambda, \phi) = n_i(R_E + 1000, \lambda, \phi)\, \exp\left[-\frac{1}{H_i}\, \frac{(R_E + 1000)(r - R_E - 1000)}{r}\right]\,, \tag{4.30}$$

where $n_i(R_E + 1000, \lambda, \phi)$ is determined with IRI-90 and H_i is a shell height. H_i can be derived from the condition of hydrostatic equilibrium for a plasma consisting of electrons and N ion species in an electric field E:

$$\frac{dp_e}{dr} = -n_e m_e g - n_e e E \tag{4.31}$$

for electrons and

$$\frac{dp_i}{dr} = -n_i m_i g + n_i Z_i e E \tag{4.32}$$

for ion species i, where p is the pressure, m the atomic mass, and Ze the charge of the particles. In the ideal gas approximation $p = nkT$, so that

$$\frac{dn_e}{dr} = -\frac{n_e m_e}{kT_e} g - \frac{n_e}{kT_e} eE \tag{4.33}$$

and

$$\frac{dn_i}{dr} = -\frac{n_i m_i}{kT_i} g + \frac{n_i Z_i}{kT_i} eE\,. \tag{4.34}$$

Multiplying both members by Z and summing over electrons and all ions gives

$$-\frac{dn_e}{dr} + \sum_{i=1}^{N} \frac{dn_i}{dr} Z_i = \frac{n_e m_e}{kT_e} g + \frac{n_e}{kT_e} eE - \sum_{i=1}^{N} \frac{n_i m_i Z_i}{kT_i} g + \sum_{i=1}^{N} \frac{n_i Z_i^2}{kT_i} eE\,. \tag{4.35}$$

Since the plasma is neutral $-n_e + \sum_{i=1}^{N} n_i Z_i = 0$, and consequently the left-hand side of Eq. (4.35) is zero, so that

$$eE = \frac{-\dfrac{n_e m_e}{T_e} + \displaystyle\sum_{i=1}^{N} \frac{n_i m_i Z_i}{T_i}}{\dfrac{n_e}{T_e} + \displaystyle\sum_{i=1}^{N} \frac{n_i Z_i^2}{T_i}}\, g\,. \tag{4.36}$$

Substituting in Eq. (4.34) and dividing both sides by n_i yields

$$-\frac{d \ln n_i}{dr} = \frac{1}{H_i} = \left(m_i - Z_i \frac{-\dfrac{n_e m_e}{T_e} + \displaystyle\sum_{j=1}^{N} \frac{n_j m_j Z_j}{T_j}}{\dfrac{n_e}{T_e} + \displaystyle\sum_{j=1}^{N} \frac{n_j Z_j^2}{T_j}} \right) \frac{g}{kT_i}\,. \tag{4.37}$$

The electron and ion temperatures are provided by IRI-90. The ion temperature is the same for each species. With Eqs. (4.30) and (4.37) the plasmaspheric density for four of the ion species in IRI-90 (O^+, He^+, O_2^+, NO^+) can be determined. The H^+ density is obtained as

$$n_{H^+} = n_e - (n_{O^+} + n_{He^+} + n_{O_2^+} + n_{NO^+})\,, \tag{4.38}$$

in order to ensure the neutrality of the plasma. However, this approach causes a problem for the He^+ density, which has a negative scale height at 1000 km (i.e. the density is still rising). Therefore, we make one more approximation in that we artificially keep the ratio of the He^+ to the H^+ densities constant at its value at 1000 km. Equation (4.38) then becomes

$$n_{H^+} = \frac{n_e - (n_{O^+} + n_{O_2^+} + n_{NO^+})}{1 + \frac{n_{He^+1000}}{n_{H^+1000}}} . \tag{4.39}$$

The He^+ density is then obtained as

$$n_{He^+} = \frac{n_{He^+1000}}{n_{H^+1000}} n_{H^+} . \tag{4.40}$$

The plasmaspheric extension of the electron and ion densities has been implemented in a subroutine called `DCA.FOR`. This subroutine takes one input parameter, `KPMAX`, corresponding to the maximum K_p over the preceding day. This parameter was added to the `NAMELIST ATMOS` (see Table 4.1).

4.2.6 Calculation of atmospheric cross sections

The collisional cross section of trapped particles interacting with the neutral atmosphere and the ionosphere serves as a measure for the relative scattering efficiency of the various constituents and processes involved.

The different collision processes relevant for electrons and protons impacting on atmospheric constituents are discussed in Technical Note 2. The main processes to consider are: excitation and ionization of the target, dissociation for target molecules, charge exchange for protons on atoms and Coulomb interaction for charged particles. The relative importance of the different processes depends on the type of particles and the energy range. For each interaction, analytic expressions for the collision cross section as a function of the kinetic energy of the incident particle have been derived in the literature. The expressions have been implemented in a computer program, `CROSS`, that takes as input the kinetic energy of the incident particle, the type of particle, both incident and target, and returns the total cross section for all relevant collision processes. Hassitt's (1964) original software does not take into account the dependence of the cross section on the kinetic energy of the incident particles.

The different atmospheric components considered in `CROSS` are essentially atomic and molecular H, He, O and N. For electron collision cross sections, all the results are valid for energies higher than 500 eV. For O, the proton cross sections are a little overestimated between 10 and 500 keV due to interpolations. The collision

Table 4.4. Values of the total cross section for collisions between energetic protons and atmospheric particles divided by the total (Coulomb) cross section for collisions between energetic protons and electrons. The values used by Hassitt (1964) are compared with the values found by the program CROSS at 500 keV and at 1 MeV.

Species	Hassitt	CROSS 500 keV	CROSS 1 MeV
e^-	1.0	1.0	1.0
O_2	7.16	7.94	19.0
N_2	6.36	7.71	17.8
O	3.58	3.43	7.9
N	3.2	3.43	7.8
He	1.01	1.18	2.8
H	0.52	1.10	2.3
O_2^+	6.72	2.87	6.51
N_2^+	6.32	2.86	6.49
O^+	3.14	1.43	3.0
He^+	0.50	0.19	0.50

cross sections of protons impacting on O_2 molecules may be underestimated below 100 keV because charge exchange has been neglected for O_2. For all other atoms and molecules, the cross sections are the best currently available values at energies above 500 eV.

For proton-ion collisions the cross sections are only valid for energies higher than 200 keV. However, the cross section for collisions between energetic protons and electrons is correct because the Coulomb interaction prevails.

It is also important to note that the experimental values are generally measured below 100 keV for electrons. Because these energies are much larger than the excitation and ionization level, the cross sections are fitted with analytic functions based on the Bethe-Born approximation and extrapolated for higher energies. When the cross sections are obtained from interpolated measurements, the program also extrapolates for higher energies than given in the tables.

We illustrate the results obtained with CROSS in Table 4.4, which shows the values used by Hassitt (1964) compared with the values found by CROSS at 500 keV and at 1 MeV. At 500 keV, the values for neutral constituents are similar, but at 1 MeV the values obtained with CROSS are much higher because the Coulomb cross section between protons and electrons decreases as E^{-2}. The ion collision cross sections are lower, due to the higher ionization threshold of ions compared to neutral atoms.

CROSS has been added as a subroutine to our copy of Hassitt's software. The choice between the original energy independent cross sections and CROSS is made with the NAMELIST parameter CROSS.

4.2.7 Application to density profiles through the SAA

Figures 4.6–4.7 represent the average number density profile through the SAA obtained with MSISE-90, IRI-90 and CA for the summer solstice and local midnight, for conditions of low and high solar activity, respectively. The averages were made first with Hassitt's cross sections as weight factors, dividing the cross sections by 100 for normalisation. Then, the cross sections obtained with CROSS were used, normalised by dividing by 10^{12}, for four proton energies: 0.1, 1, 10 and 100 MeV.

The first feature to note is that the five curves in each graph are almost identical except for a shift towards lower average density for higher energy. The main difference besides this shift is that for the lowest energy and for Hassitt's cross sections the density curve is steeper above 1000 km than the other curves for higher energies. This effect is due to the increased importance of the Coulomb cross section at lower energies.

The dependence of n_s on energy strongly influences the shell height H_s. Figures 4.8–4.9 show H_s as a function of altitude for the density profiles in Figs. 4.6–4.7.

4.3 Application of the drift shell averaged density

In this section, we report on results obtained the software described in Sect. 4.2. In Sect. 4.3.1 we show the distribution of several parameters resulting from the calculation over the world map at constant altitude. In Sect. 4.3.2 we demonstrate the usefulness of n_s by applying it to the proton flux distribution given by the AP-8 models.

4.3.1 Distribution of parameters

As a first application, we ran the software for a grid of points at altitude 1000 km. First, we calculated the (B, L) coordinates of each point—for pitch angle 90°—with BLXTRA. The resulting (B, L) were then used as input to the shell averaging software, producing values of n_s for each point in the grid. We also stored the minimum altitude reached on each drift shell, denoted by $h_{\min}$, and the local averaged number density in these points, denoted by $n_{\min}$.

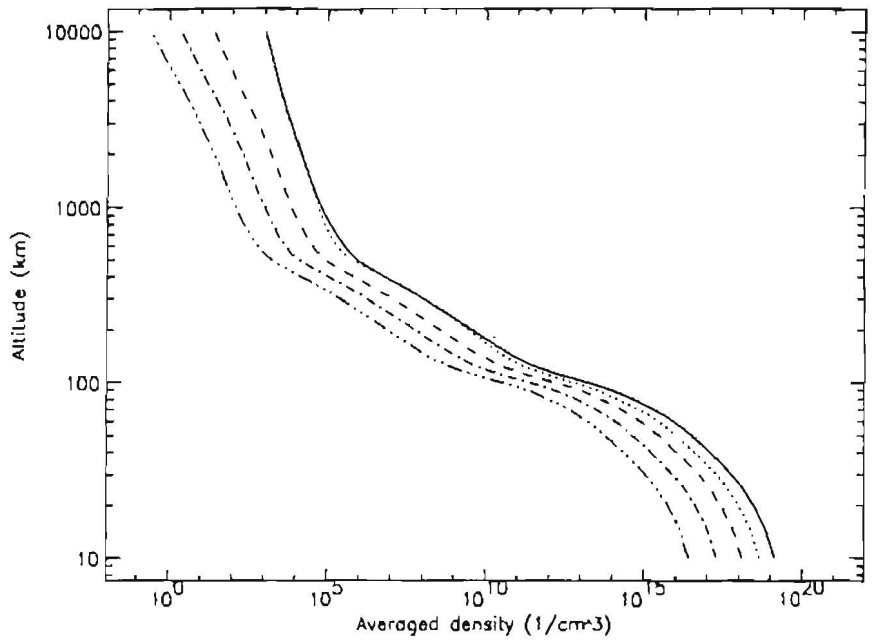

Figure 4.6. Averaged number density profiles in the SAA obtained with MSISE-90, IRI-90 and CA for the summer solstice, midnight L.T., for low solar activity. The solid line was obtained with Hassitt's cross section values, the other lines with the CROSS values for four energies (in MeV): 0.1 (dotted), 1 (dashed), 10 (dot-dashed), 100 (triple-dot-dashed).

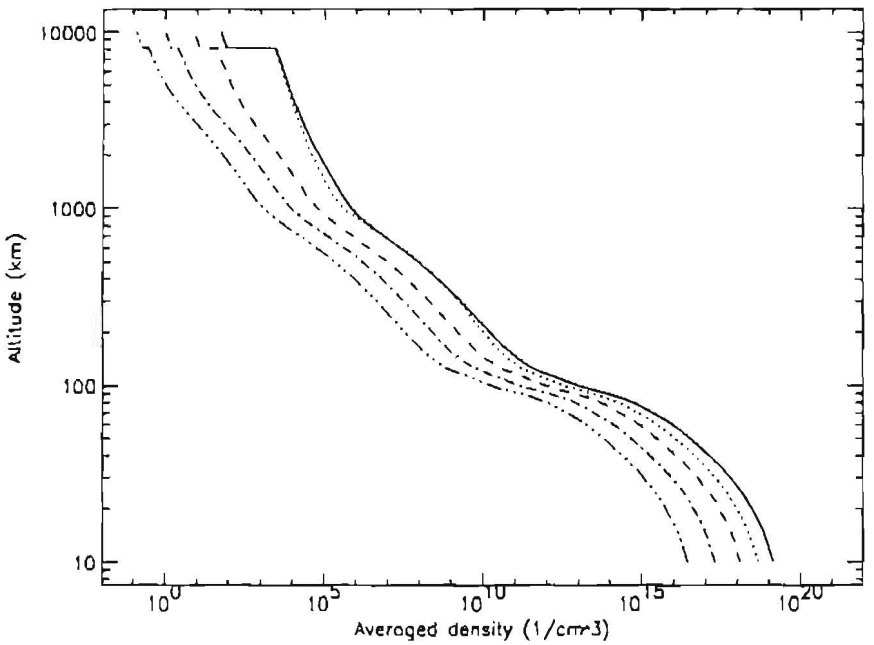

Figure 4.7. Averaged number density profiles in the SAA obtained with MSISE-90, IRI-90 and CA for the summer solstice, midnight L.T., for high solar activity. The line styles have the same meaning as in Fig. 4.6.

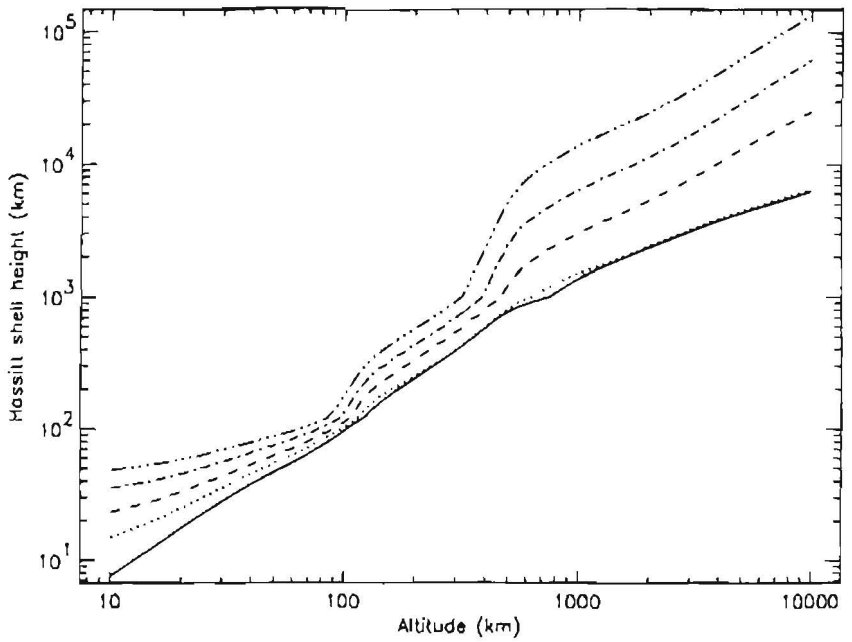

Figure 4.8. Hassitt shell height as a function of altitude for the density profiles in Fig. 4.6

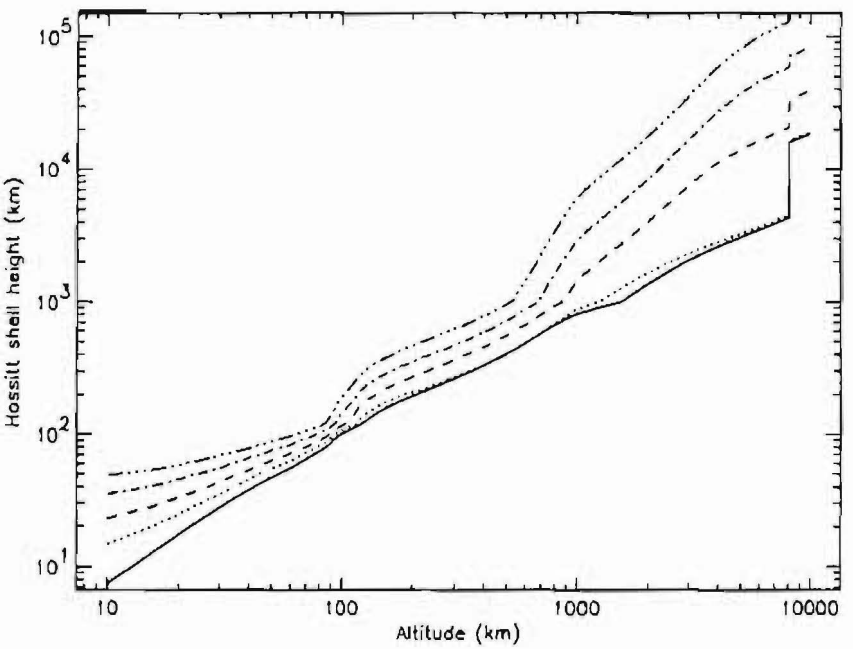

Figure 4.9. Hassitt shell height as a function of altitude for the density profiles in Fig. 4.7

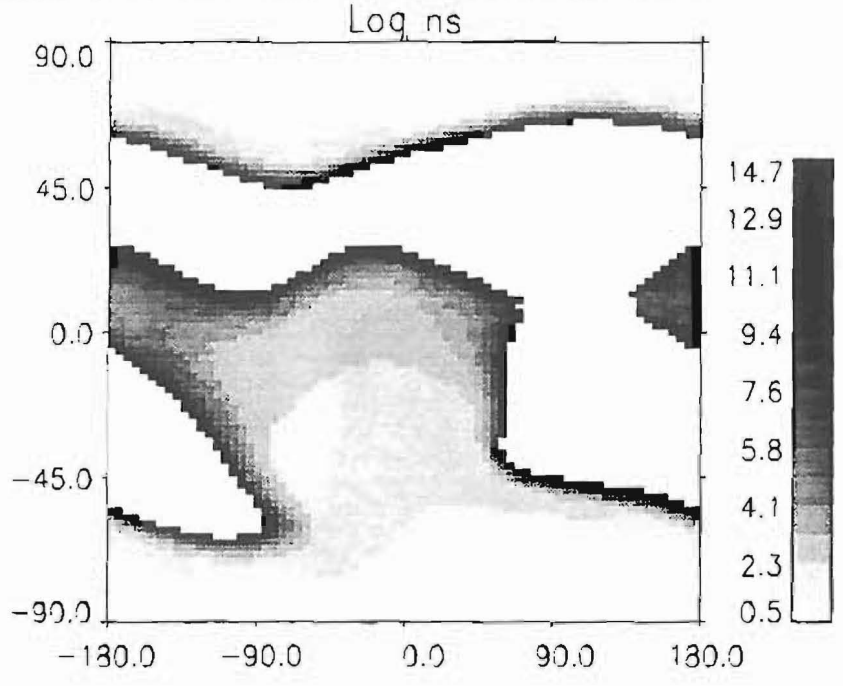

Figure 4.10. Distribution of $\log n_s$ over the world map at 1000 km

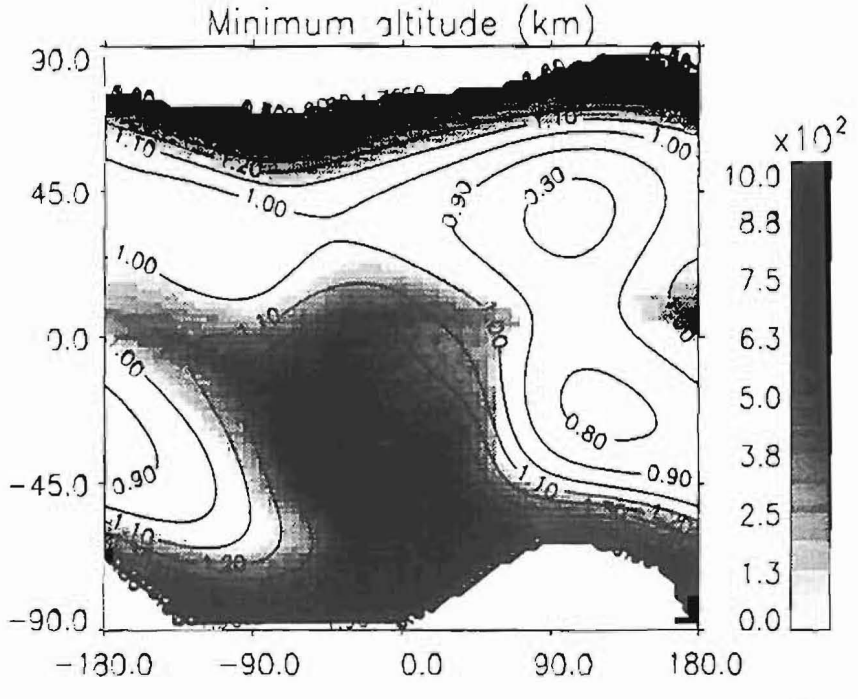

Figure 4.11. Distribution of h_{min} over the world map at 1000 km. The solid lines represent constant values of the ratio B_c/B.

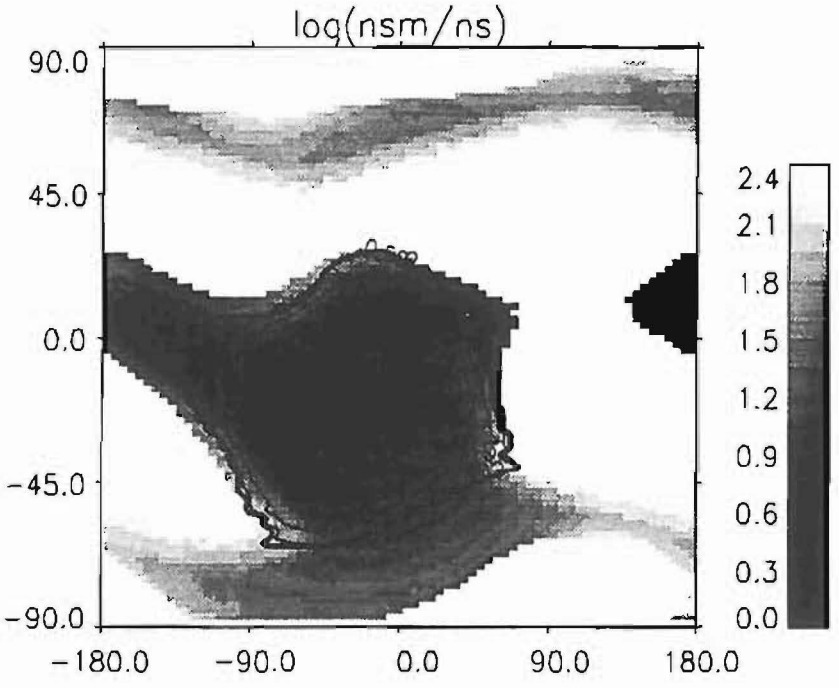

Figure 4.12. Distribution of the ratio n_{min}/n_s over the world map at 1000 km. The solid lines are lines of constant AP-8 MIN flux above 10 MeV.

Figure 4.10 shows the distribution of $\log n_s$ over the world map. The white filling indicates that the drift shell intersects the Earth's surface, so that there can be no trapped particles on this shell. Apparently, at 1000 km, n_s is defined only in a region around the SAA and in a narrow band at high latitude. At lower altitudes, these regions become gradually smaller, while they increase at higher altitudes.

The distribution of n_s has a broad minimum coinciding with the heart of the SAA. This is consistent with the fact that the geomagnetic field distribution shows a depression in the region of the SAA. Trapped particles passing through this region will not move closer to the Earth elsewhere on their longitudinal drift path. Consequently, the atmospheric density they encounter here is the maximum density they see on their drift path. The minimum altitude on the drift shells associated with the grid points at 1000 km is shown in Fig. 4.11. h_{min} indeed reaches its maximum around the centre of the SAA.

In Fig. 4.11 we superimposed the contour lines of constant B_c/B, with $B_c = B_0 0.67 L^{3.452}$. When the ratio $B_c/B > 1$ the corresponding point is above the cut-off defined by B_c and vice versa. The contour lines correspond reasonably well with the borders of regions of constant h_{min}.

Figure 4.12 shows the distribution of the ratio n_{min}/n_s over the world map. The solid lines are lines of constant AP-8 MIN flux above 10 MeV. The lines of constant

flux correspond to borders of regions of constant n_{min}/n_s, indicating that this ratio provides a good description of the flux distribution in the SAA.

4.3.2 Application to AP-8

We calculated the drift shell averaged density n_s for the AP-8 grid points represented in Fig. 4.2 with Hassitt's (1965b) software, updated as described in Sect. 4.2. Figure 4.13 shows the dependence of these proton fluxes on n_s for $L = 1.2$ and $L = 1.5$. It can be seen that for both the solar maximum (MAX) and solar minimum (MIN) fluxes, the curves for the respective L values virtually coincide (this is also the case for intermediate values of L up to $L \simeq 1.7$, which are not shown in Fig. 4.13).

It thus seems that for low L values the drift shell averaged density n_s is very well suited to represent the trapped particle distribution, as its eliminates the dependence of the flux on L.

The two curves for solar minimum in Fig. 4.13 diverge somewhat for the highest values of n_s. This may be due to inaccuracies in the AP-8 MIN model for very low altitudes. In Fig. 4.4, it can be seen that the lowest invariant altitude in AP-8 MIN displays some irregularity around $L = 1.2$ and especially for $L \geq 2.0$, where it fluctuates strongly.

Since we used extensive atmospheric and ionospheric models for the calculation of n_s, we expected the respective curves for solar minimum and maximum in Fig. 4.13 to be closer together, although they do overlap for the highest densities. Again, we need to re-investigate the solar minimum data, since AP-8 MIN resulted from the combination of different data sets.

For values of $L > 1.7$, the AP-8 flux vs. n_s curves, shown in Fig. 4.14, no longer coincide. From this we conclude that two different populations can be distinguished in the AP-8 models. Below $L \leq 1.7$ (the limiting value for L depends on the particle energy), the trapped particle flux is governed by the vertical distribution of the atmospheric density. At higher L values, the proton flux already reaches negligible values some distance above the atmospheric cut-off height. The value $L \simeq 1.7$ corresponds to the location of the maximum in the proton flux distribution for $E = 10\,\mathrm{MeV}$. This explains the lowering of the curves in Fig. 4.14 corresponding to progressively higher L values.

4.4 Conclusions

On the basis of our analysis of the AP-8 flux distribution, it appears that the drift shell averaged density n_s is very effective in organising fluxes for the lowest L values,

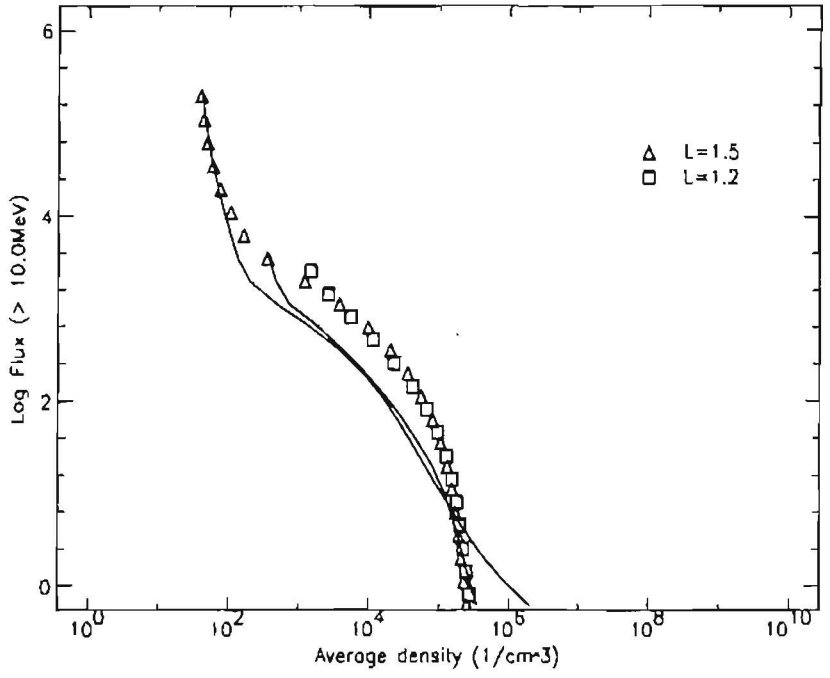

Figure 4.13. Integral AP-8 MIN/MAX proton flux above 10 MeV as a function of the drift shell average of the atmospheric density for low L values. The symbols denote AP-8 MAX values, the AP-8 MIN values are represented by the solid lines.

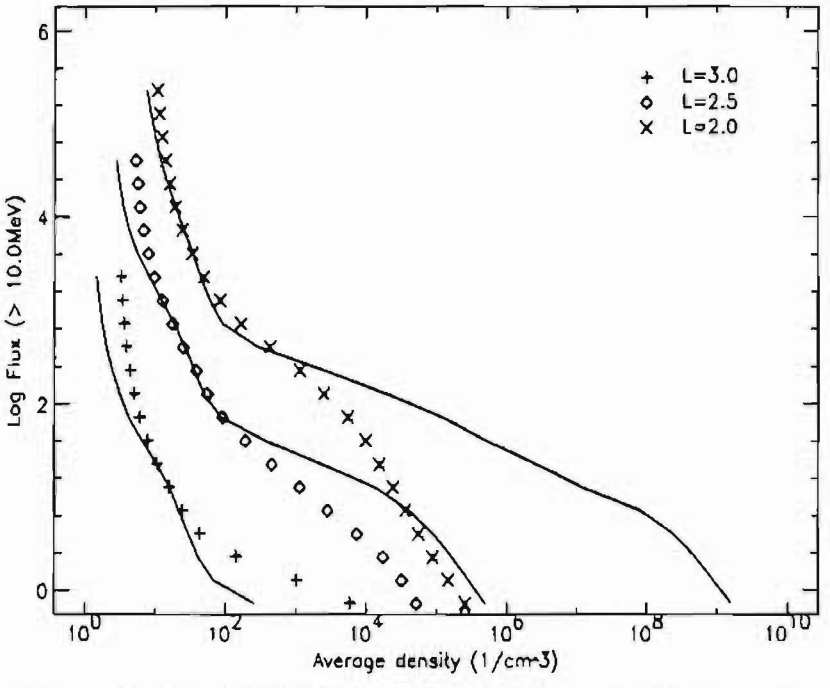

Figure 4.14. Integral AP-8 MIN/MAX proton flux above 10 MeV as a function of the drift shell average of the atmospheric density for higher L values. The symbols and lines have the same meaning as in Fig. 4.13.

and may therefore be considered a good candidate to replace L as a coordinate for the low-altitude environment.

It should be kept in mind that the AP-8 models are smoothed and extrapolated averages of a number of data sets, so that it would be preferable to look at original data sets, old or new, which have a better resolution at low altitudes. To this effect, we have started to re-analyse the AZUR proton data. The AZUR satellite (Hovestadt et al. 1972) operated from November 1969 to June 1970 in a polar orbit with perigee 383 km, apogee 3145 km and inclination 103°. It measured proton fluxes along two pitch angles, 90° and 45°, in six energy channels between 1.5 MeV and 104 MeV. The low-altitude part of AP-8 MAX is based on the AZUR proton data set.

Chapter 5

Implementation of CRRESPRO in UNIRAD

In this chapter, we describe the new proton flux model CRRESPRO developed by Phillips Lab from the PROTEL instrument onboard CRRES. Originally it was expected that BIRA/IASB would obtain the PROTEL data and produce its own low altitude proton model. Instead, BIRA/IASB has received a copy of the CRRESPRO model and integrated it in UNIRAD.

In Sect. 5.1 we describe the content and format of the CRRESPRO model. Section 5.2 reviews the way in which we adapted CRRESPRO to the AP-8 model data format for inclusion in TREP. The new version of TREP was tested on three standard orbits: a typical CRRES orbit, a circular low Earth orbit, and a circular polar orbit. In Technical Note 3, the results of the flux predictions are compared to results obtained by Phillips Lab and to the fluxes predicted with AP-8 MAX. In Sect. 5.3 we report on the comparison for the CRRES orbit.

5.1 Description of CRRESPRO

The CRRESPRO software (Meffert & Gussenhoven 1994) uses flux models created from data collected by the proton telescope (PROTEL) on board CRRES (for a detailed description of the CRRES mission and the PROTEL instrument, see Violet et al. 1993).

In March 1991, a magnetic storm caused a reconfiguration of the inner magnetosphere, resulting in, among other features, the formation of a second proton belt over a certain energy range. Because of this change, two CRRES models were created. The "quiet" model uses data from July 1990 to March 1991, and the "active" model uses data from March 1991 to October 1991. Note that the terms "quiet"

Table 5.1. PROTEL energy channel parameters: lower, middle and higher energy

Channel	E_{lo}	E_{mid}	E_{hi}
1	1.0	1.5	2.1
2	2.0	2.1	2.3
3	2.2	2.5	2.8
4	2.8	2.9	3.2
5	3.1	3.6	4.1
6	3.9	4.3	4.8
7	4.6	5.7	7.0
8	7.3	8.4	9.4
9	6.0	6.8	7.7
10	7.5	8.5	9.6
11	9.3	9.7	10.2
12	9.9	10.7	11.5
13	11.2	13.2	15.2
14	14.7	15.2	15.9
15	15.5	16.9	18.3
16	18.0	19.4	20.8
17	25.3	26.3	27.2
18	26.1	30.9	35.6
19	34.9	36.3	37.7
20	37.8	41.1	48.1
21	44.3	47.0	53.5
22	53.3	55.0	62.1
23	62.1	65.7	73.1
24	73.1	81.3	100.0

and "active" have no correspondence to quiet and active as determined by the index K_p.

The following description of the CRRESPRO models and data sets is taken from Meffert & Gussenhoven (1994).

The lower and upper boundaries and midpoint energies of PROTEL's 24 energy channels are given in Table 5.1. For each channel except channels 8 and 14 there are two data files, corresponding to quiet and active conditions, respectively.

The data files contain differential omnidirectional fluxes $j(E)$, where E is the midpoint energy for the corresponding channel. There are no files for channels 8 and 14.

Table 5.2. Integration parameters (MeV) for integral omnidirectional PROTEL flux

Channel	E_{lo}	E_{mid}	E_{hi}	ΔE
1	1.1	1.5	1.9	0.8
2	1.9	2.1	2.3	0.4
3	2.3	2.5	2.7	0.4
4	2.7	2.9	3.1	0.4
5	3.1	4.3	5.5	2.4
6	5.5	5.7	5.9	0.4
7	5.9	6.8	7.7	1.8
8	7.7	8.5	9.3	1.6
9	9.3	9.7	10.1	0.8
10	10.1	10.7	11.3	1.2
11	11.3	13.2	15.1	3.8
12	15.1	19.4	23.7	8.6
13	23.7	26.3	28.9	5.2
14	28.9	30.9	32.9	4.0
15	32.9	36.3	40.2	7.3
16	40.2	41.1	43.2	3.0
17	43.2	47.0	50.8	7.6
18	50.8	55.0	59.2	8.4
19	59.2	65.7	72.2	13.0
20	72.2	81.3	90.4	18.2

The integral omnidirectional flux $J(> E)$ can be derived from the differential omnidirectional flux. Because of overlapping energy ranges, channels 5 and 15 were omitted from the integral omnidirectional flux calculation (in addition to channels 8 and 14 which are omitted from all calculations) and new boundaries were set up to prevent multiple contributions from the same energy. The energy bounds and widths of the remaining channels are shown in Table 5.2.

$J(> E_i)$ is defined as

$$J(> E_i) = \int_{E_i}^{\infty} j(E)\, dE, \tag{5.1}$$

where E_i is the lower energy boundary of channel i, as given in Table 5.2. The integration is approximated by a summation:

$$J(> E_i) = \sum_{k=i}^{20} j(E_k)\, \Delta E_k, \tag{5.2}$$

with ΔE_k the width of channel k. The integration summation for channel i begins

at the lower boundary of that channel and ends at the new upper boundary of the highest energy channel, which is now channel 20 with an upper boundary of 90.4 MeV.

We have implemented only the integral omnidirectional flux model in UNIRAD, since this requires a significantly smaller modification of the UNIRAD software, as TREP is set up to read integral flux model data sets.

5.2 Implementation in UNIRAD

In the UNIRAD software package, the routine TREP calculates integral and differential, omnidirectional or directional, proton and electron fluences for a given satellite orbit. To this effect, the (B, L) coordinates (McIlwain 1961) for each orbital point are determined and used as input to the NASA trapped radiation models AP-8 and AE-8 (Vette 1991b).

In order to incorporate the CRRESPRO quiet and active models into TREP, the model files have to be transformed into a block data format similar to the format of AP-8, as described by Vette (1991a). This transformation is described in the following sections.

5.2.1 Conversion of model files

The CRRESPRO software provided by Phillips Lab consists of a series of binary data files and executable program files, compiled for the IBM PC and compatibles. No source files or source listings are available.

From the description of the binary file format of the differential flux data files (Meffert & Gussenhoven 1994), we wrote a FORTRAN program to convert the binary data into ASCII format. These files contain the model data as twodimensional arrays of 90 L bins by 34 B/B_0 bins. The bin limits are $(0.95 + 0.05i)\,R_E \leq L < (1.00 + 0.05i)\,R_E$ in L, while the bin limits in B/B_0 are chosen so that each bin width corresponds to 2° in magnetic latitude and the total B/B_0 range approximately covers 68° magnetic latitude in a dipole field.

The NASA models AP-8 provide integral fluxes. Consequently, TREP expects integral fluxes from the model files it accesses. In order to keep the modifications to TREP to a minimum, we decided to produce two block data files, containing the CRRESPRO quiet and active integral fluxes, respectively. The ASCII files obtained as described above were combined using Eq. (5.2) to form 40 new ASCII files containing the resulting values for $L, B/B_0, J(> E)$ for the integral channels in Table 5.2.

The AP-8 block data format stores, for each energy in the model and for each L value in the energy blocks, the logarithm of the equatorial integral flux and a series of increments in B/B_0 corresponding to a constant decrement in $\log J(>E)$. In contrast, the CRRESPRO model format gives the integral flux for a series of fixed values of B/B_0. In order to transform the CRRESPRO format into the AP-8 format, it is necessary to represent the dependence of the integral flux on B/B_0 by analytic functions. For the differential flux, Gussenhoven et al. (1993) considered a function of the form

$$j(E,\alpha_0) = j(E,90°)\sin^n\alpha_0\,, \tag{5.3}$$

where the equatorial pitch angle α_0 is defined as

$$\alpha_0 = \arcsin\sqrt{\frac{B_0}{B}} \tag{5.4}$$

and

$$B_0 = \frac{0.311653}{L^3}\,. \tag{5.5}$$

The values of the power index n were determined by least squares fitting to the model data.

A similar procedure can be followed for the integral flux $J(>E)$. Equation (5.3) is equivalent to

$$j(E,B/B_0) = j(E,1)\left(\frac{B_0}{B}\right)^{n/2}\,. \tag{5.6}$$

Correspondingly, the integral flux may be written as

$$J(>E,B/B_0) = J(>E,1)\left(\frac{B_0}{B}\right)^{n/2}\,. \tag{5.7}$$

For each of the channels listed in Table 5.2, we determined n by a least squares fit for every L value in the model files, both for the quiet and active models. As did Gussenhoven et al. (1993), we excluded the flux values in the two lowest pitch angle bins. The resulting values for n are plotted in Figs. 5.1 and 5.2 as a function of L for the quiet and active models, respectively.

In order to obtain the same format as the AP-8 trapped particle models, we inverted Eq. (5.7) to the form

$$\left(\frac{B}{B_0}\right)_i = \left\{\frac{J(>E,1)}{J[>E,(B/B_0)_i]}\right\}^{2/n}\,. \tag{5.8}$$

In AP-8, the decrement $\Delta\log J(>E) = 0.25$, i.e.

$$\frac{J[>E,(B/B_0)_i]}{J(>E,1)} = 10^{-0.25i}\,. \tag{5.9}$$

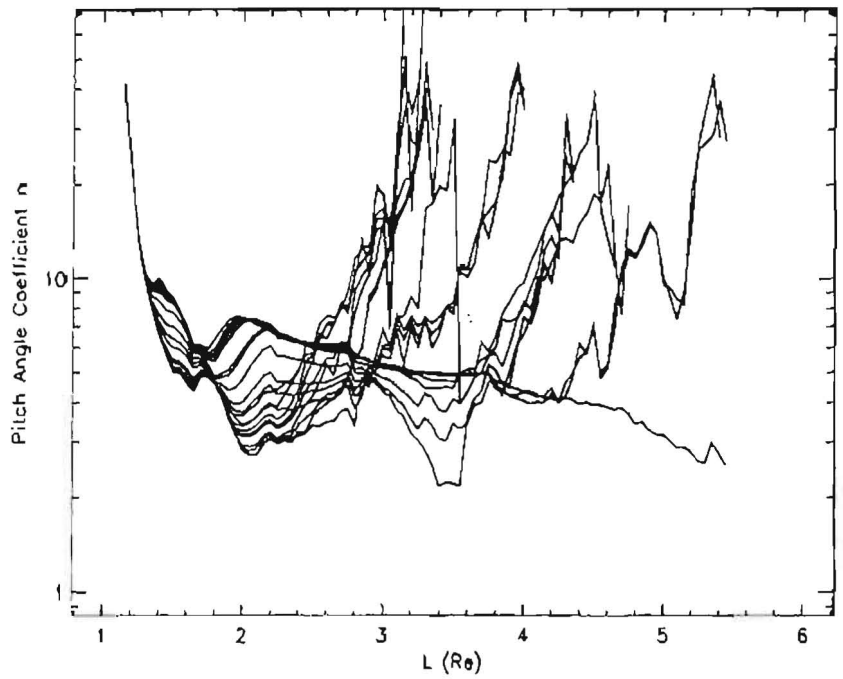

Figure 5.1. Power index of the fits of the integral flux distributions $J(> E, B/B_0)$ as a function of L, for the 20 CRRESPRO quiet models

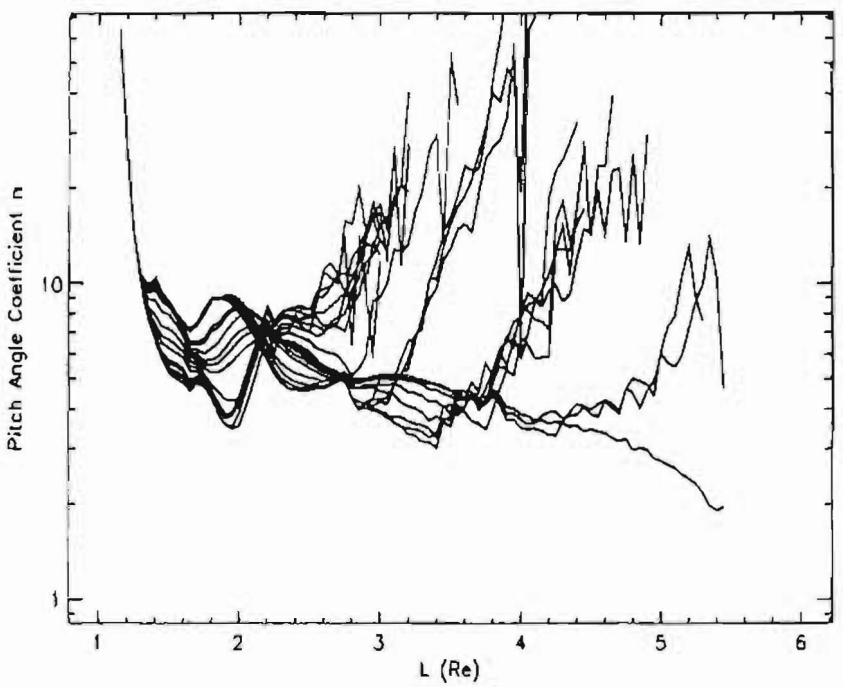

Figure 5.2. Power index of the fits of the integral flux distributions $J(> E, B/B_0)$ as a function of L, for the 20 CRRESPRO active models

With Eq. (5.8), the corresponding $(B/B_0)_i$ values are derived:

$$\left(\frac{B}{B_0}\right)_i = 10^{0.5i/n}. \tag{5.10}$$

The $\Delta(B/B_0)$ increments are given by

$$\Delta\left(\frac{B}{B_0}\right)_i = \left(\frac{B}{B_0}\right)_i - \left(\frac{B}{B_0}\right)_{i-1}. \tag{5.11}$$

Figures 5.3 and 5.4 show the $J(> E, \alpha_0)$ points in the original CRRESPRO quiet and active model files for two L values (1.6 and 2.2) and for four energies (4.3, 9.7, 26.3 and 55.0 MeV), overlaid with curves representing the fitted flux dependence [a similar figure is given by Gussenhoven et al. (1993)]. For $L = 1.6$, the fitted fluxes represent the model data well, except near the loss cone where the fit function does not fall off as the model data does. This effect is due on the one hand to the non-inclusion of the last two model points in the fitting procedure and on the other hand to the failure of a function of the form of Eq. (5.7) to fit the pitch angle range from equator to loss cone. As a consequence, the flux predicted with the fitted functions may be overestimated near the loss cone.

For higher L values, e.g. $L = 2.2$ (Fig. 5.4), the situation is somewhat different. For the lowest energies, the fit functions represent the model flux well. However, for $E > 10$ MeV the model flux does not decrease monotonically towards the loss cone, but reaches a plateau first. Gussenhoven et al. (1993) attributed this to the existence of two populations of trapped protons. Obviously, a single fit function is not sufficient to describe the pitch angle dependence of the sum of two populations, which leads to an underestimate of the fitted flux near the equator and a possible overestimate near the loss cone.

The limitations of the fitting procedure also are apparent in Figs. 5.1 and 5.2, in that the dependence of n on L is somewhat erratic. It would be better to access the CRRESPRO model data by direct interpolation between E, L and B/B_0 values instead of using a fitted dependence of the flux on B/B_0. However, this procedure requires major modifications of TREP, which are beyond the scope of this study.

The fitting of the model fluxes could be improved in two ways. Firstly, a sum of two functions of the form of Eq. (5.7) could be fitted to the model fluxes instead of just a single function. Secondly, a different fit function could be used, e.g. the function proposed by Badhwar & Konradi (1990), which has been applied to the AP-8 flux distribution (see Sect. 3.2.2). This improvement may be a topic in a follow-on TREND study.

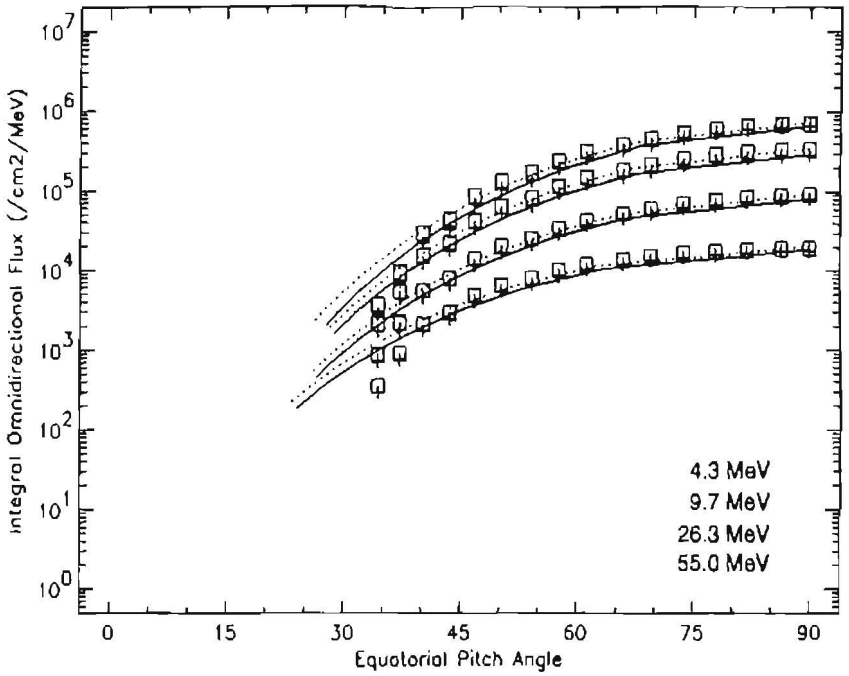

Figure 5.3. $J(> E, \alpha_0)$ for four energies and $L = 1.6$. The symbols □ and + denote the quiet and active values, respectively, in the original model data files, the dotted and solid lines represent the fitted quiet and active fluxes, respectively.

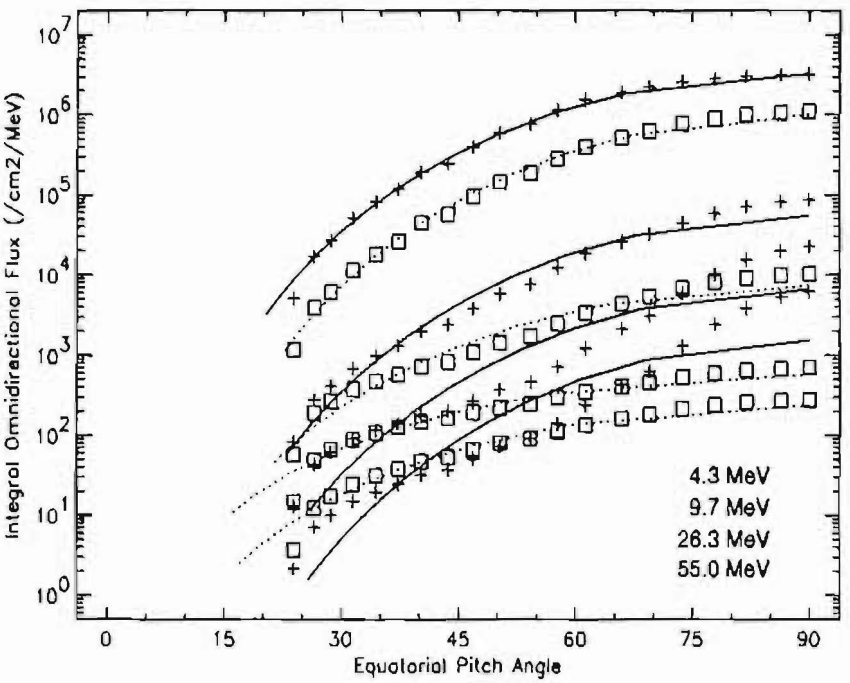

Figure 5.4. $J(> E, \alpha_0)$ for four energies and $L = 2.2$. The symbols and lines have the same meaning as in Fig. 5.3.

5.2.2 Implementation in TREP

The $\Delta(B/B_0)$ increments for each energy and L value in the CRRESPRO models were then stored in the BLOCK DATA format of the AP-8 models (Vette 1991a), in the files CRRQUI.FOR and CRRACT.FOR, corresponding to the quiet and active model, respectively.

The CRRES based electron model CRRMEA generated at MSSL (see Technical Note 10 and Sect. 9.5) also was included in TREP.

5.3 Application to a CRRES orbit

In this section we apply the CRRESPRO models, as we implemented them in TREP, to a typical CRRES orbit.

The CRRESPRO documentation (Meffert & Gussenhoven 1994) contains a sample run of the software for a typical CRRES orbit. The integral omnidirectional fluence over this orbit is listed in Table 5.3.

Using TREP, we have calculated the fluence over one day accumulated along a trajectory (represented in Fig. 5.5) with the same orbital parameters, with the newly implemented CRRESPRO models and with AP-8 MAX. For CRRESPRO we used the IGRF 90 magnetic field model, updated to 1991, and the Olson & Pfitzer (1977) quiet external field model. For AP-8 MAX we used the GSFC 12/66 model (Cain et al. 1967), updated to 1970, and corrected for the westward drift of the SAA. The resulting fluxes and the flux spectrum are represented graphically in Figs. 5.6 to 5.11. The fluences for one orbit are listed in Table 5.3.

From the table and the figures it can be seen that the differences between the quiet and active CRRESPRO fluences are small for this orbit, i.e. at most about a factor two. The fluences calculated with the CRRESPRO models implemented in TREP are within a factor of two of the fluences obtained by Meffert & Gussenhoven (1994) with the original CRRESPRO model. The causes of this difference have been discussed in Sect. 5.2.1.

The fluences obtained with AP-8 MAX are up to a factor two larger than the fluences obtained with CRRESPRO, both the active and quiet version.

5.4 Conclusions

The fitting procedure we used to implement the CRRESPRO model in TREP is not satisfactory. Either an improved fit function [like that of Badhwar & Konradi (1990), or a sum of two functions] should be used or the same software used by CRRESPRO

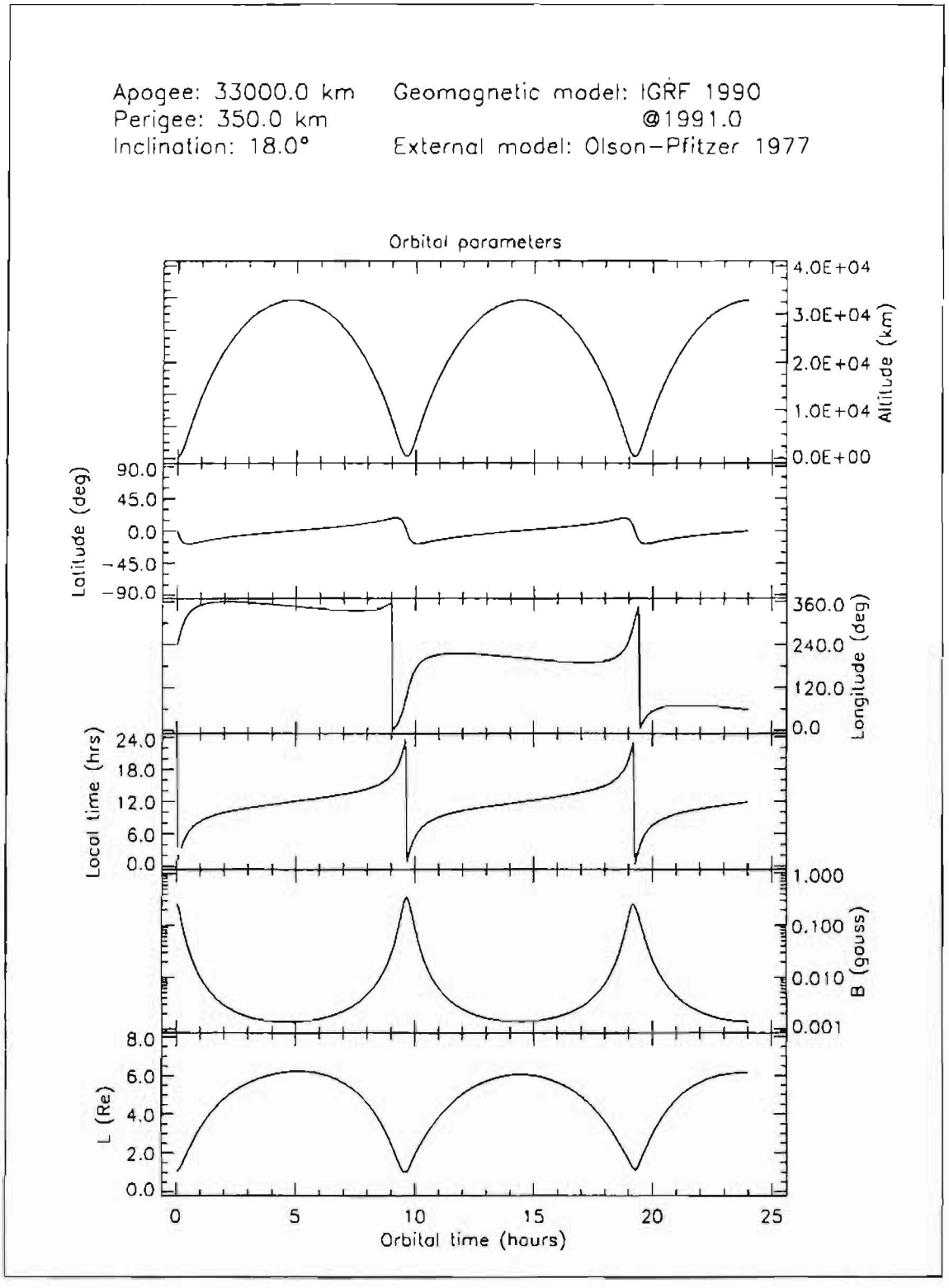

Figure 5.5. Geographic and magnetic coordinates for the sample CRRES orbit described in the text

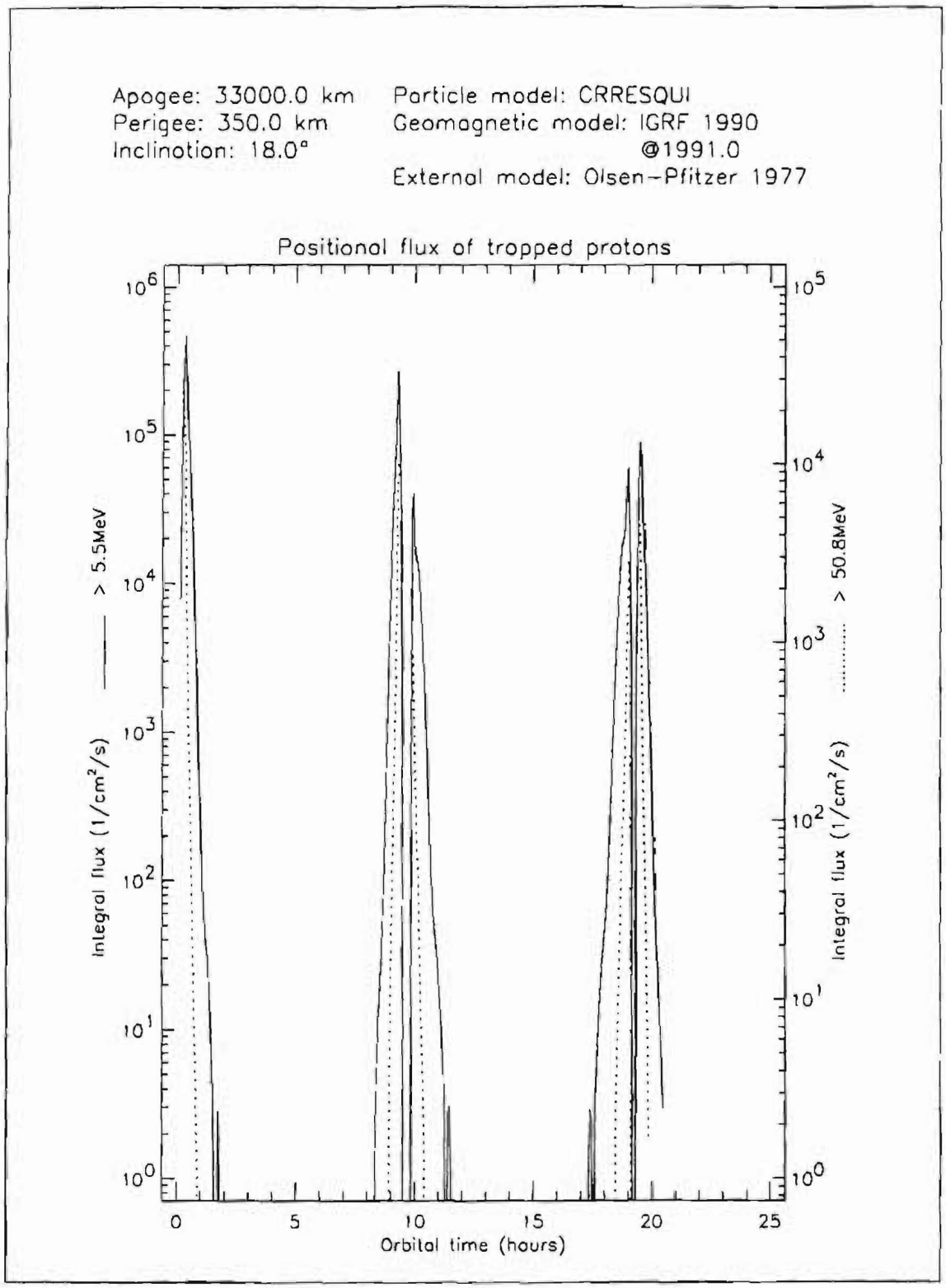

Figure 5.6. Differential CRRESPRO/QUIET proton flux along the sample CRRES orbit described in the text

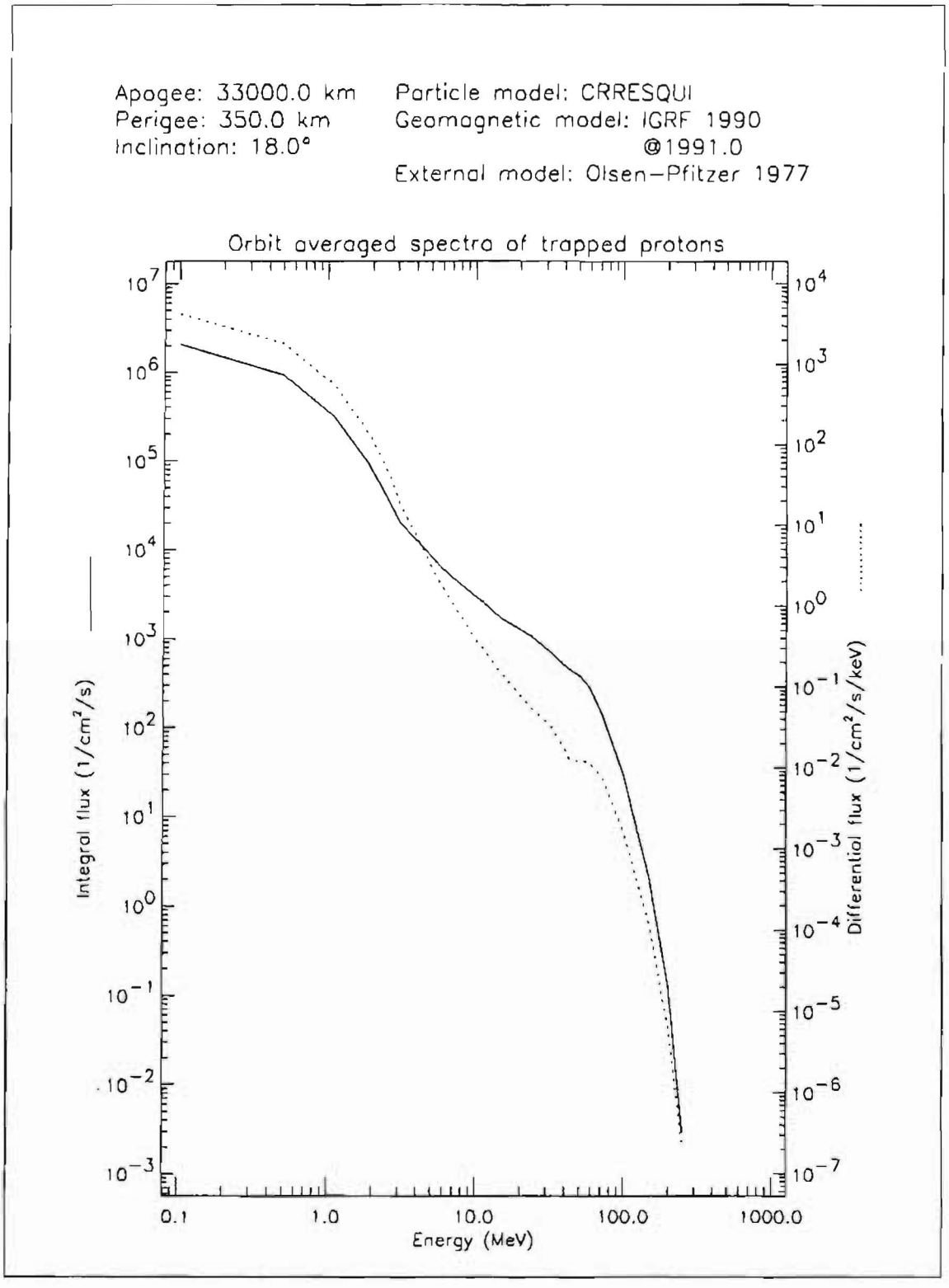

Figure 5.7. Integral and differential CRRESPRO/QUIET proton spectrum along the sample CRRES orbit described in the text

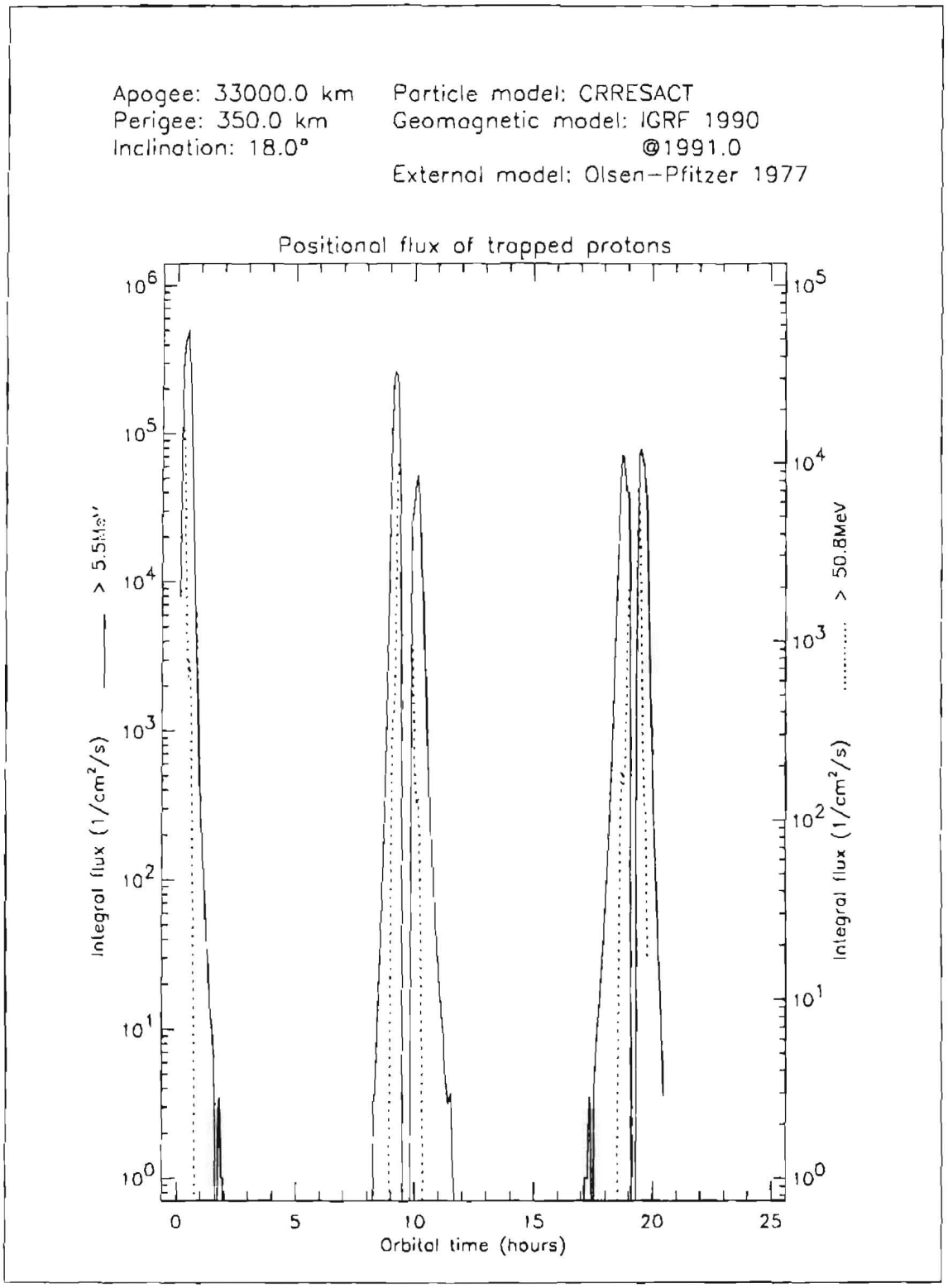

Figure 5.8. Differential CRRESPRO/ACTIVE proton flux along the sample CRRES orbit described in the text

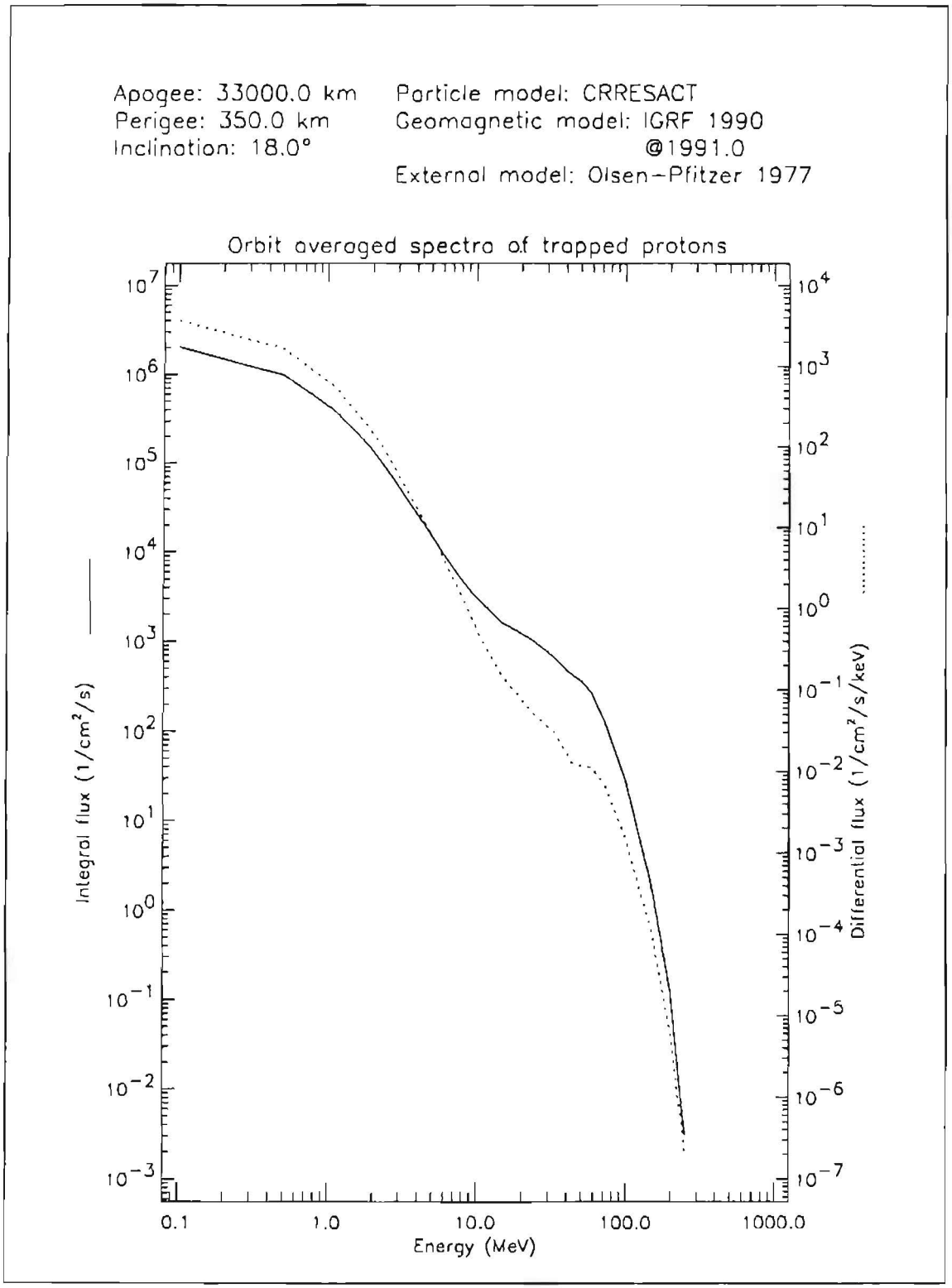

Figure 5.9. Integral and differential CRRESPRO/ACTIVE proton spectrum along the sample CRRES orbit described in the text

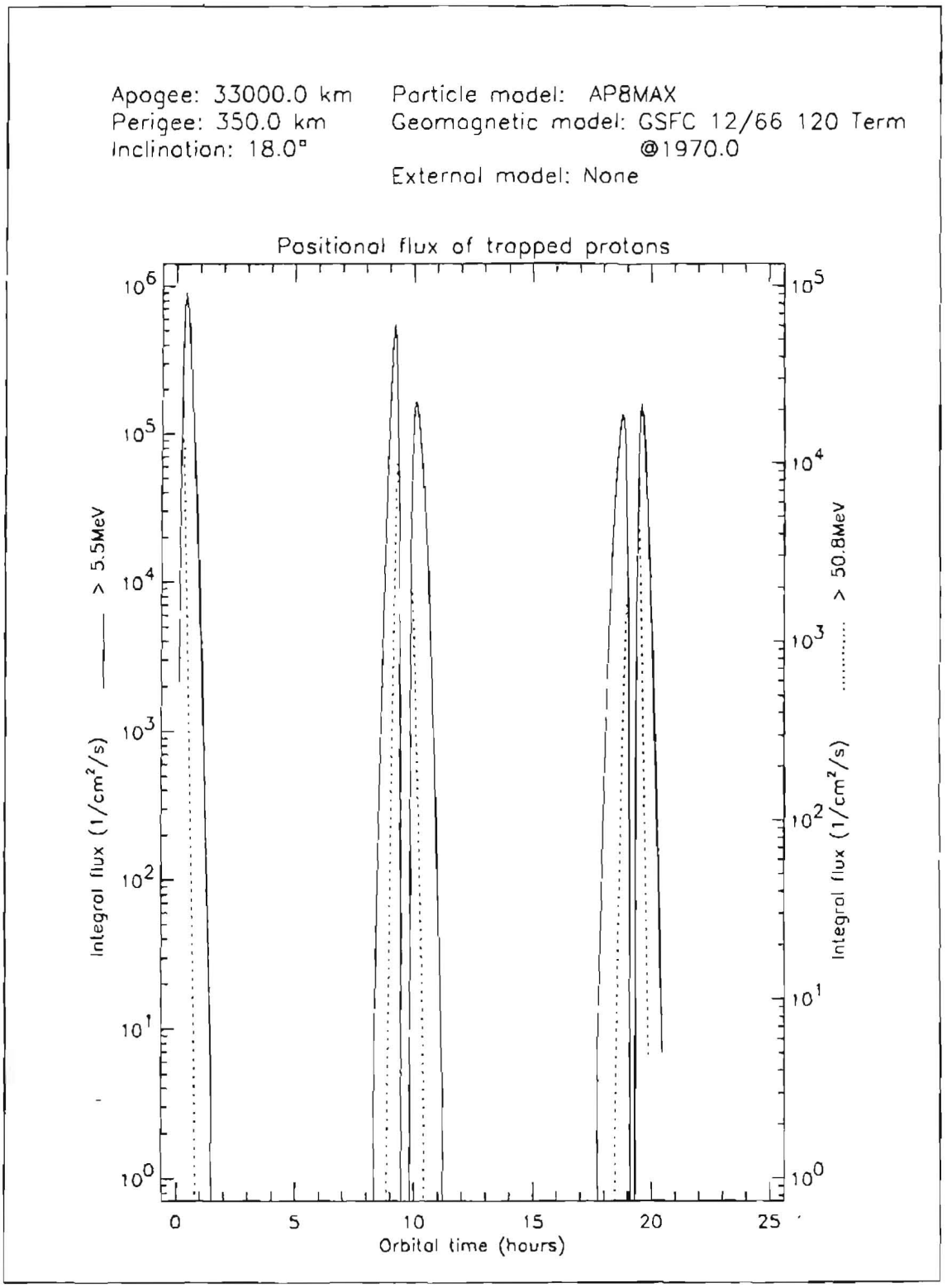

Figure 5.10. Differential AP-8 MAX proton flux along the sample CRRES orbit described in the text

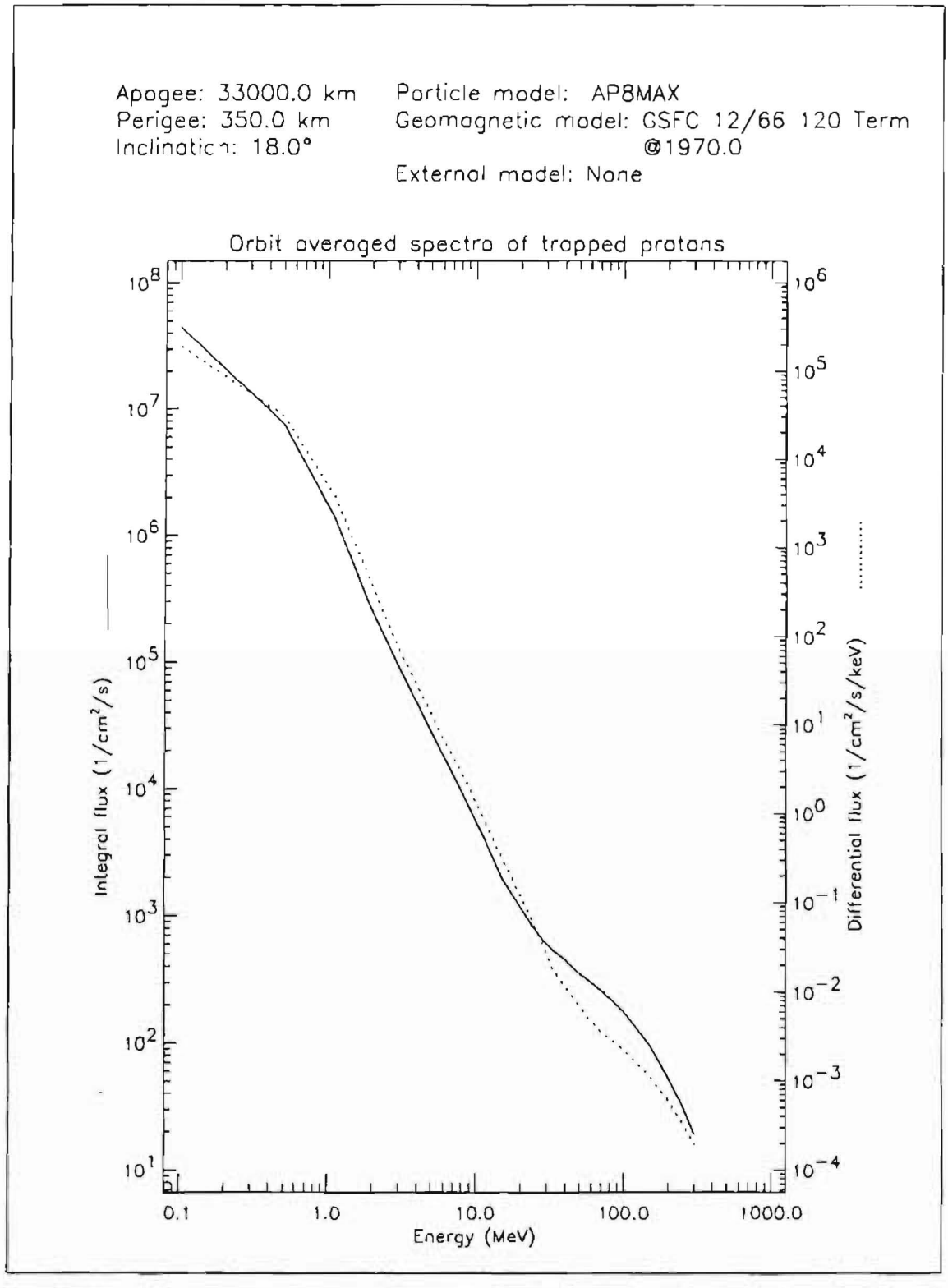

Figure 5.11. Integral and differential AP-8 MAX proton spectrum along the sample CRRES orbit described in the text

Table 5.3. Integral omnidirectional fluence $J(> E)$ in $cm^{-2}year^{-1}$ for a typical CRRES orbit. The first column gives the energy E, the second and fourth column contain the fluences obtained with the extended version of TREP, using the quiet and active CRRESPRO models, respectively. The third and fifth columns give the fluences listed by Meffert & Gussenhoven (1994). The sixth column contains the fluences obtained with AP-8 MAX.

E (MeV)	J_{qTREP}	J_{qMF}	J_{aTREP}	J_{aMF}	$J_{\mathrm{AP-8\,MAX}}$
1.1	1.29×10^{13}	1.85×10^{13}	1.69×10^{13}	2.26×10^{13}	5.12×10^{13}
1.9	4.27×10^{12}	5.68×10^{12}	7.52×10^{12}	9.32×10^{12}	1.23×10^{13}
2.3	2.55×10^{12}	3.20×10^{12}	5.23×10^{12}	6.31×10^{12}	8.07×10^{12}
2.7	1.61×10^{12}	1.87×10^{12}	3.77×10^{12}	4.45×10^{12}	5.76×10^{12}
3.1	1.10×10^{12}	1.19×10^{12}	2.83×10^{12}	3.30×10^{12}	4.26×10^{12}
5.5	4.24×10^{11}	3.53×10^{11}	7.19×10^{11}	7.51×10^{11}	1.28×10^{12}
5.9	3.76×10^{11}	3.03×10^{10}	5.96×10^{11}	6.11×10^{11}	1.10×10^{12}
7.7	2.60×10^{11}	1.95×10^{11}	3.23×10^{11}	2.94×10^{11}	6.17×10^{11}
9.3	2.03×10^{11}	1.46×10^{11}	2.18×10^{11}	1.78×10^{11}	3.97×10^{11}
10.1	1.83×10^{11}	1.30×10^{11}	1.88×10^{11}	1.47×10^{11}	3.23×10^{11}
11.3	1.59×10^{11}	1.12×10^{11}	1.56×10^{11}	1.17×10^{11}	2.50×10^{11}
15.1	1.05×10^{11}	7.22×10^{10}	9.97×10^{10}	7.13×10^{10}	1.16×10^{11}
23.7	6.75×10^{10}	4.60×10^{10}	6.44×10^{10}	4.65×10^{10}	5.00×10^{10}
28.9	5.10×10^{10}	3.47×10^{10}	4.95×10^{10}	3.58×10^{10}	3.65×10^{10}
32.9	4.23×10^{10}	2.89×10^{10}	4.11×10^{10}	2.98×10^{10}	3.17×10^{10}
40.2	3.03×10^{10}	2.07×10^{10}	2.93×10^{10}	2.09×10^{10}	2.63×10^{10}
43.2	2.78×10^{10}	1.90×10^{10}	2.67×10^{10}	1.89×10^{10}	2.44×10^{10}
50.8	2.32×10^{10}	1.59×10^{10}	2.20×10^{10}	1.54×10^{10}	2.05×10^{10}
59.2	1.74×10^{10}	1.19×10^{10}	1.63×10^{10}	1.11×10^{10}	1.81×10^{10}
72.2	8.55×10^{9}	5.84×10^{9}	8.00×10^{9}	5.40×10^{9}	1.52×10^{10}

to access the data files should be implemented in TREP. This latter improvement could be achieved in a next step provided PLGD releases the necessary software routines.

Because of these difficulties, it may be preferable just to use CRRESPRO on PC as it is distributed by PLGD and to compare the generated output to results obtained with TREP, using the AP-8 models. The writing of a subroutine to transform the output from CRRESPRO into the format generated by TREP could be envisaged.

Chapter 6

Description of CRRES experiments and data sets

The Earth's trapped radiation environment is currently described and evaluated, for engineering purposes and spacecraft design, with the empirical NASA/NSSDC trapped radiation models AP-8 and AE-8 (Vette 1991b).

The first TREND study identified specific weaknesses in the existing models and methods and identified suitable satellite data sets for updating the models. TREND recommended the use of the results of the CRRES (Combined Release and Radiation Effects Satellite) mission, in combination with archived data sets, as input for a new modelling effort. In this chapter, we review the goals and achievements of the CRRES mission, and describe the various data sets that are available.

In Sect. 1.1 we describe the orbital characteristics of the CRRES mission, and present an overview of the instrumentation. Sect. 1.2 gives a more comprehensive description of the CRRES experiments and instruments that are relevant to the TREND-2 study.

The availability and format of the data sets that came out of the CRRES experiments and are relevant to the TREND-2 project, have been discussed in detail in Technical Note 4. Since then, the format of some of the available data sets has been changed and the format descriptions have been included in the Technical Notes and the chapters of this final report that deal with the respective data sets. The format of the Science Summary Data Base (SSDB), containing one-minute averages of selected channels of seven particle detectors and of the magnetic field measurements, is described in Sect. 1.3, as well as the format of the ephemeris files.

6.1 Description of the CRRES experiment

The *Combined Release and Radiation Effects Satellite* (CRRES) Program is a joint *National Aeronautics and Space Administration* (NASA) and U.S. *Department of Defense* (DOD) undertaking to study the near-Earth space environment and the effects of the Earth's radiation environment on state-of-the-art microelectronic components and other spacecraft components.

To perform these studies, CRRES was launched with a complex array of scientific payloads. Among the experiments supported by the CRRES Program, the Phillips Laboratory Geophysics Directorate (formerly AFGL, now PLGD) Space Radiation Effects Program (SPACERAD) is of particular relevance to the TREND-2 study. One of the aims of the SPACERAD Program is to update the static models of the Earth's radiation belts and develop dynamic models of the high-energy particle populations in the near-Earth environment. In addition, radiation-induced single event upsets (SEUs) and total dose degradation of state-of-the-art microelectronics devices are measured in a known space environment.

6.1.1 Overview of the CRRES mission

The CRRES spacecraft was built by Ball Aerospace Systems Division in Boulder, Colorado under joint sponsorship of NASA and U.S. DOD. The spacecraft was originally built for launch by the Space Shuttle, but was modified for launch on an Atlas-Centaur booster after the Challenger accident.

CRRES was launched on July 25, 1990 at 19h21 UT, into a Geosynchronous Transfer Orbit (GTO) with perigee at 350 km, apogee at 33,500 km, and an inclination of 18.1°. This orbit crosses both the inner and outer radiation belts. The orbital period is 9^h52^m, and the spin rate is 2 rpm. The spacecraft spin axis is maintained such that the angle between the solar direction and the normal to the top surface, containing solar panels, is always between 5° and 15°.

The spacecraft was designed for a one year mission duration with a goal of 3 years. Unfortunately, due to a battery failure, the mission was aborted on October 9, 1991.

There are three primary mission objectives:

1. to study the effects of the natural radiation environment on microelectronic components and on high-efficiency gallium arsenide solar cells, and to map this environment;

2. to conduct Low-Altitude Satellite Studies of Ionospheric Irregularities (LASSII);

3. to conduct a series of chemical release experiments in the ionosphere and magnetosphere.

Data was recorded on satellite tape recorders continually at 16 kbit/s. The data was transmitted to the ground daily and passed to the data reduction and distribution centre at Hanscom Air Force Base, MA.

6.1.2 Overview of experiments

In the following sections, we present a brief overview of the experiments that form the payload of CRRES. Although not all experiments are relevant for the TREND-2 study, we presented an exhaustive list in Technical Note 4 for the sake of completeness.

NASA Chemical release experiments

The CRRES payload complement included 24 chemical canisters which were released during the first 13 months of the CRRES mission at altitudes varying from near apogee to near perigee over ground observation sites and diagnostic facilities. These releases formed large clouds of metal vapour, about 100 km in diameter, which interacted with the ionospheric and magnetospheric plasma and the Earth's magnetic field. These releases were studied with optical, radar, and plasma wave and particle instruments from the ground, aircraft, and CRRES.

6.1.3 DOD Low-Altitude Scientific Studies of Ionospheric Irregularities

LASSII studies naturally occurring and artificially produced ionospheric perturbations and the effects of ionospheric perturbations on communications paths. The LASSII measurements are made near perigee of selected orbits. In addition, LASSII made observations of the low-altitude chemical releases. The onboard set of LASSII instruments consists of two pulsed plasma probes, a very low frequency wave analyser including two electric field antennas and a magnetic hoop antenna, and a quadrupole ion mass spectrometer.

6.1.4 DOD Studies of the Radiation Environment

The primary focus of these studies is on the natural radiation environment and the effects of this environment on microelectronic components. CRRES travels through

the inner and outer radiation belts of the Earth, exposing state-of-the-art microelectronic components to this radiation environment to establish their capabilities for use in future space missions. Also, the radiation belts are accurately mapped so that a direct correlation can be made between the exposure and microelectronics performance.

The radiation effects portion of the CRRES mission contains 23 experiments: 3 engineering test packages, 4 field and wave instruments, 14 particle spectrometers and 2 dosimeters.

The particle detectors measure the complete particle spectrum of electrons and protons from a few eV to hundreds of MeV, and heavy ions from about 100 eV/Q up to cosmic ray energies greater than 500 MeV/AMU. Their energy ranges, energy resolution, angular resolution and line of sight are listed in Technical Note 4. Figures 6.1 and 6.2 show the energy overlap and cross-calibration ranges for electrons and ions, respectively. The lower energy particle detectors can produce 3-dimensional distribution functions of both electrons and protons. The instruments are controlled with on-board processors so they can scan in different modes to get the best energy, pitch angle and mass discrimination as the satellite moves from one particle regime to another.

6.2 Description of CRRES instruments

In this section we present a brief description of the characteristics and design of the CRRES instruments relevant for the TREND-2 study, i.e. some of the SPACERAD particle experiments and the fluxgate magnetometer. Fully detailed technical specifications of all instruments have been compiled in Gussenhoven et al. (1985), *CRRES System Description Handbook* (1990), a series of papers in the July-August 1992 issue of *Journal of Spacecraft and Rockets*, and Technical Note 6.

The SPACERAD particle detectors were designed to give measurements with high time, angular, and energy resolution of electrons (10 eV to 10 MeV), protons (10 eV to 600 MeV), and the major ion species (40 eV/Q to 15 MeV/ion). Additional information is provided by supporting experiments from the Lockheed Electron and Proton Spectrometer and Mass Composition Experiments, and the University of Chicago Cosmic Ray Experiment. In addition, SPACERAD provides dose measurements by two very different methods.

The data from these experiments are used to:

1. provide concurrent environmental specifications for the Engineering Experiments, particularly for the Microelectronics Experiment;

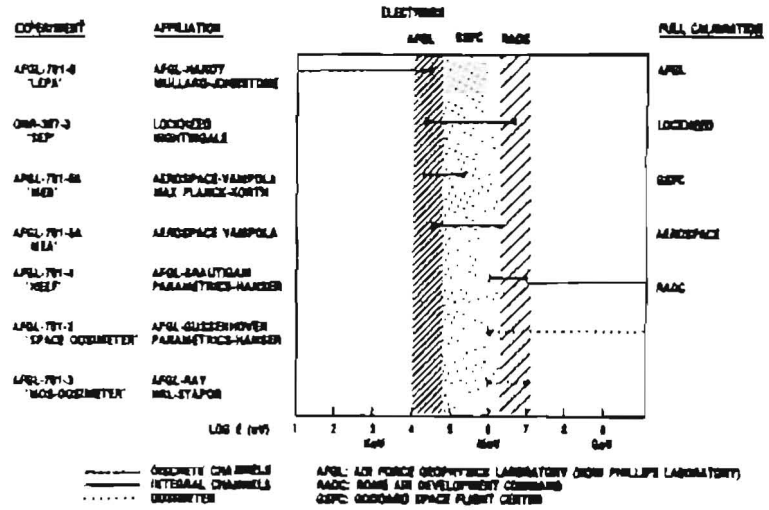

Figure 6.1. Energy ranges of the electron detectors on CRRES, with their affiliations and calibration facilities. Cross-hatching shows instrument groupings for cross-calibrations at the same facility. [from Mullen & Gussenhoven (1991)]

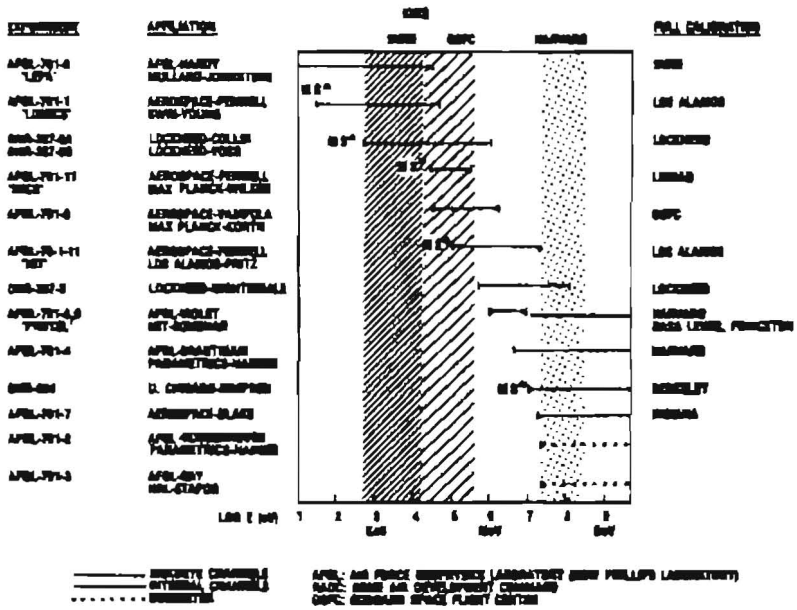

Figure 6.2. Energy ranges of the proton detectors on CRRES, with their affiliations and calibration facilities. Cross-hatching shows instrument groupings for cross-calibrations at the same facility. MS* designates instruments that differentiate ion mass. [taken from Mullen & Gussenhoven (1991)]

2. extend existing static radiation belt models in energy, pitch angle, and ion composition;

3. study in detail the dynamic processes of the radiation belts.

6.2.1 High Energy Electron Fluxmeter

AFGL-701-4

P.I.: E.G. Mullen (PLGD)
Co.-I.: D. Brautigam (PLGD)
F. Hanser (Panametrics)
B. Dichter (Panametrics)

The High Energy Electron Fluxmeter (HEEF) is a solid state spectrometer telescope designed to measure differential electron energy spectra in 10 energy channels from 1 to 10 MeV. Electrons in this energy range are the source of a significant portion of the total radiation dose received by microelectronic components in space systems operating in the Earth's radiation belts. Determining the average value and dynamic behaviour of these electrons is critical to the CRRES program.

The instrument is of a telescopic design with two solid state detectors stacked in front of a BGO scintillating crystal. In order to be counted, an electron must produce a triple coincidence of pulses in the two solid state detectors and the BGO crystal, and have an anticoincidence with particles detected in the annular plastic scintillator surrounding the BGO crystal. Each electron between 1 and 10 MeV that enters the detector through the aperture produces pulses in the two solid state detectors and photons in the BGO crystal. The photons produced in the crystal are seen by a photomultiplier tube, optically coupled to the crystal. The photomultiplier tube produces charge pulses proportional to the number of photons seen. The charge pulses seen in coincidence are all pulse-shaped in a shaping circuit. If the three pulses all fall within the proper broad pulse height range, the BGO crystal pulses are further analysed in a pulse height analyser and placed into the proper energy electron counter bin for transfer to shift registers for satellite readout. The registers are read every 0.5 s and stored by the satellite data storage and telemetry system, resulting in a data base of 2 measurements per second per channel.

The largest problem with measuring MeV electrons, especially in the CRRES orbit, is contamination due to high energy protons and bremsstrahlung. Great care was taken in the detector design to try and eliminate all counts other than the 1–10 MeV electrons which directly enter the aperture. Protons that come directly down the aperture are not counted because they have excessive energy loss in the solid state detectors (for protons with energies less than 100 MeV) or in the BGO crystal (for protons with energies greater than 30 MeV). For particles which

can penetrate the heavy shielding (greater than 140 MeV protons and greater than 20 MeV electrons), the annular plastic scintillator produces anticoincidence counts which reject the particles being counted. A 0.006 in beryllium foil stops electrons with energies less than 140 keV that directly enter the aperture. The tungsten collimators and shield reduce bremsstrahlung, and the magnesium housing reduces bremsstrahlung production from less than 10 MeV electrons.

Although all these precautions undoubtedly reduced most of the radiation induced noise, there remained a significant amount that needed to be allowed for in the ground based processing. This noise fell mainly in the lower energy channels and the fluxes measured by the instrument at higher energies could be used to calculate the size of the noise component.

A further problem with the HEEF data arose because the whole satellite was much colder than originally planned. The HEEF sensor was generally between $-2°C$ and $-12°C$ and this affected the energy channels determined by the electronics. This effect was found to be adequately compensated for if the energy levels corresponding to $-7°C$ were used throughout the mission.

6.2.2 Medium Energy Analyzer

AFGL-701-5A

P.I.: E.G. Mullen (PLGD)
Co.-I.: A. Vampola (The Aerospace Corporation)

The Medium Energy Analyzer (MEA), also called Medium Energy Electron Spectrometer (MEES), uses the principle of momentum analysis in a solenoidal magnetic field. Figure 6.3 shows the instrument in cross-section. The magnetic field, produced by permanently magnetized Indox V, points into the paper. The other structural components are made of Armco magnetic iron which has a low fringing field. A collimator on the front of the instrument is made of tungsten. In a 180° magnetic electron spectrometer, particles entering an aperture encounter a uniform solenoidal magnetic field and travel a circular path in the plane transverse to the field. After being bent through approximately 180°, the particle is detected by a planar array. First order focussing occurs in the plane. Electrons with the same energy, although at different angles, are focussed on almost the same vertical line on the detection plane. There is no focussing in the vertical direction.

At the 180° focus, the electrons impinge upon a detector array consisting of six ion-implanted silicon plates mounted in three pairs on a thick circuit card. There are a total of 18 detection areas in the array. Generation of a particle count is initiated by an electron impinging on a detector configured as a reverse-biased P-N diode and depositing most or all of its energy as charge pairs, at a rate of 3.6 eV/pair, in

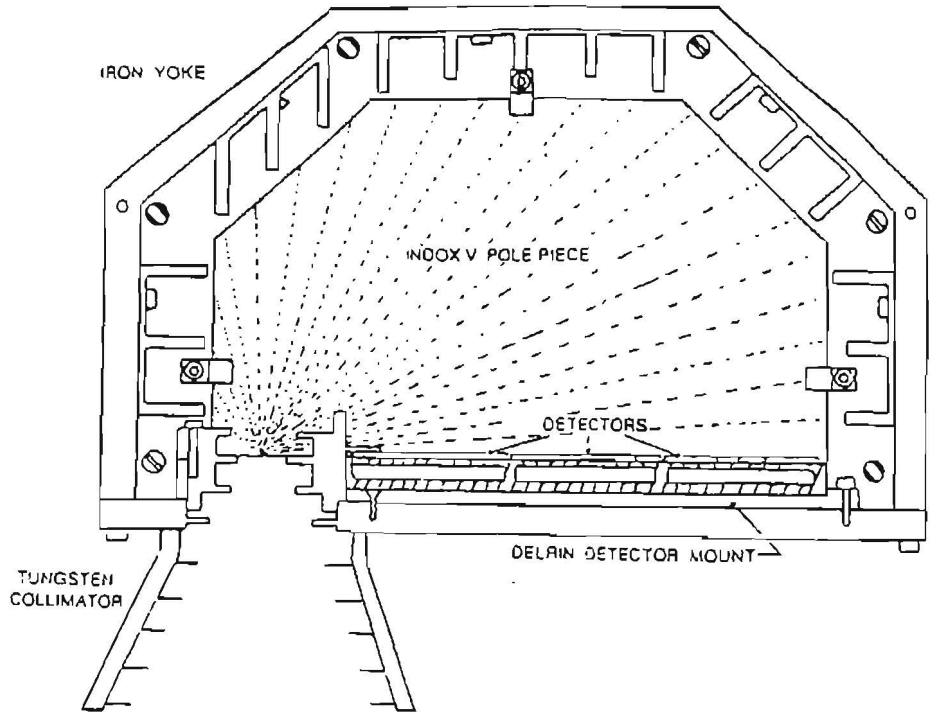

Figure 6.3. Layout diagram of CRRES MEA [from Vampola et al. (1992)]

the depletion region of the N-type silicon. The charge pairs are swept out of the depletion region by the biasing network, creating a charge pulse which is proportional to the energy of the incident electron minus energy lost as bremsstrahlung or residual electron energy (the electrons which may backscatter out of the detector).

Pulses with amplitudes below the lower discriminator threshold are considered noise or bremsstrahlung and are rejected. Pulses with amplitude above the upper discriminator threshold are due to highly ionizing particles (or long path length trajectories of very energetic particles) and are rejected as unwanted background. The low threshold ensures efficient detection of electrons which backscatter out of a detector after depositing only part of their energy. The upper threshold ensures detection of valid events in the presence of noise or low-energy bremsstrahlung which add to the pulse height. For more energetic electrons, the lower threshold is set at the energy corresponding to a minimum ionizing particle traversing a minimal path through the detector (400 keV). This assures efficient detection of energetic electrons that pass through the detector with little scattering.

Table 6.1 provides a list of the nominal energy boundaries, centre of response, geometric-energy factor (GEF), and actual channel limiting angle in the spin plane, for each detector channel. The nominal energy boundaries contain more than 90% of the total response in a channel. The centre of response is defined so that 50% of the GEF is above and 50% below this value. The peak response of the channel is

Table 6.1. Channel response for the MEA detector [from Vampola et al. (1992)]. Column 1 contains the channel number, columns 2 and 3 the nominal lower and upper energy bounds, column 4 gives the centre of response (E_c), column 5 the geometric-energy factor (GEF), and column 6 the actual channel limiting angle. Energies are given in keV, the GEF are in units of ($cm^2\,s\,sr\,keV$).

Channel	E_{min}	E_{max}	E_c	GEF	Angle
0	110	188	153	5.88	8.24
1	174	257	214	5.68	6.37
2	230	314	271	5.16	5.19
3	297	384	340	4.84	4.38
4	374	462	418	4.59	3.78
5	465	553	510	4.19	3.24
6	558	649	604	3.89	2.90
7	646	738	693	3.58	2.63
8	735	829	782	3.30	2.40
9	828	923	876	3.08	2.21
10	928	1024	976	2.89	2.05
11	1042	1139	1090	2.66	1.88
12	1131	1227	1178	2.49	1.76
13	1239	1337	1287	2.37	1.66
14	1322	1419	1370	2.23	1.56
15	1423	1520	1470	2.14	1.48
16			background		
17	1534	1633	1582	2.03	1.41

very close to this value (within 1 or 2%). The GEFs are based on the laboratory calibration data obtained just prior to final delivery in January, 1990. For the transformation to flux, counts/s must be divided by the GEF. Note that the counts in the data stream are counts per 0.512 s.

The narrow acceptance angle in the spin plane provides very good pitch angle resolution, especially at high energy. The full field of view, coupled with the angular scan of 6° which occurs during the 0.512 s data accumulation period, results in a total acceptance angle within a single data sample of about 8–18°, depending on channel. The true pitch angle distribution of the particles can be established to about 0.5° through a deconvolution procedure which is limited by the accuracy of the onboard magnetometer data and by the statistics of the counts in the samples.

6.2.3 Proton telescope

AFGL-701-8&9

P.I.: E.G. Mullen (PLGD)
Co.-I.: M. Violet (PLGD)
M.S. Gussenhoven (PLGD)

The objective of the Proton Telescope (PROTEL) is to make well calibrated, high resolution measurements of the differential energy spectrum of protons in 24 channels spaced logarithmically from 1 to 100 MeV. PROTEL consists of two solid state detector assemblies (sensors) and a data processing unit (DPU). The Low Energy sensor Head (LEH) measures 1–9 MeV protons in 8 contiguous energy channels. The High Energy sensor Head (HEH) measures 6–100 MeV protons in 16 contiguous energy channels. The entire 24 point spectrum is returned once per second. Figures 6.4 and 6.5 show the diagram of the two instruments.

The two sensors consist of a stack of silicon solid-state detectors in a shielded assembly that have to satisfy certain coincidence/anticoincidence conditions to produce particle counts. Contamination from high energy protons presents the biggest problem in producing an accurate data set. In order to minimize contamination, each sensor has a collimator, a sweeping magnet, and passive and active shielding to reduce unwanted particles. In addition, the high energy sensor also has active anticoincidence rejection via guard rings around the silicon-lithium detectors.

The aluminium collimator reduces the proton and electron fluxes from outside of the acceptance cone. PROTEL shields out electrons very effectively. The passive shielding around the detector stack has a range of 50 MeV for orthogonally impinging electrons. Protons outside of the acceptance cone whose trajectories through the detector stack could cause a false count are shielded from energies below 195 MeV to 289 MeV depending on the channel and the incoming proton's position and angle. The inside surface of the collimator has a saw-toothed pattern to reduce the forward scattering of particles into the entrance aperture, and is painted with a conductive matte black paint to minimize light scattering towards the detectors. Electrons can produce an enhanced background noise count and are diverted from the detectors by the sweeping magnet.

Both surface barrier and lithium-drifted silicon detectors are used in PROTEL. The LEH uses 5 surface barrier detectors and the HEH uses a front surface barrier detector followed by a stack of 5 lithium-drifted silicon detectors. In the LEH (HEH) the first 4 (5) detectors determine the incoming proton energy. The 5^{th} (6^{th}) detector, separated from the rest by an aluminium (brass) absorber, is operated in anticoincidence with the rest, defining an upper threshold of 9 (100) MeV. The first five detectors of the HEH also have active shielding in the form of an anticoincidence ring. The ring is part of the same silicon wafer as the detecting element, but is

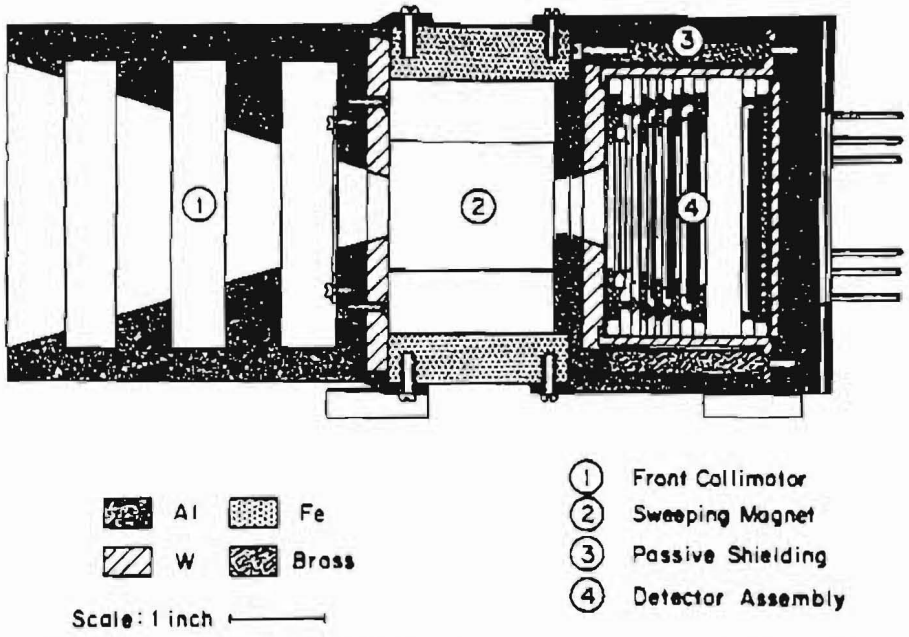

Figure 6.4. Schematic of the PROTEL high energy sensor head [from Gussenhoven et al. (1985)]

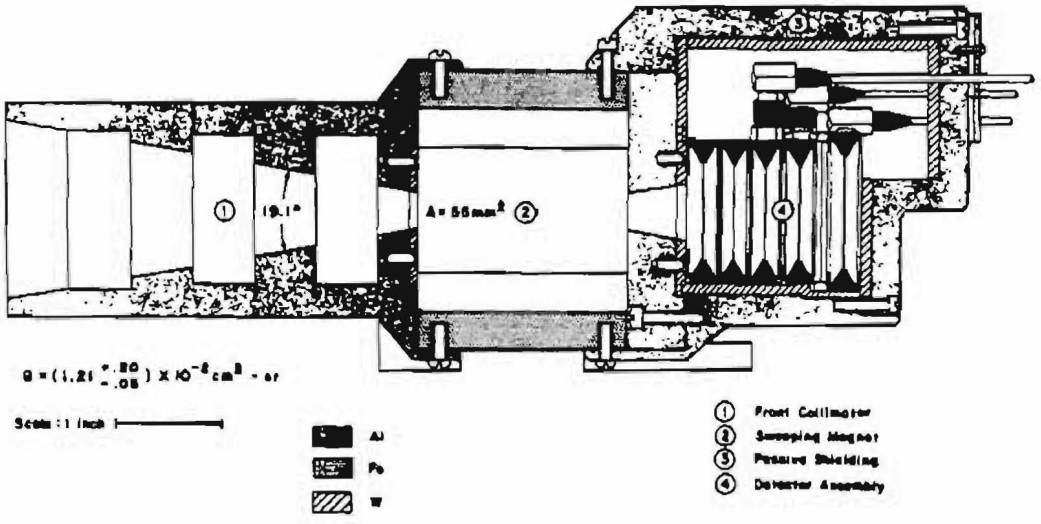

Figure 6.5. Schematic of the PROTEL low energy sensor head [from Gussenhoven et al. (1985)]

Table 6.2. PROTEL channel characteristics [from Violet et al. (1992)]

Channel	Energy Range (MeV)	E_{avg} (MeV)	E_{peak} (MeV)	Conversion factor $1/G$ $(cm^2\,s\,sr\,MeV)^{-1}$
		High Energy Head		
1	6.0–7.7	6.8	6.8	5.6
2	7.5–9.6	8.5	8.5	4.5
3	9.3–10.2	9.7	9.7	17.2
4	9.9–11.5	10.7	10.5	8.2
5	11.2–15.2	13.2	13.0	3.1
6	14.7–15.9	15.2	15.1	19.8
7	15.5–18.3	16.9	16.2	3.8
8	18.0–20.8	19.4	19.4	1.7
9	25.3–27.2	26.3	26.3	5.9
10	26.1–35.6	30.9	30.8	1.5
11	34.9–37.7	36.3	36.3	6.6
12	37.8–48.1	42.3	41.3	0.9
13	44.3–53.5	47.5	45.7	1.5
14	53.5–62.1	57.0	55.4	1.5
15	62.1–73.1	67.5	66.9	1.5
16	73.1–100.0	82.9	77.3	0.6
		Low Energy Head		
1	1.0–2.1	1.5	1.5	85.1
2	2.0–2.3	2.1	2.1	903.4
3	2.2–2.8	2.5	2.4	299.2
4	2.8–3.2	2.9	2.9	1279.7
5	3.1–4.1	3.6	3.6	135.8
6	3.9–4.8	4.3	4.2	156.1
7	4.6–7.0	5.7	5.0	99.2
8	7.3–9.4	8.4	8.6	435.1

electrically isolated, creating a second 'detector' outside the acceptance angle. Pulses in the detector stack which are coincident with pulses in the rings are rejected in order to reduce background counts produced by penetrating particles.

A proton which passes within the acceptance cone defined by the collimator of one of the sensor heads enters the detector stack where it either loses all or a portion of its energy. The amount of energy deposited in each detector is analysed by the system logic, which determines if detectors were triggered within a fixed time window

(2.0 μs, LEH; 0.5 μs, HEH). The system then evaluates the energy deposited in each triggered detector to determine in which channel, if any, to record the particle.

The instrument was calibrated at three proton accelerator beam facilities with energies ranging from 1.5 MeV to 159 MeV. The resulting channel boundaries and conversion factors for both sensors are listed in Table 6.2. The differential energy flux J, in protons/(cm^2 s sr MeV), is given by

$$J = \frac{\text{COUNTS}}{G\,\Delta t \int_{E_L}^{E_U} \epsilon(E)\,dE},$$

where G is the geometric factor, E_L and E_U are the channel boundaries, $\epsilon(E)$ is the energy-dependent efficiency, and Δt is the accumulation time of the instrument (1.0236 s).

For the best part of the CRRES orbit the shielding and anticoincidence rejection work very well, but contamination levels can become significant at the inner edge of the inner proton belt, where high fluxes occur of particles with energies higher than 100 MeV. These high-energy particles can penetrate detector shieldings and produce false counts at lower energies. The contamination levels can be estimated by modeling the contamination of the detector. The first steps included measuring the response of the HEH to > 100 MeV proton beams at various angles outside the detector acceptance cone and calculating the energy loss in various directions using a simplified materials model of the instrument. This led to the development of the PROTEL Contamination Code which computes counts that would be recorded in the HEH using a Monte Carlo integration approach and the Janni energy range tables. Both nominal performance and contamination are modeled. Indications from the model and early data are that the effects are minor and can be corrected for in the data analysis process.

6.2.4 Fluxgate Magnetometer

AFGL-701-13-1
P.I.: E.G. Mullen (PLGD)
Co.-I.: H. Singer (PLGD)

The purpose of the Fluxgate Magnetometer Experiment is to measure the ambient geomagnetic field and low frequency variations in that field from dc to 8 Hz.

The Earth's magnetic field is measured by a triaxial fluxgate magnetometer at a rate of 16 times per second in the range $\pm$45000 nT. The three axes of the magnetometer are mutually orthogonal to approximately 0.08°. The sensors are mounted in a single housing on a rigid Astromast boom. The 6.1 m boom locates

the sensors $\sim$ 7.5 m from the centre of the spacecraft to fulfill the requirement of having less than a few nT of vehicle-generated magnetic field at the sensor location. The analog electronics to operate the sensors are mounted inside the spacecraft and connected to the Electric Field/Langmuir Probe (EF/LP) experiment for power, signal processing and telemetry formatting.

The signal from each sensor is sent to the Langmuir Probe electronics where it is filtered with a 6 Hz lowpass cutoff to prevent aliasing from signals above the 8 Hz Nyquist frequency, and sampled by a 12-bit A/D convertor in the ranges $\pm$45000 nT and $\pm$850 nT to provide low and high sensitivity, respectively. For each sample from each axis, a microprocessor determines whether to enter the high or low sensitivity value into the telemetry stream. Furthermore, once per second the field strength at low sensitivity from all axes will be included in the data stream. The magnetometer data can also be sampled in a burst mode as described in the EF/LP instrument section. Additionally, the fluxgate signal will be lowpass filtered with a 20 Hz cutoff and provided to the spacecraft in analog form in two different ranges, $\pm$45000 nT and $\pm$1000 nT.

The magnetometer provides a real time signal to LEPA to enable this instrument to determine which zone in the field of view of its detectors is observing nearly along the magnetic field direction. LEPA is then able to transmit high time-resolution data, a complete energy spectrum in 0.5 s, with about 1° pitch angle resolution from the zone that is making observations near or within the particle loss cone.

On command, the signal from the near spin axis, the Y magnetometer sensor, can be amplified six times, in either the high-gain or low-gain mode, to provide better amplitude resolution at low field strengths near apogee. The increased sensitivity facilitates the detection of high-frequency, low-amplitude waves, such as ion-cyclotron waves that interact strongly with the plasma environment.

6.3 Data formats of SSDB and ephemeris

The first data set to be issued was the Science Summary Data Base (SSDB). This data base provides the user with one-minute averages of the data from selected instrument channels, which have been converted very tentatively to physical quantities. Several versions of ephemeris data were also issued. The most recent version was generated on an orbit-by-orbit basis and gives the orbital elements at one minute and five minute intervals for low and high altitudes, respectively.

6.3.1 The Science Summary Data Base

The CRRES Science Summary Data Base (SSDB) contains preliminary data of several CRRES detectors. It was released to provide the community with a quick survey of the available data, for instance to identify a period of interest in the CRRES mission for a later in-depth analysis. There has been no attempt to apply any quality control criteria to the data (removal of noise spikes etc.). Only preliminary calibration factors have been applied, and many instruments require background subtraction. However, even with these limitations, it is possible to draw some general conclusions and results from the SSDB.

The SSDB files were distributed in ASCII format. In order to obtain a more compressed format and to improve access speeds, the original files were transformed into Fortran unformatted files. At the same time, information from the ephemeris files was added, so that only one file needs to be accessed for a given orbit. The resulting SSDB files are organized on an orbit by orbit basis. They are named SSDB_EPHXXXX, where XXXX is the orbit number, left filled with zeroes. Each file contains a header record and approximately 600 data records with 21 entries per record. The contents of the header and data records are listed in Table 6.3.

Fluxes in Table 6.3 are given in units of particles/ (cm^2 s sr MeV), count rates are in counts/s. The special value -1×10^{30} is the value written for data items when dropouts occurred. For MEA, negative values for the difference between average counts and background counts are indicated by the special value -0.5×10^{30}. The model magnetic field strengths and L-values were obtained with a combination of the IGRF 90 model and the Olson & Pfitzer (1977) quiet model.

6.3.2 Ephemeris data format

Spacecraft vectors are received at PLGD from the Consolidated Satellite Test Center (CSTC). These vectors along with magnetic field models are used as the prime input to the ephemeris generation routines. These routines are run prior to the Agency Tape generation.

Satellite ephemerides are generated routinely on the basis of regularly updated position-velocity vector sets provided by the CSTC. These vector sets are quality-checked for transmittal errors and stored chronologically in a file for use in ephemeris calculations. Position-velocity accuracy requirements are achieved through the use of an ephemeris code that includes the geopotentials that account for the significant perturbation from a Keplerian orbit. Availability of regular vector sets also eliminates the need for ephemeris prediction and will permit, instead, the use of reliable interpolation techniques. Inspection of incoming vector sets for consistency is integrated into the ephemeris processing system. When switching between vector sets,

Table 6.3. Record structure of the SSDB header and data records. All entries are 4 byte REAL, except when otherwise indicated.

Entry	Description
	Header Record (INT*2)
1	Year
2	Day of year
3	Orbit number
4	Time resolution (60 seconds)
	Data Records
1	UT (seconds)
2	L (R_E)
3	Solar magnetic latitude (degrees)
4	Solar magnetic local time (hours)
5	Measured magnetic field magnitude (nT)
6	Model magnetic field magnitude (nT)
7	$(B_{measured} - B_{model})/B_{model}$
8	Electron flux, 4–5 MeV (HEEF L6-L7)
9	Electron countrate, > 2.5 MeV (Space Radiation Dosimeter LOLET 2)
10	Electron flux, 1–1.5 MeV (HEEF LL-L1)
11	Electron flux, 0.2–0.3 MeV (MEA channel 2)
12	Electron flux, 20–385 keV (EPAS 90° look direction)
13	He countrate, > 45 MeV/Nucleon (Experiment for High Energy Heavy Nuclei Composition P2)
14	Star countrate, > 75 MeV (Space Radiation Dosimeter VHILET 4)
15	Proton countrate, > 35 MeV (Space Radiation Dosimeter HILET 2)
16	Proton flux, 44.3–53.5 MeV (PROTEL HEH 13)
17	Proton flux, 3.1–4.1 MeV (PROTEL LEH 5)
18	Electron flux, 558–649 keV (MEA channel 6)
19	Geodetic altitude (km)
20	Western longitude (degrees) multiplied by 10 (INT*2)
21	Geodetic latitude (degrees) multiplied by 10 (INT*2)

smoothing is performed to suppress any discontinuities of position which exceed a predetermined level.

In addition to generating satellite coordinates, the ephemeris system provides a data base containing solar and lunar coordinates, the geomagnetic field vector and an event directory for eclipse and orbit adjust times. Solar and lunar position coordinates are computed and furnished as part of the standard ephemeris output. The following geomagnetic field parameters are also provided:

1. magnitude of field at vehicle location;
2. Earth Centred Inertial (ECI) components of magnetic field vector;
3. invariant latitude;
4. geographic location of 100 km intersection of vehicle's field line (both north and south hemispheres);
5. L;
6. magnitude and location (latitude, longitude, altitude) of minimum field intensity along vehicle's field line;
7. geographic location of vehicle's conjugate point;
8. geomagnetic local time (MLT) in hours, given by

$$\mathrm{MLT} = \frac{\mathrm{ML_{sat}} - \mathrm{ML_{\odot}}}{15} + 12\,,$$

where $\mathrm{ML_{sat}}$ and $\mathrm{ML_{\odot}}$ represent the geomagnetic longitude of, respectively, the vehicle and of the Sun at the time of interest.

Ephemeris data files are replicas of the files placed on the Agency Tapes. Data records are in 32 bit positive integer form (31 data bits and the MSB set equal to 0). Offset and bias values are provided to convert the positive integer values to true units. For altitudes less than $3\,R_{\mathrm{E}}$, the data rate is once per minute. For higher altitudes, the data rate is once per 5 minutes.

To convert the 32 bit positive integer data to proper units (e.g. km), subtract 2^{30} from the THDB value and then multiply by the appropriate factor. All factors are given as powers of 10 in the THDB. Thus, to convert WORD(i) to physical units [PHYSUNIT(i)], apply the expression

$$\mathrm{PHYSUNIT(i)} = \left[\mathrm{WORD(i)} - 2^{30}\right] \times 10^{\mathrm{FACTOR(i)}}\,.$$

Table 6.4 gives a description of the record structure of the ephemeris files and also lists the appropriate multiplicative factors as powers of 10.

Table 6.4. Record structure of the ephemeris files. The multiplicative factors in the third column are given as powers of 10.

Word	Description	Factor
1	Day number (days)	0
2	UT (milliseconds)	0
3	X, Satellite position, ECI[1] (km)	−4
4	Y, Satellite position, ECI (km)	−4
5	Z, Satellite position, ECI (km)	−4
6	VX, Satellite velocity, ECI (km/s)	−7
7	VY, Satellite velocity, ECI (km/s)	−7
8	VZ, Satellite velocity, ECI (km/s)	−7
9	Radius, Earth centre to satellite (km)	−4
10	Altitude (km)	−4
11	Latitude (deg)	−6
12	Longitude (deg)	−6
13	Velocity (km/s)	−7
14	Local Time (hr)	−7
15	Radius, MAG[2] (EMR[3])	−7
16	Latitude, MAG (deg)	−6
17	Longitude, MAG (deg)	−6
18	Radius, SM[4] (EMR)	−7
19	Latitude, SM (deg)	−6
20	Local Time, SM (hr)	−7
21	Radius, GSM[5] (EMR)	−7
22	Latitude, GSM (deg)	−6
23	Local Time, GSM (hr)	−7
24	B (nT)	−4
25	BX, ECI (nT)	−4
26	BY, ECI (nT)	−4
27	BZ, ECI (nT)	−4
28	Magnetic Local Time (hr)	−7
29	Solar zenith angle (deg)	−6
30	Invariant latitude (deg)	−6
31	B100N Latitude (deg)	−6
32	B100N Longitude (deg)	−6
33	B100S Latitude (deg)	−6
34	B100S Longitude (deg)	−6

Table 6.4. (Continued)

Word	Description	Factor
35	L (EMR)	−7
36	BMIN (nT)	−4
37	BMIN Latitude (deg)	−6
38	BMIN Longitude (deg)	−6
39	BMIN Altitude (km)	−4
40	BCONJ Latitude (deg)	−6
41	BCONJ Longitude (deg)	−6
42	BCONJ Altitude (km)	−4
43	X Sun Position, ECI (km)	0
44	Y Sun Position, ECI (km)	0
45	Z Sun Position, ECI (km)	0
46	X Moon Position, ECI (km)	0
47	Y Moon Position, ECI (km)	0
48	Z Moon Position, ECI (km)	0
49	Right Ascension of Greenwich	−6
50	B100N Magnetic Field (nT)	−4
51	B100S Magnetic Field (nT)	−4
52	MX Dipole Moment, ECI (nT)	−4
53	MY Dipole Moment, ECI (nT)	−4
54	MZ Dipole Moment, ECI (nT)	−4
55	DX Dipole Offset, ECI (km)	−4
56	DY Dipole Offset, ECI (km)	−4
57	DZ Dipole Offset, ECI (km)	−4
58–60	Vacant	

[1]ECI: Earth Centred Inertial Coordinates
[2]MAG: Magnetic Coordinates
[3]EMR: Earth Mean Radius (6371.2 km)
Equatorial radius is defined as 6378.135 km, flattening as 298.26.
[4]SM: Solar Magnetic Coordinates
[5]GSM: Geocentric Solar Magnetospheric Coordinates

Chapter 7

Statistical survey of Meteosat SEM-2 data

7.1 Introduction

This chapter contains the analysis of the SEM-2 (Space Environment Monitor on Meteosat-3) archived data set. This data set provides a record of many aspects of the geosynchronous orbit environment which is almost complete from 22 June 1988 to the present. The Meteosat-3 orbit, whilst it does not penetrate the heart of the outer radiation belt is one of the most important for spacecraft operations. Because the coverage in terms of L and latitude is small, it is possible to examine effects that are universal time and local time dependent, knowing that they are not caused by spacecraft motion through some radial structure. The aim of this study has been to examine the overall characteristics of the energetic electron environment at geostationary orbit and to relate these where possible to physical processes.

Sections 7.1.1–7.1.3 provide a brief review of Meteosat-3, SEM-2 and the archived data set. We describe problems encountered with the data set and the improvements made to the archiving process to solve them. Data analysis procedures are also described.

Local time dependence of the flux data and anisotropy and spectral indices are discussed in Sects. 7.2 and 7.3. Section 7.4 describes how Fourier analysis was used to study the local time dependence of fluxes. Wavelet analysis is used in Sect. 7.5 to deduce a repeat rate for injection events.

Section 7.6 is concerned with the average flux encountered for a specific mission duration. Key results from this study have been organized into a computer model.

Sections 7.7, 7.8 and 7.9 investigate more closely some of the specific features of the data, looking for how the flux levels are related to substorm activity and

hypothesized filling and loss mechanisms.

The work discussed in this chapter was originally presented in more detailed form in Technical Notes 6 and 7.

7.1.1 Meteosat-3

The geostationary satellite Meteosat-3 is one of a series of European Space Agency weather satellites, providing high quality optical and infrared images for weather prediction and climate research.

The first Meteosat satellite, Meteosat-1, experienced many operational anomalies, principally associated with the scanning radiometer mirror. These showed a correlation with geomagnetic activity and local time and so, in the absence of onboard plasma instrumentation, differential charging was suspected. For the second Meteosat spacecraft, steps were taken to make the satellite less susceptible to anomalies and a Spacecraft Environment Monitor (SEM-1) was included in the payload (Johnstone et al. 1985). Anomalies still occurred, although at a reduced rate and SEM-1 was able to confirm that spacecraft charging did occur. However, there was no correlation between the timing of the charging events and these anomalies, indicating that the charging was a benign process and that some other effect was causing anomalies. Suspicion fell on high energy electrons and it was decided to equip the third Meteosat spacecraft with a new Spacecraft Environment Monitor (SEM-2) detecting higher energy electrons. This instrument did indeed find the electrons responsible for most of the anomalies on Meteosat-3. A correlation between the anomalies and periods of high energetic electron flux was discovered (Coates et al. 1990) and the process of deep dielectric charging was implicated (Rodgers 1991).

It is fortunate that ESA's interest in spacecraft damage has provided a data set that can be used for wider studies of radiation belt statistics and processes.

7.1.2 SEM-2

The detectors used in the SEM-2 were provided by the Los Alamos National Laboratory (LANL), being the same as the Low Energy Electron unit flown on the Defense Support Program series of satellites (Aiello et al. 1975). The electronics were supplied by MSSL.

Five telescopes, each comprising a collimator, an aluminised mylar window and a surface-barrier detector, were positioned at 30°, 60°, 90°, 120° and 150° to the spacecraft spin axis, and each had a viewing half angle of 4°. Azimuthal coverage was provided by the spin of the spacecraft.

SEM-2 utilises surface-barrier solid-state detectors, in which the sensor is a re-

Table 7.1. SEM-2's five differential energy levels

Energy bin	Lower threshold (keV)	Upper threshold (keV)
E5–E4	42.9	59.4
E4–E3	59.4	90.7
E3–E2	90.7	134.9
E2–E1	134.9	201.8
E1	201.8	300.0

versed bias diode. Particles pass through the aluminised mylar window, which does not admit protons below 300 keV, to a region of linear electric field of a few hundred Volts. Electrons with energy below 300 keV dissipate all their kinetic energy in the detector resulting in free charges in the conduction band of the doped silicon, causing a current pulse which is detected by the anode. Discriminators then measure the current pulse which depends on the energy of the incident electron. Note that the uppermost 300 keV threshold is nominal in that it corresponds to the highest energy particle that is stopped within the detector. Electrons of energy greater than 300 keV produce a 300 keV pulse but pass through the detector without depositing any more energy.

The calibration of the SEM-2 and its integration to the spacecraft were carried out by the MSSL who supplied the read-out electronics. The total energy range of the detector, 42.9–300 keV, is divided into five differential energy ranges by the discriminators E1–E5 (see Table 7.1). The discriminator thresholds, measured using two electron beam systems (30–120 keV and 120 keV+), were found to provide energy bandwidths which were correctly spaced logarithmically, except for the lowest energy one which is slightly smaller. The thresholds were found to be consistent between the telescopes to 10% or better, and both angular and scattering tests were satisfactory (Coates et al. 1990).

Although full 3-D distributions were obtained on-board, these were not telemetered down, because of restrictions on telemetry rates. Instead one 1-D distribution of flux as a function of energy (summed over both angles) and one 2-D distribution of flux as a function of both polar and azimuthal angle (summed over energy) were transmitted. These distributions were transmitted at successively 500, 500 and 600 s intervals.

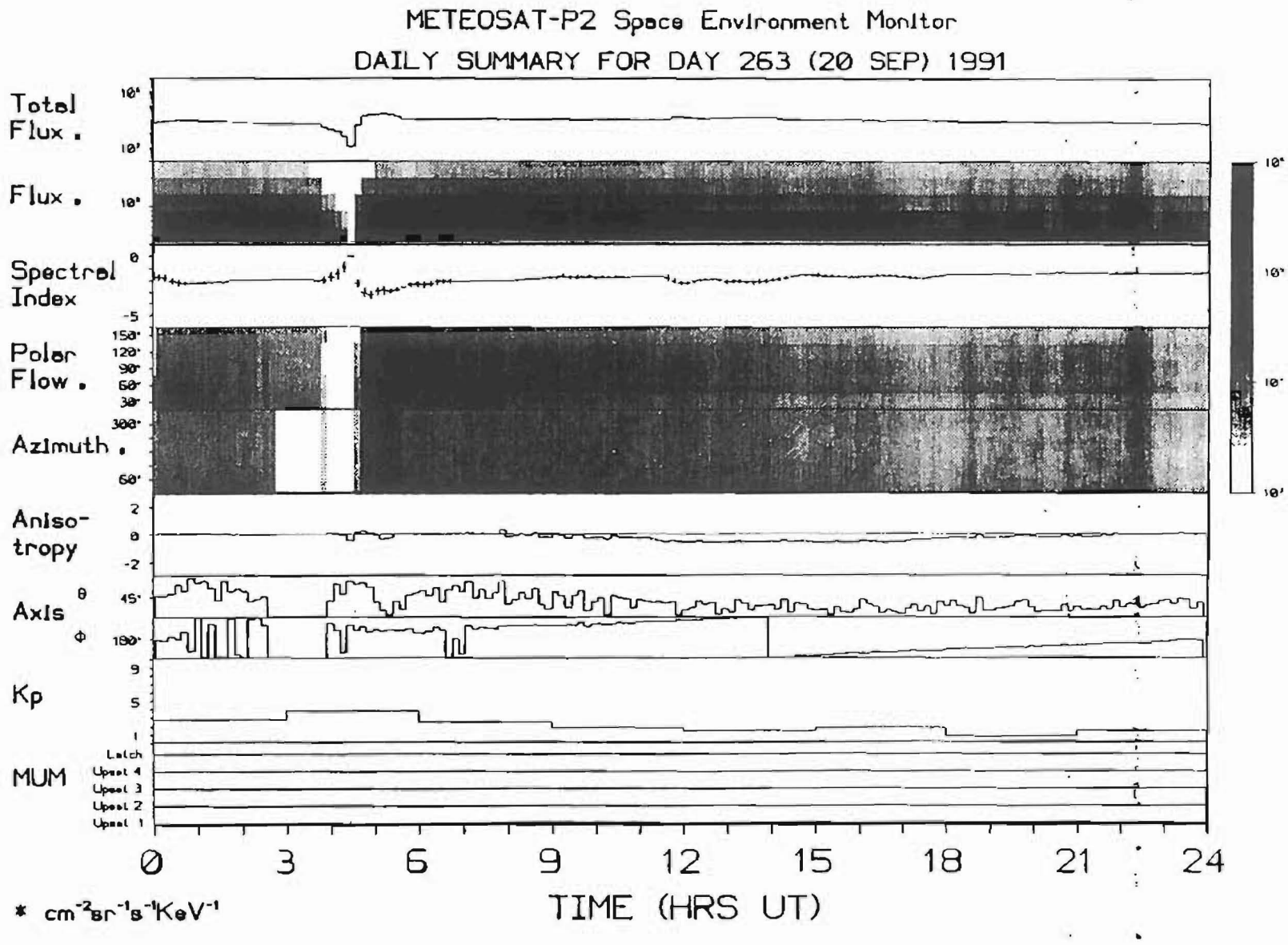

Figure 7.1. SEM-2 Daily summary plot

7.1.3 The SEM-2 data set

Since SEM-2 was turned on in orbit on 22 June 1988, data have been collected and archived in monthly units. With the exception of March and April 1991, when the instrument was switched off, complete monthly archive files exist from July 1988 to the present, providing a long, continuous time series of data describing the geostationary environment.

Daily and monthly summary plots are produced showing greyscale fluxes, spectral index, polar and azimuthal flow, anisotropy index, K_p and memory upset monitoring. An example daily plot is shown in Fig. 7.1.

Archive data files are produced by the FORTRAN archiving program called ARCHIVE_METEOSAT_P2.FOR. Two archive files are produced for each month, one high time resolution and one low time resolution. In the high time resolution files, the data are stored in the maximum time resolution of raw data, i.e. in records of 500 s, 500 s, and 600 s successively. These data were used where detailed time information about a particular variable was required, for example, in Superposed Epoch studies. For many statistical studies, this data set is unnecessarily precise and inconviently large, so low time resolution files were created with a time resolution of 30 minutes. These files are particularly convenient for the study of local time behaviour.

Both types of archive file contain records comprising 96 elements of 4 bytes each and are identical in format. The 96 variables contained in each record are shown in Table 7.2. Where data are missing, a flag of -1 is used.

A long time series of data from the SEM-2 is now available and provides a valuable source of information about the geostationary electron environment.

Problems encountered in the archived data set

One of the first results of our studies was the discovery that there were upper and lower thresholds in the flux values stored in the database. These were not inherent to the SEM-2 data but corresponded to the limits of plotting windows used to display the data in the SEM-2 Daily Summary Plots. It was discovered that the archiving program for Meteosat data had been developed from the program used to create these plots, and that the limits of the original plots had been imposed on the data. The effect of this was most pronounced at higher energies, where flux levels were quite low and frequently fell below the lower threshold. Since the spectral index was calculated after the imposition of the thresholds, this was also in error.

A number of other problems in the archive program were also discovered. Raw counts information (not converted into flux) was not stored because it had not been plotted in the Daily Summary Plots. Similarly the $K_p(\tau)$ index was missing. The data from the Memory Upset Monitor (MUM) had offets added to them and the

Table 7.2. Elements of the archived SEM-2 data set record

Element	Variable
1	Start time of bin in hours UT
2	End time of bin in hours UT
3	Total flux of electrons in energy range 42.9–300 keV, summed over all polar and azimuthal bins
4–8	Fluxes in each energy bin, summed over all polar and azimuthal bins 4: Energy range 201.8–300 keV 5: Energy range 134.9–201.8 keV 6: Energy range 90.7–134.9 keV 7: Energy range 59.4–90.7 keV 8: Energy range 42.9–59.4 keV
9	Spectral index: the slope of the logarithm of the energy spectrum, calculated using a least squares fit
10	Delta spectral index: the error on the above calculation
11–15	Polar flow: this is the flux in one of five polar angle sectors of the analyser. These bins are approximately +/- 5°: 11: 150° to spin axis 12: 120° to spin axis 13: 90° to spin axis 14: 60° to spin axis 15: 30° to spin axis
16–21	Azimuthal flow: the flux in one of six azimuthal angle sectors of the analyser. The angles are (in spacecraft coordinates, where at 0° the spacecraft looks towards the Sun): 16: 300–360° 17: 240–300° 18: 180–240° 19: 120–180° 20: 60–120° 21: 0–60°
22–51	Polar-azimuthal flux: in 30 bins, for each polar angle sector across the azimuthal angles sector
52–56	Counts in each of the five energy ranges (see 4–8)
57–86	Polar-azimuthal counts: again, in 30 bins
87	Anisotropy: the anisotropy index describes the angular shape of the plasma distribution relative to its axis of symmetry.

Table 7.2. (continued)

Element	Variable
88–89	θ and ϕ: angles describing the angular shape of the plasma distribution relative to its axis of symmetry.
90	K_p, the 3-hourly index of planetary magnetospheric activity for the whole Earth, has values 0^0, 0^+, 1^-, 1^0, 1^+, etc. (range 0 to 9) archived as 0.0000, 0.3333, 0.6666, 1.0000, 1.3333, etc. (ie. '+' and '−' are denoted by adding or subtracting 1/3, respectively).
91	$K_p(\tau)$: this is a weighted average of successive K_p as devised by Wrenn (1987)
92	Latch: this shows the occurrance of latch-ups in the test RAM (Random Access Memory)
93–96	MUM: Memory Upset Monitors give number of SEUs (Single Event Upsets) in the four memory zones of the test RAM.

MUM test sequences, which were supposed to be excluded from the archive, were included.

Improvements to the data set

The original software has been corrected by N. Flowers, M. Birdseye and S. Szita at MSSL and the database is now believed to correspond to the specification described in the SEM-2 Final Report (Coates et al. 1990). The entire data base has been re-processed from the raw data tapes, using the same format as the original archive data set. All monthly archive files from 1988 to the present have been saved to optical disk.

Longitude adjustment

Since Meteosat's longitude varies, and the time recorded with the data is Universal Time, a time adjustment equivalent to the satellite's departure from 0° longitude must be made to convert to local time. Figure 7.2 shows how Meteosat's longitude has varied from the start of 1989 to the end of 1992.

Using one value of longitude per day, the start and end times of each data bin are adjusted by an amount of time corresponding to Meteosat's position. A positive longitude (i.e. eastward of 0°) means a positive adjustment to the local time must

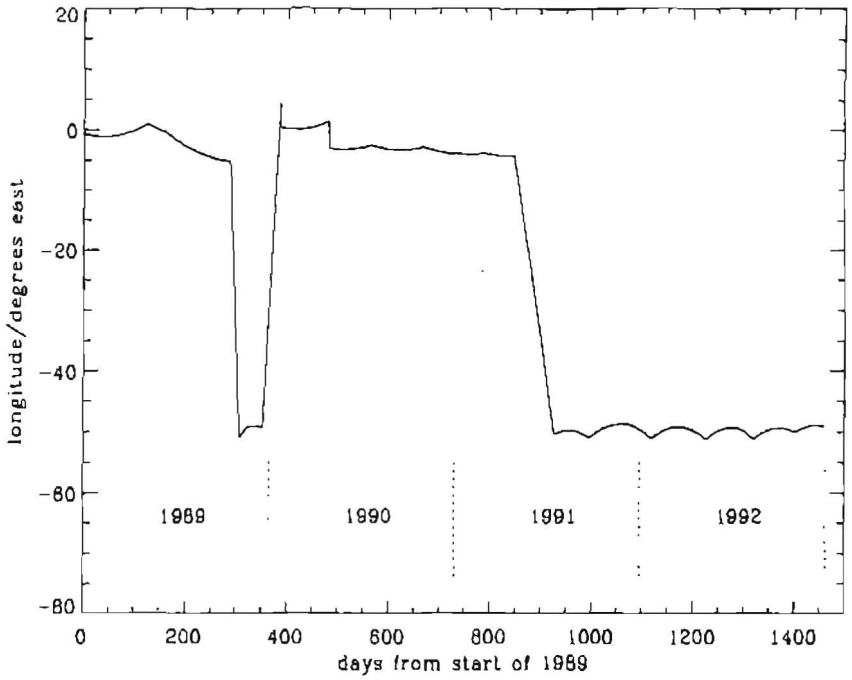

Figure 7.2. Meteosat-3's longitude, 1989–1992

be made, and a negative longitude (westward of 0°) requires a negative local time adjustment.

Analysis software

The original Meteosat SEM-2 raw data processing, archiving and archive data processing software was written by M. Birdseye (MSSL) in VAX Fortran.

Many of the programs for analysis of the processed SEM-2 data have been written in IDL (Interactive Data Language) which is very useful for handling large arrays of data. Other programs were written in Fortran, with IDL being used to display the data. Key programming initiatives include:

1. Processing of large data arrays, e.g. flux data, to get average local time profiles of a variable, and finding average, median and other chosen statistical values.

2. Binning low time resolution variables with respect to local time, to produce statistical local time plots.

3. A simple model which outputs the expected range of flux for a specified SEM-2 energy range and time of day.

4. A simple model which outputs the expected average range of flux for a specified time duration.

5. Correlation software development.

6. Superposed epoch software development.

7. Percentage rise in flux software development.

7.2 General statistical dependences

7.2.1 Flux dependence on local time

This analysis used low resolution flux data to produce statistical local time profiles. Flux versus local time plots were produced for the total energy range of the detector and for each of the five energy bands which make up the instrument's full range.

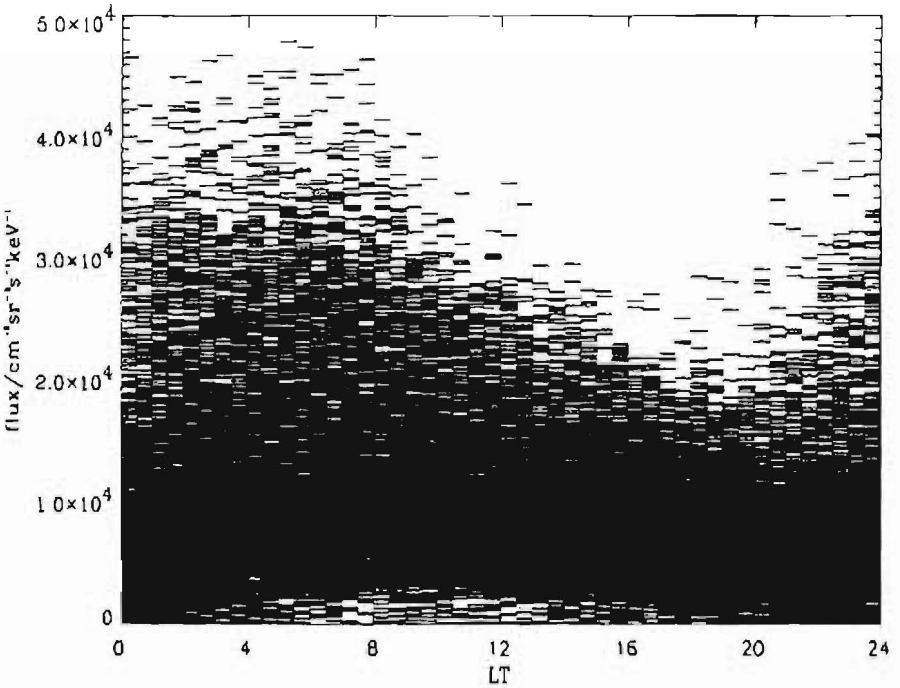

Figure 7.3. Scatter plot of total flux (42.9–300 keV) 30-minute averages versus local time, 1989–1991

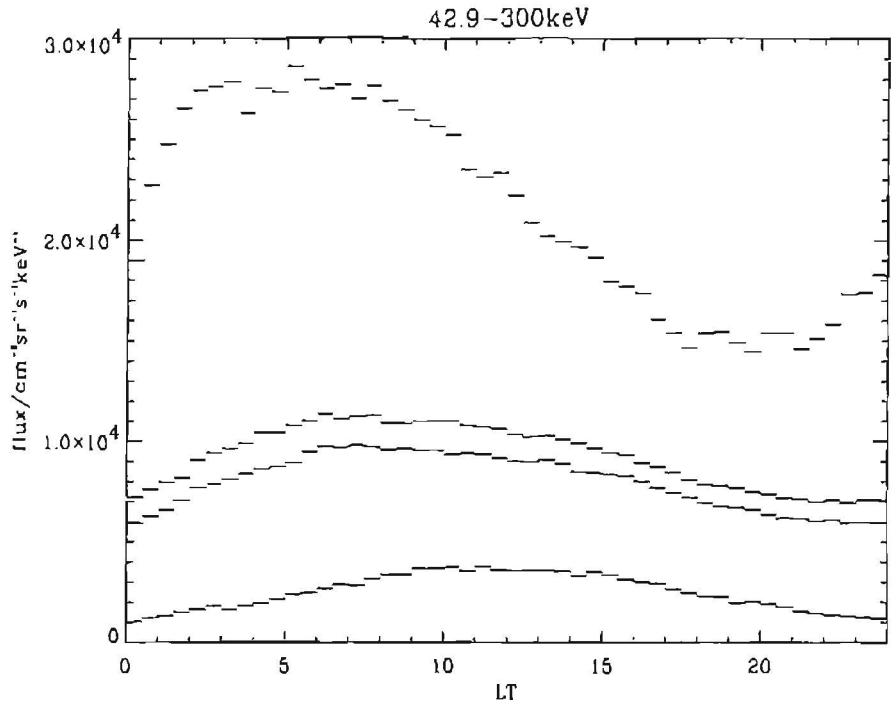

Figure 7.4. Total flux (42.9–300 keV) 30-minute averages, 1989–1991: 95% and median ±5% limits (see text)

Total flux

A scatter plot of three years of total flux (42.9–300 keV) data versus local time is shown in Fig. 7.3. The units of flux are $cm^{-2}sr^{-1}s^{-1}keV^{-1}$ and each data point is a 30-minute average. Three years of data (1989–1991 inclusive) are plotted: this means that over 50,000 data points have been used, which while producing a very busy plot shows when the most common flux values are observed and when fluxes are most variable. The range of flux values observed at local night is at least twice the range seen in daytime. The highest peak fluxes occur between 0400 and 0800, the lowest between 1600 and 2000.

The same data are presented in a different form in Fig. 7.4, which consists of four curves. The uppermost curve marks the level below which 95% of observations occurred, the lowest curve marks the level above which 95% of observations occurred and the middle two curves show the median ±5% of observations. The curves have a quasi-sinusoidal appearance. Figures 7.3 and 7.4 both show that peak fluxes and greatest variability occur in the early morning hours between 0400 and 0600.

Energy dependence

Similar plots to Fig. 7.4 for the five differential energy bands are shown in Figs. 7.5 to 7.9.

Fluxes in the four lowest energy bands exhibit similar behaviour to the total flux and to each other: the shape of the curves and the positions of minima and maxima are broadly similar. More counts are observed in the lower energy bands, so their behaviour would be expected to dominate the total energy range. The early morning variability is produced by substorm injections of particles. Injection events occur near midnight and the injected electrons then drift eastward, toward the morning hours. The amplitude of the event decreases the later it is observed in local time (Lezniak et al. 1968, Parks et al. 1968).

The highest energy band shows different local time dependence: the curves peak later in local time, at around 1000–1200, and are almost symetrical about their maxima. The range of fluxes observed in this energy band is more consistent throughout the 24-hour period than for the lower energy bands. These are radiation belt electrons. This highest energy band flux does not appear to show influence of substorm injection particle fluxes. It corresponds quite well to the change in magnetic field intensity as the spacecraft moves in its orbit. Figure 7.10 shows the local time variation of the magnetic field based on the Tsyganenko field model. The shape of this curve arises because of the non-dipole nature of the field which causes the satellite to effectively see a lower L-shell around noon than elsewhere. In the case of the lower energy ranges, the effect of substorms injections dominates these trapped fluxes.

Cayton et al. (1989) divided the 30–2000 keV electron energy spectrum into two components: a "soft" component (30–300 keV) characterized by substorm injections and a "hard" component (300–2000 keV) which shows little variability on the timescale of substorms. The first four of the SEM-2 energy bands (42.8–201.8 keV) correspond to the "soft" electron component whilst the highest energy band (201.8–300 keV) corresponds to the "hard" component.

Model program predicting observed flux ranges at given local times

A simple computer program has been written to output the range of fluxes expected for a local time specified by the user. The routine, FLUX_LT, is written in VAX Fortran. Input parameters are local time and chosen energy range. The program can supply fluxes for any of SEM-2's energy ranges (i.e. the total range and the five smaller energy ranges). The output parameters are the average flux and parameters derived from the data presented in the statistical plots: the median flux and the fluxes above and below which 95% of observations occur.

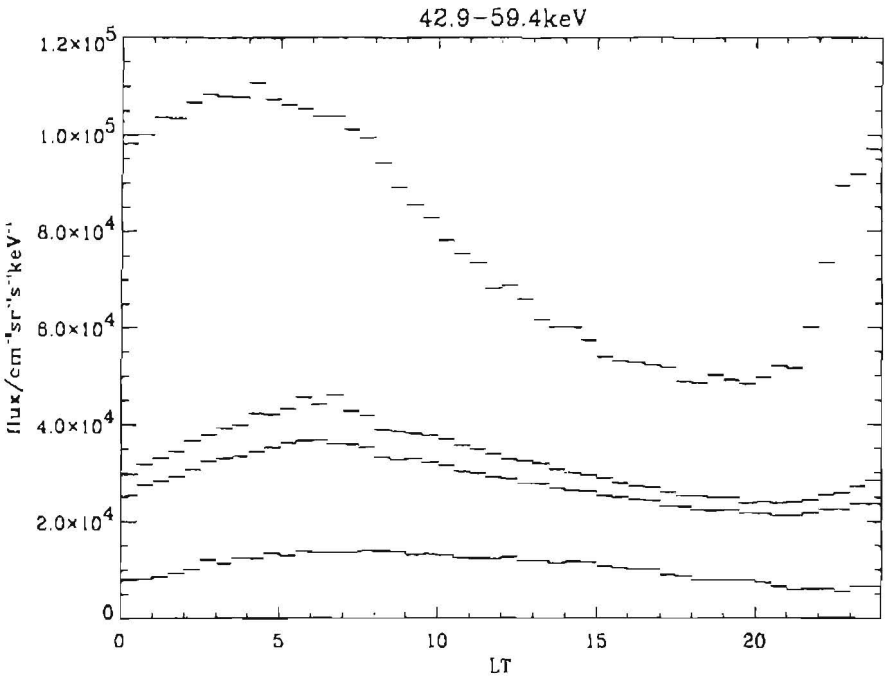

Figure 7.5. Low resolution flux averages for SEM-2's E5–E4 differential energy band versus local time (see text)

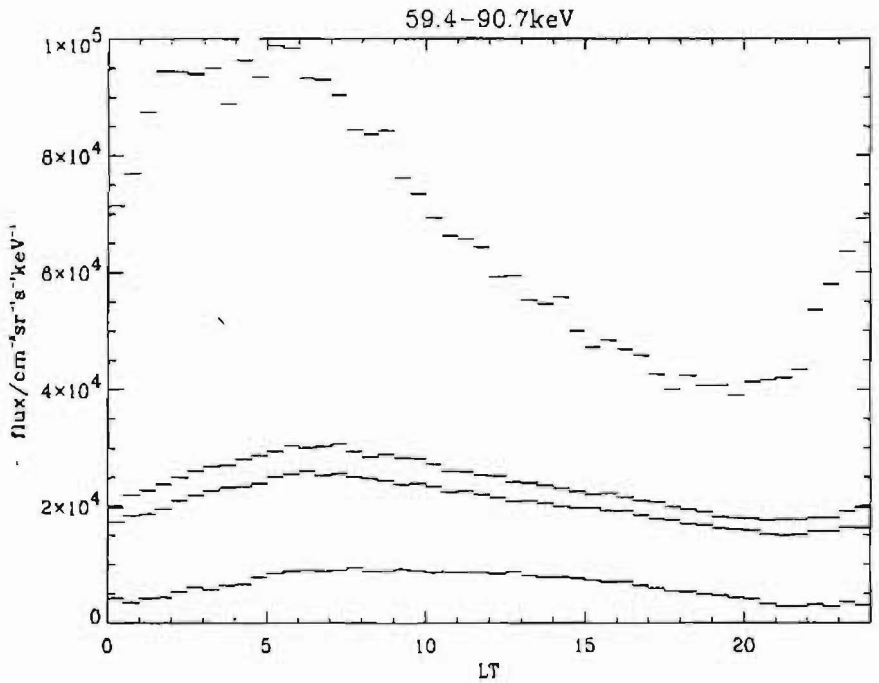

Figure 7.6. Low resolution flux averages for SEM-2's E4–E3 differential energy band versus local time (see text)

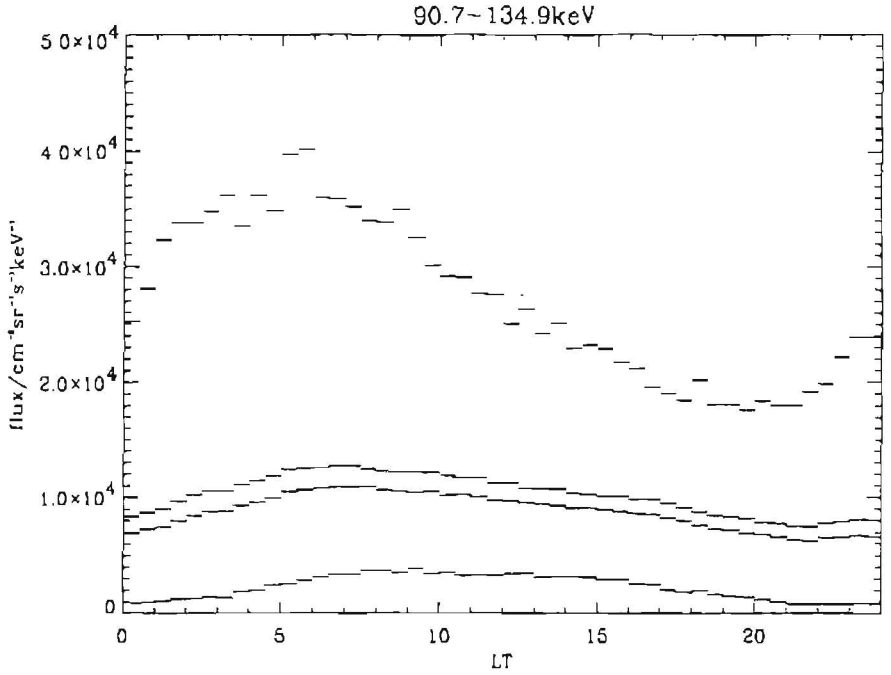

Figure 7.7. Low resolution flux averages for SEM-2's E3–E2 differential energy band versus local time (see text)

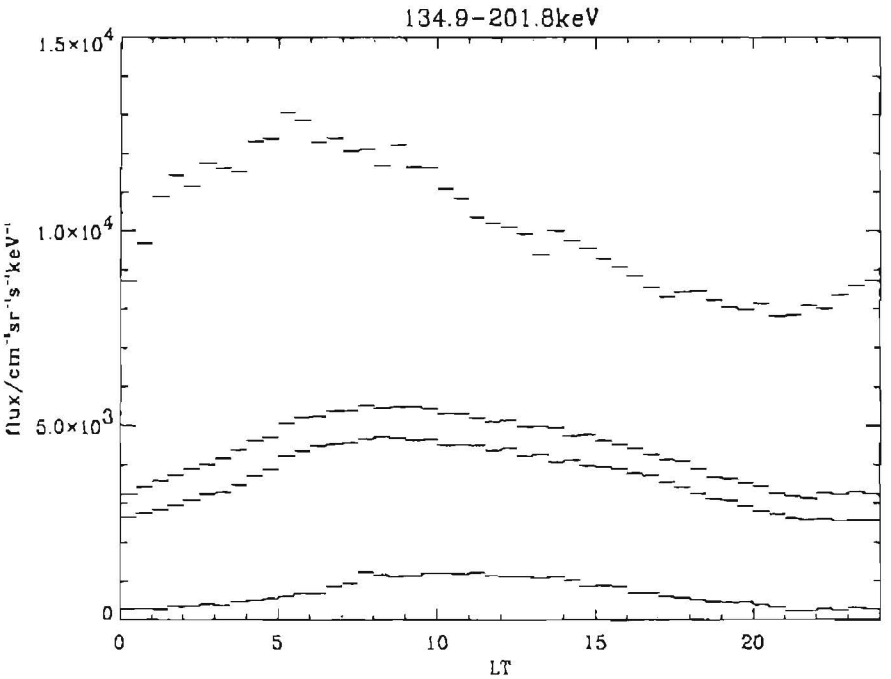

Figure 7.8. Low resolution flux averages for SEM-2's E2–E1 differential energy band versus local time (see text)

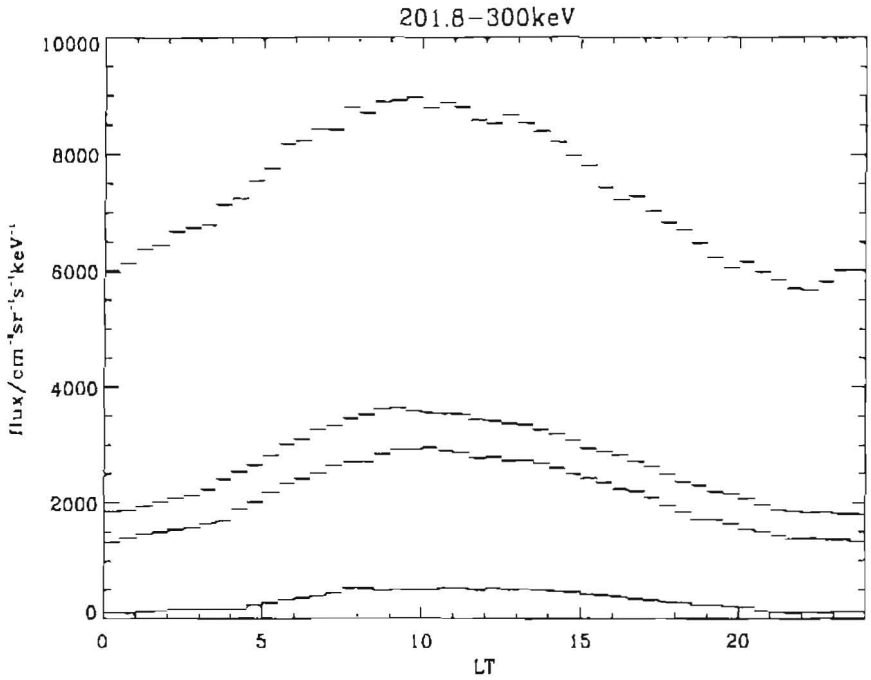

Figure 7.9. Low resolution flux averages for SEM-2's E1 differential energy band versus local time (see text)

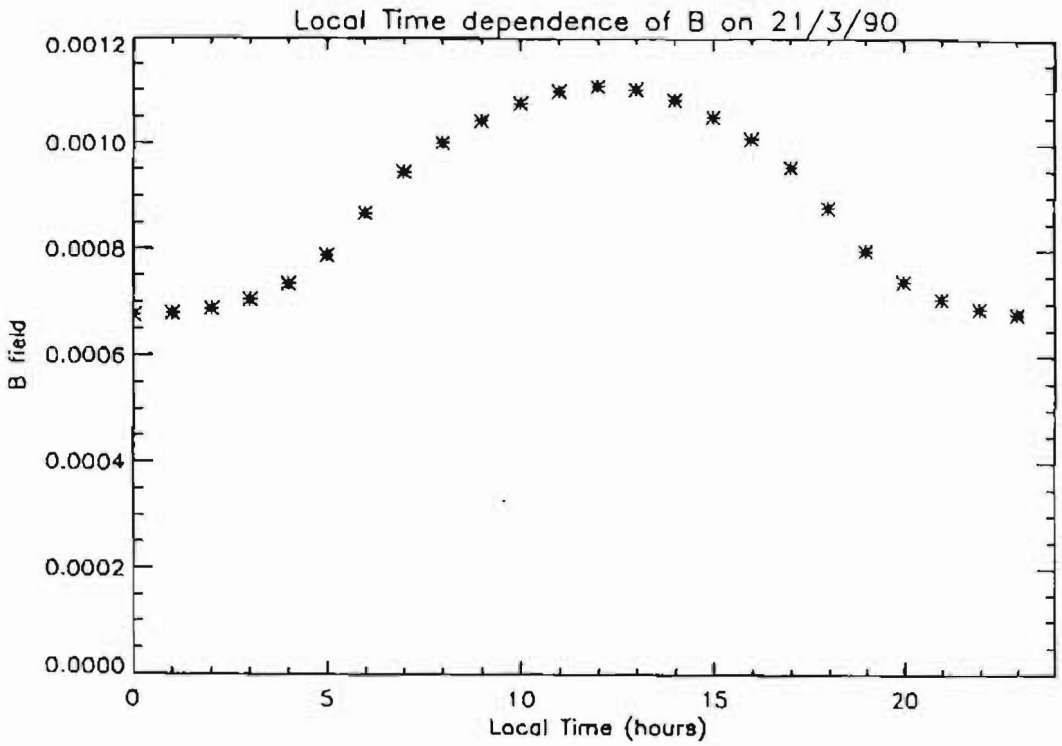

Figure 7.10. Variation of modelled magnetic field (in gauss) with local time

7.2.2 K_p Dependence of flux

The K_p index

The K_p index provides a measure of the level of geomagnetic disturbance. It has three-hourly values ranging from 0 at low disturbance to 9 at high disturbance on a logarithmic scale, using + and − for between-integer values, e.g. 1^+, 2^-, 2, 2^+, 3^-, etc. In the archive files, + and − are recorded using the integer number ± 0.3333. The value of K_p is worked out from the deviation of the magnetic trace from the quiet situation for each particular observatory, then an average of all observatories is taken (Parks 1991).

Dividing the flux data according to K_p index

The flux data was divided up into four groups according to the value of K_p at the local time of the flux measurement, ranging from low to high magnetospheric activity. The four K_p ranges chosen were:

- K_p between 0^0 and 1^+
- K_p between 2^- and 3^+
- K_p between 4^- and 5^+
- K_p between 6^- and 9^0.

By finding the corresponding K_p value at the observation time, the flux data can be binned accordingly.

Total flux K_p dependence

The data set used for this analysis was three years of low resolution total flux data, 1989–1991. The total fluxes are shown in scatter plots in Fig. 7.11, divided into four separate groups by the limits of K_p defined in the last subsection. The number of good data points that fell into each of the four K_p ranges is given in Table 7.3.

The same data has been used to make the statistical plots shown in Fig. 7.12 (the outer two lines are the levels above and below which 95% of fluxes occurred, the inner two lines mark the median ±5% of observations). As K_p increases, the range of fluxes observed increases, the local time behaviour becomes increasingly disordered and the diurnal variation becomes more pronounced.

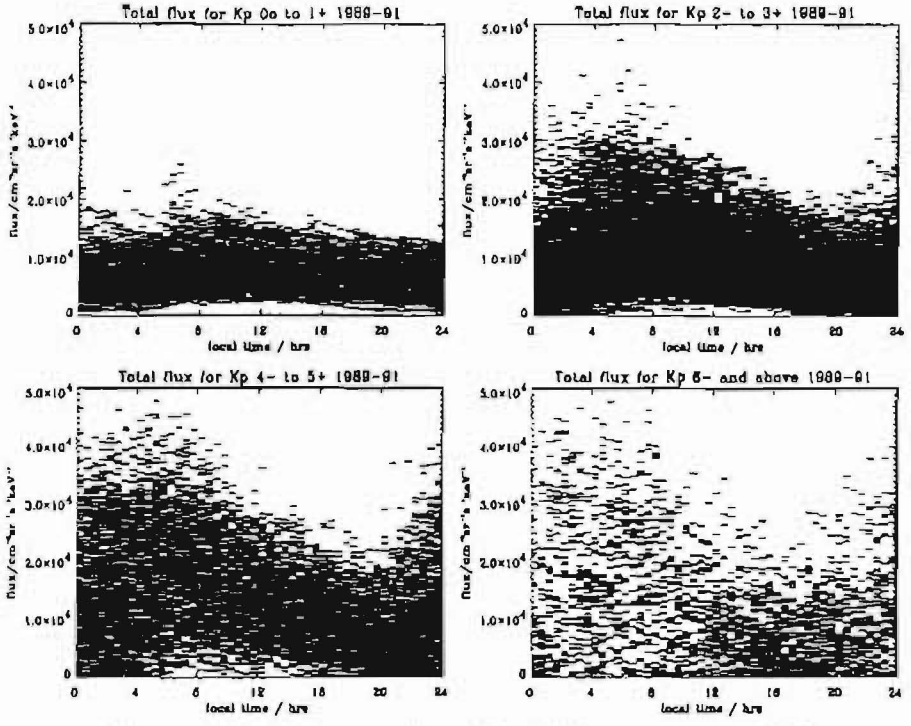

Figure 7.11. Scatter plots of total flux in ranges of K_p

Table 7.3. Total flux points in K_p ranges

K_p range	No. of data points
0^0–1^+	10585
2^-–3^+	24901
4^-–5^+	11102
6^-–9^0	2549

K_p dependences for each energy range

Figures 7.13 to 7.17 are the same type of plots as Fig. 7.12 for each of SEM-2's five energy ranges, with fluxes divided according to K_p.

The four lowest energy ranges all show significant increases in flux levels as K_p increases, with high variability seen in the early hours. For each energy range, the graphs show less predictable behaviour as K_p increases. This tendency starts at a lower K_p range the lower the energy range is. For the lowest K_p range, the range of fluxes increases towards lower energies.

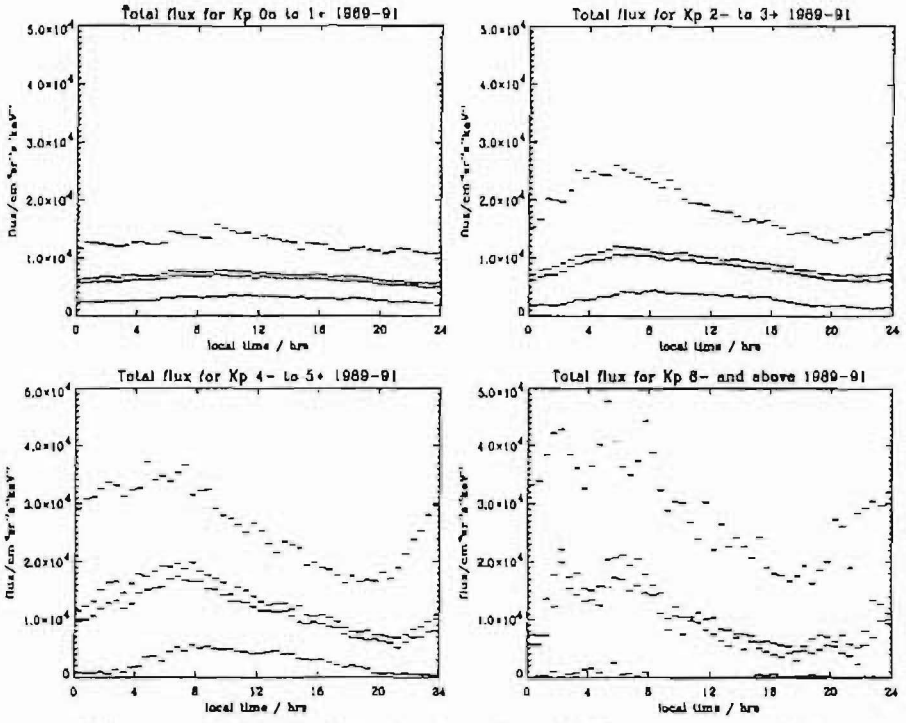

Figure 7.12. Statistical plots of total flux in ranges of K_p

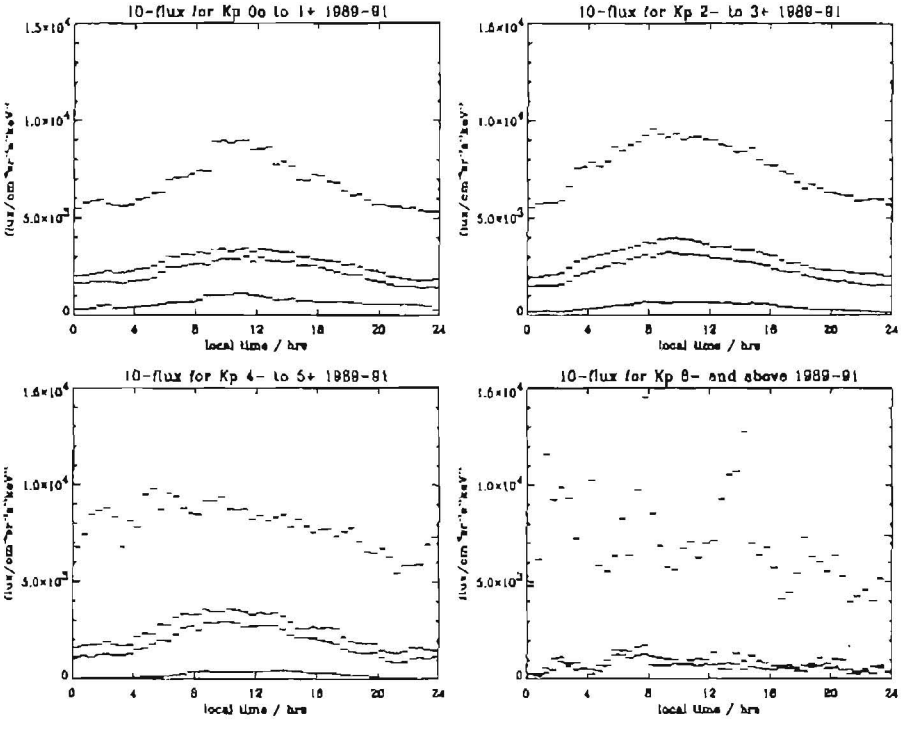

Figure 7.13. Statistical plots of E1 flux in ranges of K_p

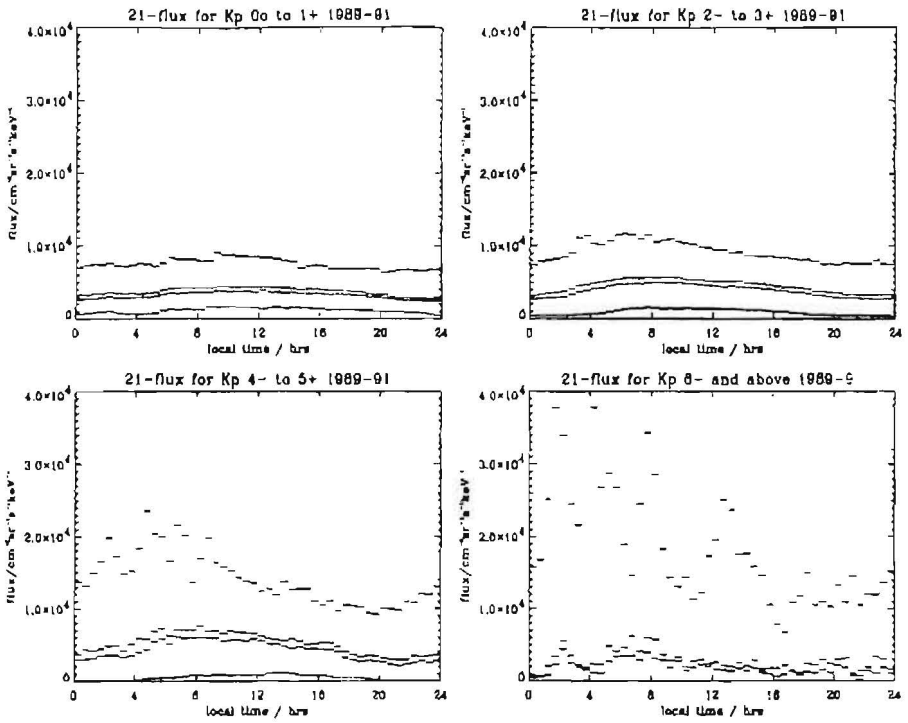

Figure 7.14. Statistical plots of E2–E1 flux in ranges of K_p

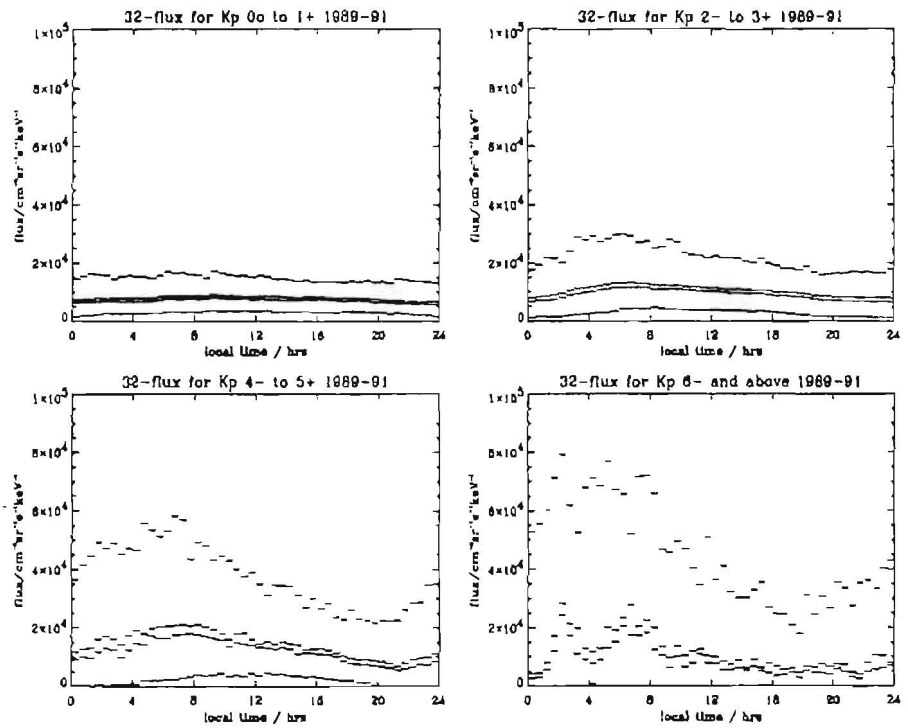

Figure 7.15. Statistical plots of E3–E2 flux in ranges of K_p

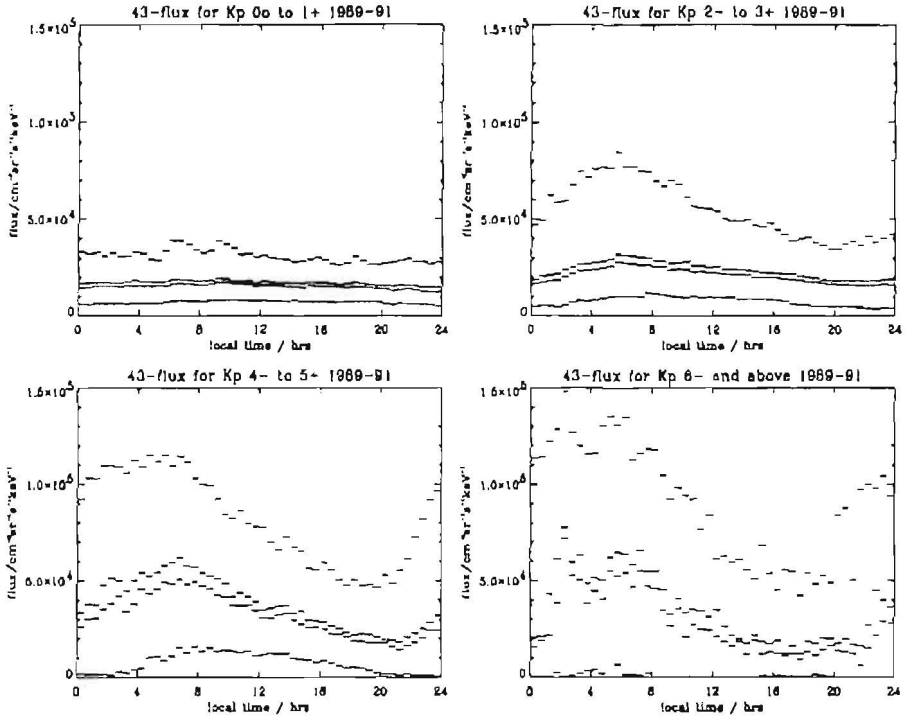

Figure 7.16. Statistical plots of E4−E3 flux in ranges of K_p

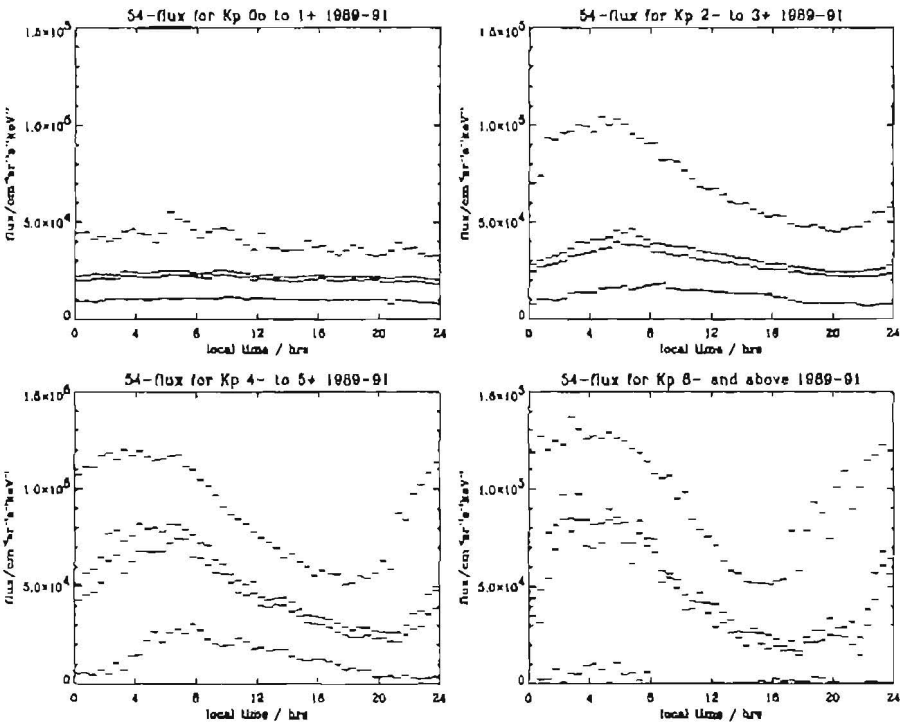

Figure 7.17. Statistical plots of E5−E4 flux in ranges of K_p

The highest energy range, E1 flux, shown in Fig. 7.13, shows little change in flux range and levels as K_p changes, although the plot becomes more haphazard as K_p increases.

7.3 Spectral index and anisotropy

In Sects. 7.3.1 and 7.3.2 statistical plots of spectral index and anisotropy are discussed.

7.3.1 Spectral index

The spectral index stored in the archive files is the slope of the logarithm of the energy spectrum calculated using a least squares fit, an error on which is also available from the archive file. It is usually negative because there are generally more lower energy than higher energy particles: in the SEM-2 low resolution archive data, the value of spectral index generally lies between 0 and -6.

A strongly negative spectral index corresponds to a soft energy spectrum, where the particle population dies away with increasing energy, whereas a weakly negative spectral index corresponds to a hard spectrum, with many particles above the energy range of the analyser.

Figure 7.18 shows spectral index versus local time, using one year (1990) of data, where the outer two lines again show the limits above and below which 95% of observations occurred, and the inner lines show the median $\pm$ 5% of observations. The most negative values of the spectral index, indicating a soft energy spectrum, occur in the early morning where injection events were seen in the lower energy fluxes. The least negative values are seen on the dayside where the geostationary orbit passes through increased magnetic field values, and larger fluxes of higher energy trapped particles would be expected, creating a harder energy spectrum.

7.3.2 Anisotropy

The anisotropy index describes the angular shape of the plasma distribution relative to its axis of symmetry, which may be assumed to be in the direction of the magnetic field.

A positive anisotropy value is characteristic of a field aligned distribution, whereas a negative anisotropy value corresponds to a distribution which is enhanced perpendicular to the magnetic field direction. Trapped or loss cone distributions therefore have a negative anisotropy index.

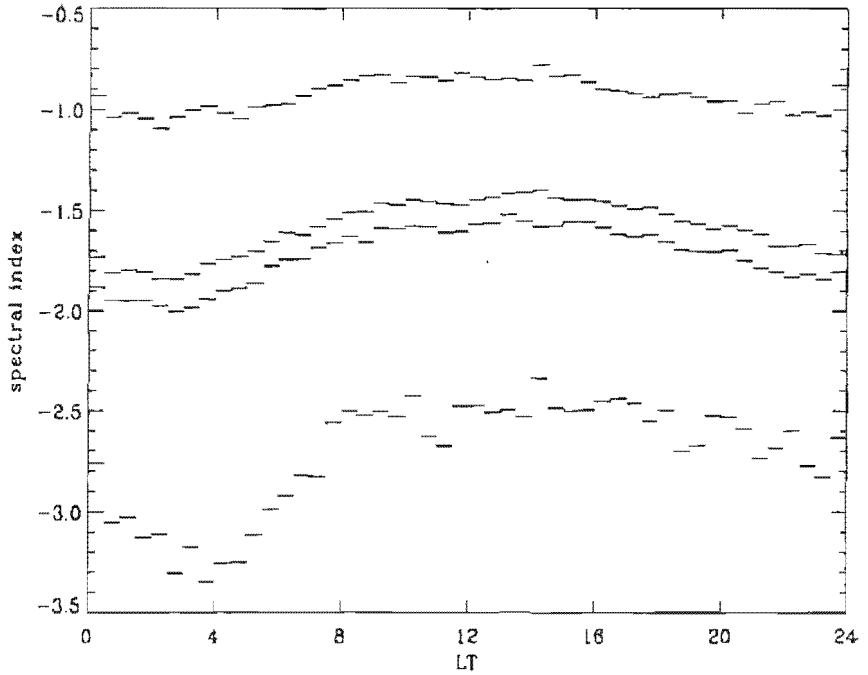

Figure 7.18. Spectral index versus local time

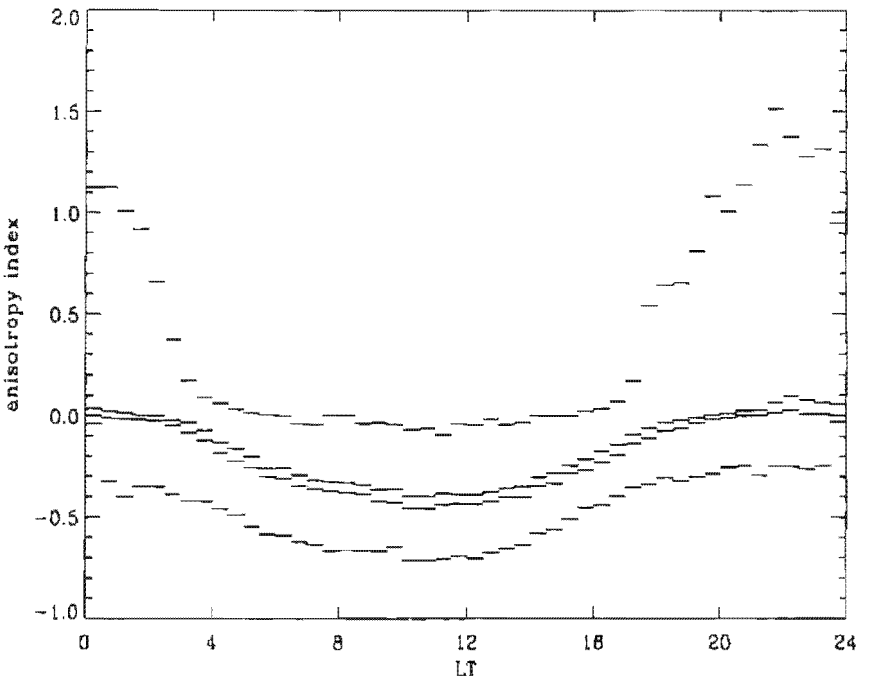

Figure 7.19. Anisotropy index versus local time

Figure 7.19 shows the same type of statistical plot for the anisotropy index as Fig. 7.18. It shows that between 0400 and 1700, 95% of anisotropies are negative, reflecting a trapped distribution. Between 1700 and 0400, 50% of anisotropies are positive, which reflects the more tail-like magnetic field structure on the nightside, causing particles to be more field-aligned. These characteristics agree with the findings of Baker et al. (1978), who noted that the lower energy electron distribution became cigar-like prior to substorm onset, and pancaked following the injection event. They found the injection event was observed at geosynchronous altitudes at a median time delay of 95 minutes after the onset of the cigar-like phase (the mode of the time delay being shorter). The uppermost curve in Fig. 7.19 turns sharply upward at 1600–1800, with the most positive values around 2200. From Figs. 7.5 and 7.6, the uppermost curve shows electron flux in the lower energy bands starts a steep increase at around 2200, with peak fluxes at 0400. We are therefore seeing a change towards cigar-shaped distributions 4 hours prior to the first evidence of injection events.

7.4 Fourier analysis of data

7.4.1 Reasons for Fourier analysis

Fourier analysis was employed to investigate the quasi-sinusoidal diurnal variation shown by the local time plots of flux (Figs. 7.3 and 7.4).

Initial investigation showed that a single sine wave does not provide an adequate fit for this average diurnal variation: a sine wave of the correct frequency lags the real data for half the period and leads for the other half. Figure 7.20 shows a pure sine wave superimposed on the three-year average total flux profile (smoothed with a five-point boxcar) repeated four times to show that the frequency of the sine wave matches.

Fourier analysis was used to try to identify this average diurnal variation. It was hoped that if it could be filtered from the data, it might then be possible to see other phenomena more clearly than when superimposed on this larger effect. For example, the flux data shows spikes with a duration and separation of a few hours occurring successively over large sections of the spectrum, but these spikes are not rigidly periodic and are picked out by Fourier analysis.

The software package used for the Fourier analysis is ARK, written by A. Smale, R. Corbet and K. Mukai of the Oxford High Energy Astrophysics Group, and modified by C. Jomaron of MSSL to accommodate the large data sets available from Meteosat.

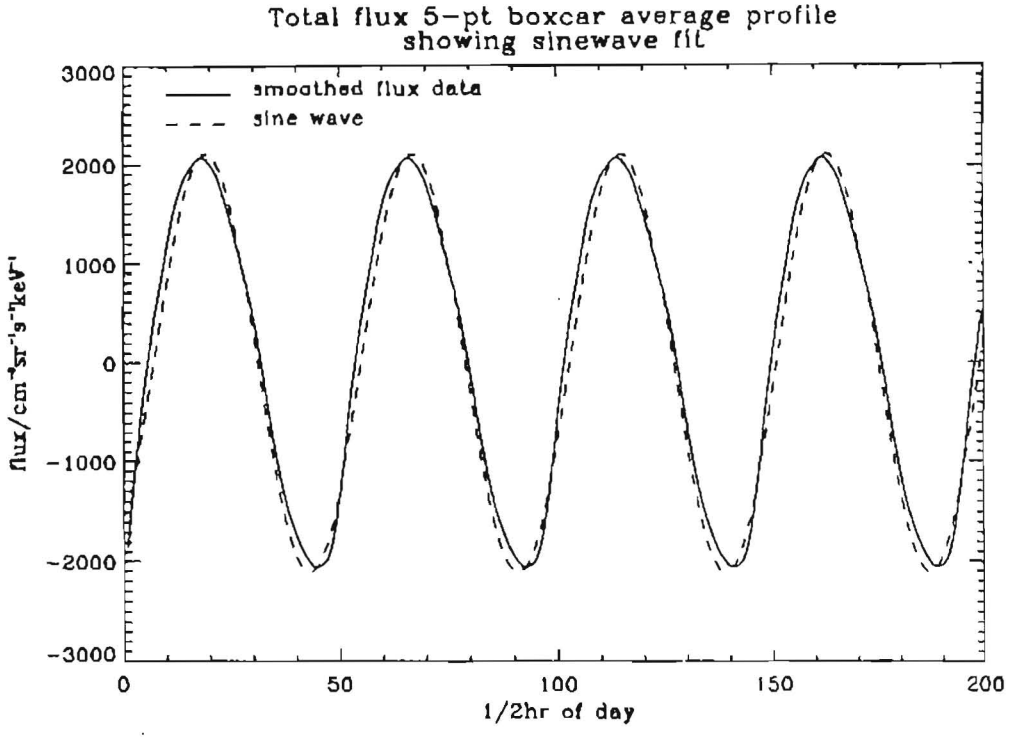

Figure 7.20. Quasi-sinusoidal diurnal flux variation

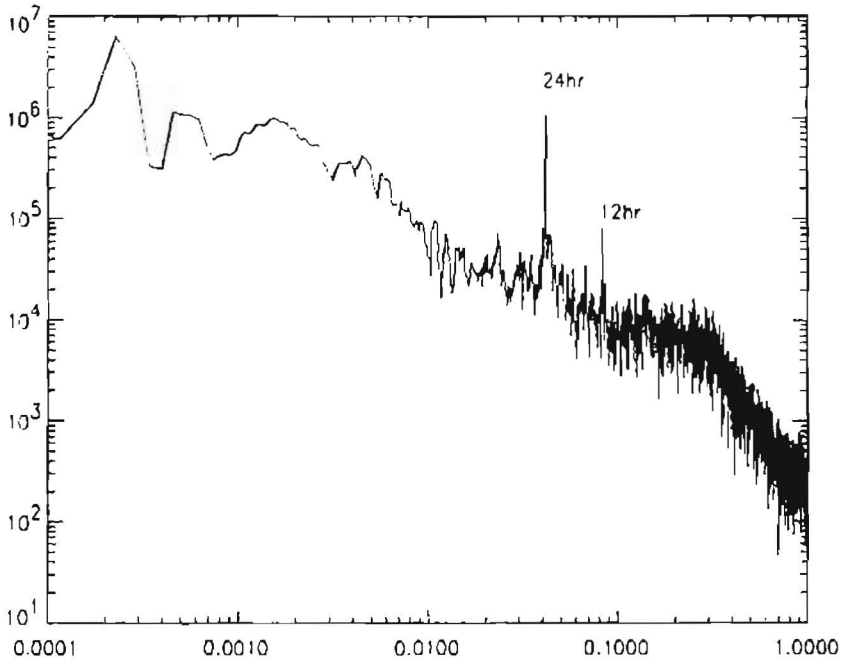

Figure 7.21. Frequency spectrum of 1990 total flux (42.9–300 keV) 30-minute averages, smoothed with a 15-point boxcar average (power vs. frequency)

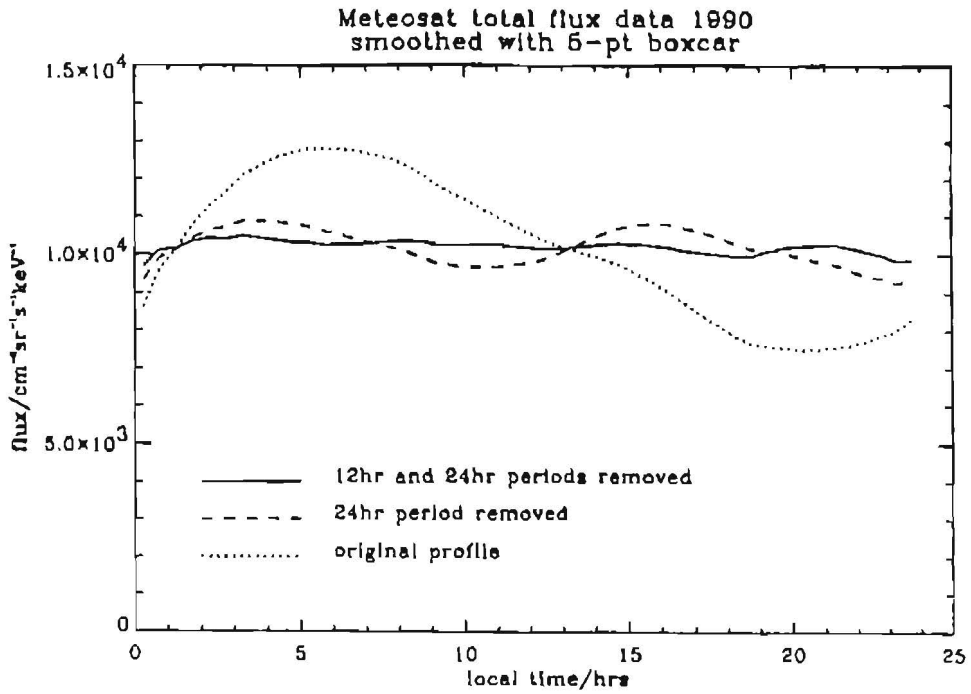

Figure 7.22. Removal of 12 and 24 hour period sinewaves

7.4.2 Fourier transform of total flux data

The frequency spectrum of one year (1990) of low resolution total flux data is shown in Fig. 7.21. For this plot the data has been smoothed with a 15-point boxcar average, which makes the spectrum look a lot less noisy.

There is a strong peak at a frequency corresponding to a 24 hour period and a smaller significant peak at 12 hours. A broad peak which has its maximum at around 27 days (approximate period of solar rotation) is also identified. This spectrum has three regions of different gradients. The first follows a gentle slope down to where the 12 hour peak occurs, the second is roughly horizontal up to approximately 0.34 hours^{-1} (equivalent to a period of about 3 hours), and the third follows a steep gradient downwards.

Figure 7.22 shows average total flux versus local time (dotted line). The curves in this figure are averaged over local time and have been smoothed with a five-point boxcar. After removing the 24 hour period sinewave found in the Fourier analysis the average is then shown by the dashed line: there is still periodic behaviour. Having removed the 12 hour period as well, the average becomes a reasonably flat line (solid line). This shows that the average diurnal variation can be approximated fairly well by the combination of the two sinewaves.

Figure 7.23 shows the 24 hour period sinewave (dotted line) and 12 hour period

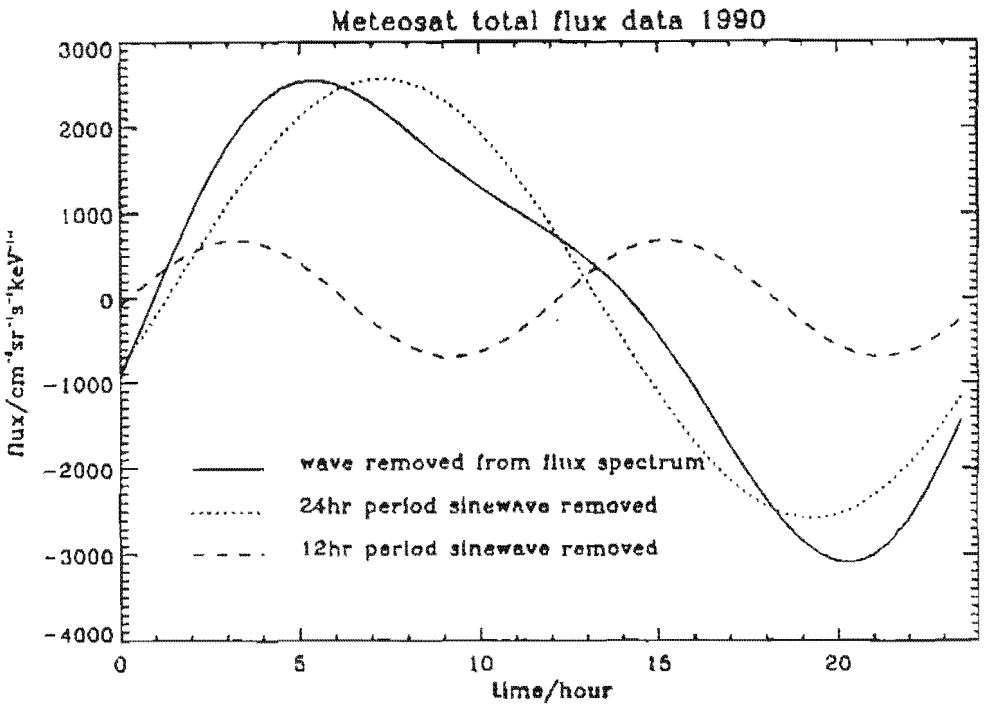

Figure 7.23. Profile of combined 24 hour and 12 hour periods

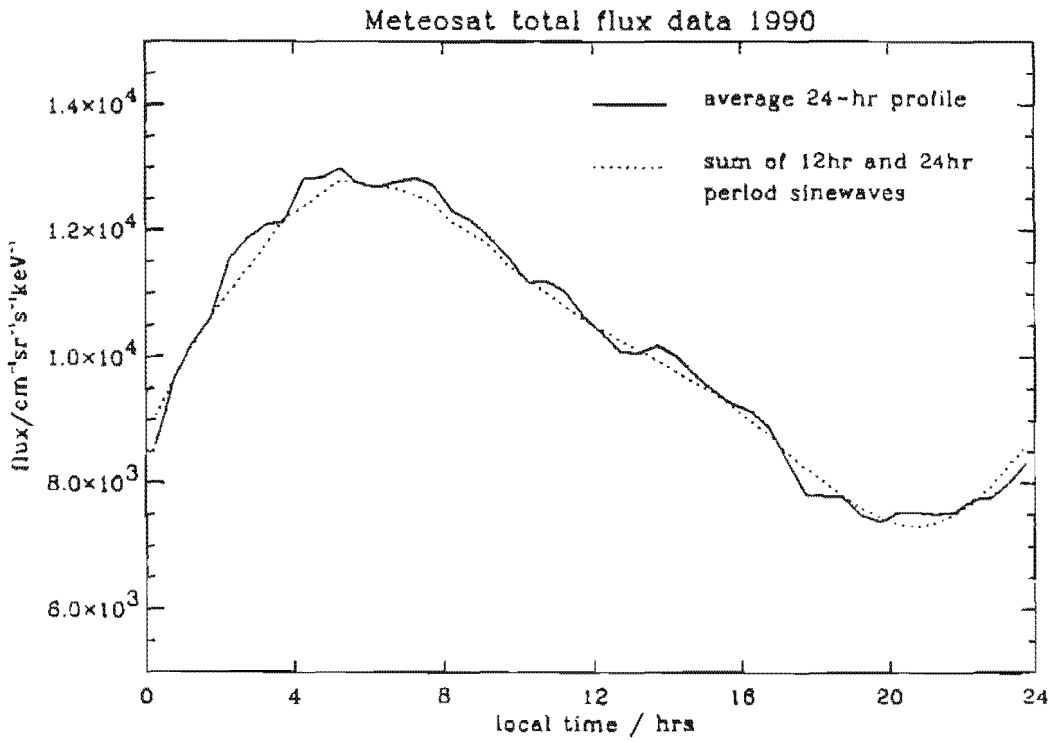

Figure 7.24. Fitting combined 24 hour and 12 hour sines to average flux spectrum

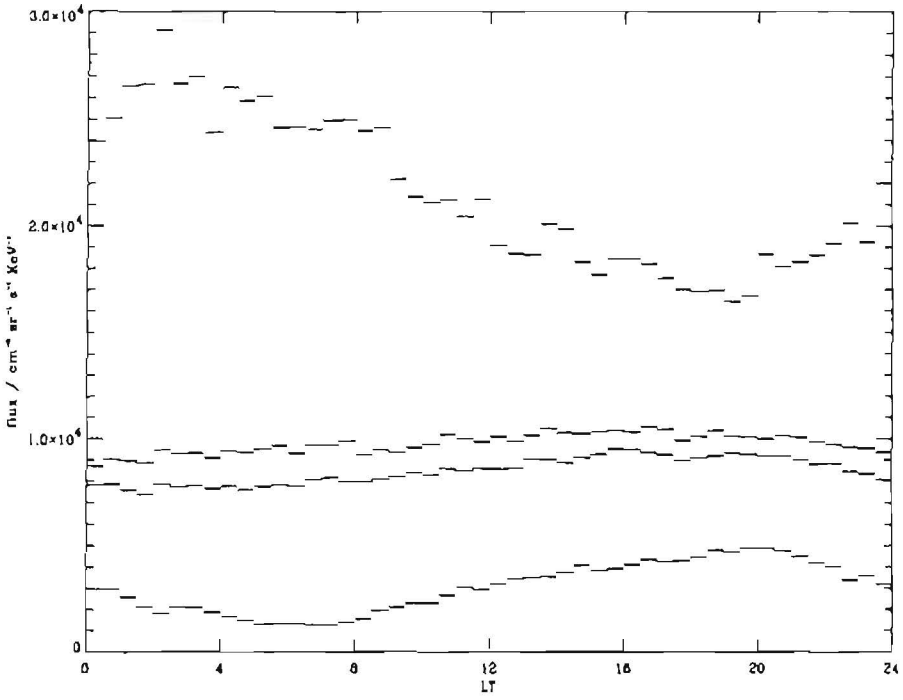

Figure 7.25. Total flux versus local time, 24 and 12 hour period sine waves removed

sine wave (dashed line) at their correct phases and amplitudes in the local time plot as found from the Fourier analysis. Combining these waves at their given phases and amplitudes results in the solid line.

How well this composite trace fits the actual flux spectrum is shown by Fig. 7.24. The sum of the 24 hour and 12 hour period sine waves, shown by the dotted line, is a good approximation to the shape of the average total flux spectrum, which is shown, unsmoothed, by the solid line.

The 12-hour period wave arises because the local time behaviour is not rigidly sinusoidal. Any periodic wave form can be represented by its fundamental frequency plus its harmonics. In this case, the sum of the fundamental frequency plus the first harmonic only was sufficient.

After Fourier filtering the data in this manner the same type of statistical plot as Fig. 7.4 was performed. This is shown in Fig. 7.25. Although the average of the filtered year's data is flat, the limits of this plot show that a local time dependence still exists in the variability of fluxes. There is still greatest variability in the early morning, and least variability in the afternoon, and the upper and lower limits have been brought into antiphase. The median flux is now largest in the afternoon rather than the morning hours as in the original data (see Fig. 7.4). It therefore appears that although the underlying average diurnal variation has been removed, there is

still the influence of injection events in the filtered data.

7.4.3 Fourier transforms of individual energy ranges

Figure 7.26 shows the frequency spectrum for the E5−E4 flux (42.9–59.4 keV), SEM-2's lowest energy range. The 24 hour and 12 hour peaks are clearly seen and have a similar ratio as the same peaks in the total flux frequency spectrum. This spectrum is close in shape to the spectrum for total flux. There is a slight difference in that whereas the total flux spectrum seemed to slope gently down to a plateau region starting at 0.34 hours^{-1}, the transition between these two sections of the E5−E4 flux spectrum is smoother.

The E1 flux spectrum (201.8–300 keV) (Fig. 7.27) exhibits several differences from both the total flux and the E5−E4 flux spectra. There is no obvious peak at 12 hours, though the 24 hour period peak is strong. The shape of the overall spectrum is also different. Whereas the total flux frequency spectrum appeared to comprise three sections of different gradients (see previous section and Fig. 7.21), the E1 flux spectrum appears to have a reasonably constant slope until, as for Figs. 7.21 and 7.26, it turns sharply down at around 0.34 hours^{-1}.

7.5 Wavelet analysis

Wavelet analysis is a relatively new technique which allows the frequency decomposition of a signal whilst keeping temporal localization. It does this by using a wave packet or *wavelet* which is non-zero for only a finite time interval. This means that wavelet analysis can locate transient frequencies in a signal which might not be detected with Fourier analysis.

Wavelets are sets of functions of the form:

$$\Psi_{a,b}(x) = |a|^{-1/2}\,\Psi\left(\frac{x-b}{a}\right), \tag{7.1}$$

where a is a dilation parameter which dilates or contracts the wavelet Ψ, and b is a translation parameter which shifts the wavelet along the time axis. Figure 7.28 shows the Morlet wavelet which was used for this analysis.

The data used for this analysis is the low resolution unsmoothed flux data. The wavelet plots shown in Fig. 7.29 each comprise two panels: the upper panel shows the original signal (flux versus time), and the lower panel shows the modulus of the wavelet transform as a colour scale plot. The vertical axis here is linear in period, and the horizontal axis is the same linear time axis as for the signal plot in the upper panel.

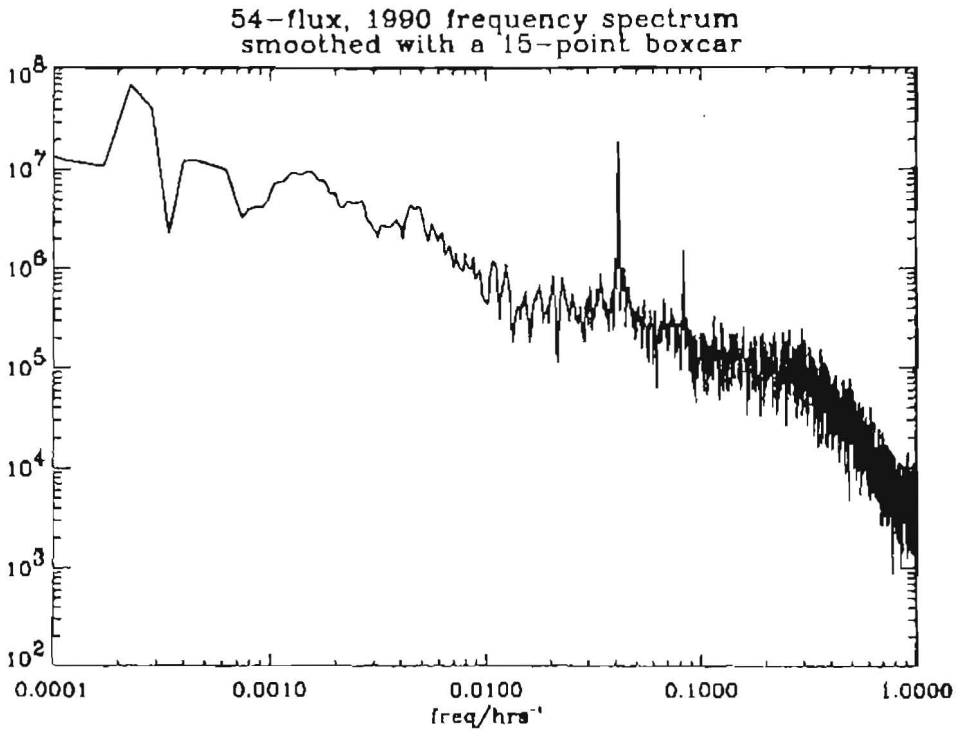

Figure 7.26. 1990 E5–E4 flux frequency spectrum

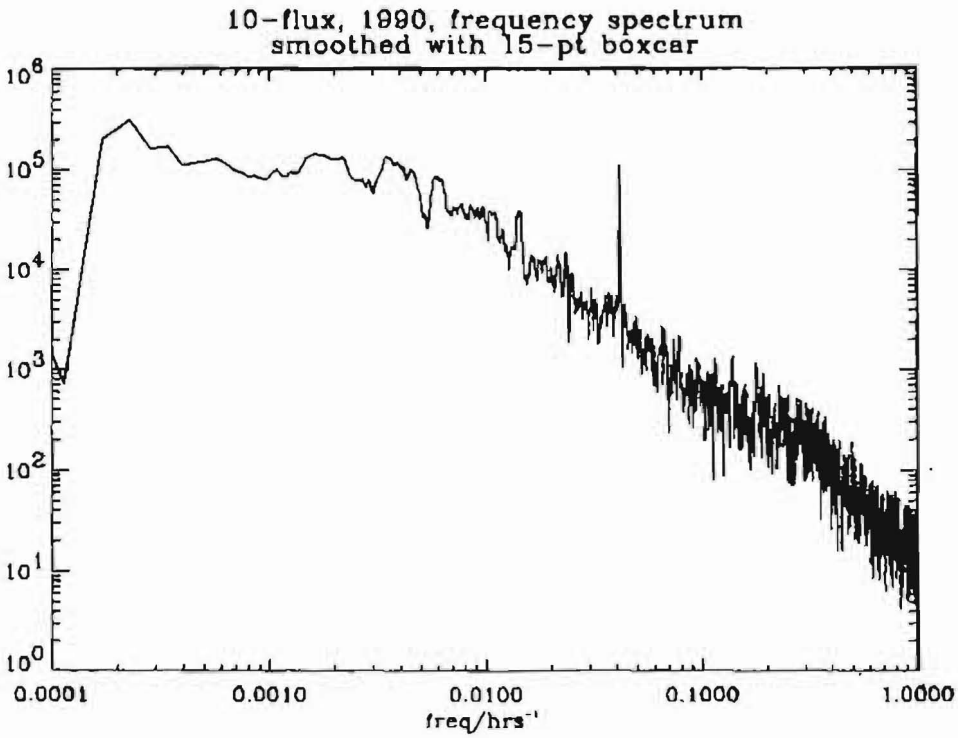

Figure 7.27. 1990 E1 flux frequency spectrum

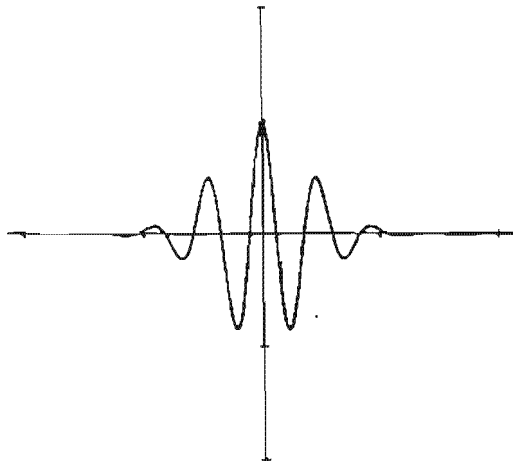

Figure 7.28. Morlet wavelet

Figure 7.29 (top) shows a sample of total flux (42.9–300 keV) data from 1990 with its wavelet transform. 58 days of data are shown. The diurnal variation dominates the colour plot, and is more noticeable in intervals of higher flux. It is apparent however that the local time behaviour is not precisely periodic. Figure 7.30 summarises the information in the three wavelet plots: each curve represents one wavelet colour plot, showing the sum of the moduli of the wavelet transform for each period. The solid line shows the sum of the moduli for the top wavelet plot. A dominant peak is seen at 24 hours.

Figure 7.29 (middle) shows the same time interval of flux data as the top plot, but here the year (1990) of data was Fourier filtered as described in Sect. 7.4 (i.e. 24 and 12 hour period frequencies removed). It is obvious from the colour plot that removal of an average diurnal variation for a whole year's data is not adequate to take local time dependence out of the data altogether. The dotted line in Fig. 7.30 shows that the 24 hour period is still significant, but is no longer as dominant as before.

It seemed necessary to act further to remove the local time dependence so that injection event signatures could be located irrespective of local time. This was achieved by "stretching" the data: from Fig. 7.25, for each 30-minute local time bin, two factors were calculated. The first factor was that needed bring the uppermost curve in Fig. 7.25 to a constant level, that of the maximum point. The second factor was that needed to bring the lower curve down to the level of the minimum point. Every data point in each particular time bin which fell above the median was multiplied by the first factor, and those below the median multiplied by the second factor. Repeating the same statistical plot with this modified data set gave four reasonably flat curves. Figure 7.29 (bottom) shows a wavelet transform of the same section of data as the middle plot, but with this further modification of "stretching"

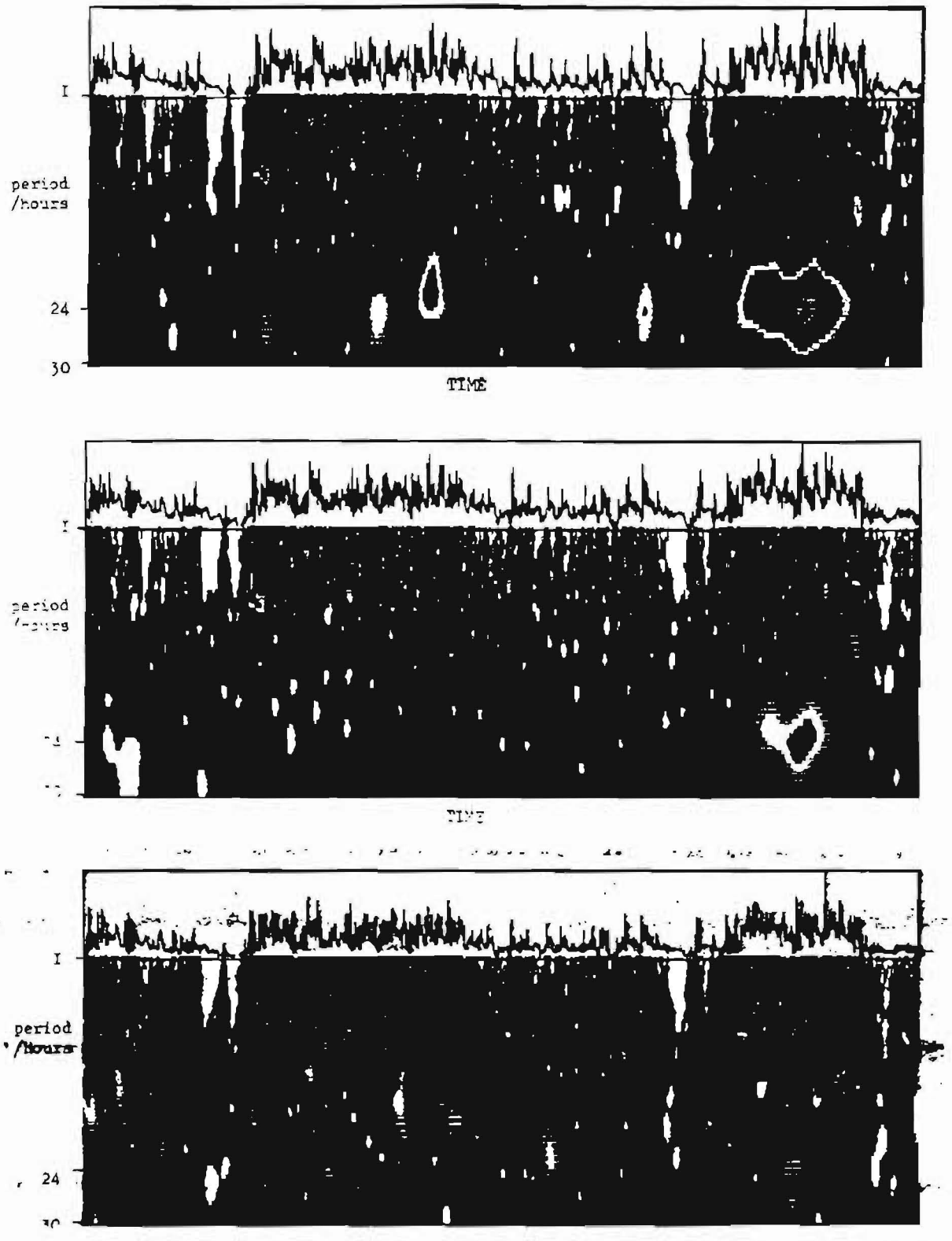

Figure 7.29. Wavelet plots: raw data (top), Fourier filtered data (middle), "stretched" data (bottom)

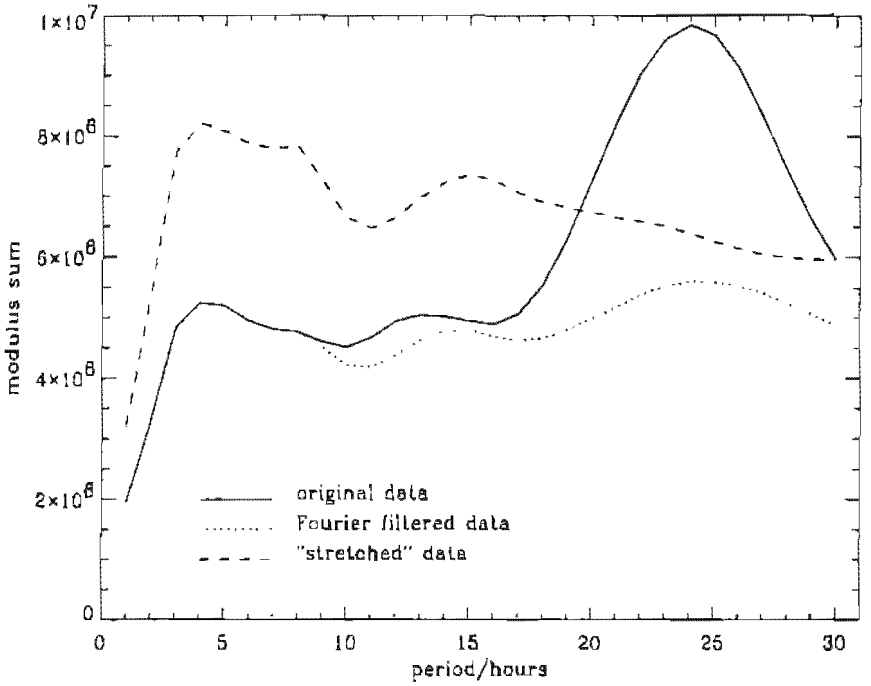

Figure 7.30. Modulus of wavelet transform summed across each period for the same sample of data in three stages of analysis

the data to remove the local time dependence. Here the shorter period transient waveforms are made more visible because the diurnal variation has been diminished.

The dashed line in Fig. 7.30 shows the modulus sum for this wavelet plot: the lower periods are now enhanced and the local time dependence has been effectively removed. There is a steep rise in the modulus sum up to the 3 hour point, followed by a maximum at 4 hours. This seems to imply a minimum separation time between injection events of 3 hours and a most common separation of 4 hours. However, since the choice of wavelet may influence the result, investigations are continuing with other wavelets: it is hoped that using a wavelet which more closely resembles the typical shape of a flux injection event would yield more accurate results.

7.6 Flux probability

The object of this analysis was to work towards establishing limits on the radiation dose that would be encountered by a spacecraft in geostationary orbit during a given mission lifetime. This is important to spacecraft design: for example, whether radiation hard components are necessary for a mission with a short lifetime.

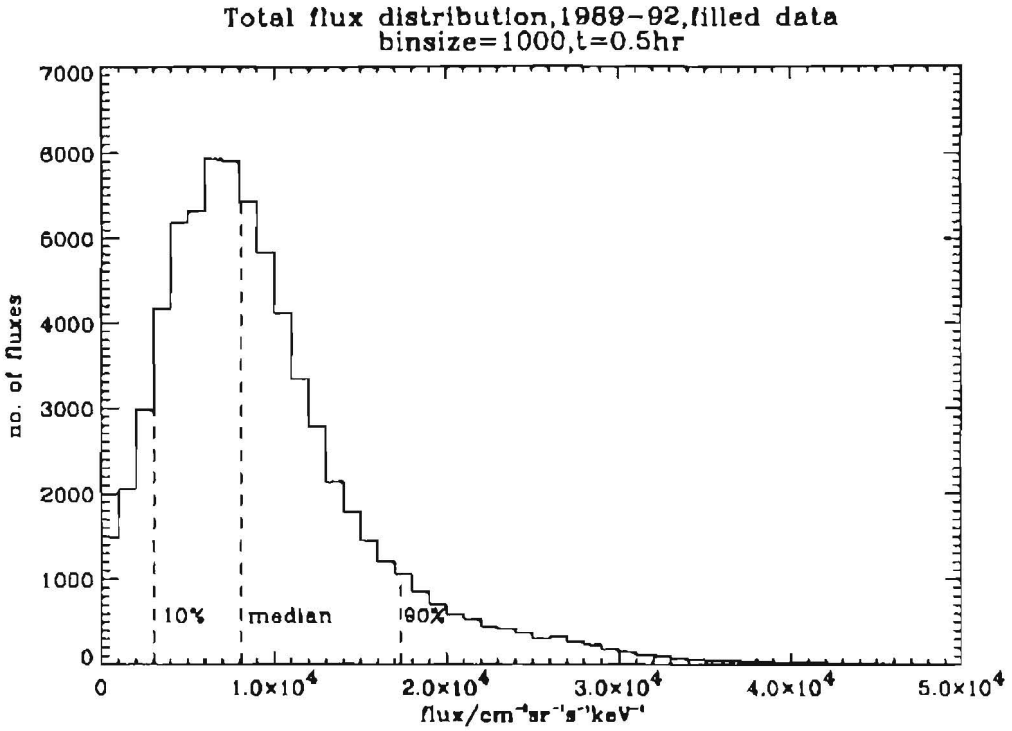

Figure 7.31. Histogram of 30-minute averaged total fluxes

7.6.1 Flux histograms

Figure 7.31 shows the distribution of low resolution total flux measurements (30-minute averages) over five years (1989–1993 inclusive). The bin size is 1000 $cm^{-2}sr^{-1}s^{-1}keV^{-1}$. The data used included small gaps filled by linear interpolation, but one larger (two month) gap was excluded altogether. The position of the median flux is marked on the histogram. Also marked are the lines above and below which 90% of flux measurements occurred.

Figure 7.32 shows similar histograms which were produced using averaged fluxes for longer time periods. Each two consecutive low resolution fluxes were averaged to give a time series of hourly averages. The time bin size was doubled repeatedly up to 16384 hours, which is nearly 2 years. Keeping the histogram flux bin size to 1000 $cm^{-2}sr^{-1}s^{-1}keV^{-1}$, the distribution narrows as the length of the time bins increases. The median flux and two flux limits, as illustrated in Fig. 7.31, were found for each distribution.

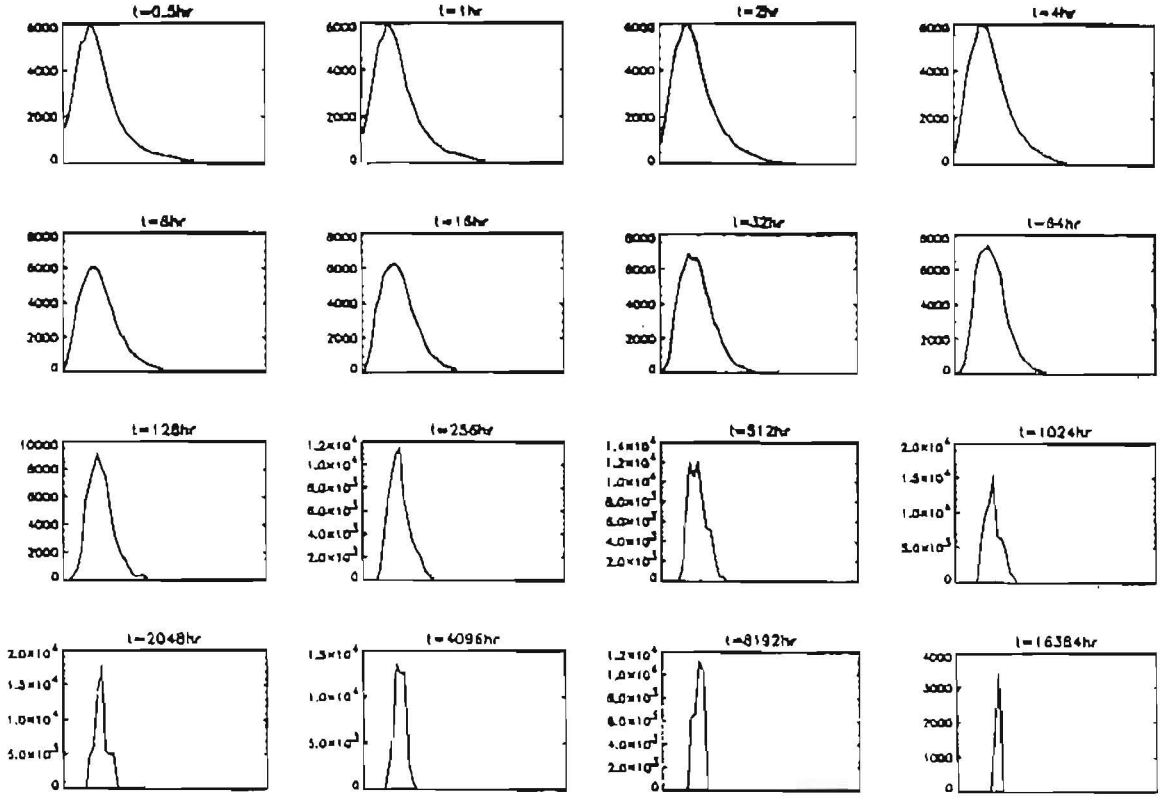

Figure 7.32. Histograms of total fluxes with increasing time bins

7.6.2 Flux vs. duration time model

The flux histogram analysis was carried out for each of the SEM-2's differential energy ranges. The results have been organised into an energy dependent model of fluxes at geostationary orbit. Table 7.4 lists our calculated limit values of average flux (the median and the levels above and below which 90% of fluxes occur) for each of the SEM-2's energy ranges, for each accumulated time period from 1 hour doubled repeatedly up to 16384 hours.

Using the medians, 10% and 90% values from these data, further plots were constructed, shown in Fig. 7.33. These are graphs of the averaged flux points obtained from the histogram analysis versus the logarithm of the time binsize in hours. The solid lines on the plot are the median flux and the 90% limit lines. All the lines converge towards the average flux as time bin size increases. The range between the median flux and the upper 90% level is in general larger than the range between the median and the lower 90% level. The large range of the average fluxes at short time bin values diminishes as the time period increases. This implies that the longer a period of time considered, the more certainly can be predicted the total flux encountered.

Table 7.4. A probability model of fluxes at geostationary orbit. Fluxes are in $cm^{-2}sr^{-1}$ $s^{-1}keV^{-1}$. For each energy band three limits are given: the level above which 90% of fluxes are observed (the 10% column), the median, and the level below which 90% of fluxes are observed (the 90% column).

Time	42.9–300 keV			42.9–59.4 keV			59.4–90.7 keV		
/hr	10%	Median	90%	10%	Median	90%	10%	Median	90%
1	2982	8027	16916	12472	27724	66123	7761	20290	48755
2	3168	8161	16661	13239	28627	64173	8215	20840	47859
4	3377	8314	16330	14123	29547	61690	8840	21483	46549
8	3648	8467	15694	15344	30742	57935	9553	22210	44443
16	3977	8678	15034	16820	32365	53176	10511	23223	41959
32	4371	8789	14546	18509	33093	50752	11643	23683	40404
64	4830	8848	14090	20111	33173	49027	12896	23904	38905
128	5440	8914	13294	22525	33381	46658	14936	24195	36637
256	6078	9025	12638	24643	33366	44559	16468	24318	34934
512	6694	9108	12066	25930	34056	42366	17867	24748	33334
1024	6862	9183	11815	26198	34281	41801	18184	25260	32595
2048	6964	9116	11532	26617	34210	40756	18515	25191	31762
4096	7373	9125	10715	28439	34492	38612	19861	25415	29383
8192	7973	9019	10281	31063	33195	36905	22019	24389	28053
16384	8283	8572	10175	31000	32941	36583	22390	23614	27761

Time	90.7–134.9 keV			134–201.8 keV			201.8–300 keV		
/hr	10%	Median	90%	10%	Median	90%	10%	Median	90%
1	2776	8856	19558	801	3704	8033	409	2229	6055
2	2959	9018	19500	869	3737	8000	431	2234	6024
4	3206	9209	19136	968	3782	7912	469	2251	5956
8	3525	9421	18534	1119	3831	7783	529	2287	5850
16	4013	9712	17813	1340	3908	7526	622	2349	5674
32	4460	9870	17179	1564	3937	7224	739	2403	5451
64	5065	9973	16483	1855	4028	6866	904	2505	5130
128	5873	10118	15534	2194	4075	6439	1132	2587	4708
256	6582	10149	14768	2599	4145	6112	1512	2702	4370
512	7357	10309	14179	2873	4191	5744	1753	2794	3848
1024	7493	10376	13824	3013	4238	5589	1882	2765	3674
2048	7660	10339	13459	3002	4314	5547	1948	2803	3584
4096	8092	10312	12400	3337	4433	5091	2040	2821	3353
8192	8862	10188	11877	3934	4500	4859	2066	2912	3165
16384	9258	9625	11757	3784	4691	4898	2475	2563	3138

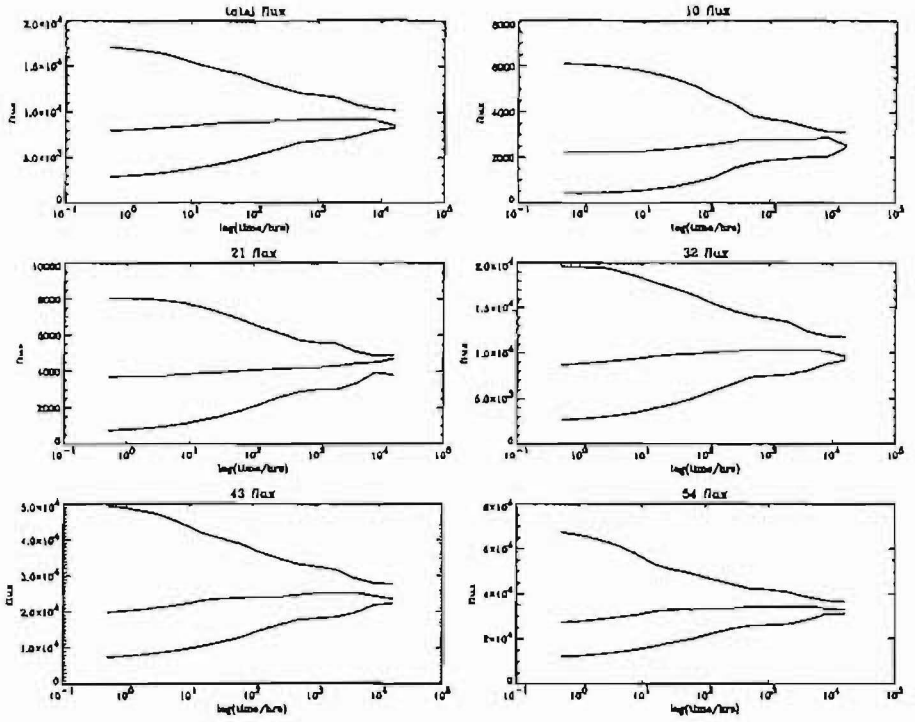

Figure 7.33. Average fluxes versus accumulation time: 90% of observations occur below upper line, middle line shows median of observations, and 90% of observations occur above lower line

These graphs show that the range of average fluxes observed decreases for increased accumulation times, the limits of the range converging towards the mean flux. The implications for spacecraft design are that absorbed dose, which depends on a material's properties and on fluence (flux integrated over time), may deviate substantially from an average value during short missions, whereas the absorbed dose during a long mission can be more safely predicted. At the longest time bin sizes the curves become less smooth which is due to smaller numbers of data points being available for longer accumulation periods.

The data used to construct Fig. 7.32 is given in Table 7.4.

A model program has been written to supply the expected average flux for a given time duration. The routine is written both in IDL and in VAX Fortran and uses a look-up table of the results from the analysis.

The flux energy range and time duration are the input parameters to the model. All SEM-2's energy ranges can be used. The program uses a look-up results table of fluxes, performing linear interpolation between points to read off the values corresponding to the input duration time. Output parameters are the median flux, and the fluxes above and below which 90% of fluxes occur. Results are output to a

document file.

Although it was hoped that using a large data set to produce this model would improve the statistics, the solar cycle becomes an important issue. Either using data for a whole solar cycle or else treating solar maximum and minimum separately would produce a more generally useful model.

7.7 Correlation analysis

7.7.1 Energization, radial diffusion and recirculation

The energy range of SEM-2 covers a transition region. The electrons in the lower energy levels starting at 42.9 keV are part of the ambient thermal electron population of the ring current region. These have typical temperatures of 5 to 20 keV, make up the bulk of the electron density and play a key role in the bulk plasma dynamics of the magnetosphere, including substorm injection events. At the higher energy ranges, up to 300 keV, the electrons are part of a longer-lived population of much lower density, commonly called the radiation belts. Although the total density of this population is small, it is the cause of SEU interactions that are so damaging to spacecraft. It is natural to presume that the high energy electrons are somehow produced from the plentiful low energy population, but the mechanism for this is not clear.

During a substorm, the reconfiguration of the magnetic field causes electrons in the geosynchronous region to be moved earthwards, resulting in a decrease in the fluxes of these electrons at geosynchronous orbit. This process causes adiabatic energization of the transported electron population because it takes them to regions of higher field strength, while requiring conservation of the first adiabatic invariant. The heated electrons are subject to wave-particle interactions that cause radial-diffusion, i.e. movement to higher or lower L shells depending on the density gradient. This can result in electrons returning to the geosynchronous environment from the lower altitude population. This process also conserves the first adiabatic invariant and so the energy the electrons gained during the field reconfiguration is lost in this process. Recently, Fujimoto and Nishida (1990) have proposed a form of radial diffusion that does not conserve the first adiabatic invariant. In their process, radial diffusion takes place at low altitude, near the magnetic poles. In this region, particles moving to higher L shells do not experience a significant change in magnetic field strength and so they are able to keep almost all of their energy. One effect of this diffusion is to leave the electrons more field aligned than before, but pitch angle diffusion eventually occurs to make the distribution more isotropic without significantly changing the electron energies. In situations of continuous substorm activity, the same electrons may be subject to repeated inward movement, energization and

outward diffusion (a process called "recirculation"), leading to a pumping up of the electron energy in the outer radiation belt. Monte Carlo simulations (Fujimoto & Nishida 1990) have shown that the outer radiation belt is enhanced a few days after the enhancement at lower L values.

7.7.2 Correlation plots

In the SEM-2 data we have examined this hypothesis by comparing electrons in the top and bottom energy channels of the instrument. The lower energy electrons should reflect substorm activity, and the upper energy electrons the radiation belt. Figure 7.34 shows log daily fluxes of electrons between 42.9 and 59.4 keV (upper trace) and between 201.8 and 300 keV (lower trace). There are sufficient peaks and troughs in common to suggest some connection between the data sets. A correlation was performed between these two energy channels for the entire 4 years of data. The results are shown in Fig. 7.35. This figure plots the correlation coefficient versus a time lag that was introduced between the two data sets. There is a strong peak in this correlation coefficient when the high energy fluxes lag the low energy fluxes by 1 day. This time lag is consistent with the recirculation process.

Figure 7.36 show the correlation between K_p and the time-lagged fluxes in the 42.9–59.4 keV range. A peak extrapolated from this curve would be around 0.5 days, indicating that substorm plasma signatures are generally seen half a day after the rise in planetary magnetic activity. Figure 7.37 shows the correlation between K_p and fluxes between 201.8 and 300 keV. The electron fluxes lag 2 days behind K_p. Such a lag could be built into an empirical dynamical model of the radiation belts.

7.8 Superposed epoch analysis

Flux peaks observed in the low energy electrons (below 200 keV) are due to substorm *injection events*. These events occur during magnetic substorms (Fairfield 1992) when packets of hot electrons are produced around local midnight, probably around 7–10R_E from the Earth. These packets then drift round to the dawn side of the Earth.

The technique of superposed epoch analysis was used to examine the characteristics of the flux peaks observed during substorm injection events. In this section a flux peak was defined as having flux over 1.5×10^5 cm^{-2}sr^{-1}s^{-1}keV^{-1} in the energy range 43–60 keV, in a ten-minute time bin. The flux in the time bin had also to be higher than the flux in the preceding and following time bins, i.e. a peak. There are many flux peaks lower than this threshold flux but the level was set to restrict the number of events to a manageable level.

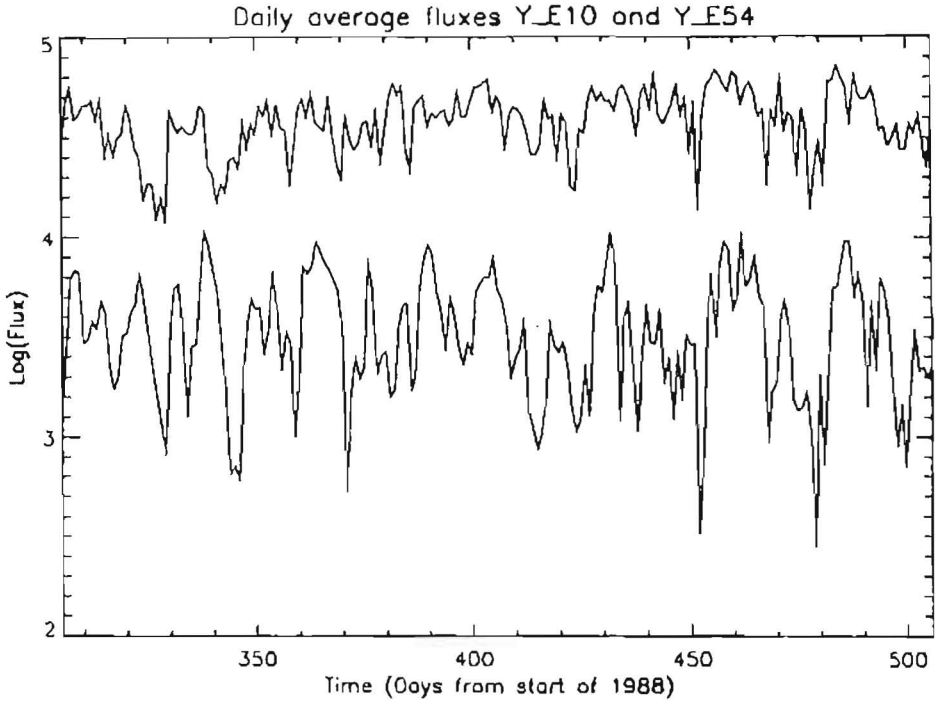

Figure 7.34. Log flux versus UT for 42.9–59.4 keV (upper trace) and 201.8–300 keV (lower trace)

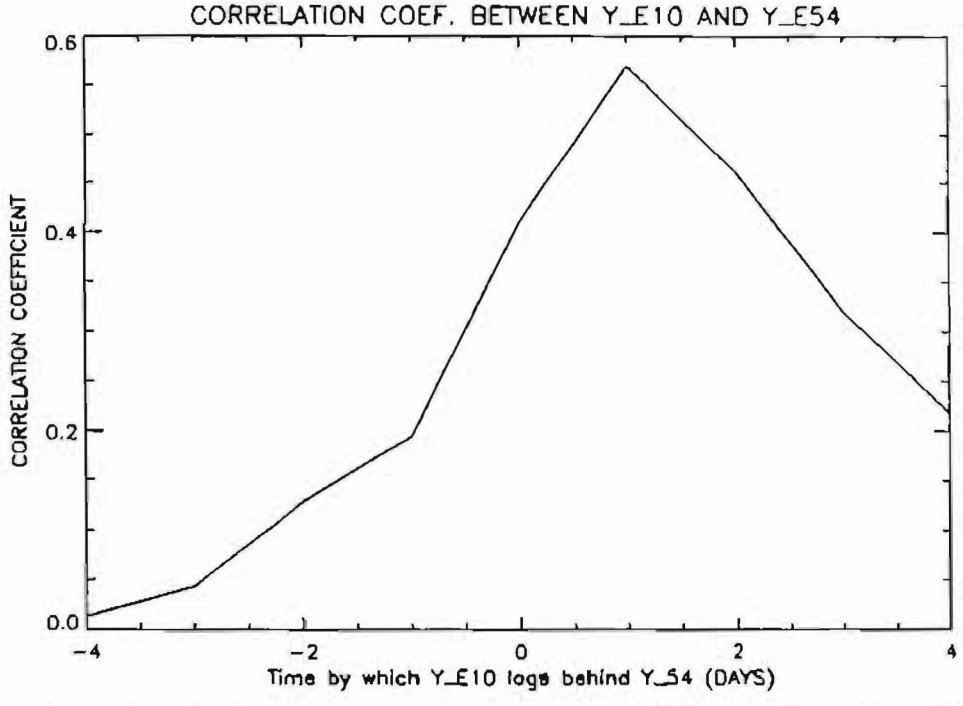

Figure 7.35. Correlation coefficient between 42.9–59.4 keV and 201.8–300 keV fluxes as a function of time lag

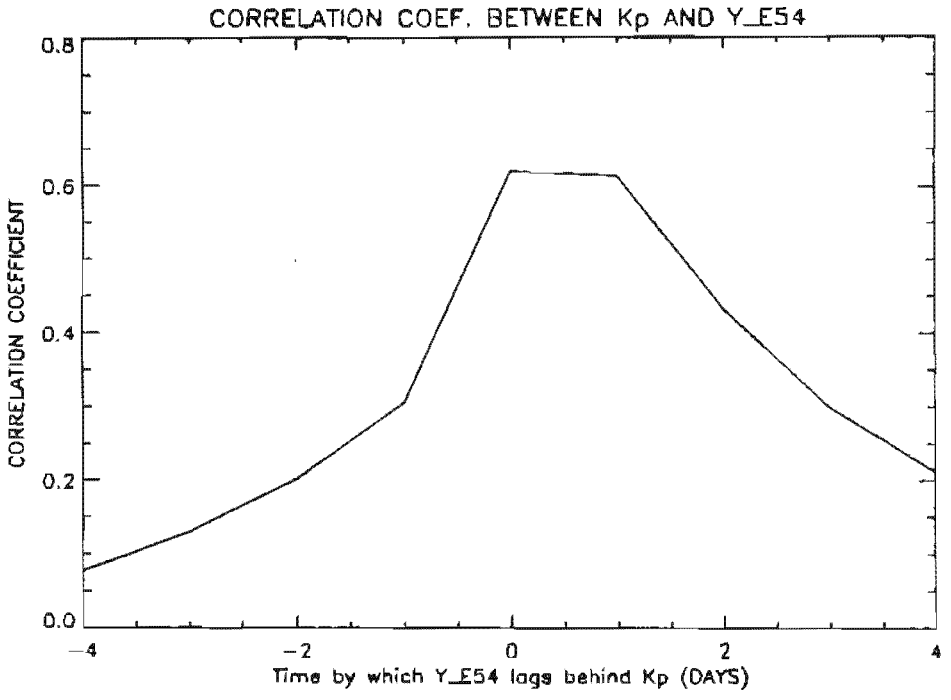

Figure 7.36. Correlation coefficient between K_p and 42.9–59.4 keV flux, as a function of time lag

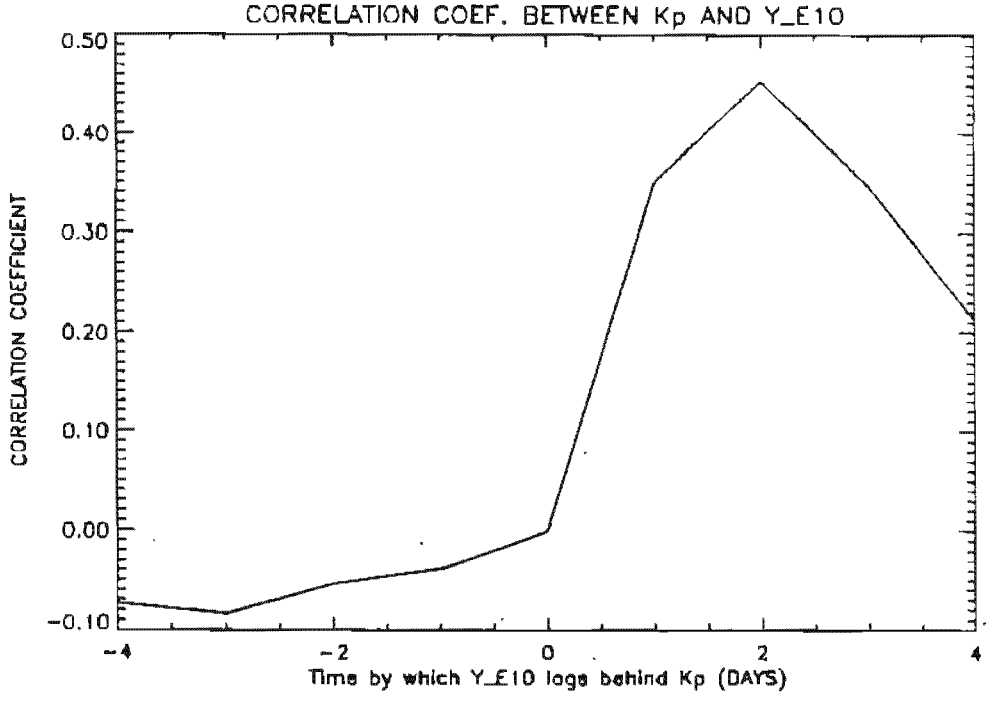

Figure 7.37. Correlation coefficient between K_p and 201.8–300 keV flux, as a function of time lag

Figure 7.38 shows the average flux in the lowest energy channel (43–60 keV) within the period ±12 hours around the peaks. The flux shows two strong features, a very sharp flux peak and a broad "hump" which reaches a maximum about 3 hours after the peak. This hump is not associated with the peak, as will be seen in later plots.

Figure 7.39 shows the average flux in all 5 energy levels, calculated for the first 200 peaks (to reduce processing time). The flux peak is very strong in the lowest energy channel and in the 60–91 keV channel. At higher energies the peak becomes weaker and there is no peak in the highest energy channel (201.8–300 keV).

Figure 7.40 is a composite figure showing flux in the low energy (43–60 keV) channel for all the peaks in 1989. The peaks were divided according to the local time at which they were detected. The traces are as follows:

- solid line: 2100–2400,
- dotted line: 0000–0300,
- dashed line: 0300–0600,
- dashed-dotted line: 0600–0900.

There were no sigificant numbers of peaks outside this range. It can be seen that the "hump" which followed the peak in Fig. 7.38, has a different position relative to the peak in each of these four traces. This is because the hump is staying in the same place in local time. It is simply the peak seen at 0500 in the local time analysis and is clearly not related to the flux peak. It can be seen that the width of the peak increases as local time moves from midnight round to the dawn side. If the drift rate of the event is assumed roughly constant, this indicates that the packet of injected plasma spreads out as it moves round the Earth.

Figures 7.41, 7.42, 7.43 and 7.44 show superposed epoch plots for the same four local time bins. Each figure, corresponding to a three-hour local time band shows all five energies. The time axis has been reduced to ±4 hours. In the 21–24 hour period (Fig. 7.41) the flux enhancement is seen simultaneously irrespective of energy. In the 0–3 hour period (Fig. 7.42), the flux peaks earlier in the 60–91 keV energy range than in the 43–60 keV range. This effect becomes more pronounced in the 0300–0600 period (Fig. 7.43) and 0600–0900 (Fig. 7.44) period. This energy dispersion occurs because the drift velocity of the electrons is energy dependent. A rough mathematical analysis of this effect follows.

Although $\boldsymbol{E} \times \boldsymbol{B}$ drift is important for magnetospheric electrons below 1 keV (Spjeldvik & Rothwell 1985), the main drift effects on electrons above 10 keV come

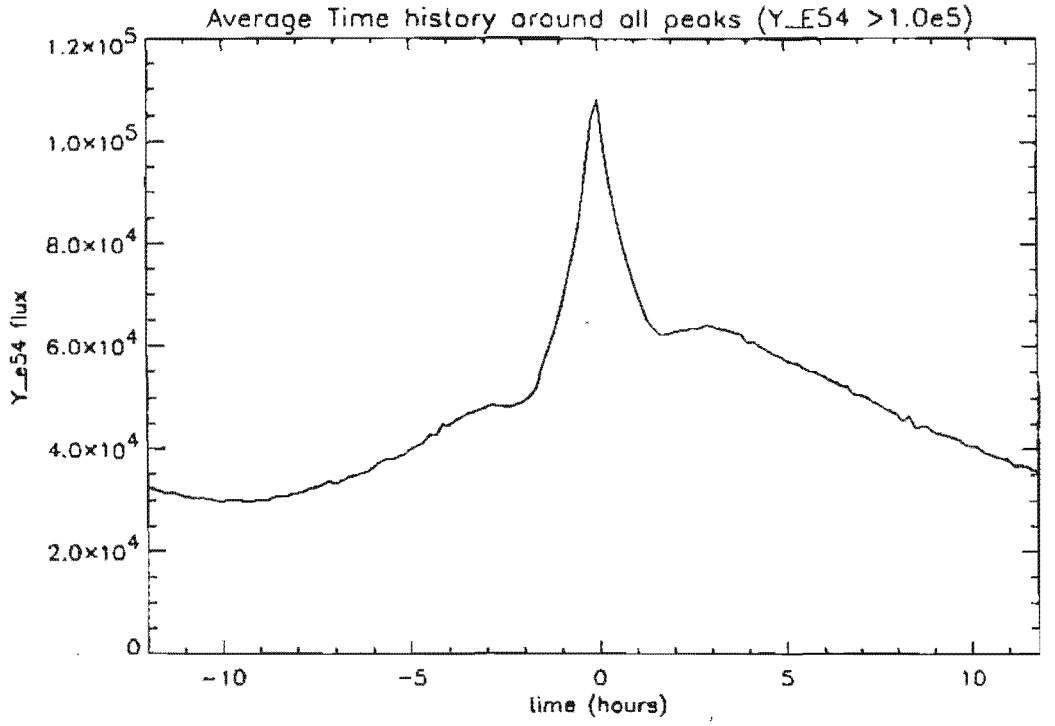

Figure 7.38. Average fluxes around peak for lowest energy channel

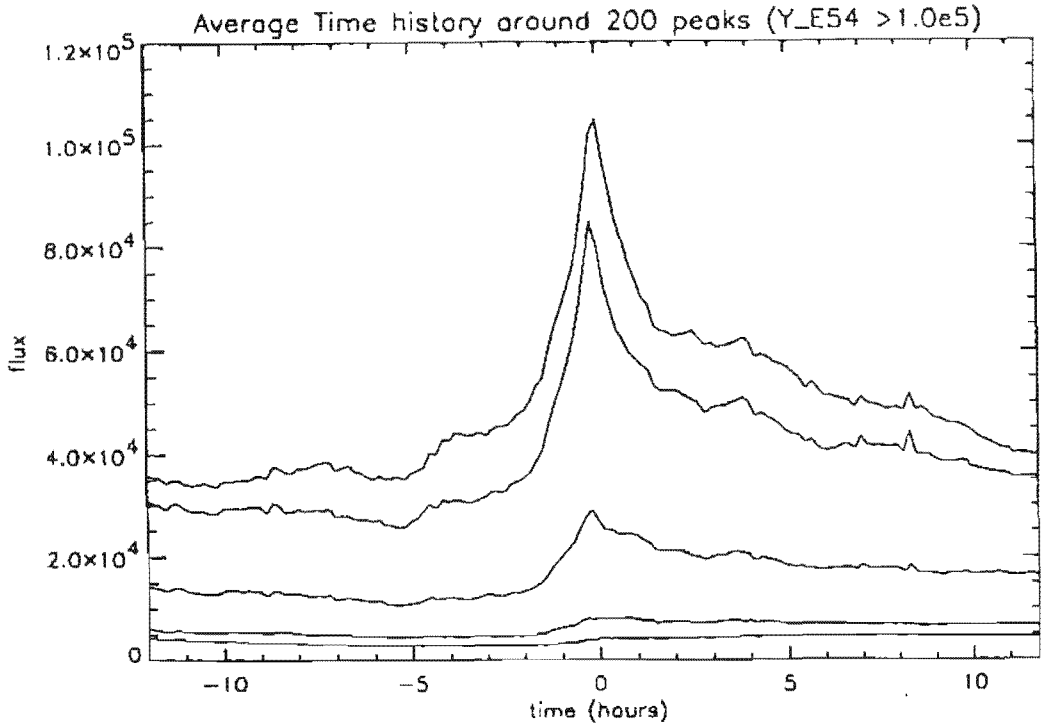

Figure 7.39. Average fluxes around peak for all energies. Lowest energy is at the top. Highest energy is at the bottom.

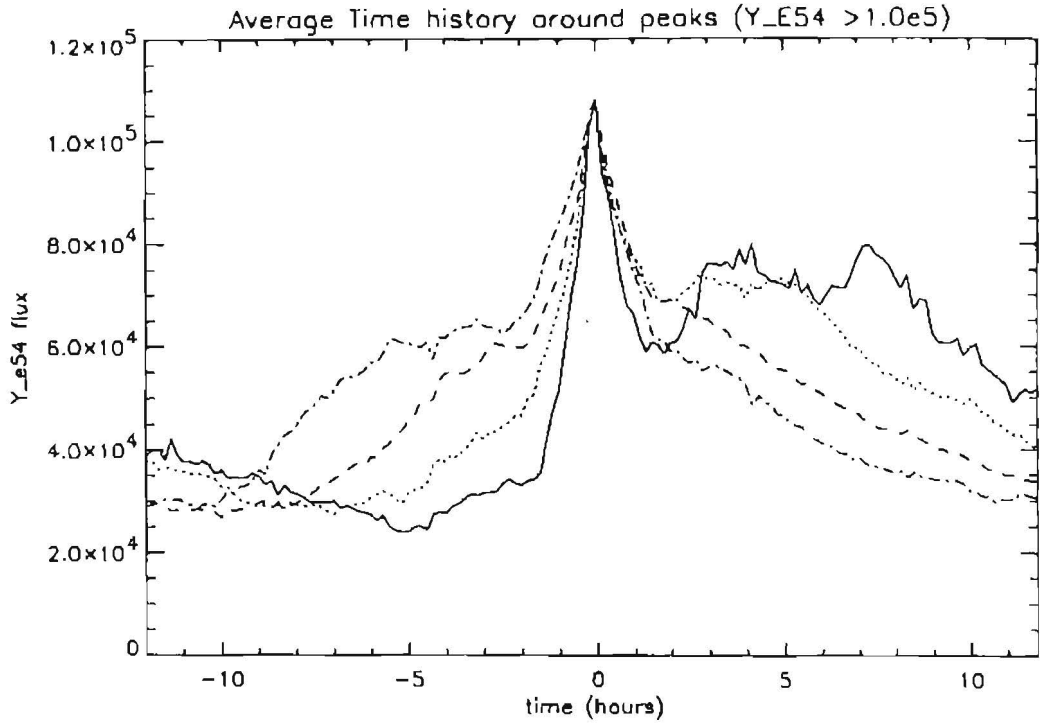

Figure 7.40. Average fluxes around peak for different local times (see text)

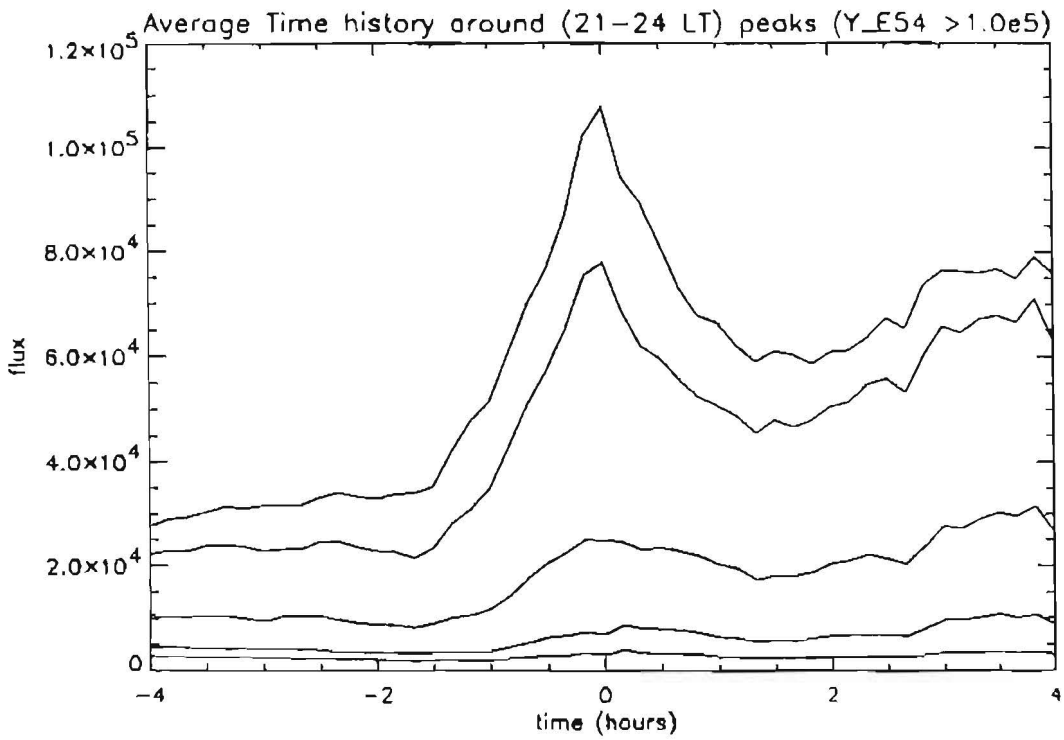

Figure 7.41. Average fluxes around peak for all energies in 2100–2400

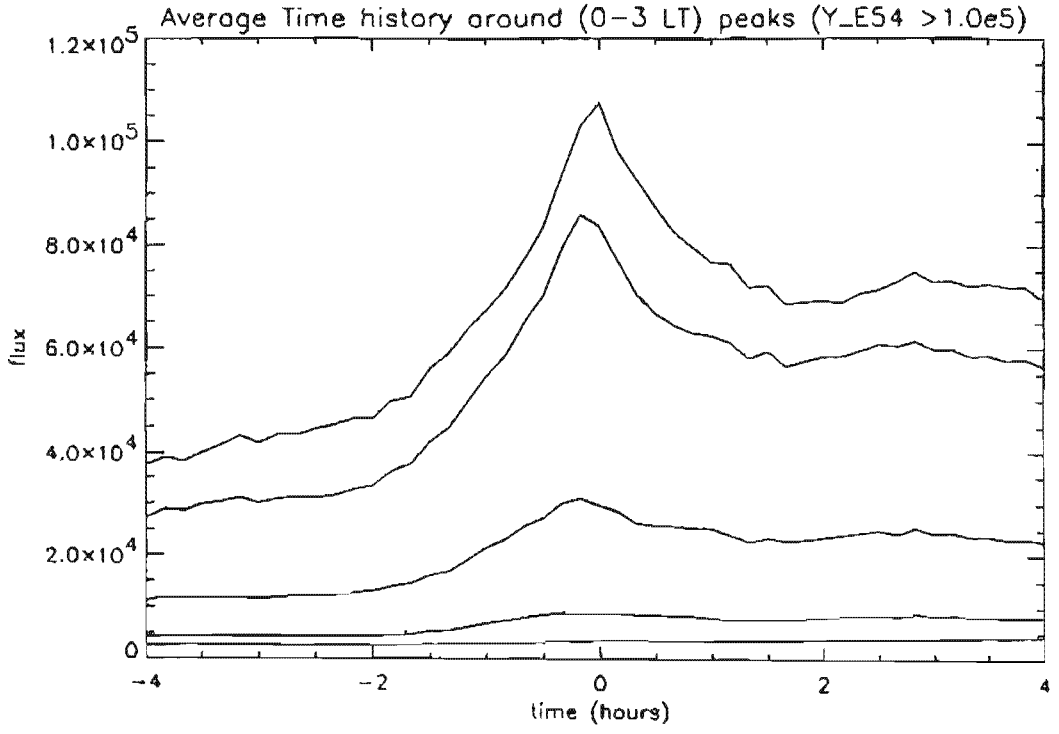

Figure 7.42. Average fluxes around peak for all energies in 0000–0300

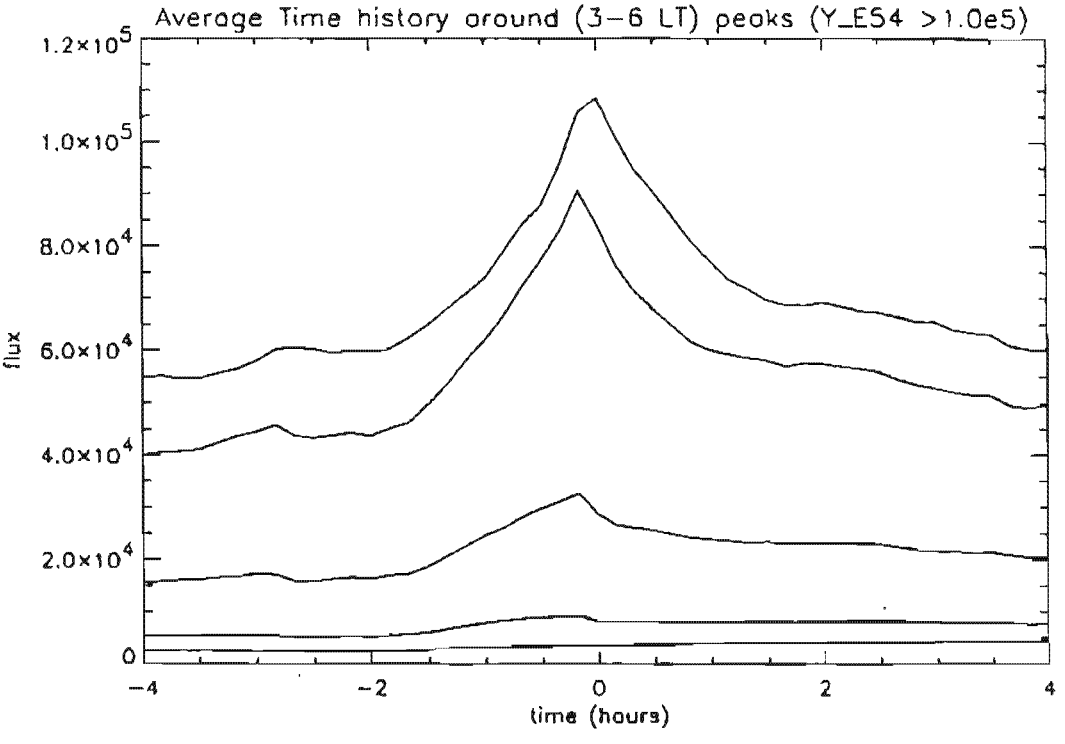

Figure 7.43. Average fluxes around peak for all energies in 0300–0600

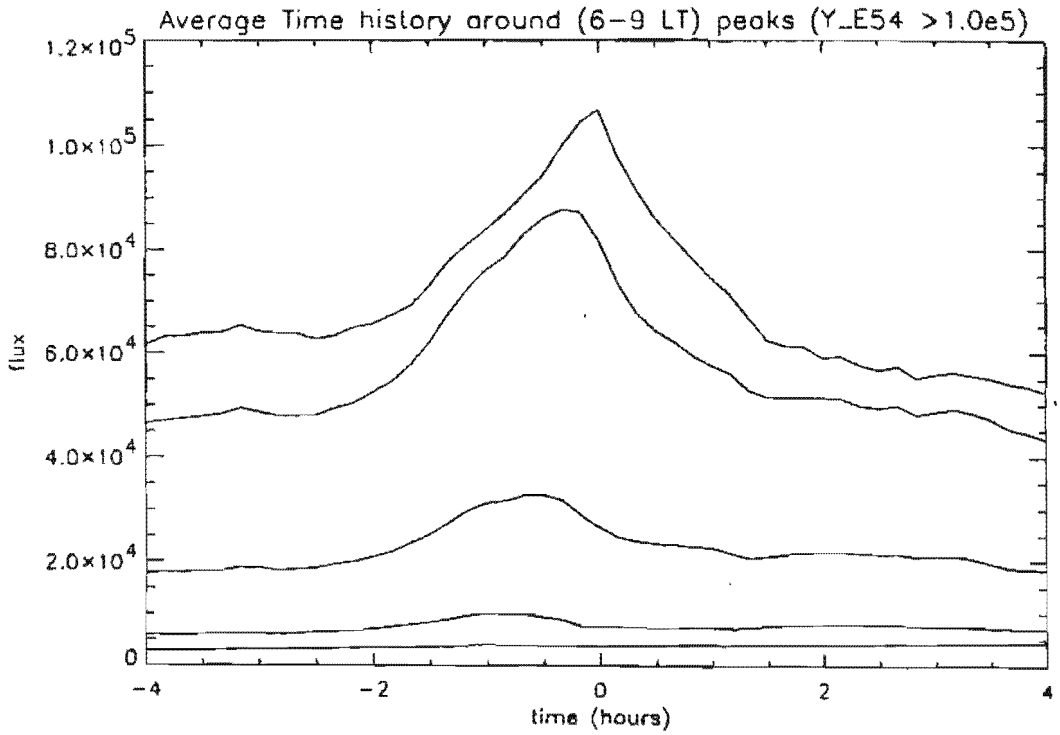

Figure 7.44. Average fluxes around peak for all energies in 0600–0900

Table 7.5. Calculated drift velocities

Energy	$v_{\parallel}$, $v_{\perp}$	Drift velocity
43 keV	$8.69 \times 10^7\,\mathrm{m\,s^{-1}}$	$30.5\,\mathrm{km\,s^{-1}}$
60 keV	$1.02 \times 10^8\,\mathrm{m\,s^{-1}}$	$42.1\,\mathrm{km\,s^{-1}}$
91 keV	$1.26 \times 10^8\,\mathrm{m\,s^{-1}}$	$64.1\,\mathrm{km\,s^{-1}}$

from gradient and curvature drift:

$$\text{drift velocity} = V_{R_c} + V_{\nabla B} = \frac{m}{q}\frac{1}{R_c B}\left(v_{\parallel}^2 + \frac{1}{2}v_{\perp}^2\right) . \tag{7.2}$$

Assuming the radius of curvature R_c to be $3.3\,R_E$ and the typical magnetic field $\boldsymbol{B}$ at geosynchronous orbit is 1×10^{-3} gauss, and assuming the electrons have equal parallel and perpendicular velocities, then the drift velocities at the three lowest energies are as given in Table 7.5.

If it is assumed that these velocities do not change, then we can calculate the distance from the satellite that the substorm originated, from the energy dispersion

Table 7.6. Calculation of distance from drift velocity

Local time	Channels	$t_b - t_a$	Distance
21–24	91–135 and 43–60	0 min	0–2.7 R_E
0–3	91–135 and 43–60	10 min	2.7–8.1 R_E
3–6	91–135 and 43–60	10 min	2.7–8.1 R_E
6–9	60–91 and 43–60	20 min	15–25 R_E

of the measured fluxes. For peaks measured at energy levels a and b:

$$d = v_a t_a = v_a v_b \frac{t_b - t_a}{v_b - v_a} . \tag{7.3}$$

Based on the different arrival time of peaks in Figs. 7.41 to 7.44, the distances are as given in Table 7.6: the limits on the distance are calculated knowing that the data has ten minute time resolution, so a given time ±5 minutes gives the possible range in distance.

The 10 minute time resolution of the data makes these numbers not particularly accurate but we can conclude that events seen at 2100–2400 are produced locally, those seen between 0000 and 0600 are produced in the near tail region, maybe between 7 and 12 R_E, and that those seen between 0600 and 0900 are produced further tailwards. A full trajectory analysis taking each event individually and using a model magnetic field would make a valuable future study.

7.9 Loss rate analysis

It was inferred from Sect. 7.2 that substorms provide the largest contribution of fluxes to the lower SEM-2 energy bins. In this section we examine how this flux could be lost. There are two factors likely to play a role in the loss of electrons from geostationary orbit. The first is pitch angle diffusion into the loss cones. Electrons injected into the "bounce" loss cone will be lost to the top of the atmosphere within a bounce period, just a few seconds. Electrons injected into the "drift" loss cone will not be lost until their drift trajectories encounter the South Atlantic Anomaly, a process taking up to a few hours. The second factor is radial diffusion, as discussed in Sect. 7.7. Because this is dependent on the square of the drift velocity (Spjeldvik & Rothwell 1985), it has a larger effect for higher energies. When electrons diffuse to large enough L values, they pass through the magnetopause and are lost.

Table 7.7. Pairs of days devoid of injection events

3+4	Jul 1989
11+12	Jul 1989
13+14	Oct 1989
2+3	Sep 1990
4+5	Nov 1990
5+6	Nov 1990
14+15	Nov 1990
10+11	Dec 1990
21+22	Dec 1990
6+7	Jan 1991
18+19	May 1991
19+20	May 1991

To examine loss rates it was desirable to find periods in which no renewed plasma injection was occurring. This was done by selecting periods when there were two consecutive days with mean $K_p < 1$. These occurrences were very rare and were further reduced when days with clear injection signatures were excluded. The 12 pairs of days which remained from the 4 year data set are shown in Table 7.7.

Figure 7.45 shows flux in the 43–60 keV range for the 3rd July 1989 (solid line) and 4th July 1989 (dotted line). A striking feature of this data is the lack of a noticeable local time behaviour. The fluxes show a monotonic decrease in time. Figure 7.46 shows that the ratio of the fluxes on the two days is 0.6, indicating that 40% of the flux is lost from one day to the next. The other pairs of days generally showed similar behaviour.

A more quantitative study was carried out using the whole data set, divided into 2-hour data periods. Figure 7.47 shows the percentage flux rise in a two hour time bin, compared to the previous one. The energy range was again 43–60 keV. Evident from this plot is that there are many more decreases in flux than increases, indicating that the flux generally has brief rises, followed by long declines. The strength of the decline varies over a wide range.

In Fig. 7.48, the same type of data are shown, except that only periods with $K_p < 1$ are considered, so that presumably few new injection events will be occuring. The range of percentage change is now quite narrow and peaks strongly at -5%. This corresponds to a daily loss rate of 46%. This is strong evidence that the loss of flux is quite constant, at a rate of about 40%, in this energy band, during quiet conditions.

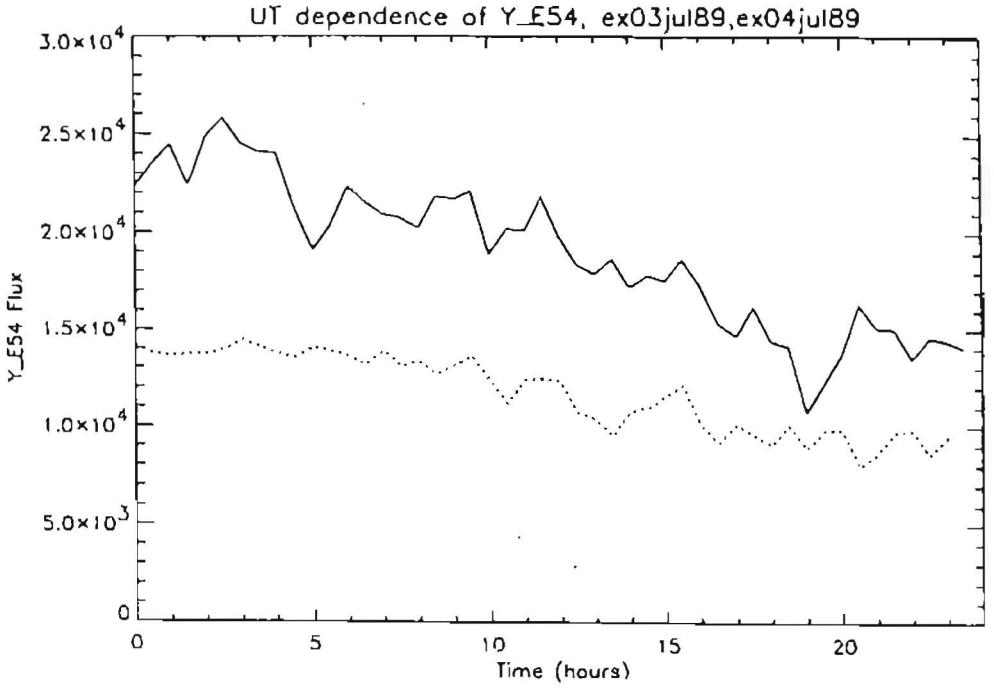

Figure 7.45. Flux in 43–60 keV range for 3rd July 1989 (solid line) and 4th July 1989 (dotted line)

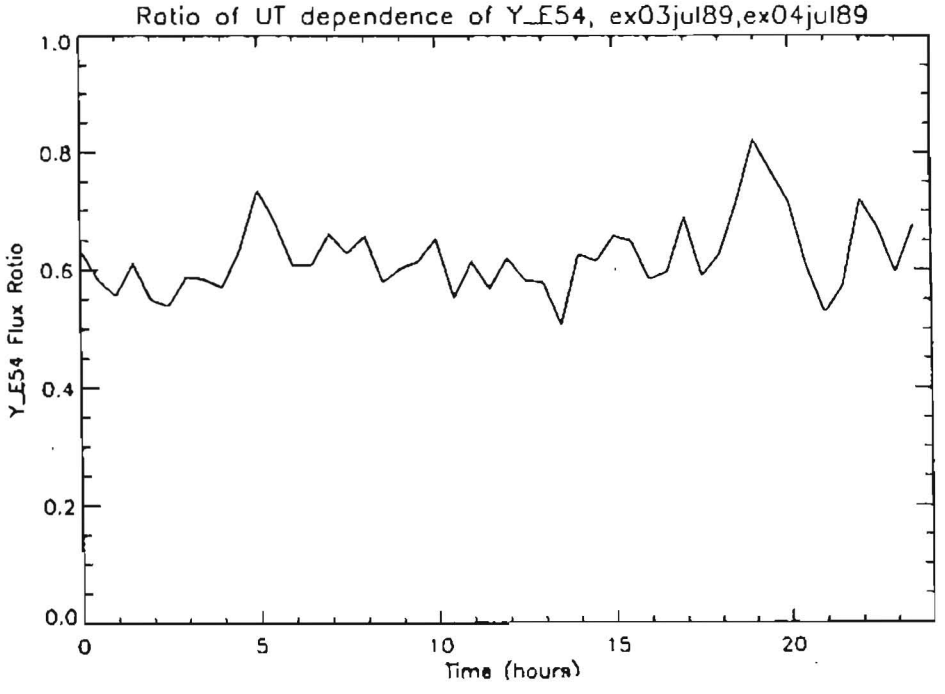

Figure 7.46. Ratio of fluxes in 43–60 keV range at the same UT on 3rd July 1989 and 4th July 1989

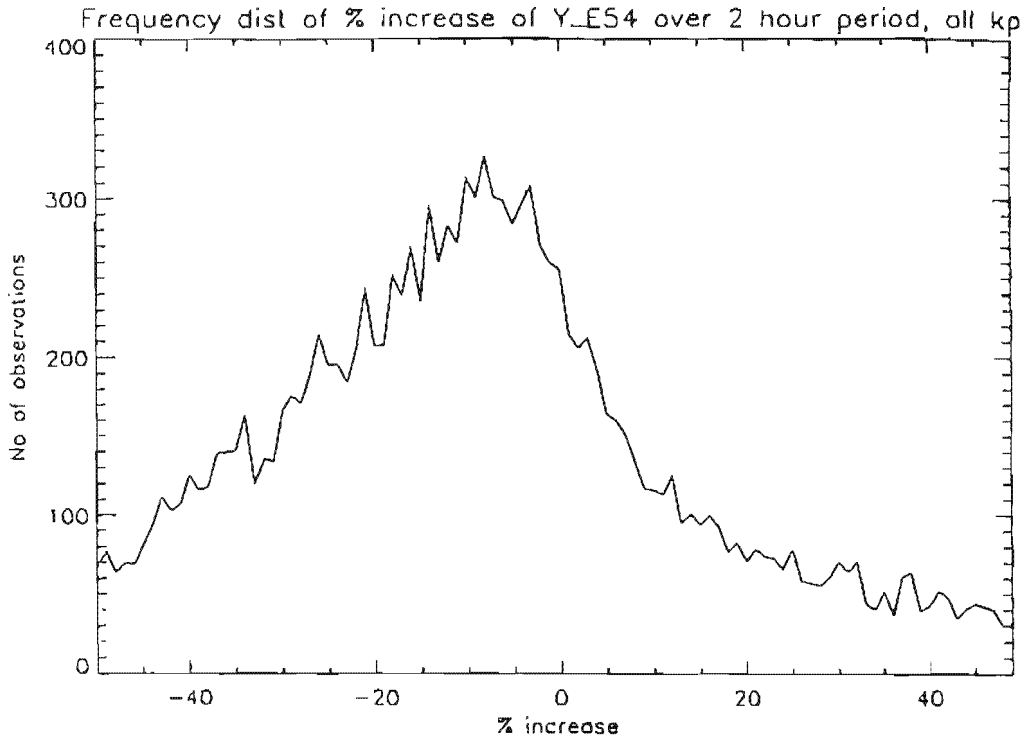

Figure 7.47. Percentage increase in 43–60 keV flux, for all K_p

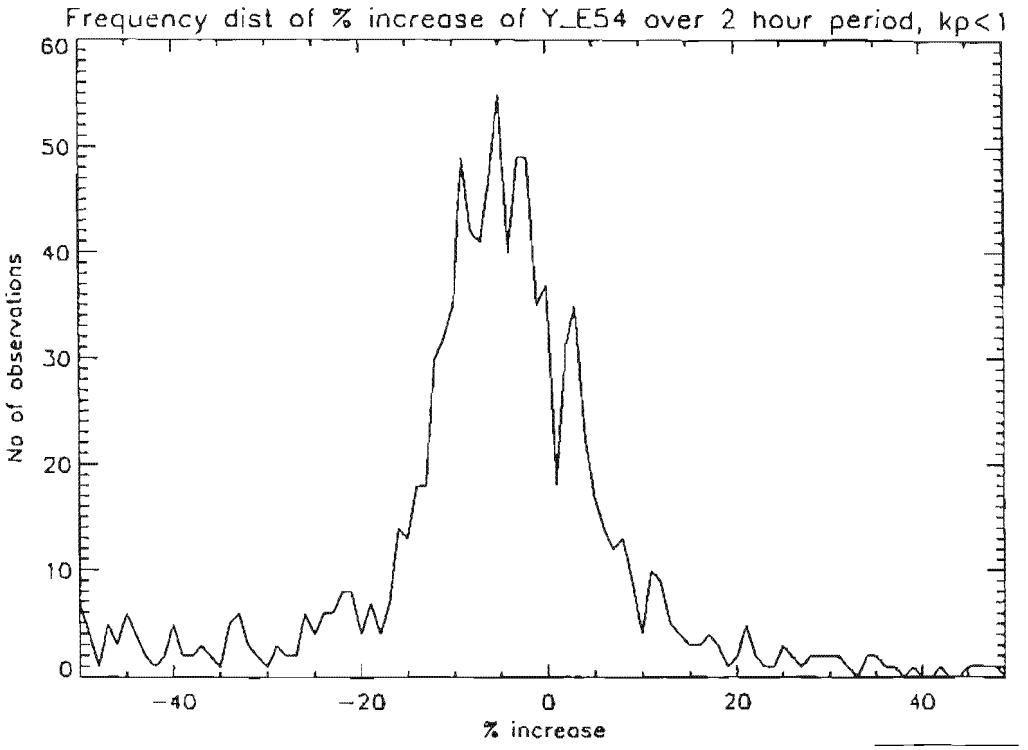

Figure 7.48. Percentage increase in 43–60 keV flux, for $K_p < 1$

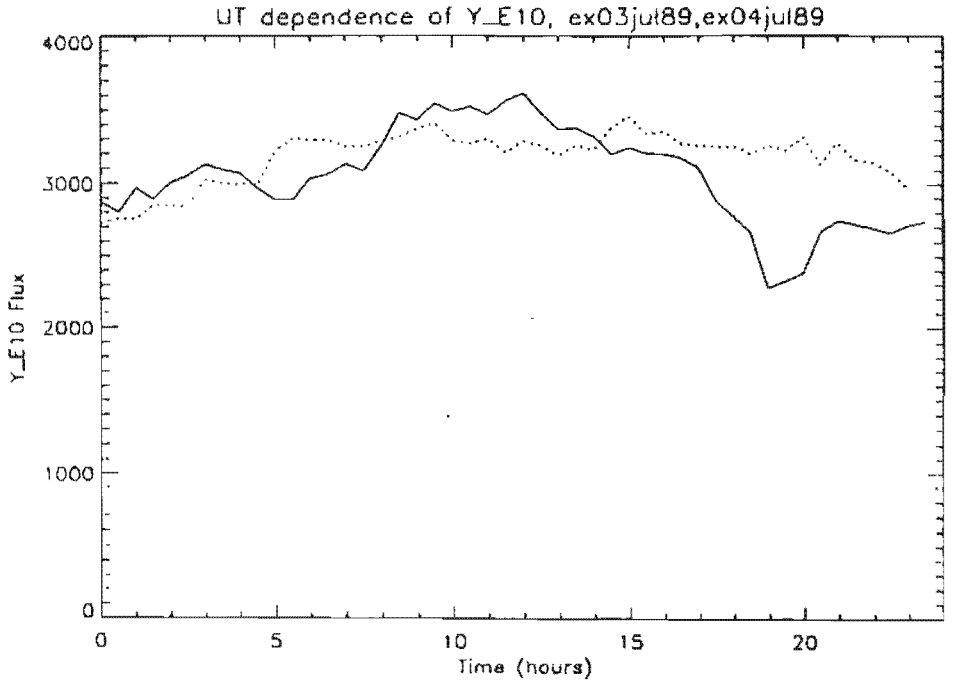

Figure 7.49. Flux in 201.8–300 keV range for 3rd July 1989 (solid line) and 4th July 1989 (dotted line)

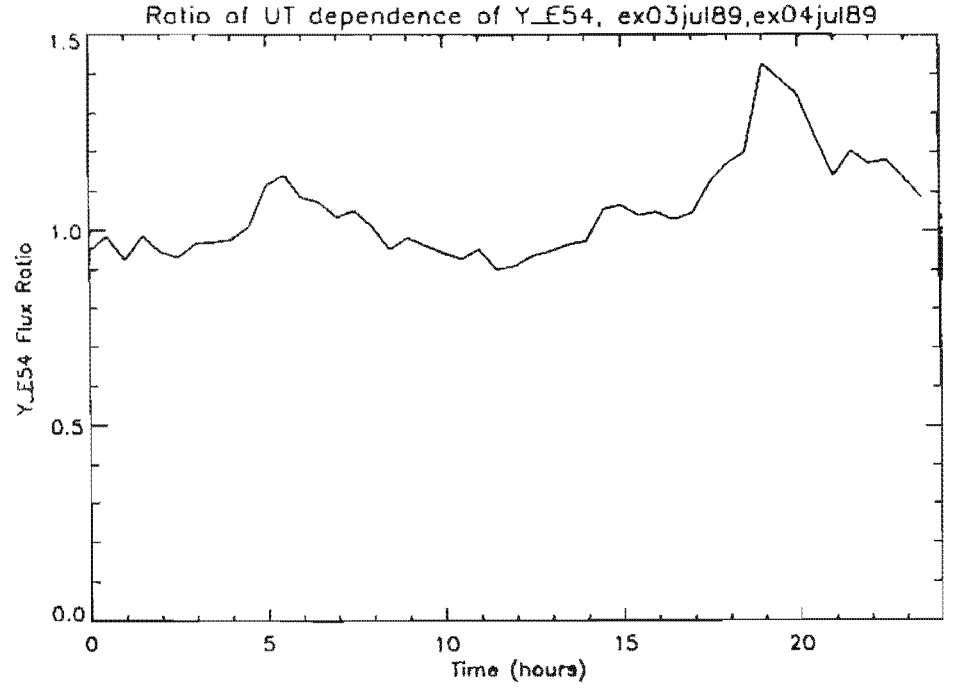

Figure 7.50. Ratio between fluxes in 201.8–300 keV range at the same UT on 3rd July 1989 and 4th July 1989

It has not been possible to assess similar loss rates for the higher energy electrons. Figures 7.49 and 7.50 show the fluxes and flux ratios for the same two quiet days shown in Figs. 7.45 and 7.46. There is no clear trend. Other quiet days showed variable flux ratios. This is not surprising, since we saw earlier that the fluxes at these energies are controlled by the low energy fluxes of the previous day.

7.10 Conclusions

As a result of a detailed investigation of the electron environment, we now have a good understanding of the dynamical behaviour of the electrons between 43 and 300 keV.

Statistical analysis of SEM-2 data has revealed strong patterns in local behaviour of fluxes, anisotropy and spectral index.

Our principle results are as follows:

- Local time analysis of the SEM-2 electron flux data in the energy range 42.9–300keV from geostationary orbit revealed two electron populations with different local time behaviour.

  SEM-2's highest energy range (201.8–300 keV) showed peak fluxes close to midday. These are trapped electrons. The geostationary orbit of Meteosat-3 takes it through stronger magnetic fields on the dayside than the nightside in the Earth's non-dipole field.

  SEM-2's four lower energy ranges have peak fluxes and increased variability in the early morning. This variability is the result of the injection events associated with magnetospheric substorms which occur close to local midnight beyond geostationary altitudes. The electrons then drift eastward. Reaching geostationary orbit in the early morning, the observed amplitude of the event then decreases the later in local time it is observed.

- A simple model program (FLUX_LT) has been developed to return expected flux ranges at a specified local time, for all of SEM-2's energy ranges.

- As K_p increases, the range of fluxes observed for electrons with energies below 200 keV increases, and the early morning peaks become larger. Fluxes of electrons above 200 keV showed no increase in range as K_p increased: the peak fluxes showed no major increase at higher K_p. At all energies in the detector's range, the local time flux distribution appears to become less predictable, though it should be noted that only 5% of the flux observations occurred at a K_p of 6^- or above.

- The anisotropy index tends to be positive on the nightside, where the tail-like field produces a field aligned distribution, and positive on the dayside, characteristic of trapped and loss cone distributions. The diurnal profile of the anisotropy index shows a sharp change towards more field aligned distributions about four hours before evidence of injection events is seen in the diurnal profiles of lower energy bands of electron flux.

- In local time averaged data, we see a change in anisotropy four hours before we see the first injection events in the flux profile.

- The spectral index has its most negative values at 0400 when the flux spectrum is enhanced for the lowest energy ranges. The less negative daytime values of the index correspond to the harder energy spectrum encountered on the sunward side of the orbit, where the satellite passes through a stronger magnetic field.

- Using Fourier analysis it was possible to approximate the diurnal variation observed in the flux in SEM-2's total energy range (42.9–300 keV) by a combination of two sine waves having periods 24 hours and 12 hours. Removal of the two sine waves at their correct phases and amplitudes left the average flux versus local time plot flat, although the variability due to injection events was still in the data. Both 12 and 24 hour period components were present in the frequency spectrum of the lowest of SEM-2's five differential energy bands. Only a 24 hour period component was significant in the highest energy band.

- Wavelet analysis illustrated that the diurnal variation was not a constant one and seemed more evident at times of higher flux. This would suggest that removal of an average diurnal variation over an extended time period would prove inadequate to take the local time dependence out of the time series. This was shown to be the case by a wavelet transform of the Fourier filtered data: the diurnal frequency was still seen at certain times. The further modification of artificially compensating for the local time dependence by "stretching" the data enhanced the lower period waveforms in the data. A minimum separation time between injection events of 3 hours and a most common separation of 4 hours were suggested.

- By considering average fluxes over increasing time periods, we have shown how the expected average flux range decreases as time duration increases. This data has been used to create a simple model (`FLUX_PROB`) which returns details of expected average fluxes for a given time duration.

- A clear correlation exists between high and low energy electron fluxes. The time lag of 1 day between these different energy components is consistent with the recirculation model of radiation belt filling.

- Sharp peaks in the low energy fluxes were caused by the injection of electrons into the magnetosphere by substorms. A simple analysis of the energy dispersion of these events and the fact that the observations were strongly clustered around 5 hours local time point to these events originating from a localised region of the near tail.

- Flux loss at low energies, when no new injection events occurred, happened at a rate of around 40% per day.

Meteosat-3's SEM-2 has been a valuable source of information on the long term characteristics of the radiation belts, apart from fulfilling its primary function of measuring the local radiation environment for anomaly diagnosis. To continue to improve our knowledge of the radiation belts, such instruments should regularly be included on satellites in geostationary and radiation belt crossing orbits.

Chapter 8

Comparison of SEM-2, LANL and CRRES data

More details on the work described in this chapter can be found in Technical Note 8.

8.1 Introduction

Before producing quantitative models of the radiation belts, it was important to question whether the absolute measured flux levels from the instruments concerned are accurate. This is difficult to calculate from theory and ground calibrations. One way to test the accuracy of the data sets used in the TREND-2 study is to compare them quantitatively with each other. This chapter describes comparisons made between the data sets derived from the Spacecraft Environment Monitor (SEM-2) on Meteosat-3, the Los Alamos National Laboratory (LANL) instrument on a number of geostationary satellites and data from the High Energy Electron Fluxmeter (HEEF) and Medium Energy Analyser (MEA) (a.k.a. Medium Energy Electron Spectrometer or MEES) on the Combined Release and Radiation Effects Satellite (CRRES). This comparison is a complicated process because these instruments have limited overlap in energy, time and position in the magnetosphere.

As a further check on data quality, a brief comparison with the existing AE-8 electron model was performed.

The European Meteosat-3 satellite was launched in June 1988 and is still operational at the time of writing. SEM-2 has been operated for almost all of this period. Its long duration has made it extremely valuable for statistical studies and it overlapped the duration of the CRRES mission, except during March and April 1991, when SEM-2 was switched off. The Los Alamos instruments were carried on many

US geostationary satellites. The data available to this study come from 1976-059, 1977-007, 1979-053, 1981-025 and 1984-037. Data from two further satellites 1982-019 and 1984-129 are not yet available. CRRES was launched in July 1990 with a desired mission lifetime of three years. Although it failed after just 15 months, in October 1991, it obtained very good data on the radiation belts, including the discovery of a new temporary third radiation belt (Blake et al. 1992). Data from two radiation instruments on CRRES are included in this study.

Meteosat-3 and the satellites carrying the LANL instruments were geostationary, whereas CRRES travelled in an 18° inclination elliptical orbit between 350 km and 33,584 km ($5.25R_E$). In terms of L, CRRES typically reached an L value of 7.0 and so passed through field lines corresponding to geosynchronous orbit at $6.6R_E$.

8.2 Data descriptions

8.2.1 Meteosat-3 spacecraft environment monitor

SEM-2 (Coates et al. 1990) was provided to ESTEC by MSSL under ESA contract No. 7879/88/F/TB. Subsequent analysis and interpretation has also been carried out by MSSL in the intervening period, with much of the work being performed under contract to ESTEC.

SEM-2 consists of an array of five collimator systems looking at angles +60°, +30°, 0°, −30°, −60° to the spacecraft spin axis. This axis is parallel to the Earth's spin axis. Azimuthal angular coverage is provided by the spacecraft spin. The angle width determined by the collimators is approximately ±5°. At the back of each collimator is a solid state surface barrier detector. The detector-collimator system was provided by LANL and is identical to the low energy part of their instrument, described in the next subsection. In this type of solid state detector, the number of electron-hole pairs created by an incoming particle is a function of the path length of the particle in the material. This path length is a function of energy. Hence the electric signal is a function of energy except for trajectories that pass through the material without depositing all their energy (e.g. for very high energy particles and corner-crossing paths). Energy bands are created via the electronics system by dividing the signals into pulse height bands. The electronics for SEM-2 were created by MSSL and so the energy bands are different from the LANL detectors. These energy bands are 42.9–59.4 keV, 59.4–90.7 keV, 90.7–134.9 keV, 134.9–201.8 keV, and 201.8–300 keV. Azimuthal angle bins are 0° to 60°, 60° to 120°, 120° to 180°, 180° to 240°, 240° to 300°, 300° to 360°, where 0° corresponds to the solar look direction. A more complete description of the SEM-2 instrument is given in Technical Notes 6 and 7 of this study.

Table 8.1. Time coverage of the LANL data

Satellite	Start Date	End Date
1976–059	79/01/03	81/08/31
1977–007	79/01/03	81/06/16
1979–053	81/04/29	86/05/25
1981–025	81/03/27.	85/03/31
1984–037	84/04/24	88/10/31

SEM-2 data are summed over variously 500 and 600 s, to fit telemetry resources.

8.2.2 LANL Charged Particle Analysers

LANL has an extensive set of data (Baker et al. 1982) covering electrons in geosynchronous orbit from 30 to 15,000 keV and protons from 145 keV to 150 MeV. A subset of these data, the Los Alamos Synoptic Data set, was provided for the TREND study by T.E. Cayton during the first phase (Lemaire et al. 1991), carried out under ESTEC contract No. 9011/88/NL/MAC.

The low energy electron analyser (LoE) (Belian et al. 1978) is identical to SEM-2, except that it is divided into six integral energy bands instead of the five differential energy bands used by SEM-2. These bands are 30–300 keV, 45–300 keV, 65–300 keV, 95–300 keV, 140–300 keV, and 200–300 keV. The instrument has the same polar angles as SEM-2 but the angular information has been lost in the summed data set available to this study. The data are provided as hourly averages over all look directions.

The high energy electron analyser (HiE) (Belian et al. 1978) was a single collimator, pointing perpendicular to the satellite spin axis. Angular resolution was $\pm 4°$. It had the following energy bands: 200–2000 keV, 300–2000 keV, 400–2000 keV, 600–2000 keV, 900–2000 keV, 1400–2000 keV.

During the first phase of the TREND study the LANL data were augmented with auxilliary information including $K_p$and (B, L) based on model calculations. A detailed description of these calculations and of the LANL instrument can be found in the final report of TREND (Lemaire et al. 1991). The LANL data cover the following time intervals with 1 hour time resolution but there are frequent data gaps. The time coverage is shown in Table 8.1.

8.2.3 CRRES

Two of the instruments on CRRES were particularly suited to the TREND study. Both instruments have required a great deal of post-launch calibration, especially in the middle of the radiation belts where noise problems are most significant. Both data sets are now believed to optimally calibrated. A detailed description of the CRRES payload can be found in Technical Note 4. The HEEF and MEA instruments are described in Sect. 6.2.1 and Sect. 6.2.2, respectively.

High Energy Electron Fluxmeter

The effort involved in carrying out the noise analysis and temperature correction for HEEF meant that little analysis could be done by the instruments' builders in Phillips Lab until the best correction functions could be calculated. This process is now complete and the raw data are being processed. Phillips Lab have agreed to create a special data set for our study with HEEF data for $L \geq 5.5$ and over, binned by energy, time and pitch angle. This restricted L range is to allow comparison with the SEM-2 and LANL data bases, without duplication of Phillips Lab's own program of modelling the radiation belts.

MEA

Data from the MEA (also called MEES) instrument (Vampola et al. 1992) have been supplied to the TREND study by Dr. A.L. Vampola who is acting as a consultant to MSSL.

This instrument uses magnetic fields to select the energies of incoming particles between 0.1 and 1.7 MeV. The particle trajectories are bent by a perpendicular magnetic field onto an array of eighteen detectors. The detector array is encountered after a 180° rotation. This position is a focus and means that the position on detector array is a direct measurement of the energy, despite differences in the entry angle of the particles. The detectors are silicon plates which produce electrical pulses proportional to the incident energy. The pulse height is used to discriminate against radiation-induced noise. This use of two independent energy measuring techniques makes noise rejection very efficient. A further virtue of this instrument has been that very high count rates were measured. This has meant that the statistics available for background calculation are excellent. One of the 18 detectors was shielded from the incident fluxes to act as the background detector. In the inner radiation belt, this correction was essential for the higher energy levels of the instrument. Although the real fluxes fell below the noise background, an adequate correction could be made because of the good statistics. The background correction factor actually used in the processed MEA data corresponds to the background when the instrument looks

perpendicular to the magnetic field. This is applied to spin-averaged flux data for which this background is excessive, leading to some cases in the inner radiation belt where flux apparently increases in energy.

The high count rate of MEA was higher than predicted before launch and resulted in some problems. In the inner radiation belt, where fluxes are highest, the counts rates for low energies at angles nearly perpendicular to the magnetic field exceeded the counting speed of the electronics and resulted in fewer electrons being measured than were incident on the detector. The effect of this saturation has been included in the decompression look-up table, so that the data go from compressed counts to decompressed corrected counts in one step. Correction of saturation effects is only effective, however, up to the limit where the incident-versus-measured count curve turns over. Above this limit, an increase in flux produces a decrease in measured counts and there is no longer a single incident flux corresponding to the measured counts. By examining the data by eye, these effects are easily seen so that the affected data can be avoided.

8.3 Data comparisons

8.3.1 SEM-2 and LANL

In order to compare LANL data with SEM-2 data, the integral isotropic LANL fluxes with units $cm^{-2}s^{-1}$ were converted to differential flux with units $cm^{-2}sr^{-1}s^{-1}keV^{-1}$.

Figure 8.1 shows a plot of SEM-2 data from 1990, averaged in 30 minute bins of local time, for the energy channel 43–60 keV. This can be compared roughly to Fig. 8.2 which shows LANL fluxes for the 1976-059 satellite for the energy range 45–65 keV. The SEM-2 data peaks at a flux of $4.8 \times 10^4\,cm^{-2}s^{-1}sr^{-1}keV^{-1}$ while the 1976-059 data peaks at $9.38 \times 10^4\,cm^{-2}s^{-1}sr^{-1}keV^{-1}$, a factor of almost 2. The peaks in both data sets occur at the same local time, around 05 hours. However, the shapes of the local time distributions are not the same because the flux minima have about the same levels, around $3 \times 10^4\,cm^{-2}s^{-1}sr^{-1}keV^{-1}$. It is unlikely that these differences are due to the different epochs of the data. It is more likely that there is some calibration factor that is not adequately known in one or both of the instruments and possibly some difference in the background also. When comparing the SEM-2 data with the other LANL instruments, the situation is even worse. These curves, shown in Figs. 8.3 to 8.6 have the same shape as 1976-059 but are over a factor of 10 higher. In these figures, the peak fluxes varied between 1.18×10^6 and $1.85 \times 10^6\,cm^{-2}s^{-1}sr^{-1}keV^{-1}$. There clearly is some problem in the relative calibration of these instruments.

The same differences exist in the higher energy channels too. When the SEM-2

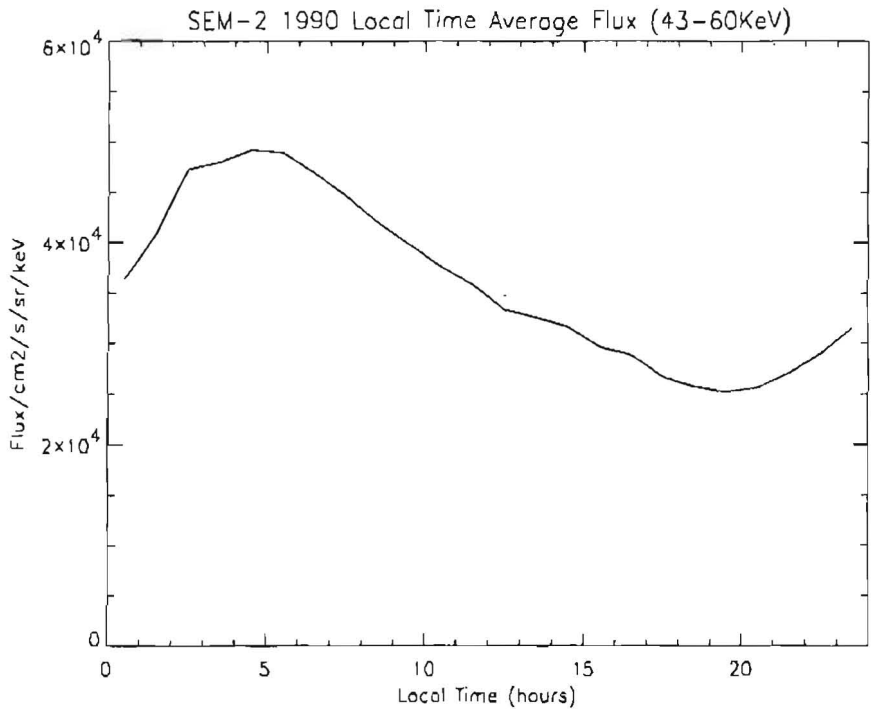

Figure 8.1. SEM-2 fluxes (43–60 keV), as a function of local time

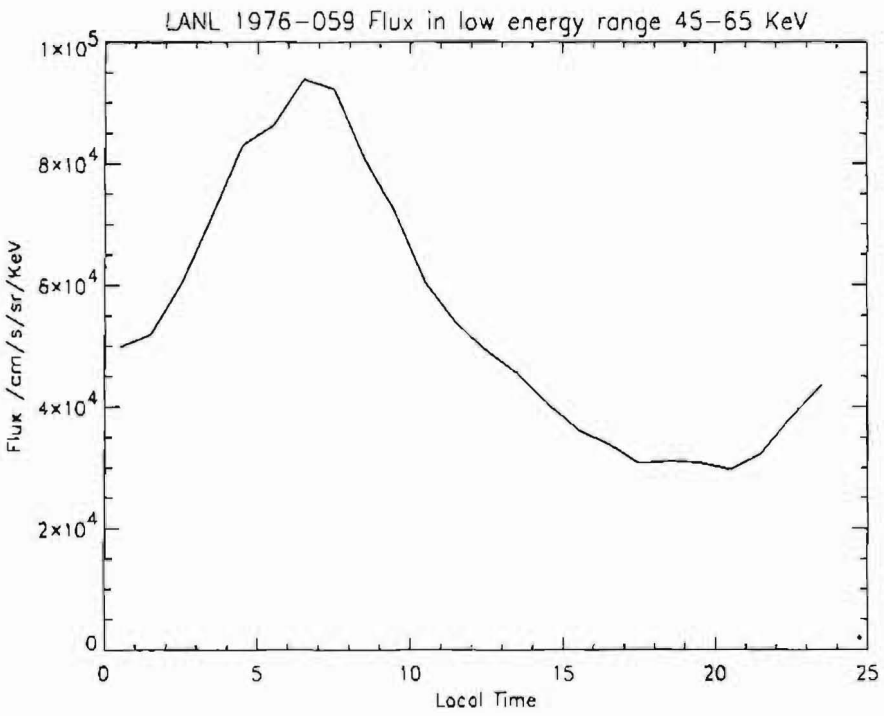

Figure 8.2. LANL 1976-059 fluxes (45–65 keV), as a function of local time

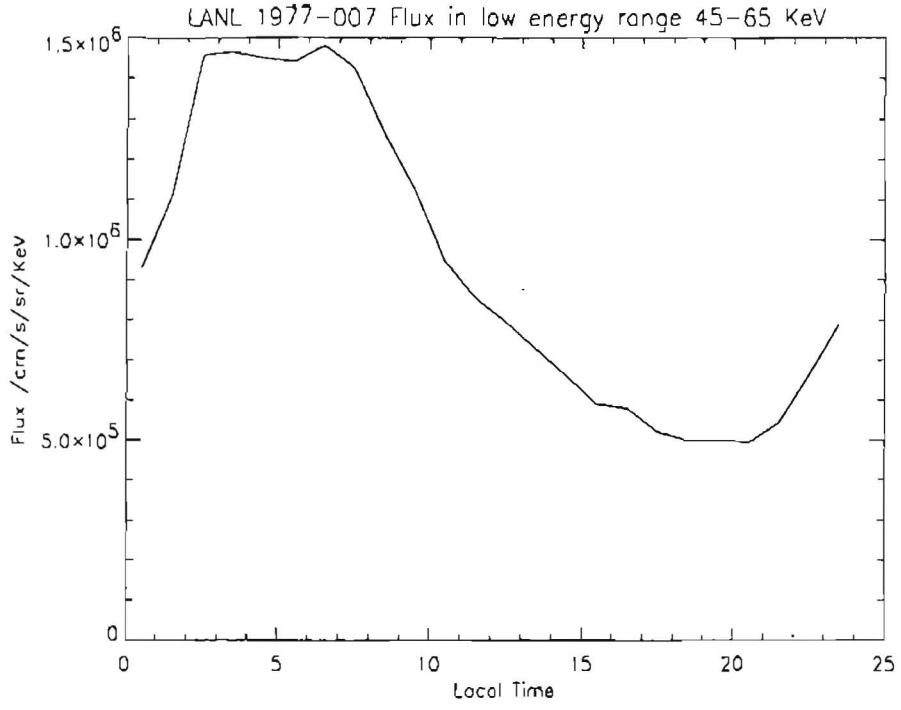

Figure 8.3. LANL 1977-007 fluxes (45–65 keV), as a function of local time

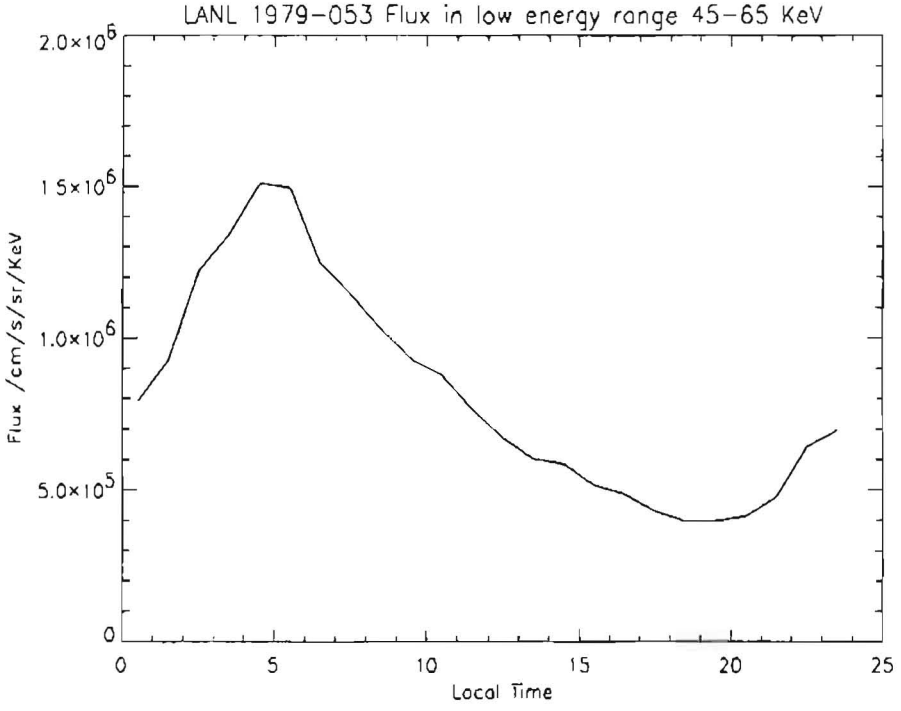

Figure 8.4. LANL 1979-053 fluxes (45–65 keV), as a function of local time

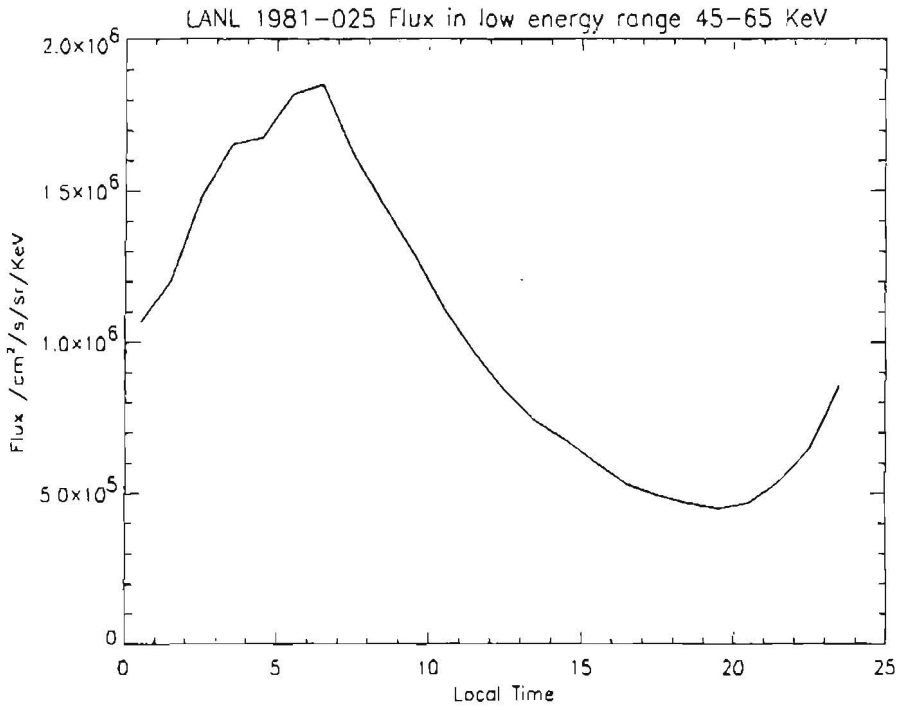

Figure 8.5. LANL 1981-025 fluxes (45–65 keV), as a function of local time

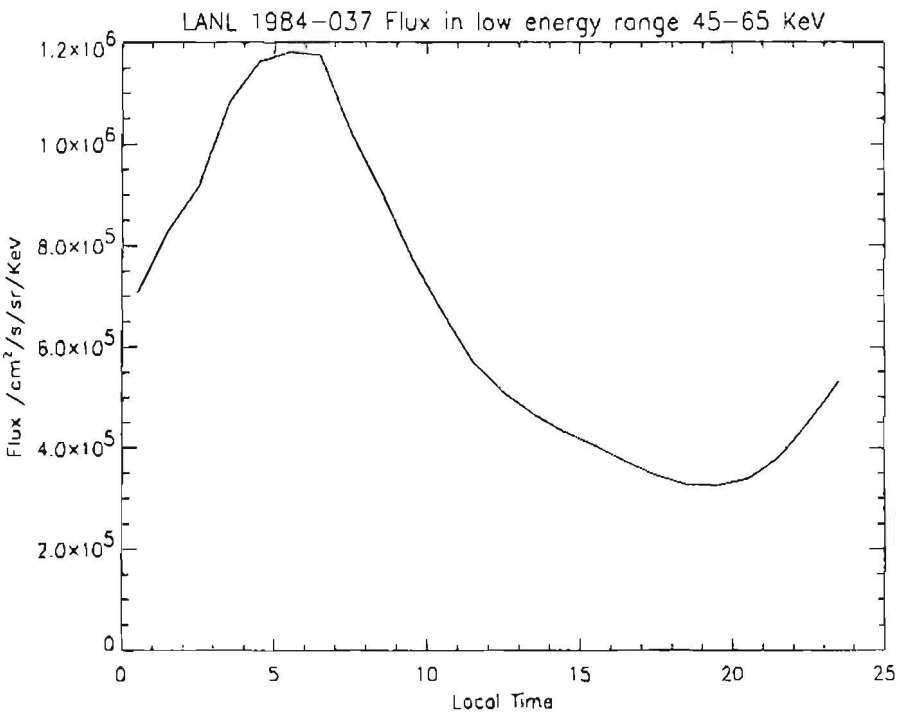

Figure 8.6. LANL 1984-037 fluxes (45–65 keV), as a function of local time

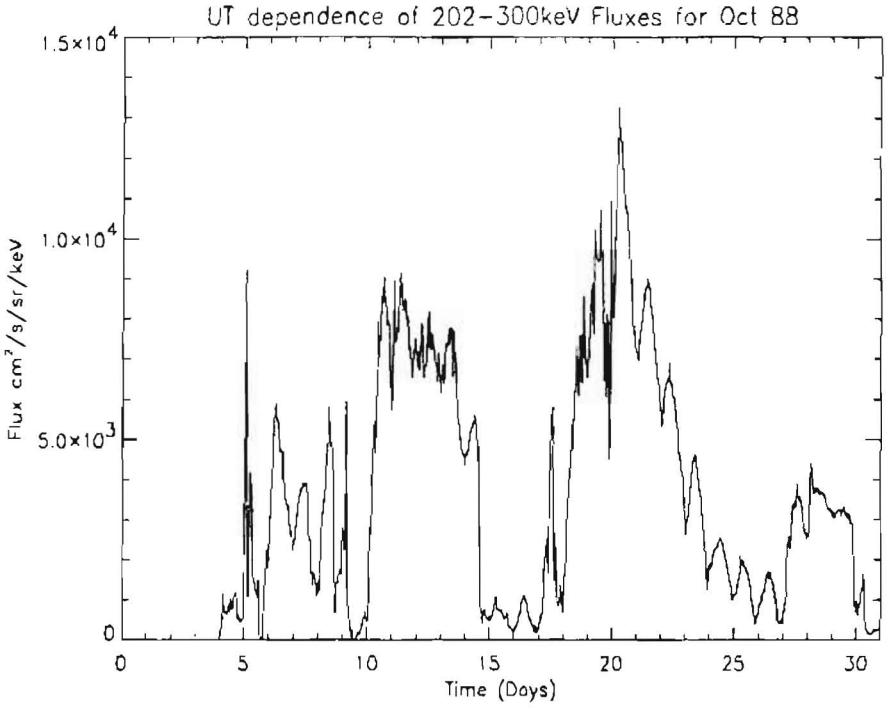

Figure 8.7. SEM-2 fluxes (202–300 keV) for October 1988

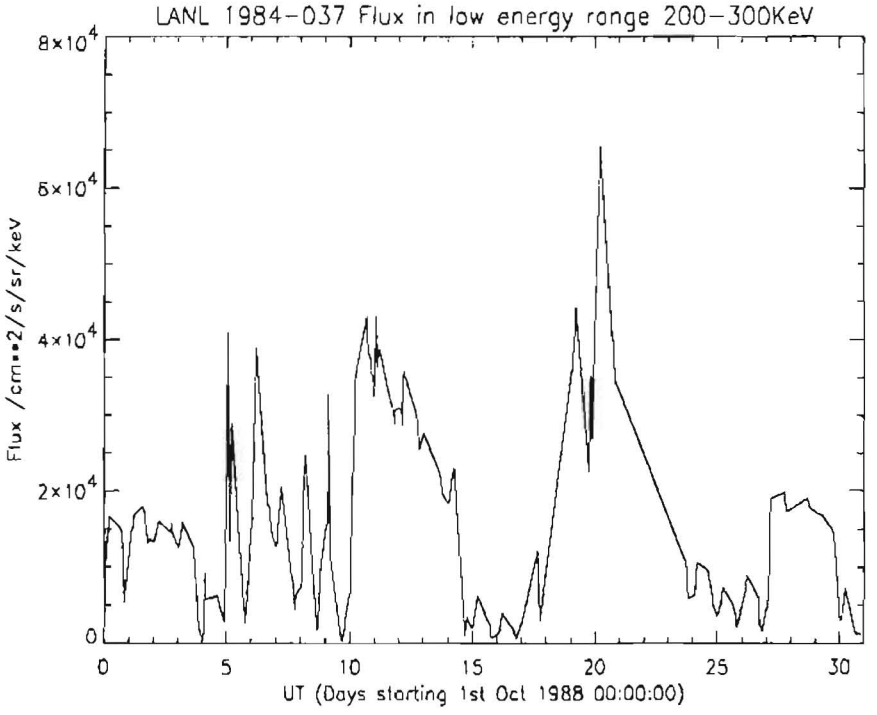

Figure 8.8. LANL 1984-037 fluxes (200–300 keV) for October 1988

instrument was calibrated by MSSL it was found that the calibration factors did not agree at all well with the values supplied by LANL and it so may be that better figures for the LANL instruments does not exist. Contacts with the LANL group have revealed that they are aware of the discrepancies between different LANL instruments but they have, as yet no revised calibration figures.

Data from Meteosat-3 overlaps for a period of about three month with 1984-037 in 1988. This lets us compare the two data sets directly. The highest energy bin for SEM-2 and the LoE instrument were selected for comparison because the flux in this energy range is slowly varying. Figure 8.7 shows SEM-2 fluxes for October 1988 and Fig. 8.8 shows corresponding LANL fluxes. The dynamic agreement between the two data sets is excellent, although the LANL fluxes are apparently a factor of 4 higher than SEM-2's. Although the LANL data are given as 1 hour averages, there were many gaps in the data that were revealed by this plot.

The variability of the LANL fluxes was calculated in a similar way to the analysis performed on SEM-2 data in Chapter 6 of this report. The 5, 45, 55, and 95 percentiles for fluxes averaged over one hour of local time were calculated. In the energy range 200–300 keV, a good qualitative agreement was seen between both the LoE and HiE LANL detectors and SEM-2. Nevertheless the question of absolute

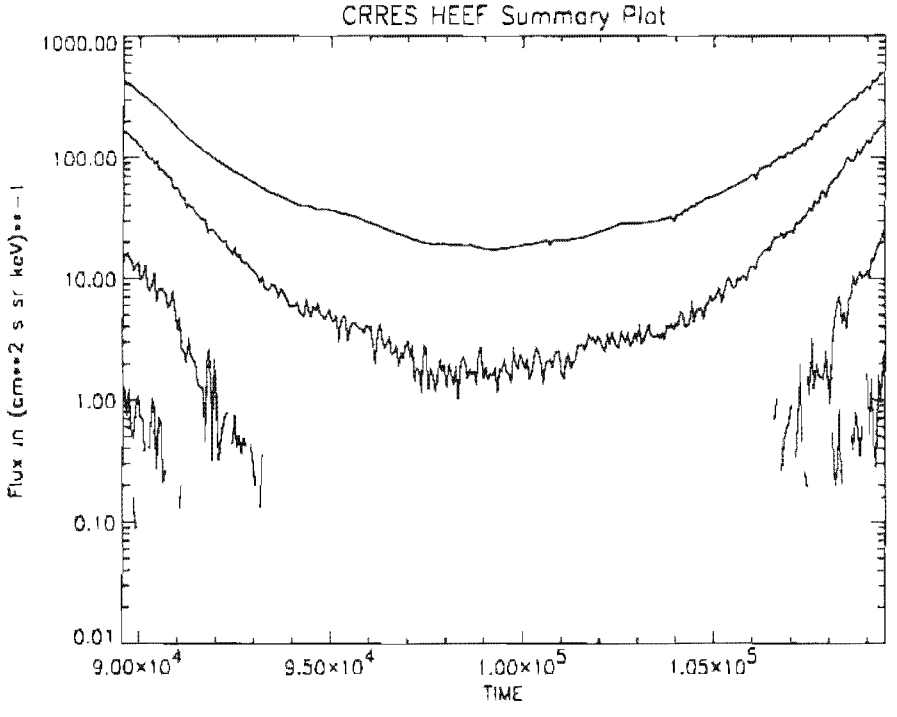

Figure 8.9. HEEF Summary plot for orbit 290. The lowest energy channel is at the top, with higher energies below.

calibration factors remained.

8.3.2 HEEF and MEA

Figure 8.9 shows HEEF calibrated fluxes plotted against time for CRRES orbit 290, beyond $L = 5.5$. All eleven energy bins are plotted but only the two lowest energy channels register non-zero fluxes over the whole time period. In contrast, the MEA data for the same period showed significant counts at all energies.

Figure 8.10 compares directly the HEEF and MEA fluxes in comparable energy channels. There appears to be a small systematic error resulting in MEA fluxes exceeding HEEF fluxes before apogee and the reverse after apogee, at least on this day. A simple timing error does not seem possible. Nevertheless the relative calibration of the two data sets is excellent.

A comparison of the MEA and HEEF spectra was is shown in Fig. 8.11. The data are summed over pitch angle and over a 1000 s interval between 108,000 and 109,000 on the same day. This period was chosen because L was just over 5.5 and significant counts existed in five of the HEEF energy channels. This shows good agreement between the two instruments where they overlap in energy. It also shows that even the modest increase in energy coverage provided by the HEEF data can be important. The "knee" in the log spectrum is only apparent because of the HEEF data.

8.3.3 MEA and SEM-2

The CRRES orbit has an apogee of $5.25R_E$ and thus never reaches the altitude of geostationary satellites like Meteosat-3 at $6.6R_E$. However, CRRES's orbit is inclined to the equatorial plane which enables CRRES to usually pass through field lines connected to geostationary orbit, once or twice per orbit. By extracting data from these times, a comparison with SEM-2 data can be performed. The 214 keV MEA channel was chosen as being close to the 200–300 keV channel on SEM-2. MEA data between L values of 6.25 and 6.75 were selected. The L values came from the CRRES ephemeris data. Figure 8.12 shows, as a continuous line, the SEM-2 flux and the MEA flux as diamonds. The MEA data occurs in short bursts as the satellite passes through the L range, with long gaps in between. In general the quantitative comparison is very good. Most of the MEA points lie close to the SEM-2 line. The main exception to this occurred in days 28 to 30 when there were very large flux peak in both the SEM-2 and MEA data but they did not coincide in time. It is possible that these events were strongly dependent on the different local times of the two satellites.

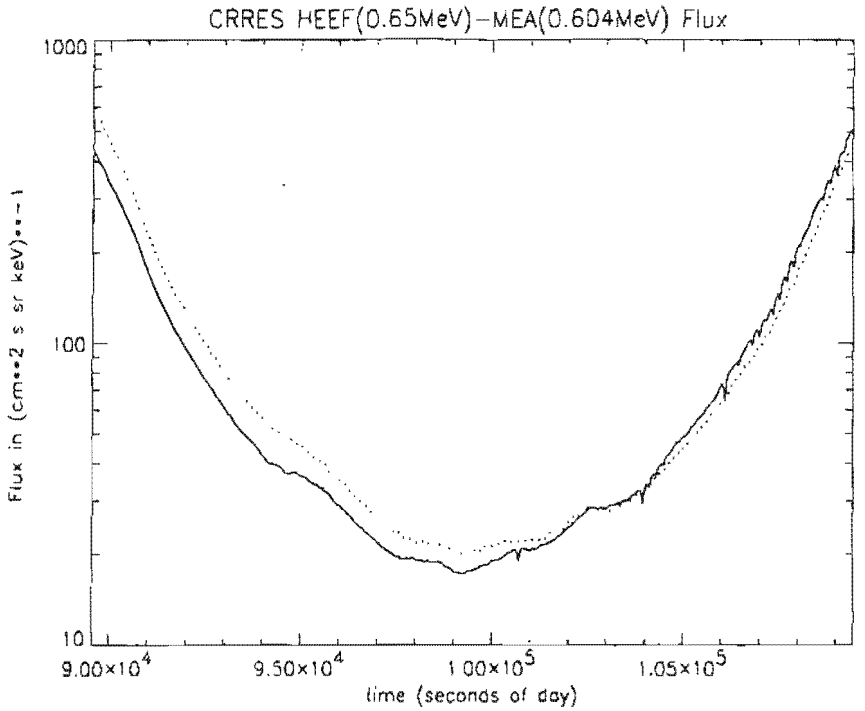

Figure 8.10. Fluxes for HEEF (solid line) and MEA (dotted line) against time

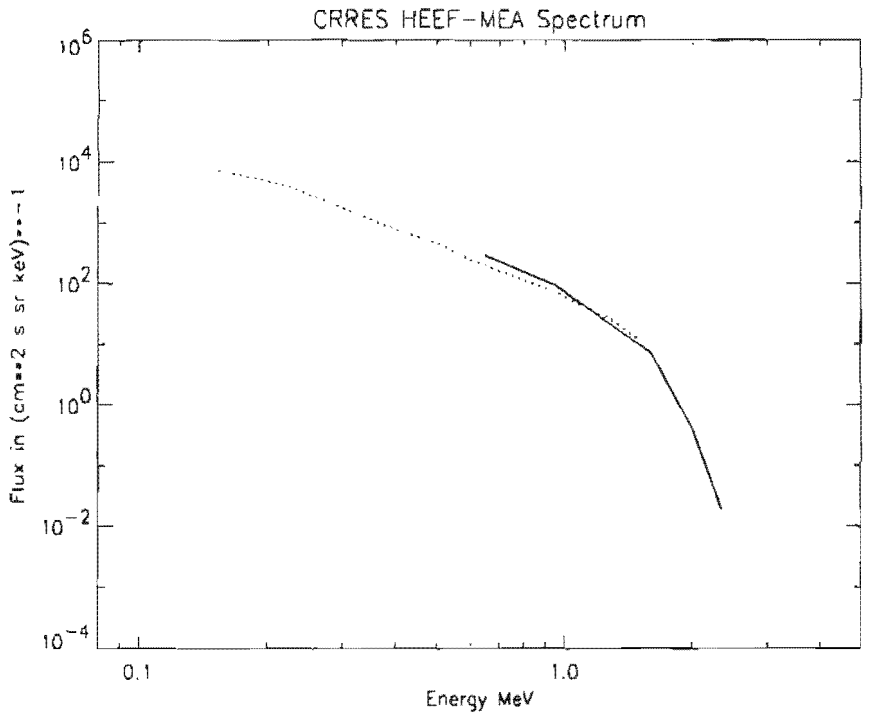

Figure 8.11. Energy spectrum for HEEF (solid line) and MEA (dotted line) between 108,000 s and 109,000 s on orbit 290

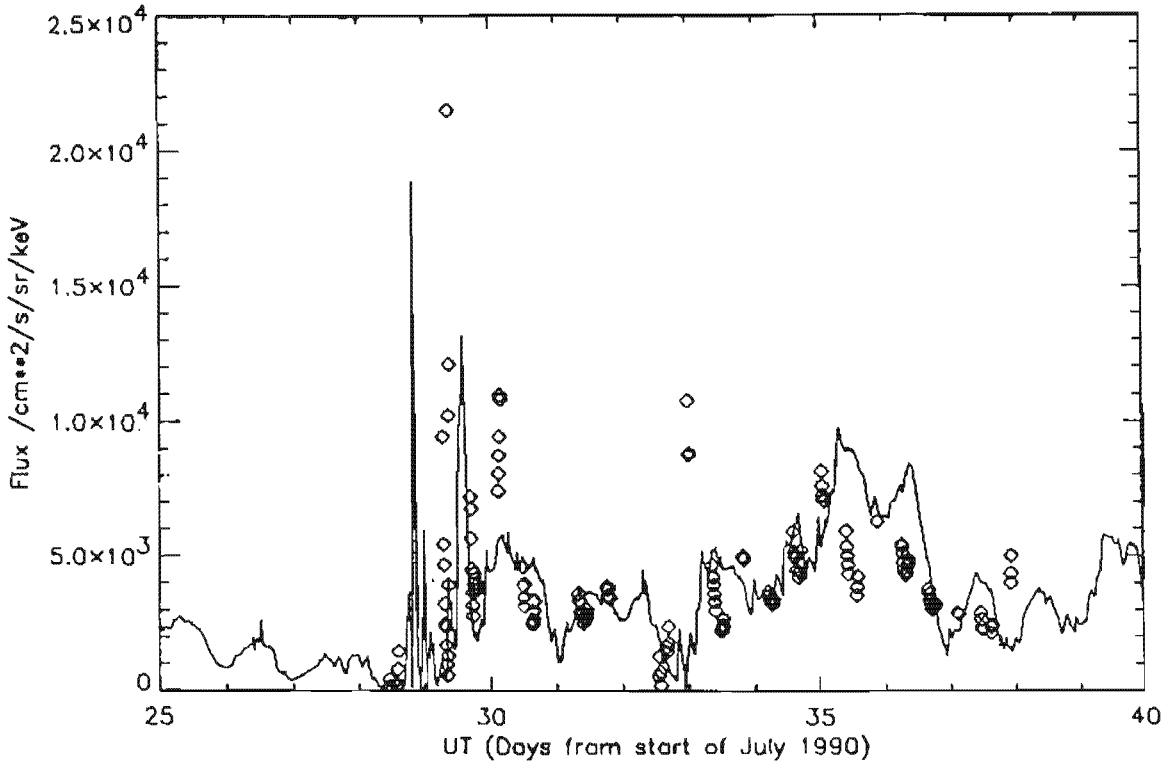

Figure 8.12. Comparison between SEM-2 flux (202–300 keV) and MEA (214 keV) flux in July and August 1990

8.4 SEM-2 Comparison with AE-8

The AE-8 model gives fluxes as a function of B/B_0 and L for an L range of 2 to 11. In order to compare with SEM-2 results the Meteosat-3 positions had to be converted to (B, L) space. This was done using the subroutine BLXTRA, developed in the first stage of the TREND study and updated in this second stage. The Tsyganenko (1989) external field model was used, superimposed on the internal DGRF model. (B, L) positions for every data record in 1989 were calculated, taking into account the K_p index, and the fluxes were summed according to the L value. Because B/B_0 remained very close to 1.0 for nearly all the data, B/B_0 was taken to always be 1.0 in subsequent comparisons.

Figure 8.13 shows SEM-2 fluxes in the energy range 202–300 keV as a function of L. Also plotted, as a dotted line, are the fluxes predicted from the AE-8 MAX model at 250 keV. The solar maximum version of AE-8 was appropriate because solar maximum occurred in 1989 or 1990, however AE-8 MIN produces fluxes that are less than one percent different for this energy and range of L. A B/B_0 value of 1.0 was input to the model. The output from AE-8 is omnidirectional flux, so

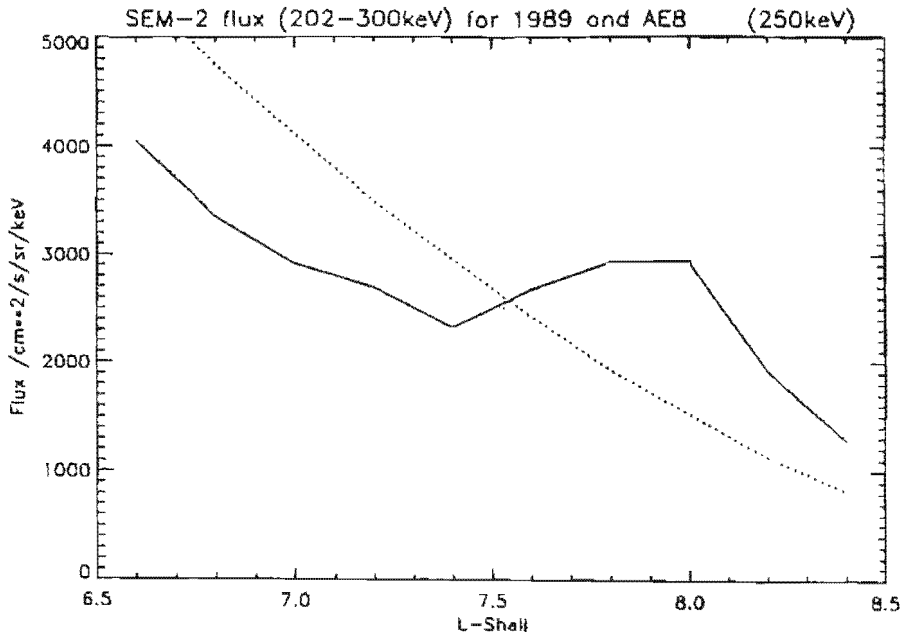

Figure 8.13. Comparison between average SEM-2 flux (202–300 keV) for 1989 and AE-8 MAX, as a function of L

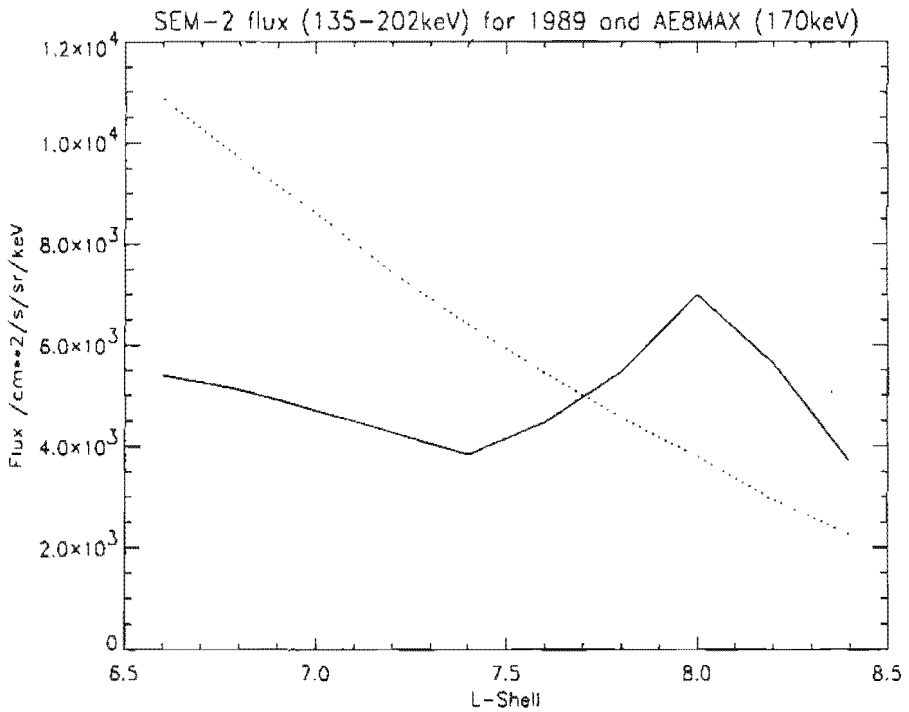

Figure 8.14. Comparison between average SEM-2 flux (135–202 keV) for 1989 and AE-8 MAX, as a function of L

this was divided by 4π to convert to flux per steradian. The SEM-2 flux is lower than the AE-8 model flux by 25 to 30% below $L = 7.4$. Thereafter, the SEM-2 flux increases so it exceeds the AE-8 flux by a similar amount. This behaviour of the SEM-2 flux probably occurs because the higher L values occur only on the nightside where substorms occur and lower L values occur only on the dayside.

This effect is more pronounced at lower energies. Figure 8.14 shows SEM-2 data between 135 and 202 keV, compared to the AE-8 MAX flux at 170 keV.

8.5 Conclusions

SEM-2 data and the AE-8 model comparisons indicated that the model underestimated the flux at lower L values and overestimated at higher L values. The disagreement between data and model decreased as energy increased. The AE-8 and SEM-2 results are consistent because at low energies there is a strong local time variation in fluxes due to substorm injection events and the SEM-2 coverage of L values is also local time dependent.

The main aim of this subsection of the study was to investigate how well data from one instrument can be combined with data from a different instrument to increase the energy and/or L coverage of the combined data sets. We have seen that there is good agreement with between the CRRES HEEF and MEA instruments. In the data set available to this study, the HEEF data extend the MEA energy range only slightly because of HEEF's low counting statistics in all but the bottom two energy channels. MEA data agree well with SEM-2, using L to compare data from different positions. In comparing LANL data with SEM-2 and comparing between the different LANL instruments, we did discover significant variations in flux by up to a factor 15.

Hence, it appears reasonable to use MEA, HEEF and SEM-2 data in the creation of new radiation belt models. Because the calibration of LANL data has not been resolved, this data base is presently incompatible with the others.

Chapter 9

Survey of CRRES data

This chapter describes the use that was made of the CRRES data. This has been limited to the MEA data. In Chapter 8 we saw that the HEEF data agree well with the MEA data where they overlap and since HEEF goes to higher energies it would undoubtedly have been a valuable source of data. However, the data made available to this study were restricted to L values greater than 5. Here there was only a significant count rate in the bottom two energy channels which overlap with the MEA energy range. Hence the addition of these HEEF data to the study would provide only a minimal increase in information. Some non-CRRES data sources have also been used when appropriate. Further details of the work described in this chapter can be found in Technical Notes 9 and 10.

9.1 The MEA data

The CRRES Medium Energy Analyser (MEA) (Vampola et al. 1992) measures electrons in the range 110–1633 keV in 17 energy bands plus one background channel. A detailed description of the instrument is given in Sect. 6.2.2.

9.1.1 Background subtraction

The detector uses a system of measuring the energy twice. The deflection of the incoming electron in the magnetic field acts as the first energy measurement. The second energy measurement is provided by the pulse height produced in the solid-state detectors. This measurement is used to provide on-board noise rejection. Pulses corresponding to energies significantly above the nominal energy being selected by magnetic deflection are assumed to be due to highly ionizing particles, such as protons, and are rejected. A lower pulse height threshold is also set. This is well below

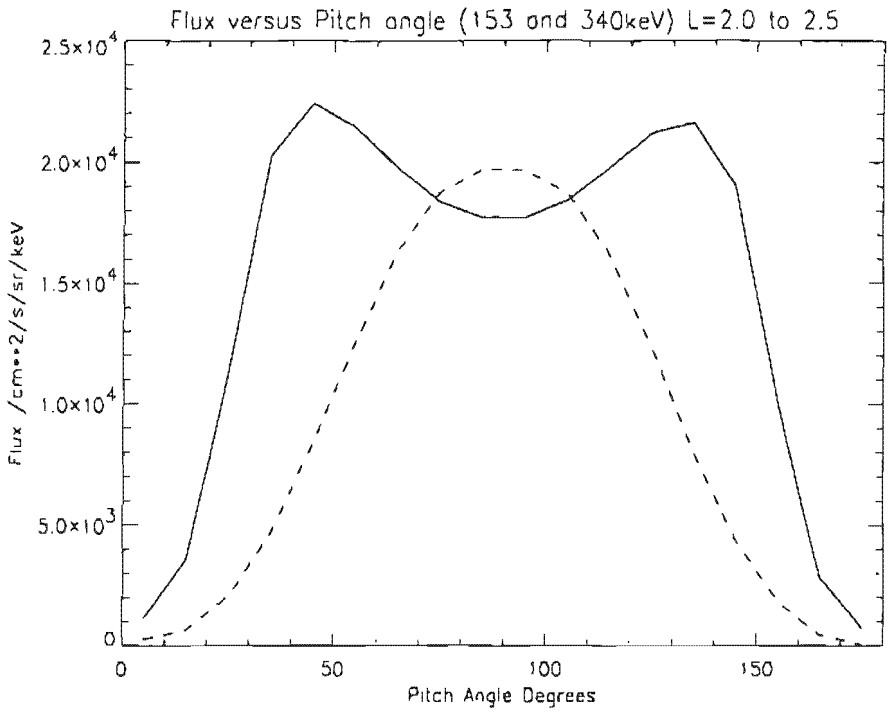

Figure 9.1. Pitch angle distribution for $2.0 < L < 2.5$ for energies 153 keV (solid line) and 340 keV (dashed line)

the nominal energy so that electrons which backscatter out of the detector without depositing much energy are still detected. Of the 18 energy bins, the 17^{th} acted as a background channel. Noise is believed to come from two sources, high energy particles and Bremsstrahlung radiation.

In the inner radiation belt, the background channel is expected to underestimate the noise levels, especially in the higher energy channels. In the outer radiation belt, real noise levels are expected to be lower than that seen in the background channel, particularly at lower energies. To account for this the following background subtraction algorithm is used:

$$\text{counts} = \text{measured counts} - (\text{background counts} \times \text{scale factor}) . \tag{9.1}$$

The scale factor has different values in the inner and outer radiation belts.

9.1.2 Counts saturation

The fluxes observed by the MEA in the inner radiation belt were so high that effects of detector dead time became significant. This dead time had been well calibrated on the ground so that tables of true flux versus counted flux were available to correct the

count values. The limit of this process occurs when total count saturation occurs and the observed count rate thereafter decreases as the real count rate increases further. This cannot be corrected by calibration because the function describing real counts in terms of observed counts is double valued. Figure 9.1 shows, as a solid line, the pitch angle distribution of flux between $L = 2.0$ and 2.5 for the lowest energy channel. Despite correction for deadtime effects up to total saturation, the fluxes are severely depressed about 90° whereas the true fluxes are expected to peak at this value. They are seen to peak here in higher energy channels such as the 340 keV channel plotted as a dashed line. This pitch angle data provides a possible way of correcting the data. As will be shown later, the pitch angle distribution is similar over a wide energy range and the pitch angle curve at a higher energy can be applied to the lower energy channels.

9.1.3 Field model calculation

The CRRES data come with some field parameters calculated at Phillips Lab. These use the IGRF 85 internal field model and the quiet Olson & Pfitzer (1977) external field model. The external field model does not depend on K_p.

9.2 Reduced database calculation

The CRRES MEA database is extremely large. 313 orbits have been copied to 12 sides of magneto-optical disks. First analyses of data in terms of local time etc. were carried out using the raw data. Even on a fast Alpha machine, this analysis took about 2 hours per disk side. The slowness of this processing has much to do with the fact that byte order swapping is being done on every data point. This is different for different data types. Also the lack of record structure in PC created files means that each block is read into a huge array and each data value has to be extracted individually from it. This also involves the manipulation of counters to keep track of where in the block array the next data are to be found. This extreme slowness meant that few different statistical studies would be possible from the raw data.

It was therefore decided that a reduced database would be needed to speed up data processing. A program, called `BLCRRESBIN`, was written. Its functions were as follows:

- Read data from the .MEA files, extracting the data values from the block array and reversing byte order as appropriate.
- Calculate, for every data point, auxiliary parameters such as B and L.

Table 9.1. Output parameters for the reduced MEA data files

Parameter	Units	Comment
Time	min	minutes of day
L	R_E	Phillips Lab calculation
B	nT	Phillips Lab calculation
B_0	nT	Phillips Lab calculation
longitude	degrees	
latitude	degrees	
altitude	km	
B	nT	BLXTRA calculation
B_0	nT	BLXTRA calculation
local time	hours	
$B_m(18)$	nT	Derived from Phillips Lab B
$\alpha_0(18)$	radians	Derived from Phillips Lab B
$B_m(18)$	nT	Derived from BLXTRA B
$\alpha_0(18)$	radians	Derived from BLXTRA B
$L_m(18)$	R_E	BLXTRA calculation
Flux(18,18)	$cm^{-2}s^{-1}sr^{-1}keV^{-1}$	Flux for each energy and pitch angle

- Bin the data into 5 minute averages.
- Write the data in record-structured VAX byte-ordered format.

The resulting files are small enough so that all 313 files fitted comfortably onto one magneto-optical disk side. The five minute averaging is rather coarse for the period close to perigee because the spacecraft moves a considerable distance in that time. However, except for these lowest altitude measurements it is satisfactory. Since our interest in this study is primarily with the outer radiation belt, we consider this time binning acceptable. The output parameters are listed in Table 9.1. The (B, L) calculations were performed with BLXTRA using the Tsyganenko (1989) external field model and IGRF 85 internal model.

9.3 Large-scale dependences

9.3.1 Energy spectrum

Figure 9.2 shows the mean energy spectrum between $L = 4.0$ and $L = 4.5$. Also plotted in this figure is the standard deviation of the data. The spectrum becomes

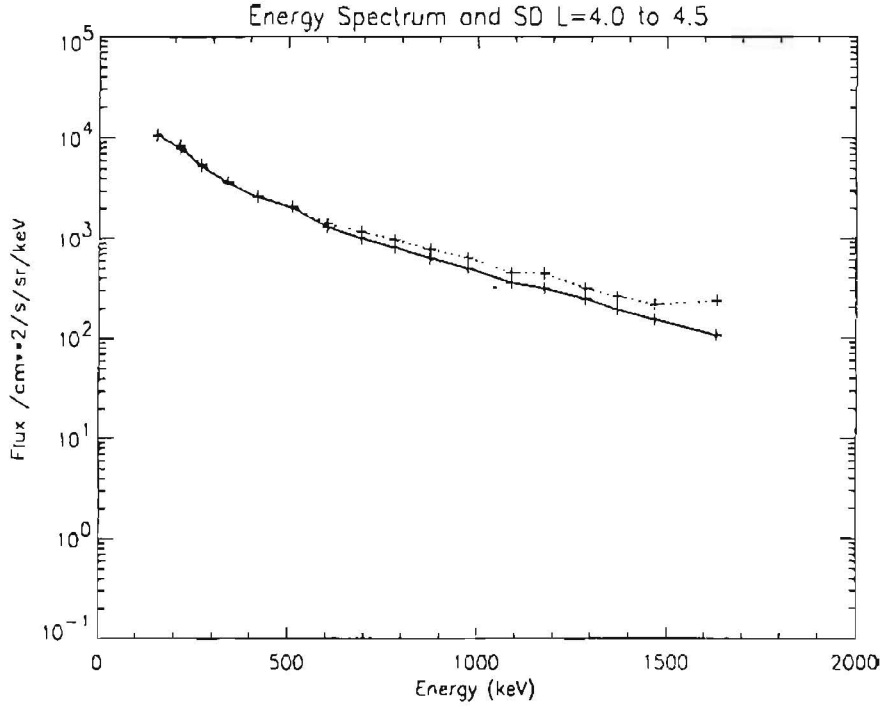

Figure 9.2. Energy spectrum for $4.0 < L < 4.5$

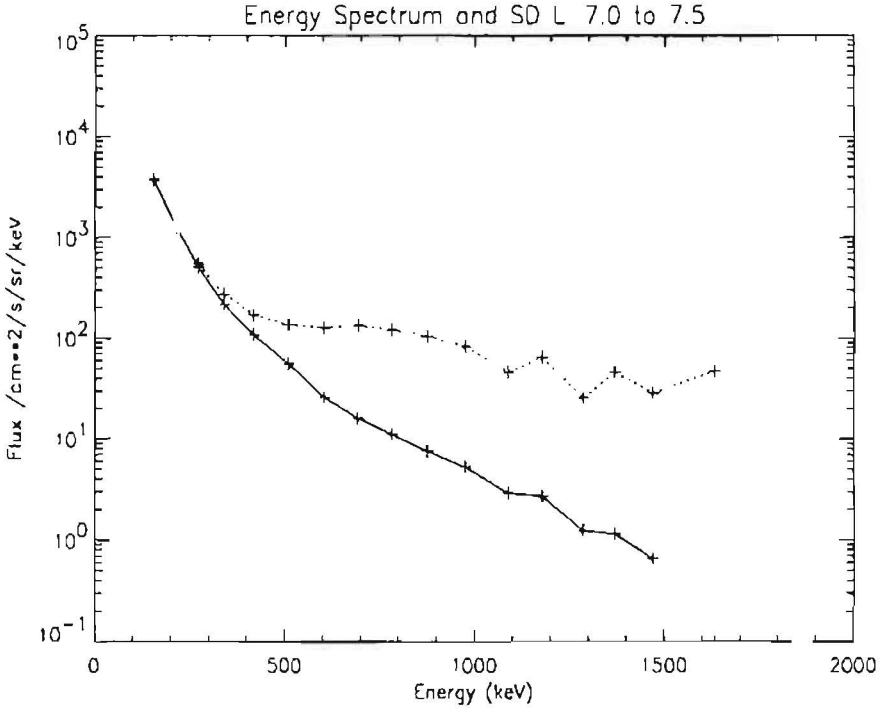

Figure 9.3. Energy spectrum for $7.0 < L < 7.5$

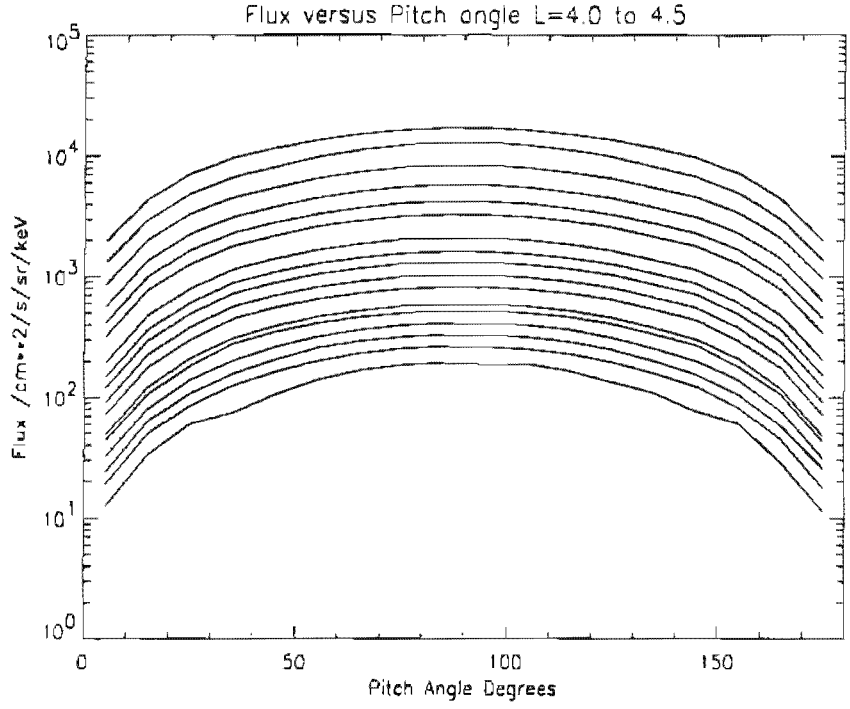

Figure 9.4. Pitch angle distribution for $4.0 < L < 4.5$

progressively steeper (softer) at higher L values however and whilst the spectrum is reasonably well approximated by a log function for lower L values, this becomes increasingly untrue for higher L. Figure 9.3 shows the spectrum for $7.0 < L < 7.5$. The standard deviation increases as a fraction of average flux as energy and L increase. It appears that there is a constant level below which the standard deviation will not fall, even if fluxes are very low. It is likely that this is the standard deviation of the subtracted background. This has important consequences for the ability of MEA to measure natural standard deviations and must be borne in mind where standard deviation is being used to assess appropriate coordinate systems for models.

9.3.2 Pitch angle dependence

Figure 9.4 shows the dependence of flux on pitch angle in the L range between 4.0 and 4.5. All 17 energies of the instrument are shown, with the lowest energy at the top and descending in order of energy so that the highest energy is at the bottom. The flux is highest at 90° and lowest near the loss cones. This behaviour is typical of plasma that is stably trapped. All 17 energy channels have a similar pitch angle variation which means that the pitch angle variation of higher energy channels could be used to improve low energy data when counts saturation occurs.

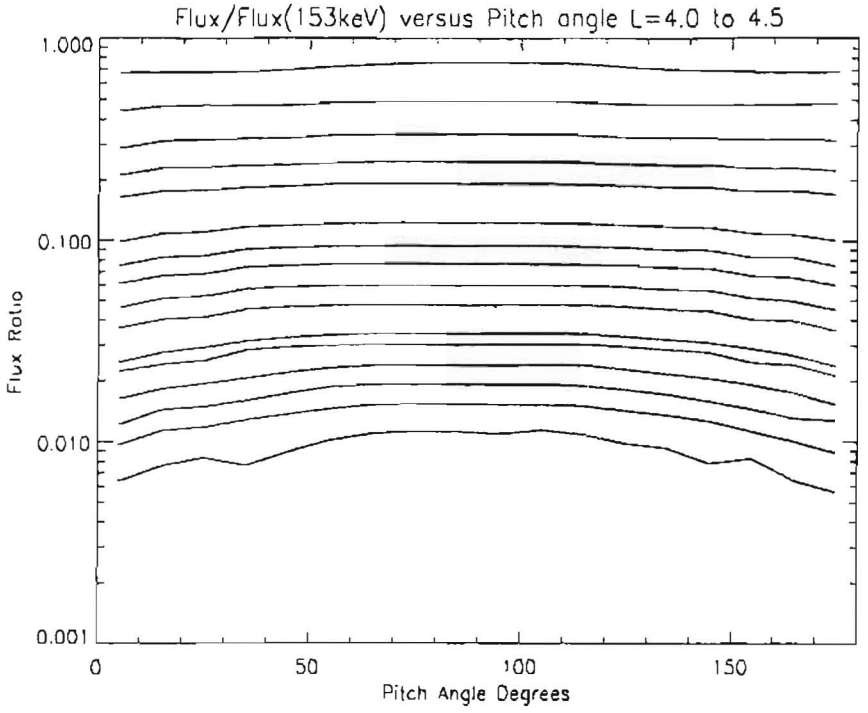

Figure 9.5. Pitch angle distribution of flux divided by flux in the lowest energy channel for $4.0 < L < 4.5$

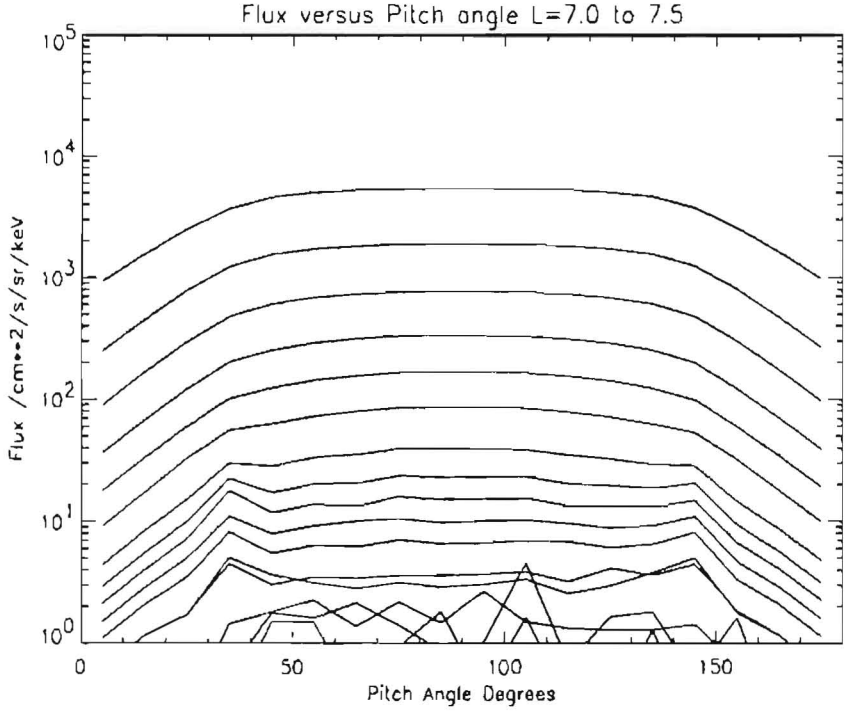

Figure 9.6. Pitch angle distribution for $7.0 < L < 7.5$

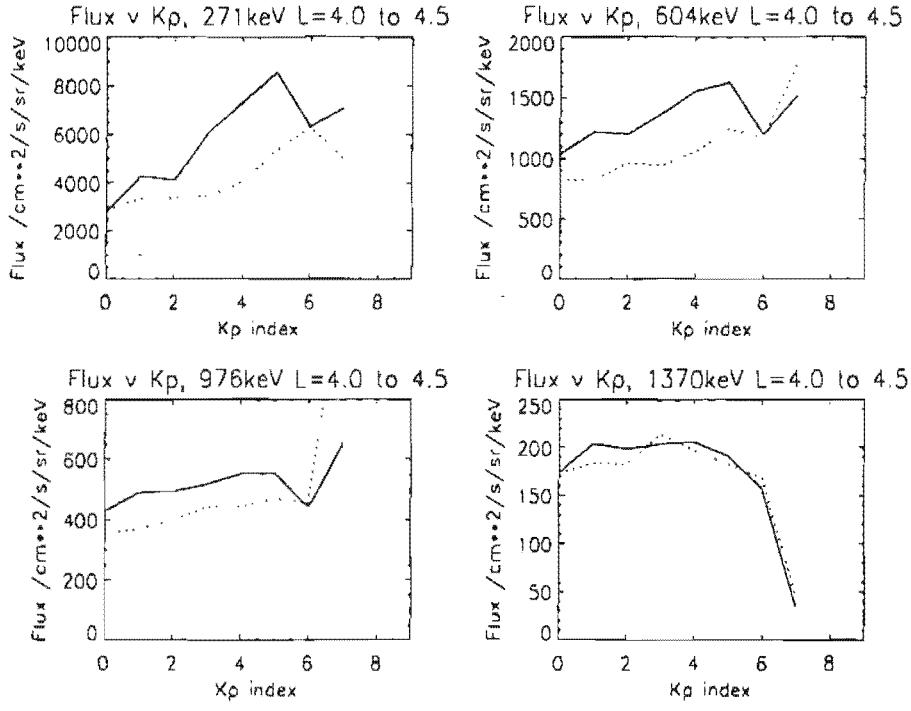

Figure 9.7. Dependence of average flux (solid line) and its standard deviation (dotted line) on K_p, for 271 keV, 604 keV, 976 keV and 1370 keV with $4.0 < L < 4.5$

Figure 9.5 shows the ratio of fluxes in the 17 highest energy channels as a fraction of the flux in the lowest, 153 keV, channel. The flux in the next lowest energy channel shows an increase at 90° indicating that the lowest channel may experience some counts saturation effects even in this L shell range. At the highest energies the fall-off around the loss cone becomes steeper than at low energy, indicating that the pitch angle diffusion rate increases with increasing energy.

Pitch angle distributions for $5.0 < L < 5.5$ and $6.0 < L < 6.5$ were very similar to $4.0 < L < 4.5$. However, deviation from this pattern was seen at $7.0 < L < 7.5$, as shown in figure 9.6. This shows peaks around 35° and 145° for the higher energies. This agrees with the observation of "butterfly distributions" reported by other researchers.

9.3.3 Magnetic activity

Figure 9.7 shows 4 plots of isotropic fluxes averaged over the L range of 4.0 to 4.5. Flux as a function of K_p at each of four energies is represented by a solid line with the standard deviation shown by a dotted line. No periods of K_p greater than 8 were observed. At 271 keV there is a trend for flux to increase with increasing K_p.

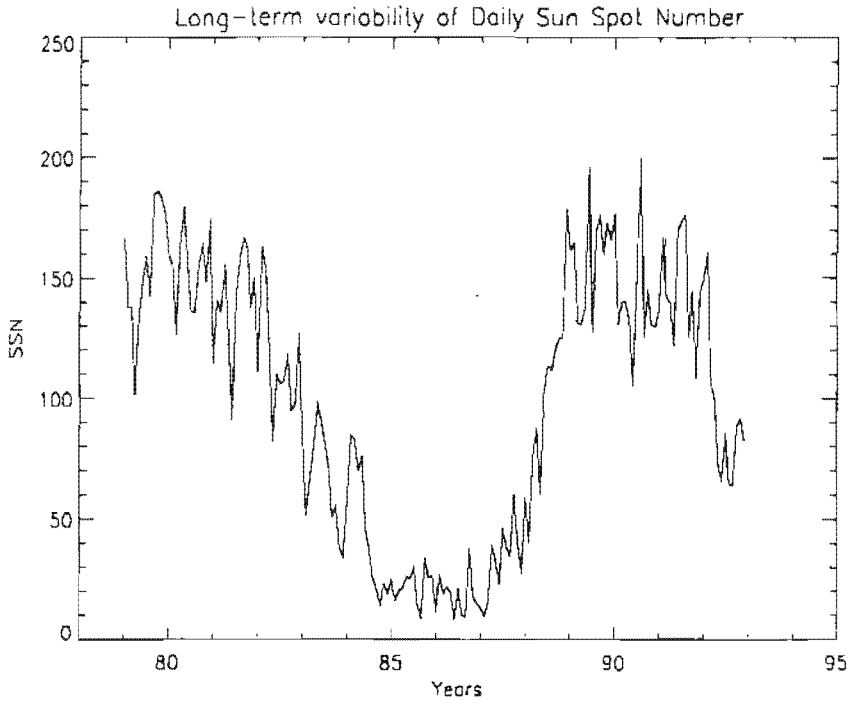

Figure 9.8. Daily sunspot number plotted as monthly averages

As energy increases the slope of the flux rise becomes smaller, as seen at 604 keV and 976 keV. At higher energies still, flux is independent of K_p below $K_p = 4$ but falls steeply at higher values.

9.3.4 Solar cycle variations

The Sun goes through an 11 year cycle during which the change in the number of sunspots is the most obvious feature. Changes in solar wind conditions are known to follow a similar cycle and changes in magnetospheric conditions are driven by the solar wind. Figure 9.8 shows the sunspot number as a monthly average of daily values plotted from 1979 to 1992. Solar maximum occurs around 1980 and 1990, with solar minimum around 1986. The cycle is not symmetric, with a gradual fall from maximum to minimum but a rapid rise back up again.

The lifetime of CRRES was quite short compared to the solar cycle but SEM-2 on Meteosat-3 had data coverage lasting several years. SEM-2's highest energy bin (202–300 keV) was most representative of the radiation belts and corresponded closely in energy to one of the energy bins (200–300 keV) of the LANL instrument which was flown on several geostationary satellites. It was shown in Technical Note 8 that an excellent qualitative agreement existed between fluxes in the 200–300 keV

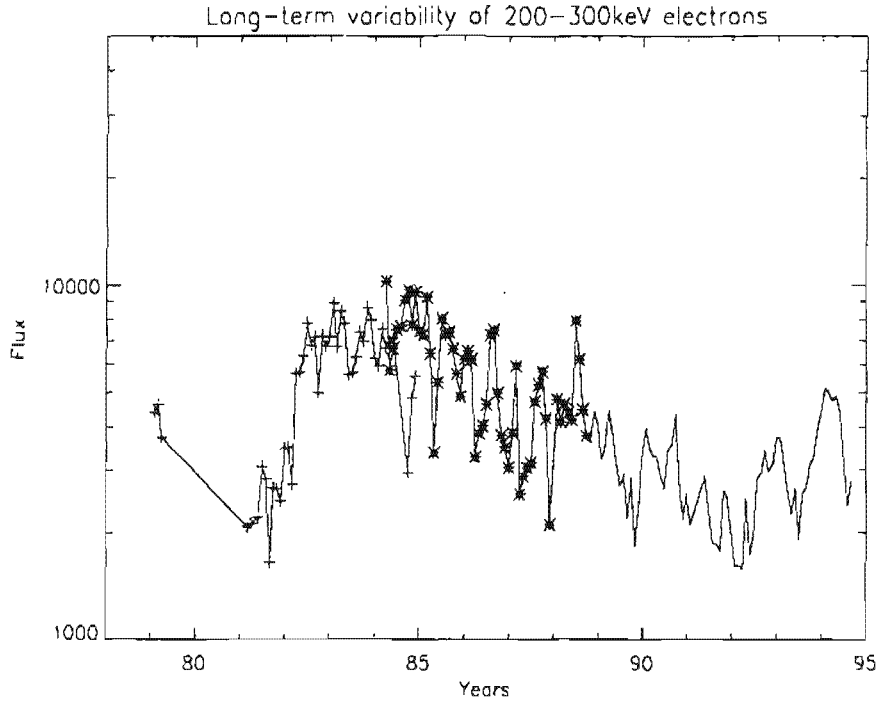

Figure 9.9. Combined plot of fluxes from LANL 1981-025 (+), LANL 1984-037 (*) and SEM-2 (solid line)

range of the LANL instrument on 1984-037 and the 202–300 keV range on SEM-2 during October 1988. The LANL fluxes were, however, on average 3.78 times higher than SEM-2's. The LANL data were reduced by this factor to bring them into quantitative agreement with SEM-2. LANL data from 1981-025 was used to further extend the data range. No direct comparison with SEM-2 was possible since there was no overlap in time. Where the 1984-037 and 1981-025 data overlapped, individual months differed but there was a rough agreement in flux levels. Because of this, the same factor was applied to the 1981-025 data to give a combined data set over 15 years long. These data are plotted in Fig. 9.9. This shows apparent minima in 1981 and 1992 and a maximum around 1985. This is in approximate antiphase with the sunspot number. This is in agreement with AE-8 predictions, which shows lower fluxes at solar maximum than minimum, at this energy and position. At lower L values, AE-8 predicts the opposite relation.

9.4 Comparisons of coordinate systems

The CRRES MEA data set is ideal for inclusion in new models of the magnetosphere. As it is impossible to make simultaneous radiation measurements across the entire

magnetosphere it is necessary to group data points from different times and locations together. The choice of parameter that is used to group data points together is what we mean here by coordinate system. To get the expected flux from such a model, it is simply a matter of converting the desired satellite position into the coordinate system. The choice of coordinate can make a large difference to the model's accuracy and usefulness. The most popular existing models are organised in terms of the magnetic field intensity B and McIlwain's (1961) L parameter. However, there are several reasonable variations on a simple B, L coordinate system and since there is an infinity of bin sizes, there is an infinite number of different ways to organise the data.

We would expected a good outer radiation belt coordinate system to:

1. cover the outer radiation belt well,
2. probably produce systematically varying fluxes,
3. group high fluxes with high fluxes and low with low,
4. be simple to use.

In this section we have chosen several possible coordinate systems to test. All use the L parameter. In the database L was calculated at the spacecraft location and at the particle mirror point using the Olson & Pfitzer (1977) quiet model and the Tsyganenko (1989) model respectively. However, no significant differences were found between these values and so only one version of L will used in the data presented here. In contrast, there is generally a large difference between B at the spacecraft and mirror point.

9.4.1 Local time and L

Experience with data from the Meteosat-3 geostationary satellite showed that local time (LT) was a good parameter for organizing the data. In this section we investigate whether we could simply use local time and L to cover the entire outer magnetosphere. This coordinate system would be very simple to use. We chose bin sizes of $\Delta L = 0.5$ and 0.5 hours in local time. Figure 9.10 shows, as a grey-scale plot, the fluxes in each bin in the 976 keV energy channel. A box has been drawn round each bin with more than 10 data samples and all others have been set to zero. It is clear that the model does not cover the outer or inner magnetosphere well. The strange distribution of bins arises because the spacecraft trajectory follows a sinusoidal track in (LT, L) space that only gradually evolves with time. Because some of the data come from early in the mission and some later on, there are two distinct lobes to the data. This means that this coordinate system tends to alias spatial variation with long-term temporal changes.

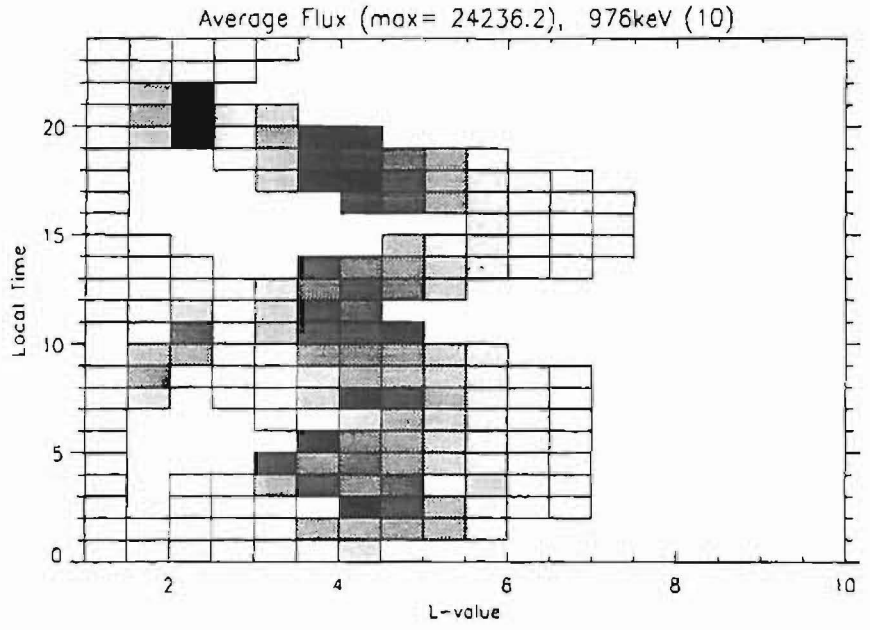

Figure 9.10. Greyscale plot of average fluxes at 976 keV, binned in the (LT, L) coordinate system

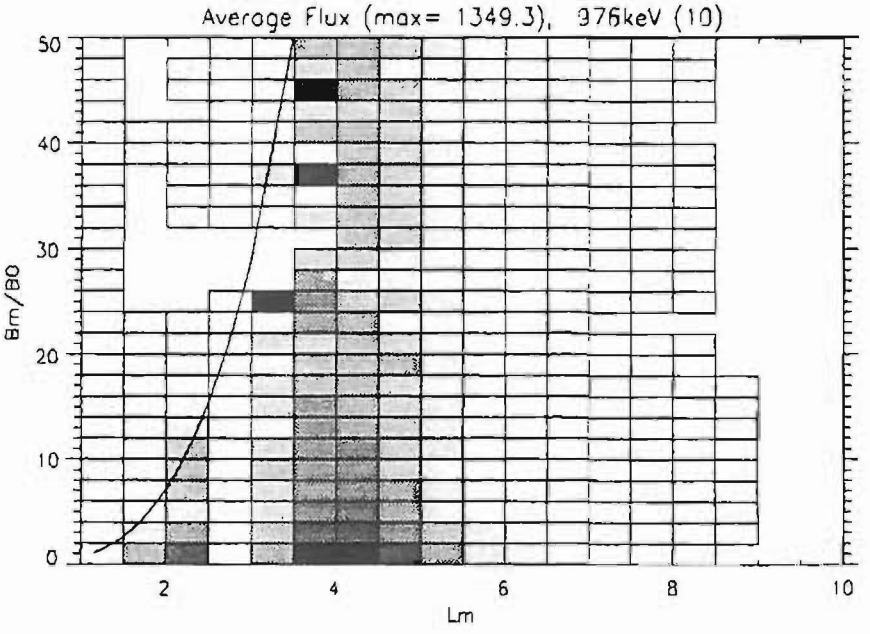

Figure 9.11. Greyscale plot of average fluxes at 976 keV, binned in the $(B_m/B_0, L)$ coordinate system

9.4.2 B_m/B_0 and L

The coordinate pair (B_m, L) are adiabatic invariants. With Def. (3.17), B_0 also is an adiabatic invariant since it only depends on L. Hence the B_m/B_0 system is a logical candidate. For this coordinate system, we used a bin size of $\Delta B_m/B_0 = 2$ and $\Delta L = 0.5$. Figure 9.11 shows, in the format used in Fig. 9.10, the average fluxes in the 976 keV channel. Also plotted, as a dotted line, is the atmospheric cut-off magnetic field intensity, transformed into this coordinate system. Vette's (1991a) formula for B_c/B_0 is used:

$$\frac{B_c}{B_0} = \begin{cases} 0.6572\, L^{3.452} & 1.2 < L < 3.23 \\ 1.0523\, L^{3.050} & 3.23 < L\,. \end{cases} \tag{9.2}$$

One can see in Fig. 9.10 that the coverage of all space is not complete but most of the gap occurs within the loss cone, where fluxes are expected to be very small anyway. Two distinct radiation belts are visible and the cut-off of the inner belt at the edge of the loss cone is clear. This cut-off is evidence that the data from the inner radiation belt is really electron data and not noise produced by contamination from energetic protons. Such contamination would be more or less isotropic. In the outer belt fluxes are highest at low values of B_m/B_0, apart from a few "rogue" points.

Because of the parabolic shape of the loss cone boundary in this coordinate system it is very hard to cover both inner and outer radiation belts. The bin size chosen covers the inner belt only coarsely and yet 25 such bins do not extend as far as the loss cone in the outer belt.

9.4.3 $\log(B_m/B_0)$ and L

To counter the problem of the (B_m, L) coordinate system in adequately covering the inner and outer radiation belts, the $[\log(B_m/B_0), L]$ system was used. As is shown in Fig. 9.12, the loss cone no longer rises steeply in the outer radiation belt. The chosen bin size was $\Delta \log(B_m/B_0) = 0.2$ and $\Delta L = 0.5$. The inner belt is still coarsely sampled. Because the outer belt is no longer over-sampled, the systematic increase in flux as one approaches $B_m/B_0 = 0$ is clearer than in the $(B_m/B_0, L)$ case. The fluxes are seen to extend well into the loss cone in the outer belt. This result is unlikely to be true and arises from the limited pitch angle resolution of the instrument which is made worse by the coarse binning of the reduced database. Near 90° pitch angle, a small change in pitch angle leads to a large change in $\log(B_m/B_0)$.

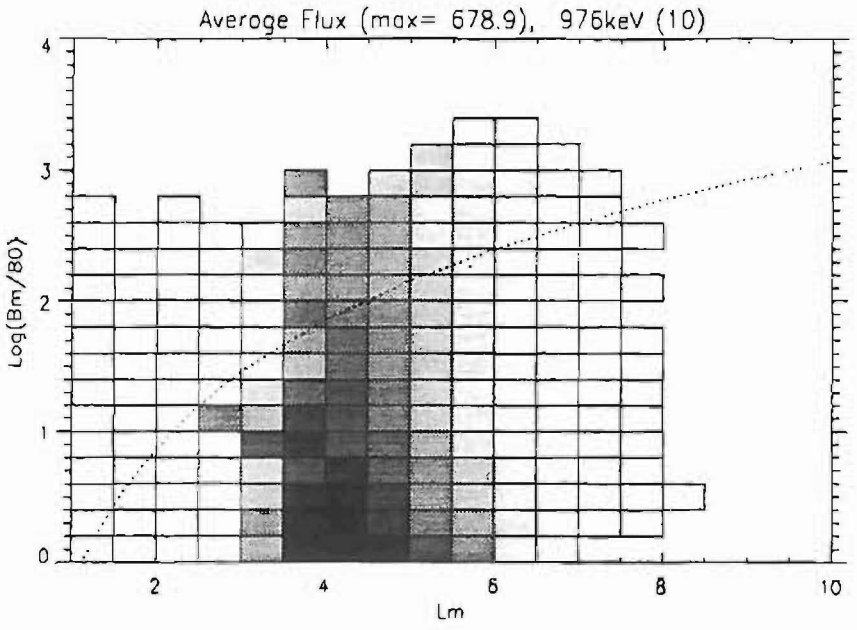

Figure 9.12. Greyscale plot of average fluxes at 976 keV, binned in the $[\log(B_m/B_0), L]$ coordinate system

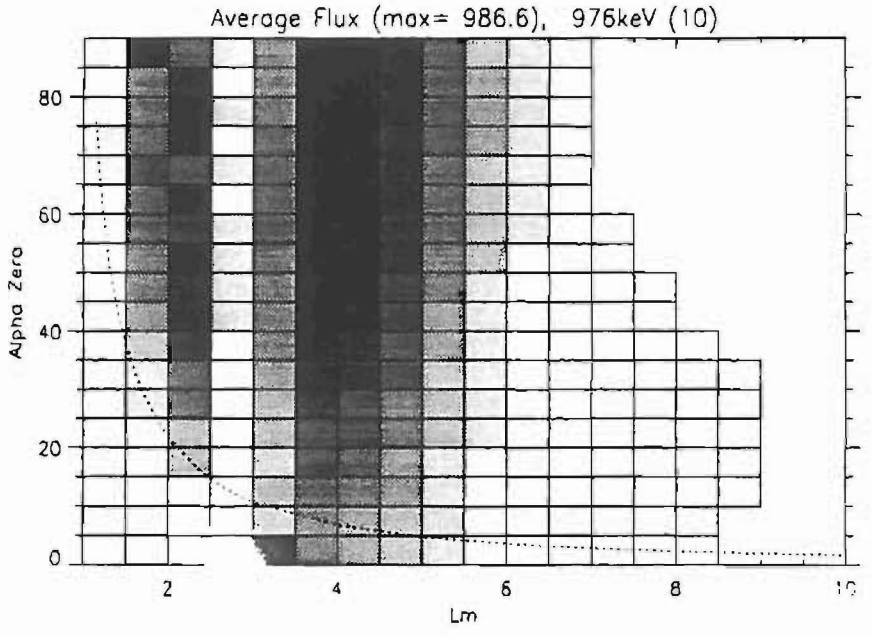

Figure 9.13. Greyscale plot of average fluxes at 976 keV, binned in the (α_0, L) coordinate system

9.4.4 α_0 and L

The final coordinate system used the equatorial pitch angle α_0 of the observed particles and L. There is no new information used in employing this coordinate system because α_0 is simply a function of B_m/B_0:

$$\alpha_0 = \sin^{-1}\sqrt{\frac{B_0}{B_m}}. \tag{9.3}$$

Figure 9.13 shows the average fluxes at 976 keV binned in this coordinate system. The bin sizes were $\Delta\alpha_0 = 5°$ and $\Delta L = 0.5$. The coverage of the radiation belts is complete and gives more equal resolution in the inner and outer belts than the $[\log(B_m/B_0), L]$ system. The systematic variation in both the inner and outer belts is very clear. Fluxes again extend into the loss cone in the outer belt but only by one or two bins because the bin size is more in keeping with the accuracy of the data.

9.4.5 Standard deviation

The standard deviation provides a measure of the variability of individual measurements that went into one binned average. Since we are looking for coordinate systems that group similar fluxes together, we can use lowness of standard deviation as a measure of the effectiveness of the coordinate system. However, as well as depending on the coordinates, standard deviation will also be affected by the bin size, the noise level and temporal variations that are unconnected with the magnetospheric magnetic field structure.

In this study, standard deviation was calculated routinely but there was found to be little difference between different coordinate systems. It was believed that the temporal variability of the data was masking any benefits of an improved coordinate system. To lessen this effect, data were selected for times when K_p was less than 1. We also compared standard deviations for a low energy channel so that the effects of noise level would be smaller but not so low that count saturation effects would be seen. Channel 5, at 510 keV, was chosen.

Figures 9.14 and 9.15 show the standard deviation divided by the mean flux for the $[\log(B_m/B_0), L]$ and (α_0, L) coordinate systems. The $[\log(B_m/B_0), L]$ system has low standard deviation above $L = 4$ and at the peak of the inner radiation belt. The (α_0, L) system has low standard deviation above $L = 4$. Thus in the outer magnetosphere there is little to distinguish these two systems by this test. It does however, warn us that models produced in this way will be most appropriate for the outer belt. The poorer behaviour at lower L values is probably due to the coarse time binning of the original database.

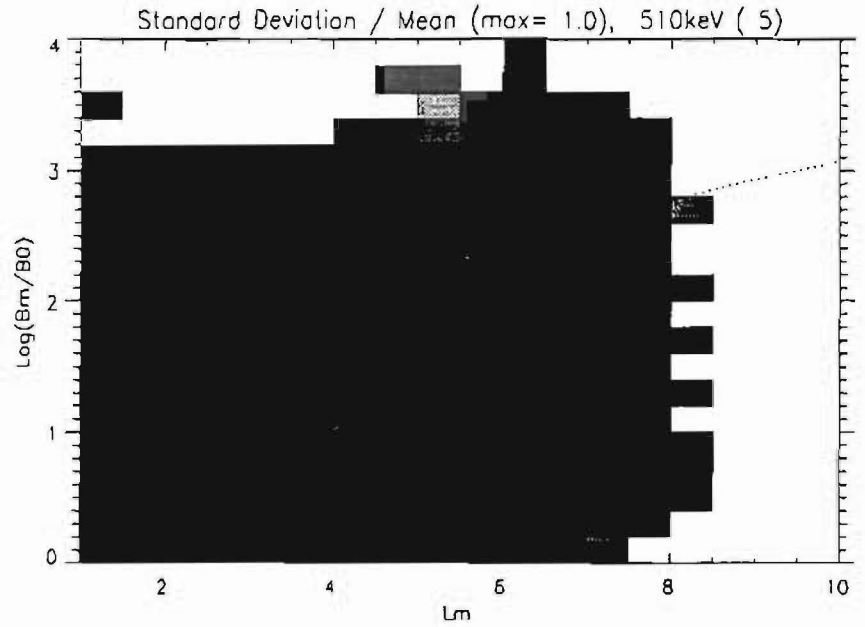

Figure 9.14. Greyscale plot of the standard deviation of fluxes at 510 keV, binned in the $[\log(B_m/B_0), L]$ coordinate system

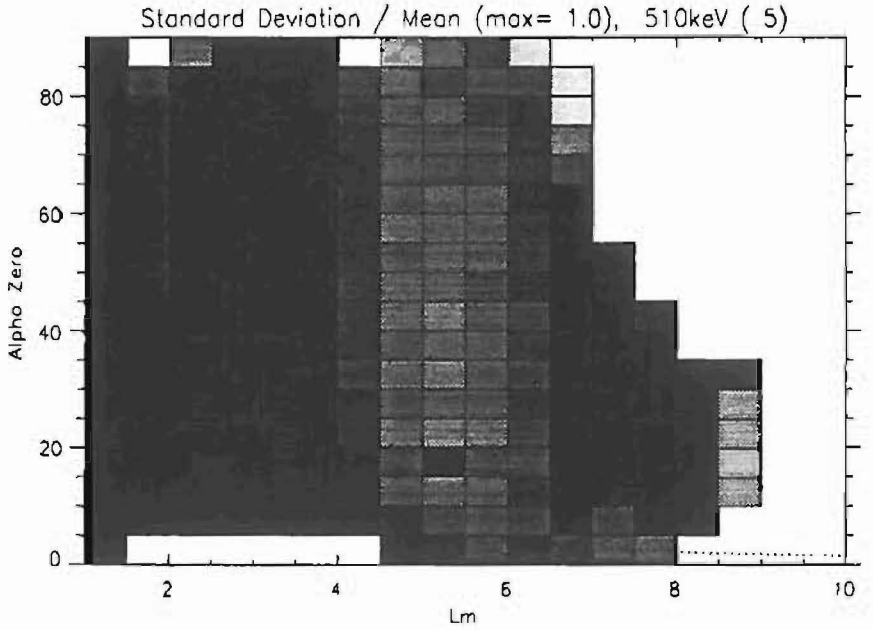

Figure 9.15. Greyscale plot of the standard deviation of fluxes at 510 keV, binned in the (α_0, L) coordinate system

Table 9.2. Evaluation of the different coordinate systems

System	Coverage	Systematic	S.D.	Simplicity
(LT, L)	Bad	Bad		Easy
$(B_m/B_0, L)$	Poor	OK		OK
$[\log(B_m/B_0), L]$	Good	Good	OK in outer	OK
(α_0, L)	Good	Good	OK in outer	OK

9.4.6 Coordinate conclusions

To draw a conclusion about which coordinate system is 'best' requires value judgements about how to weight their different characteristics. We have attempted to summarize these characteristics in Table 9.2.

It seems obvious however that the (LT, L) system is not good enough, despite being mathematically simpler than its rivals, because its coverage of the magnetosphere is too incomplete. It showed little evidence of systematic changes in flux from one area to the next, presumably because of aliasing between time and location. Similarly, the $(B_m/B_0, L)$ model fails because of the difference in resolution of the inner and outer belts if a constant bin size is used. Both the $[\log(B_m/B_0), L]$ and (α_0, L) systems had good coverage, produced systematic flux variations and acceptable standard deviation in the outer belt. There is little quantitatively to distinguish these two. However, the (α_0, L) system is much simpler to visualise. In addition, for near-equatorial input data, this system does not exaggerate the data resolution in the loss cone. Hence we strongly recommend the use of this system in further development of outer radiation belt models from the CRRES data set.

9.5 Outer radiation belt model development

This section is a summary of work described in detail in Technical Note 10. The models developed were from the 313 orbits in the new database. It is intended that the models shall be improved in a following study, when a new database, with higher time resolution, more data and correction for counts saturation is available.

9.5.1 Introduction

The AE-8 model (Vette 1991a) is the most widely used and respected electron radiation belt model in current use in the West. It covers the inner and outer radiation

belts between L values 1.2 and 11.0 with energy range from 0.04 MeV to 7.0 MeV. However, the data used to create the model comes from the 60's and 70's. One goal of this study was to create a new model based on more recent data. Because CRRES had a good complement of radiation belt instruments and passed through both belts, it has provided an ideal data source for the development of new models. It should be noted that other models based on the CRRES HEEF instrument have been developed (e.g. Brautigam et al. 1992) and these cover higher energy fluxes.

We had two goals in forming a new model: to make it easy to compare with AE-8 and to use the best available coordinate system. It was decided that these goals were not compatible and so two models were developed, one using $(B/B_0, L)$, as in AE-8, and the other using (α_0, L).

9.5.2 A new AE-8 compatible model

The AE-8 model characterises omnidirectional integral fluxes as a function of particle energy, B/B_0 and L. It was decided that maximum ease of use would be obtained if a new model presented the same parameters in a similar coordinate system. The new model could then be introduced into existing software by replacing a single block of data statements.

AE-8 Data processing

The AE-8 data come primarily from the Proton-Electron detector on AZUR, the Electron Spectrometers on OV1-19 and OV3-3, and the Omnidirectional Spectrometers on ATS-5 and ATS-6 Vette (1991a). In addition, empirical functions from an earlier model (AE-4) were used in the data processing.

For each omnidirectional AZUR flux measurement, the corresponding B, L and local time were calculated. The magnetic field parameters were derived from an internal magnetic field model only. The data were first transformed to the same local time by dividing the fluxes by an empirical function Φ:

$$\Phi(>E, J, \phi) = K(>E, L)\, 10^{C(>E,L)\cos(\pi(\phi-11)/12)}. \tag{9.4}$$

This is of the same form as used in AE-4 but the parameters $C(>E, L)$ and $K(>E, L)$ were obtained by fits to the AZUR data when plotted as fluxes versus local time. The fluxes were then transformed to the equator (where $B/B_0 = 1$) by dividing by the function G, defined as:

$$\left.\begin{aligned} G(b, L) &= b^{-m(L)} \left(\frac{b_c - b}{b_c - 1}\right)^{m(L)+0.5} && b < b_c \\ G(b, L) &= 0 && b \geq b_c \end{aligned}\right\}, \tag{9.5}$$

Table 9.3. AE-8 Data format

Outer loop	Middle loop	Inner loop	
length			number of bytes for this energy
energy 1			energy in MeV × 6400
	length		number of bytes for this L value
	L 1		$L \times 2100$
	flux		Log(flux)×1024
		B/B_0	Value corresponding to a decrease in log flux of 0.25× 1024

where $b = B/B_0$. The empirically fitted values of m came from AE-4. b_c came from fitting the AZUR data so that nearly all the data points with significant flux had $b < b_c$.

The data from the OV-19 electron spectrometers were unidirectional and subject to considerable background noise. The data were projected to the same local time at the equator using similar equations to the AZUR data except that a unidirectional form of Eqs. (9.5) was used. The fluxes were normalized according to the AZUR fluxes above 4.5 MeV to remove the effects of noise. A similar technique was used for OV3-3. The ATS-5 and ATS-6 data were cross calibrated and used as omnidirectional fluxes.

The output of this model comprised the equatorial fluxes as a function of L and the dependence of these fluxes on B/B_0. Since the equatorial fluxes were obtained from local fluxes via Eqs. (9.5), a function of B/B_0, there is a circular element to this processing since the found B/B_0 dependence must to some extent depend on G.

AE-8 Model format

The most natural way to store a model organized in B/B_0 and L is as a 2-D array of fluxes binned according to these parameters. However AE-8 was written at a time when computer memory and storage was very limited and so much effort went into creating a more compact model. The model data were written in FORTRAN as a single `BLOCK DATA` statement, the format of which is described in Table 9.3.

All the parameters are stored as `INTEGER*2` bytes. The table loops over all the energy, L and B/B_0 values. The values of the scaling factors for energy, L, B/B_0 and log(flux) are given in `DATA` statements contained within the same `BLOCK DATA` segment.

MEA Data processing

The MEA fluxes are unidirectional and differential in energy. For unidirectional data with good angular coverage, the use of empirical approximations was not necessary since there is enough information to determine the omnidirectional flux everywhere along a field line. Hence, although the new model has been designed to be as similar to AE-8 as possible, the way in which it was produced was completely different.

The differential flux in each energy bin was first converted to integral flux. For the highest energy bin, a nominal bin width of 100 keV had to be assumed.

The data from 313 CRRES orbits were summed according to the (α_0, L) coordinate system described earlier. The range of the data was restricted to L between 3 and 8 because of the problems associated with the coarse temporal binning of the data and saturation of low energy channels which both become significant at lower L values. The energy range was limited to the first 16 energy bins, i.e. 153–1470 keV.

No explicit treatment of local time effects was performed. This was because we used a realistic magnetic field model [IGRF 85 internal field plus the quiet Olson & Pfitzer (1977) external field]. AE-8's need to describe local time variation arose because only an internal field model was used.

Omnidirectional fluxes at the equator were simple to find, since the summed data are stored as a function of equatorial pitch angle. The fluxes are simply summed over all pitch angles. Account must be taken of the total solid angle subtended by each pitch angle bin, which is approximately $2\pi \sin\alpha_0$:

$$J(>E,L) = 2 \sum_{\alpha_0=0^\circ}^{90^\circ} J(>E,L,\alpha_0)\,\Delta\alpha_0\, 2\pi \sin\alpha_0 \,. \tag{9.6}$$

At a location away from the equator we transform the equatorial pitch angles to their values at this location, specified by B/B_0. The transformed pitch angle α_T is given by:

$$\alpha_T = \arcsin\left(\sin^2\alpha_0 \sqrt{\frac{B}{B_0}}\right) . \tag{9.7}$$

In order to calculate the omnidirectional flux away from the equator we use the solid angles subtended by the transformed pitch angle bins. The total flux is simply given by:

$$J(>E,L) = 2 \sum_{\alpha_T=0^\circ}^{90^\circ} J(>E,L,\alpha_0)\Delta\alpha_T\, 2\pi \sin\alpha_T \,, \tag{9.8}$$

where α_T is the local pitch angle calculated by transforming α_0 to the local position. Figure 9.16 shows the omnidirectional log(flux) distribution. The fluxes are calculated at positions along each field line where different values of α_0 mirror and

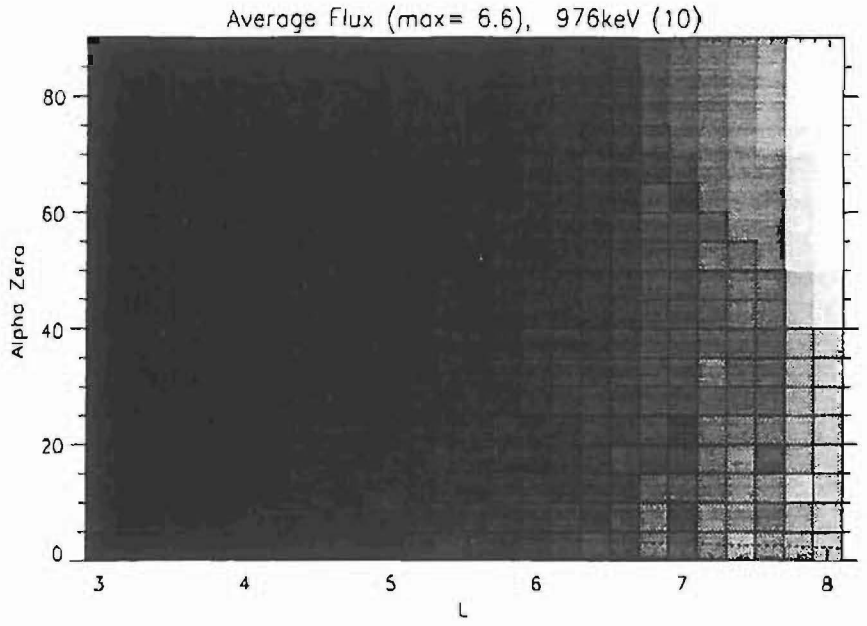

Figure 9.16. Omnidirectional log(flux) at 976 keV (see text for explanation of α_0 axis)

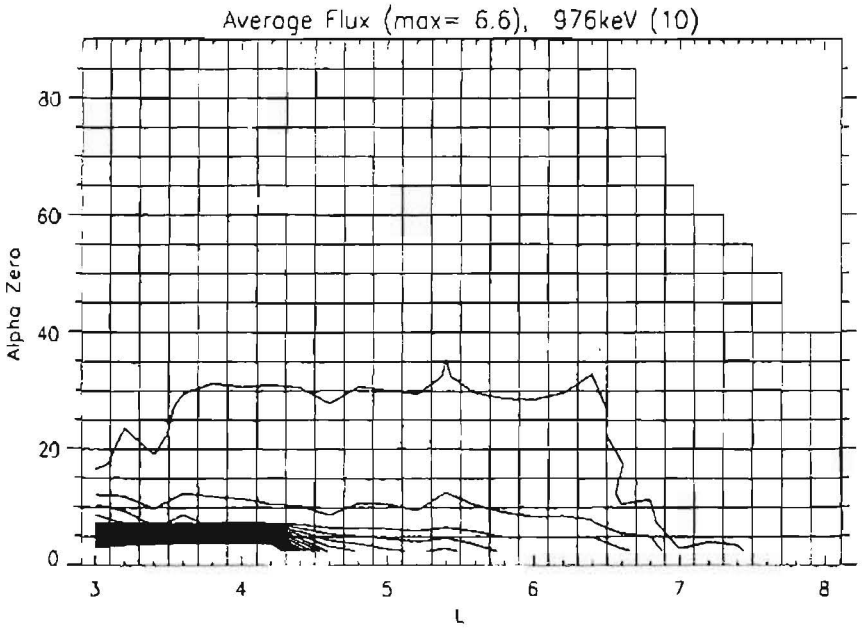

Figure 9.17. Contour plot showing contours at 0.25 intervals from the value of log(flux) at $\alpha_0 = 90°$

it is this α_0 value that is used as the abscissa. The data coverage is not complete in pitch angle above $L = 6.5$.

The data in figure 9.16 shows that omnidirectional flux decreases towards 0°, except at low L values where there are some high fluxes at low equatorial pitch angle. These data lie inside the loss cone where fluxes are expected to be very small. Significant fluxes appear here in the CRRES data because of the finite angular resolution of the instrument and of the summed database. Because the representation of the AE-8 model assumes that fluxes always decrease monotonically away from the equator, an AE-8 compatible model must not include fluxes that decrease and then increase. Because of this, fluxes within the loss cone are removed. The same simplification was made in the AE-8 data processing.

The value of α_0 corresponding to successive 0.25 decreases in log(flux) from the equatorial value was found by stepping through the α_0 array and doing a linear interpolation between the closest pair of values. Figure 9.17 shows contours at successive 0.25 differences from the 90° value. The values of B/B_0 at the mirror point corresponding to the α_0 contours in this plot were used for the model. Above $L = 6.5$ these contours are clearly affected by the incomplete α_0 coverage of the data, so the model is limited to the range $3 < L < 6.5$.

MEA Model format

From the data processing just described, the data to be included in the model are the equatorial omnidirectional integral log(fluxes) as a function of L and the values of B/B_0 corresponding to successive drops of 0.25 for each L value. These were written to a `BLOCK DATA` statement in exactly the same way as AE-8 for each energy.

9.5.3 A new model based on L_m and α_0

In the second model, we have not restricted ourselves to compatibility with AE-8 and have hence been able to choose a more natural representation of the data. The model consists of differential fluxes binned according to L_m (L evaluated at the mirror point) and the equatorial pitch angle α_0. Although we had found little quantitative difference between (α_0, L) coordinates based on the quiet Olson & Pfitzer (1977) model and (α_0, L_m) coordinates based on the Tsyganenko (1989) model, we used the latter model. The reasons for this were that: Tsyganenko (1989) is currently the most accurate model available, the value L_m is invariant whereas strictly L is not, Olson & Pfitzer (1977) does not account for magnetospheric activity.

Data processing

Differential unidirectional fluxes from the database were summed over the same 313 orbits as the model described earlier. K_p was used as an input to the Tsyganenko (1989) external magnetic field model. IGRF 85 was used for the internal part of the field model. B and L_m were calculated from this model using the BLXTRA subroutine. B_0 was determined using Eq. (3.17). The bin widths were $\Delta\alpha_0 = 5°$ and $\Delta L = 0.5$. The mean and standard deviation were calculated for all energies in each (α_0, L_m) bin.

Figure 9.18 shows mean fluxes and Fig. 9.19 the standard deviation at 976 keV. The standard deviation is intended to be used as a measure of the variability of the fluxes from the mean. However, when flux levels were low, e.g. at high energies or high L values, the statistics of the subtracted background counts become dominant. In other words, although the noise has been removed from the mean fluxes it has not been removed from the standard deviation. This is discussed in Sect. 9.3.1. This problem affects different data bins to different extents. Hence the model at present outputs only mean fluxes.

Model format

The model consists of an ASCII computer file written in FORTRAN and contains a 3-D array of unidirectional differential flux as a function of energy, α_0 and L. The model goes from $L = 3$ to $L = 8$ but not all data bins are filled. Empty bins are represented by the number -1.000.

No software presently accompanies this model so interpolation and transformation into local pitch angle are left to the user. The equations for calculating local omnidirectional fluxes from an equatorial pitch angle distribution have been described in Sect. 9.5.2. As this was not energy dependent it applies equally well to differential and integral fluxes.

9.6 MEA Comparison with AE-8

Because AE-8 (Vette 1991a) outputs integral omnidirectional flux above a certain energy and MEA data consist of differential unidirectional fluxes, they are not easily compared. However, creating the AE-8 compatible model put them in directly comparable form.

AE-8 used an internal magnetic field model only, whereas the MEA model was binned according to a model with an external component [Olson & Pfitzer (1977)]. However, AE-8's empirical local time term mimics the local time dependence of the

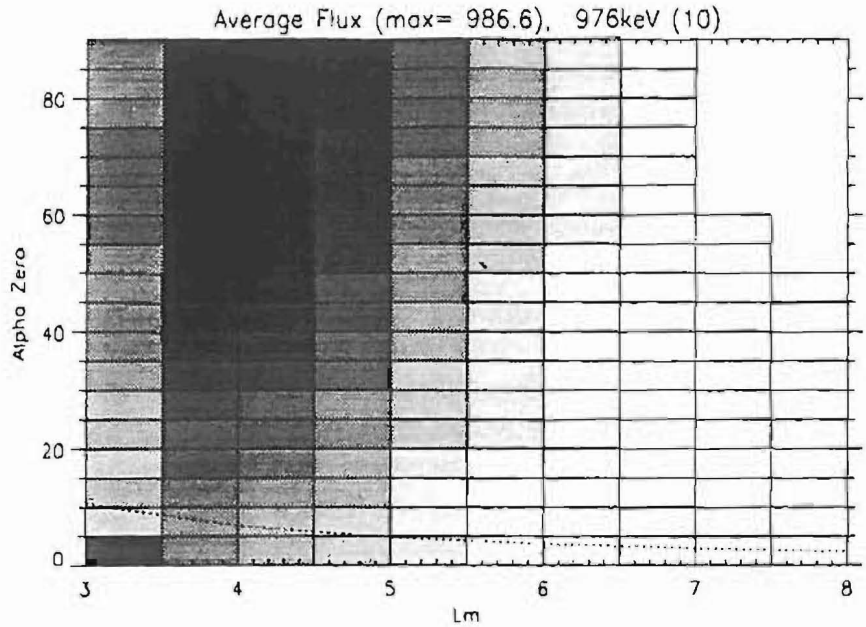

Figure 9.18. Greyscale plot of mean fluxes in the (α_0, L_m) coordinate system

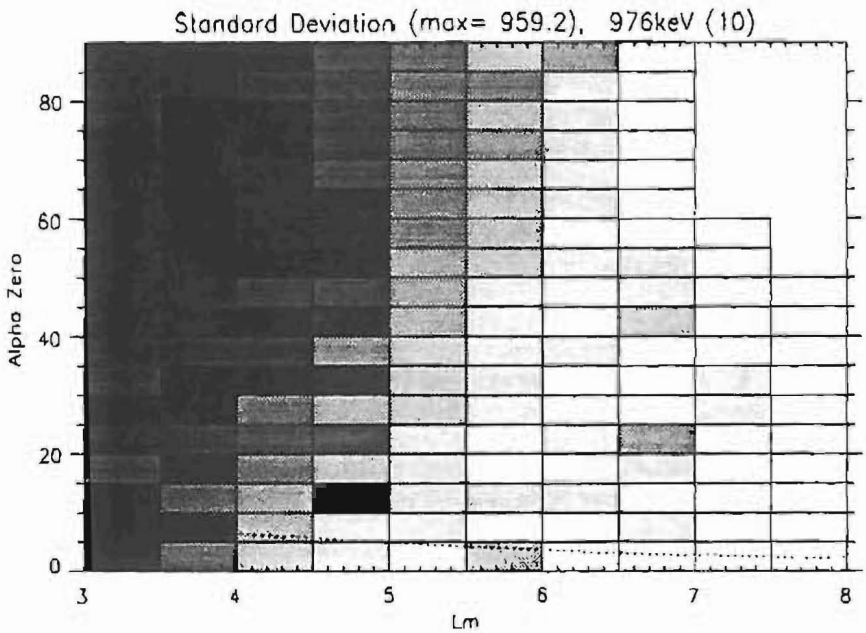

Figure 9.19. Greyscale plot of standard deviation of fluxes in the (α_0, L_m) coordinate system

magnetic field and so the two models should be comparable. Comparisons with AE-8 are limited to MEA's energy range (0.153–1.56 MeV). Figure 9.20 shows equatorial omnidirectional fluxes at two energies plotted as a function of L for the MEA data, and AE-8 MAX and AE-8 MIN. The MEA flux differs by up to a factor of 5 from the AE-8 MAX data and an order of magnitude from AE-8 MIN.

Figure 9.21 shows the dependence of flux on B/B_0 for the same two energies at $L = 3$. The two AE-8 models have identical slope indicating that they are not independent. Between $B/B_0 = 1$ and $B/B_0 = 12$ the AE-8 flux drops by more than an order of magnitude. The MEA data shows a much flatter slope at both energies, dropping by less than a factor 3.

At $L = 5$, as shown in Fig. 9.22, the AE-8 models are nearly identical. There is also better agreement with the MEA data, although this still drops less rapidly with B/B_0.

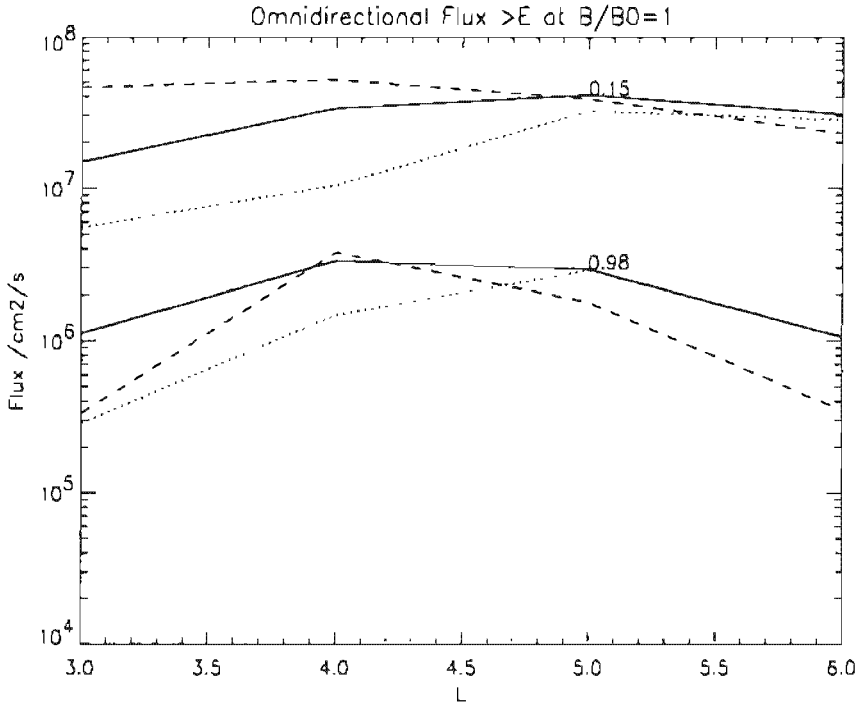

Figure 9.20. Flux of AE-8 MAX (solid line), AE-8 MIN (dotted line) and MEA data (dashed line) against L for 0.15 MeV (top three traces) and 0.98 MeV (bottom three traces)

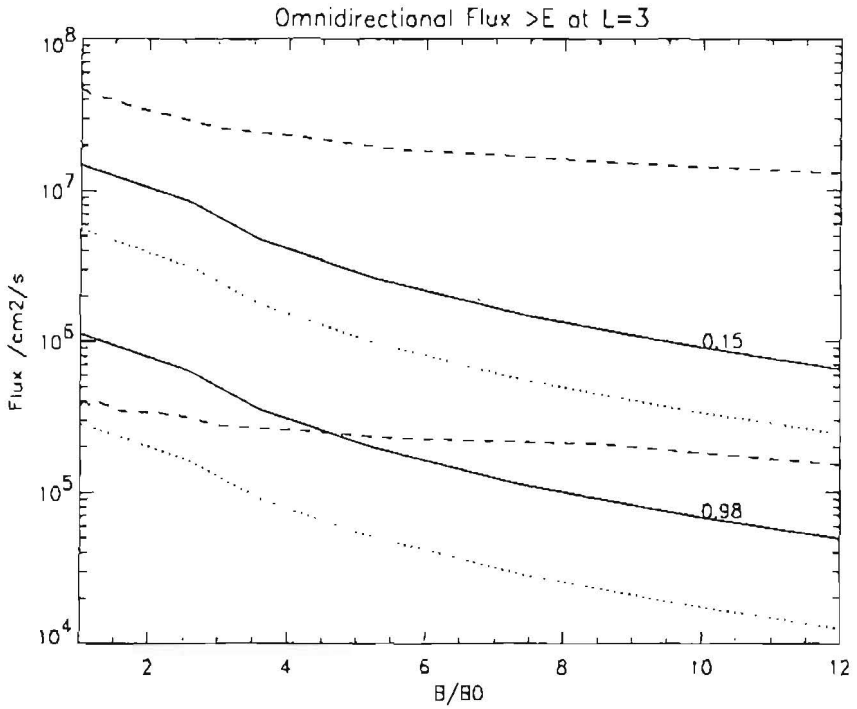

Figure 9.21. Flux of AE-8 MAX (solid line), AE-8 MIN (dotted line) and MEA data (dashed line) against B/B_0 for 0.15 MeV (top three traces) and 0.98 MeV (bottom three traces), for $L = 3$

9.7 Conclusions

The MEA instrument has provided a large database appropriate for studies of both the inner and outer radiation belts. The noise experienced by the instrument was significant but count rates were large and signal to noise remained good. Dead-time correction effects were accounted for up to the point where observed counts decreased as real counts increased. This count saturation problem applied only to low energy channels in the inner radiation belt.

A reduced database was created from 313 orbits of data. This was done to allow many tests to be performed on the data without excessive computing loads. A survey of the data was performed using this database. Electron spectra became softer at low energies as L increased. The spectra also became progressively less logarithmic. Pitch angles were peaked at 90° at all energies, something that was expected for a trapped population. Evidence for "butterfly" distributions, peaking at 45° and 135°, was seen at high energy and L values. At low energy, flux increased with K_p but this effect became less pronounced at higher energies and at 1370 keV high K_p produced a decrease in flux. The CRRES coverage in local time was not complete

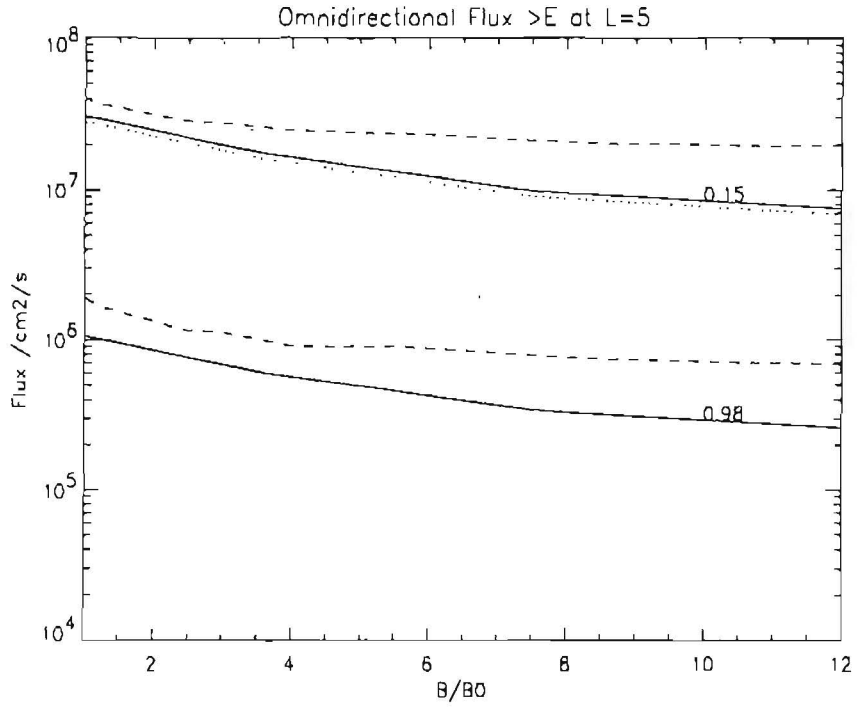

Figure 9.22. Flux of AE-8 MAX (solid line), AE-8 MIN (dotted line) and MEA data (dashed line) against B/B_0 for 0.15 MeV (top three traces) and 0.98 MeV (bottom three traces), for $L = 5$

for any L value in the outer radiation belt. However, in data not presented here, there appeared to be no local time dependence of flux when a single L value was selected. This is the result expected if the magnetic field model used to calculate L is realistic. Satellites with longer lifetimes were used as data sources to look at solar cycle variations. An anticorrelation of radiation belt flux at geostationary orbit with sunspot number was seen.

A number of different coordinate systems were used to organize the MEA data, to test their suitability for a new model. Two systems, $[\log(B_m/B_0), L]$ and (α_0, L) were found to cover the outer belt well, organized the data so that systematic changes in flux level were seen and had an acceptably small standard deviation in the outer belt. The (α_0, L) coordinate system had the additional advantage of being more conceptually simple and did not exaggerate the MEA pitch angle resolution in the loss cone. Hence this system is our recommendation for use in a new model.

Two new models were developed from the MEA model. One was binned using the same coordinate system as AE-8. The other used the preferred (α_0, L) system. These are early versions of models that we plan to develop in a following study.

MEA data were compared with the integral isotropic fluxes predicted by AE-8.

The MEA data were broadly similar to AE-8 MAX near the equator but dropped less steeply away from the equator.

Chapter 10

Analysis of GOES electron data

10.1 Introduction

The GOES-7 satellite of the *National Oceanographic and Atmospheric Administration* (NOAA) is a geostationary Earth observation satellite. It carried a set of radiation sensors (Williams 1976) which measured protons in 7 energy channels, alpha particles in 6 energy channels and electrons in 1 energy channel. The energy bins are listed in Table 10.1.

The GOES-7 database extends from 1988 to 1993, and data coverage is nearly continuous. The satellite was situated at 108° west. In this study we have been concerned with the characteristics of the outer radiation belt which is dominated by electrons and hence it is the single electron channel that has been of interest.

Table 10.1. Central energies of the radiation detectors on GOES-7

Proton channels		Alpha channels		Electron channels	
1	2.4 MeV (0.6–4.2 MeV)	1	6.9 MeV	1	> 2 MeV
2	6.5 MeV (4.2–8.7 MeV)	2	16.1 MeV		
3	11.6 MeV (8.7–14.5 MeV)	3	47.2 MeV		
4	29.5 MeV (15.0–44.0 MeV)	4	120.0 MeV		
5	60.5 MeV (39.0–82.0 MeV)	5	210.0 MeV		
6	142.0 MeV (84.0–200.0 MeV)	6	415.0 MeV		
7	305.0 MeV (110.0–500.0 MeV)				

10.2 Data processing

The GOES data were supplied to ESTEC courtesy of H. Sauer at NOAA. They presently reside on an ESTEC data directory and are accompanied by some display software written in PV-WAVE by C. Tranquille at ESTEC. These programs have been used where appropriate and information contained in them, e.g. on data format, has been used in writing new programs. New display software was written in IDL (which is nearly identical to PV-WAVE) and more CPU-intensive processing was done in FORTRAN.

10.2.1 Correction for energetic protons

Figure 10.1 shows measured electron fluxes for March 1991. There are a number of peaks in the data but the most dramatic feature is the sudden rise in fluxes by more than four orders of magnitude that occurred on around day 23 of the month.

Figure 10.2 shows the proton flux over the same period. The same flux peak is observed in the protons. In fact the shape of the rise and fall is almost identical in the two cases. Similar rises are seen in the other proton energy channels. The proton data are typical of a solar proton event. It appears that these energetic protons are producing false counts in the electron instrument. Since the data contamination produced by these protons can exceed the electron fluxes by several orders of magnitude, it cannot be ignored even in long-term averages. Sauer at NOAA stated that although the electron detector was known to be sensitive to protons above about 35 MeV, the contamination was spectrum dependent and there was no NOAA-approved method of subtracting it.

To test possible functional forms for the noise, the data around the solar proton event on 22nd March 1991 were used, considering only the period when the assumed noise fluxes were above $10^4\,cm^{-2}s^{-1}sr^{-1}$. This threshold was set because when noise fluxes are very high it is reasonable to ignore the real electron contribution entirely. There were 295 data points in this period.

First function

In the attempt to find a suitable function, the noise was taken to be simply proportional to the 6.5 MeV proton flux. This was the proton flux that appeared to vary in the most similar way to the electron noise. However, the log scale of Figs. 10.1 and 10.2 is deceptive and this function results in a noise ratio (calculated/observed) that varies between 1 and 3. This function was considered inadequate.

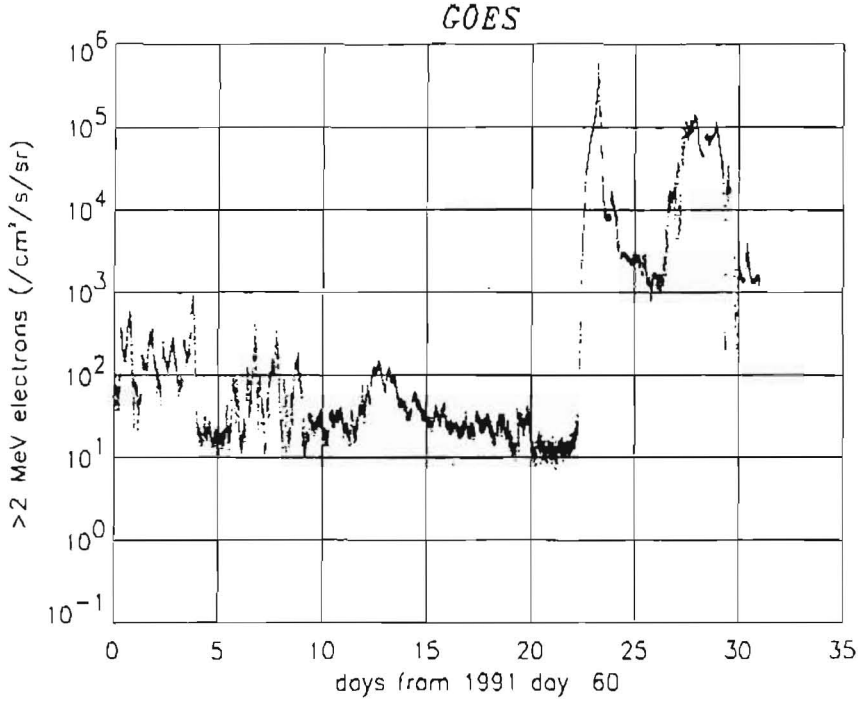

Figure 10.1. GOES electron flux for March 1991

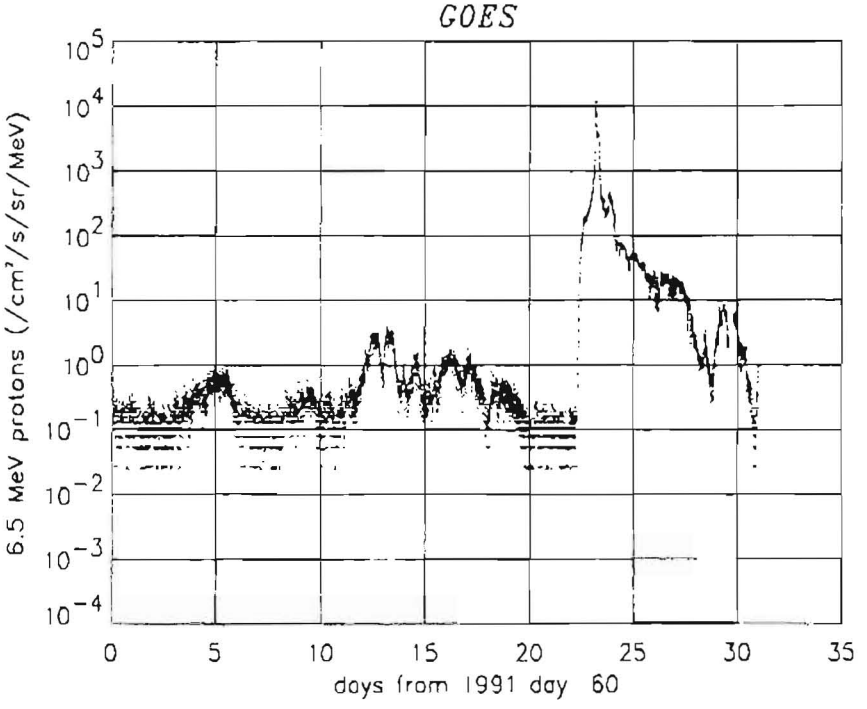

Figure 10.2. GOES 6.5 MeV proton flux for March 1991

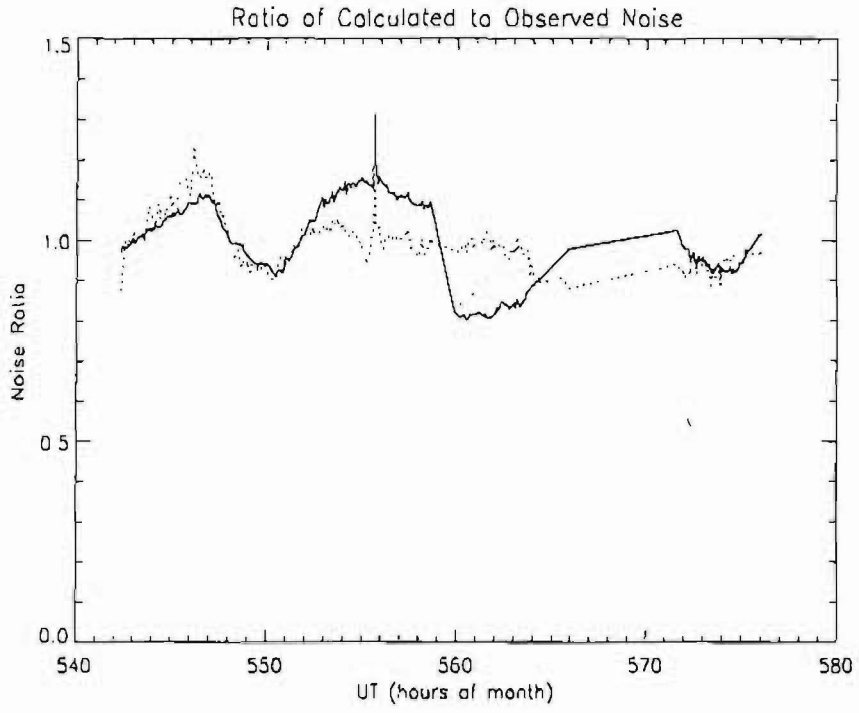

Figure 10.3. Ratio between calculated and observed contamination using the second and third functions (dotted and solid lines respectively)

Second function

In the second attempt, it was assumed that the noise fluxes were an unknown linear function of the proton flux in all seven energy channels. The best fits to the contributions of each energy were found by Single Valued Decomposition (SVD). The resulting function produced a noise ratio of $1 \pm 30\%$ and is plotted in Fig. 10.3. There were some problems with this technique. Some energies made a negative contribution to the flux in this fit which is not physical. Also, one of the worst fitted points was the very first one which leads one to suppose that had the test data started a little earlier, the fit may have been much worse. It was considered that this function was not ideal.

Third function

This function was based on the hypothesis that all protons above a certain energy are recorded as noise counts in the electron detector. Only the effective threshold energy needs to be found plus a scaling factor to account for the unknown proton geometric factor of the electron detector.

The total flux of protons detected on GOES can be approximated by multiplying

the flux in each energy bin by the energy between that bin and the one below, i.e.:

$$\begin{aligned}\text{Flux} &= 2.4 \times \text{proton}(1) + 3.7 \times \text{proton}(2) + 5.5 \times \text{proton}(3) + 17.9 \times \text{proton}(4) \\ &\quad + 30.0 \times \text{proton}(5) + 81.5 \times \text{proton}(6) + 163.0 \times \text{proton}(7)\,, \qquad (10.1)\end{aligned}$$

where proton(i) is the flux in proton energy channel i. This function describes the total flux from 0 to 305 MeV. The ratio between this function and the observed noise is not however constant. By ignoring all flux below a certain energy we found the total flux above an energy threshold instead. The threshold was gradually moved upwards until the ratio between the proton flux and the electron contamination became nearly constant. The best result was found with an energy threshold of 7.5 MeV. Figure 10.3 shows the result achieved by this method.

The scaling factor is simply given by the ratio of the average of this function to the average observed contamination. In this way a noise ratio of $1 \pm 30\%$ was achieved. This result was no better than the SVD result but has the advantage of being physically more meaningful and hence is less likely to produce disastrously wrong results at other times. Hence, this was chosen as the contamination function. The scaling factor was increased to cover the possible 30% undercalculation of the contamination. This was done so that we can be sure that all the contamination was removed.

Hence the final contamination algorithm is:

$$\begin{aligned}\text{noise} &= 26.8\,[2.1 \times \text{proton}(3) + 17.9 \times \text{proton}(4) + 30.0 \times \text{proton}(5) \\ &\quad + 81.5 \times \text{proton}(6) + 163.0 \times \text{proton}(7)]\,. \qquad (10.2)\end{aligned}$$

Figure 10.4 shows uncorrected electron flux and the contamination factor for March 1991. The contamination gives a very good approximation to the peak on 23rd March and shows that a smaller peak on 13th March was entirely caused by protons. Many true enhancements in the electrons are also visible. It can be clearly seen that the apparent lower limit to electron fluxes is determined by a background flux that is always present in the ion data. As will be discussed in Sect. 10.2.3, this flux is due to a second contamination flux that affects both the ions and electrons. Because it appears in the ion data, our correction algorithm automatically removes it from the electrons. To show that the algorithm works well at other times, a similar plot for May 1991 is shown in Fig. 10.5.

10.2.2 Removal of spurious data points

It was observed that spurious data points started to appear in the data set more and more as time went on. An example of this problem is shown in Fig. 10.6 showing

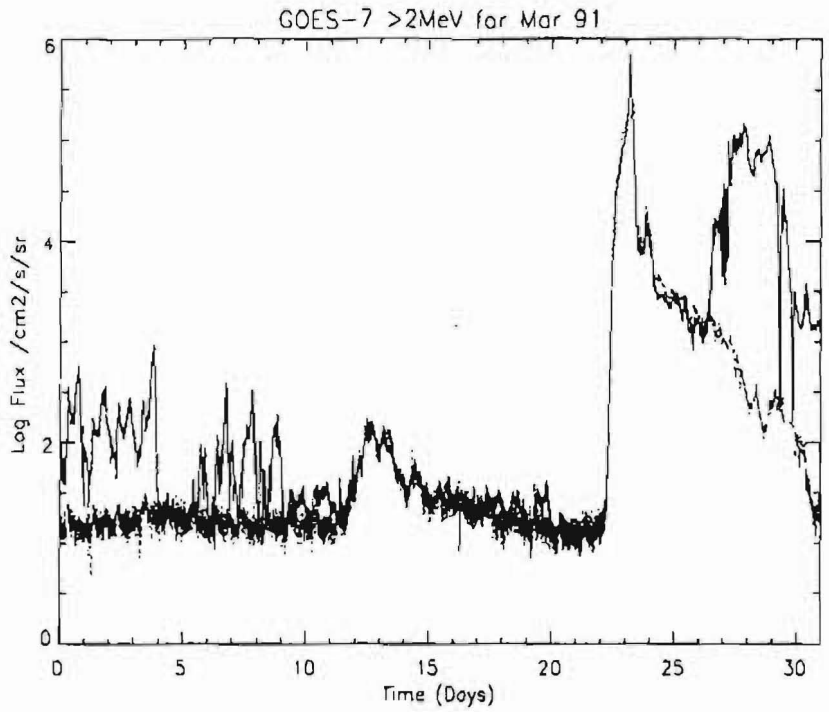

Figure 10.4. Uncorrected electron flux (solid line) and calculated proton contamination (dotted line) for March 1991

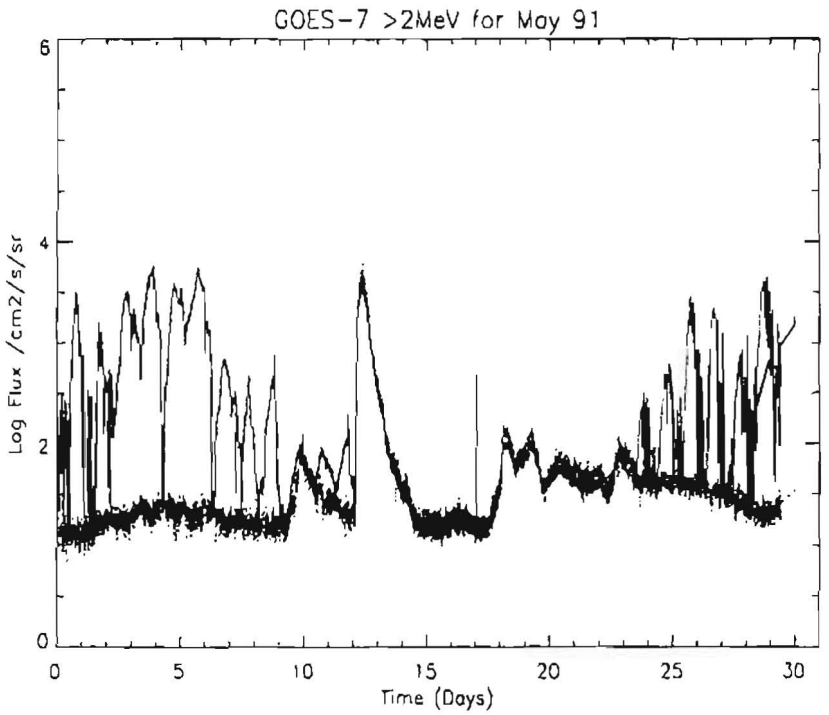

Figure 10.5. Uncorrected electron flux (solid line) and calculated proton contamination (dotted line) for May 1991

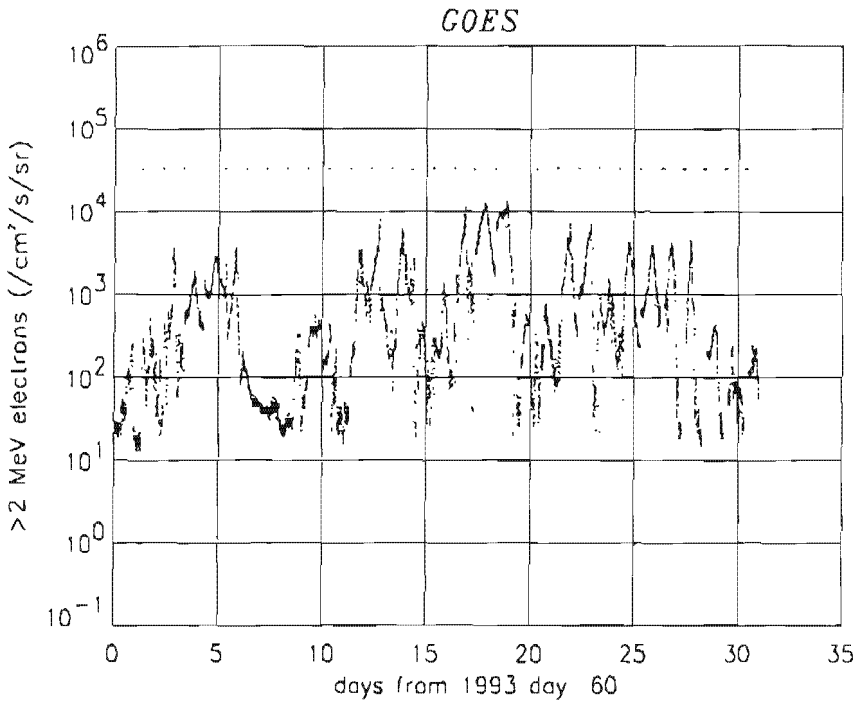

Figure 10.6. Uncorrected electron fluxes for March 1993

electron fluxes for March 1993. Fortunately all these points had the same value, 32700, which probably arose from a misinterpretation of the number -1, which is frequently used as a "no-data" flag, when transferring the data from machine to machine. Data points with this value were removed in the analysis that follows. In addition, the flux value 5.14002E+32 occurred occasionally in the data and these data points were also removed.

10.2.3 Change from uncorrected to corrected data files

Figure 10.7 shows the proton flux for the entire database in the 305 MeV channel. A sudden jump in fluxes occurs on 1st January 1992. The sudden decrease in fluxes occurs where a correction began to be applied to the proton fluxes. The correction was applied to all proton energies but not to the electrons.

According to Sauer, the protons were corrected for out-of-aperture, and out-of-energy-range response according to preflight laboratory calibrations. This was done assuming that the spectrum over each channel was representable by a power law, on a point by point basis on the 5-minute averages. The running background levels were also subtracted for each channel.

The changes to the calibration of the proton fluxes require a small change in

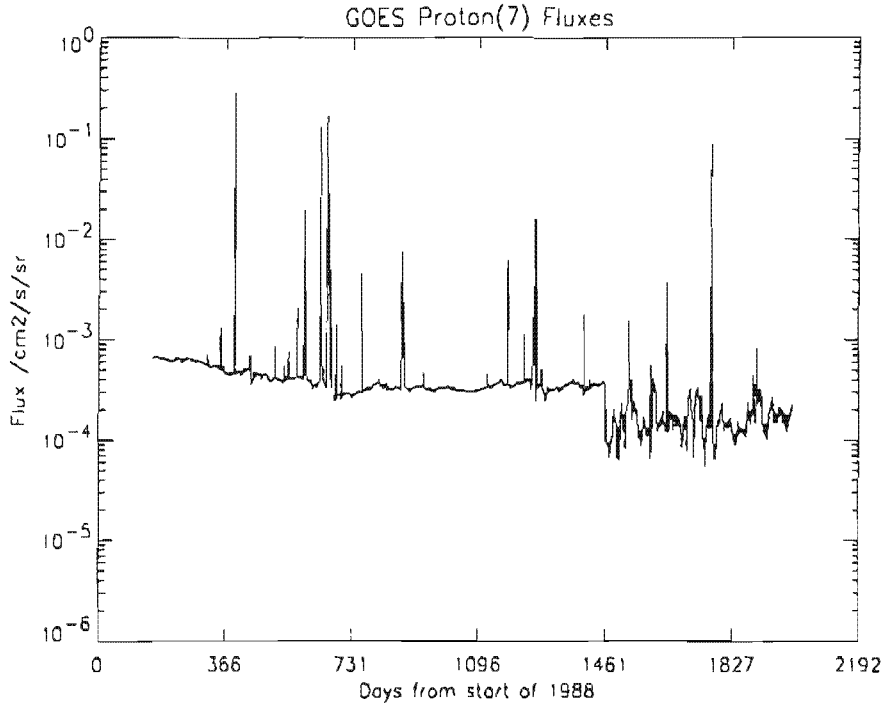

Figure 10.7. 305 MeV proton fluxes. Tick marks are at yearly intervals on the time axis.

the contamination algorithm used by us to correct the electrons. However, the subtraction of the background level is more critical. The background comes probably from galactic cosmic radiation. Once the proton fluxes have had this component removed, they cannot be used to remove it from the electrons. Using corrected proton fluxes, the contamination algorithm worked well when proton fluxes were high but left a substantial uncorrected contamination flux in the electrons at quiet times. The uncorrected proton data for 1992 to 1995 are held at ESTEC but have not yet been transferred to the VAX data disk, so in this study we have used data quantitatively only before 1992.

10.3 GOES Analysis

As Figs. 10.4 and 10.5 showed, GOES-7 > 2 MeV electron fluxes varied very widely. Flux increases typically happened over periods of 2 or 3 days and could raise fluxes by as much as 4 orders of magnitude. These raised levels usually lasted no longer than 10 days and often decreased as quickly as they began.

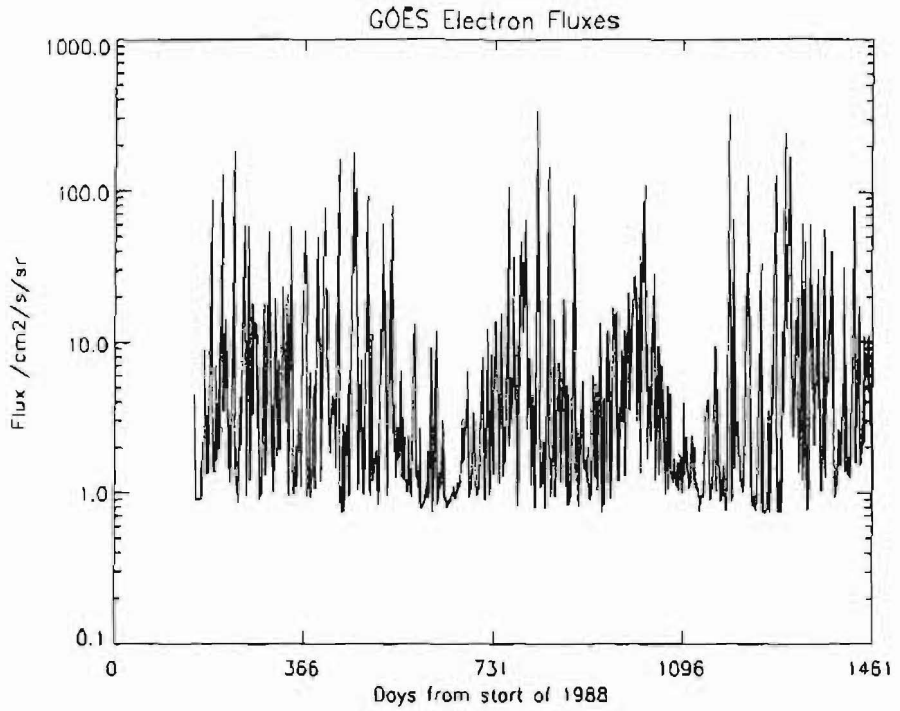

Figure 10.8. > 2 MeV Electron fluxes. Tick marks are at yearly intervals on the time axis.

10.3.1 Long term behaviour

Figure 10.8 shows corrected electron fluxes from 1988 to the end of 1991. The fluxes were processed into daily averages by averaging the log of the flux to reduce the effect of any error in the contamination subtraction. The spikiness of the data occurs because of the duration of enhanced flux levels of just a few days. There are periods of generally low flux in the second half of 1989 and the beginning of 1991.

10.3.2 Autocorrelation analysis

The autocorrelation coefficients of the data displayed in Fig. 10.8 were calculated for time separations of 0 to 365 days and are shown in Fig. 10.9. This was done to look for preferred periods between similar features in the data. There are clear peaks at 27 day intervals corresponding to the solar rotation period. Peaks at this period can be seen in Fig. 10.8. Enhanced correlation at half this period are also seen, possibly as a result of crossing magnetic sector boundaries in the solar wind. The amplitude of the correlation coefficient variations becomes smaller at around 6 months separation perhaps indicating that the 27 day cycle is not consistantly strong.

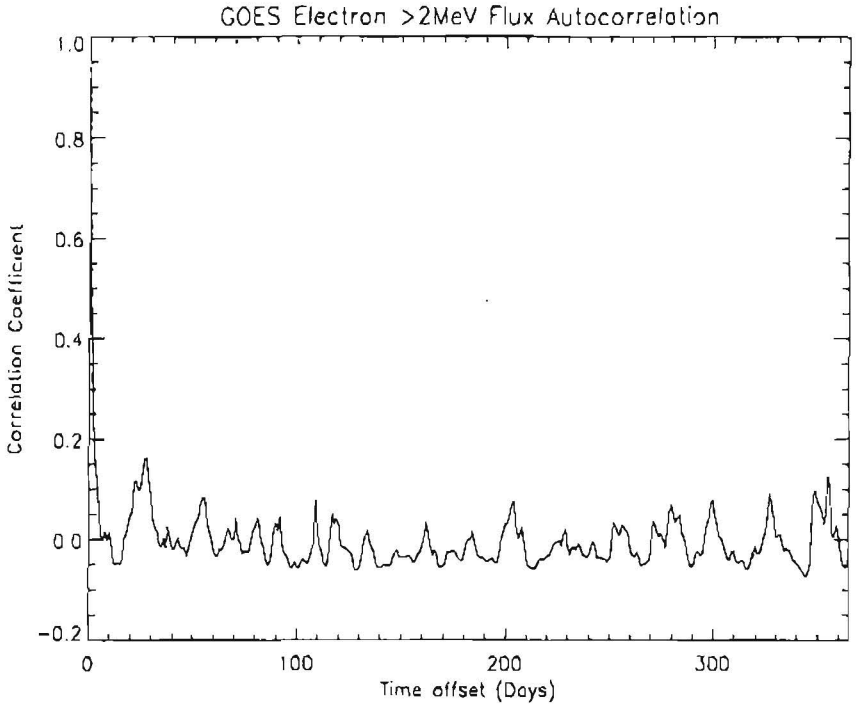

Figure 10.9. Autocorrelation coefficient versus time offset for > 2 MeV electron fluxes

The autocorrelation function for uncorrected 6.5 MeV protons was also found but is not presented here. These protons are not trapped radiation belt particles but come straight from the Sun. The proton enhancements were not as regular as the electrons and their separation was typically 22 days rather than 27. The reason for this period is not known.

10.3.3 Comparison with Meteosat SEM-2 data

Both Meteosat-3 and GOES-7 were launched in 1988. The SEM-2 monitor on Meteosat-3 and the radiation instrument on GOES-7 have provided almost continuous coverage since that time. Hence there is a long period with data from both satellites. Both are geosynchronous but they are widely separated in local time. GOES-7 remained at 108° west. Meteosat-3 was initially at 0° west and later moved to around 50° west. SEM-2's peak energy bin is 202–300 keV and so the GOES-7 data provides valuable new data from a similar orbit.

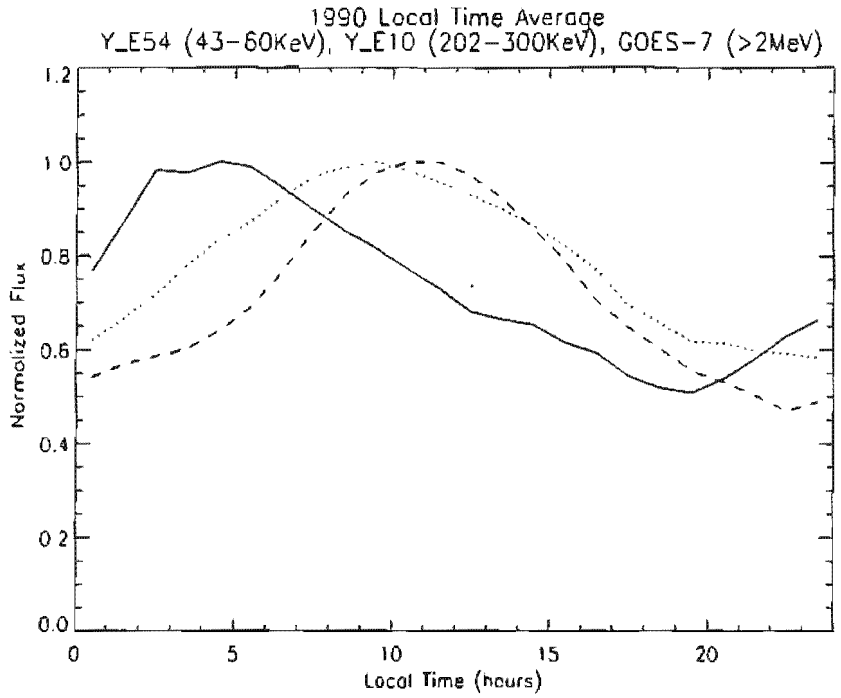

Figure 10.10. Normalized flux versus local time for SEM-2 43–60 keV (solid line), SEM-2 202–300 keV (dotted line) and GOES-7 > 2 MeV (dashed line)

Local time variation

Figure 10.10 shows the local time dependence of electron flux for two SEM-2 energies and the GOES-7 data. For each energy, the flux was divided by the peak flux to make a direct comparison of their diurnal variation easier. The SEM-2 43–60 keV fluxes peak around 04 hours and have a non-sinusoidal profile. Comparison with substorm injection event statistics (Rodgers & Johnstone 1995) have established that this diurnal variation reflects the local time distribution of substorm injection events. The GOES-7 > 2 MeV fluxes peak at around 11 hours and are approximately sinusoidal in profile. As discussed in Technical Note 6, this is consistent with the variation in L as a geostationary spacecraft moves in local time. Hence the GOES data are typical of trapped radiation with a negative gradient in L at geostationary orbit. The SEM-2 202–300 keV flux variation is similar to the GOES flux but displaced an hour earlier in local time. This implies that along with trapped radiation there are some substorm-related fluxes at this energy. This is an inference that we could not have made without the GOES data.

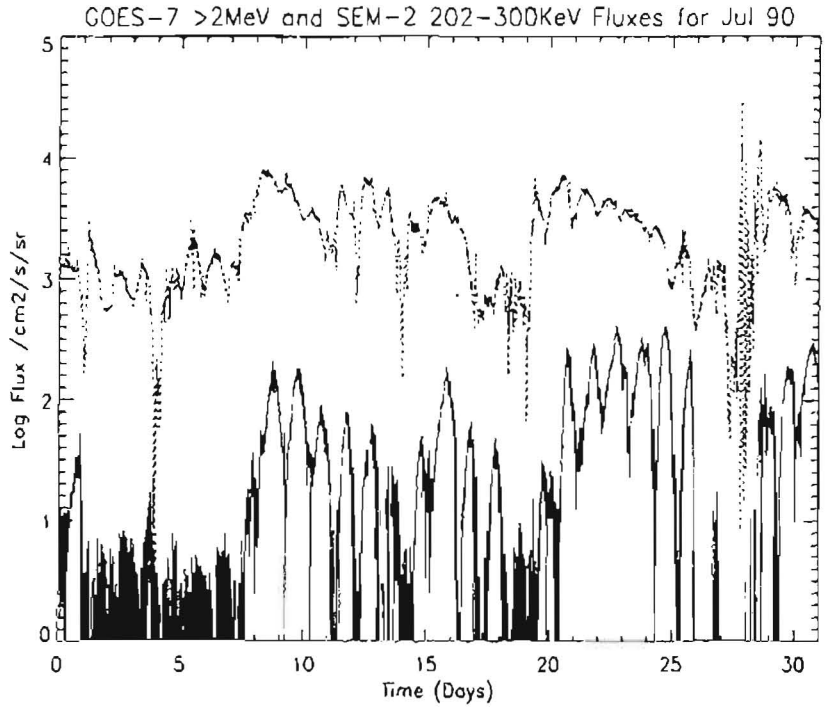

Figure 10.11. SEM-2 202–300 keV fluxes (dotted line) and GOES-7 > 2 MeV (solid line) background-subtracted fluxes for July 1990

Temporal comparison

Although an hour by hour comparison between fluxes at Meteosat and GOES-7 is difficult to interpret because of the separation of the satellites, they are ideal for looking at variations over timescales of a day or more. Figure 10.11 shows both GOES-7 and SEM-2 202–300 keV fluxes for July 1990.

There is a very strong similarity between the two data sets. The variation in the higher energy fluxes is stronger both diurnally and in terms of general flux increases than in the lower energy fluxes. However the major flux enhancements are seen at both energies. To carry out a quantitative comparison, the Meteosat and GOES data were made into daily averages so that diurnal effects would be eliminated.

The correlation coefficients between the logs of GOES > 2 MeV flux and SEM-2 flux at 43–60 keV and 202–300 keV were calculated for a range of time offsets between the data sets. The daily-averaged background-subtracted GOES data were used. The results are plotted in Fig. 10.12. This shows that there is typically a 2-day gap between flux changes at 43–60 keV and > 2 MeV. A gap of around 0.5 days exists between changes at 202–300 keV and > 2 MeV.

A similar correlation was performed between GOES log fluxes and K_p, the plan-

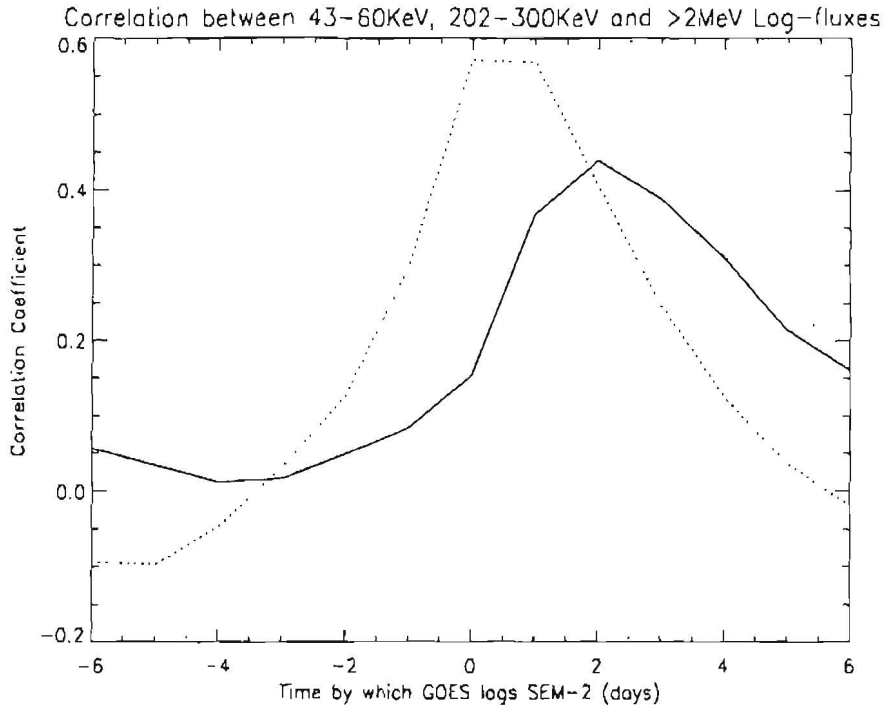

Figure 10.12. Correlation coefficient as a function of time offset for > 2 MeV fluxes compared with 43–60 keV fluxes (solid line) and 202–300 keV fluxes (dotted line)

etary magnetic activity index. The results presented in Fig. 10.13 show that GOES fluxes lag K_p by typically 3 days.

The source of energetic electrons in the outer radiation belt has not yet been established. These particles are far more energetic than the bulk of the magnetospheric plasma and so a powerful heating mechanism is needed if there is an internal magnetospheric source. An external non-magnetospheric source seems unlikely however. The GOES-7 results add strength to the argument, made in Technical Note 6, that there is a mechanism at work which acts on ambient magnetospheric electrons and progressively energizes them up to the energy of the radiation belts. Over a three-day period, we see first a rise in magnetic activity, then a rise in 43–60 keV fluxes associated with substorms, then a rise in low-energy radiation belt fluxes at 202–300 keV and finally a rise in high-energy radiation belt fluxes > 2 MeV.

10.4 Conclusions

GOES-7 > 2 MeV electron data form a long continuous database that is of great use in studying the characteristics and processes of the outer radiation belt. Although the data are severely contaminated by proton and probably cosmic ray fluxes, the

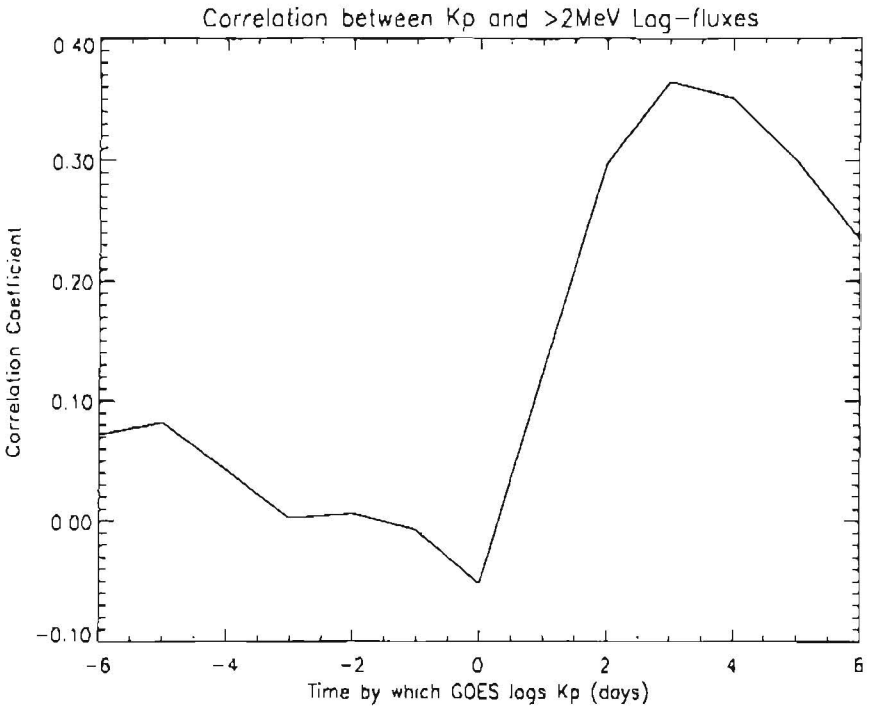

Figure 10.13. Correlation coefficient as a function of time offset for > 2 MeV fluxes compared with K_p

presence of complementary proton data enables noise from both of these sources to be removed. The algorithm developed to do this was highly successful. The data show that fluxes at geostationary orbit are variable over periods of a few days, changing by as much as two orders of magnitude in this time.

Periods of 27 and 13 days were found in the data, indicating a dependence on solar rotation and sector boundary crossings. GOES proton data exhibited a 22 day period. Diurnal variation in electron fluxes was stronger than at low energies in Meteosat SEM-2 data. This indicated that the slope of the fluxes in terms of L is more negative at higher energy.

GOES electron fluxes peaked around 11 hours local time, this provided evidence that 202–300 keV fluxes, which peaked earlier, experienced some flux contribution due to substorm injection events.

Cross-correlation between GOES fluxes and SEM-2 fluxes at 43–60 keV and 202–300 keV as well as K_p was performed with a range of time separations. This showed that changes in K_p, 43–60 keV flux, 202–300 keV flux and > 2 MeV flux occurred in sequence, with a total elapsed time of 3 days. This provides strong evidence for a process of heating ambient magnetospheric plasma up to radiation belt energies over this time scale.

References

Aiello, W.P., Belian, R.D., Conner, J.P., Higbie, P.R., Martin, W.B., Singer, S.: 1975, *An Energetic Particle Detector for a Synchronous Satellite*, IEEE Trans. Nucl. Sci. **NS-22**, 575

Allen, C.W.: 1985, *Astrophysical Quantities*, The Athlone Press

Anderson, A.D., Francis, W.E.: 1964, *A semitheoretical model for atmospheric properties from 90 to 10,000 km*, Lockheed Missiles and Space Company 6-74-64-19

Angerami, J.J., Thomas, J.O.: 1964, *The Distribution of Electrons and Ions in the Earth's Exosphere*, J. Geophys. Res. **69**, 4537–4560

Badhwar, G.D., Konradi, A.: 1990, *Conversion of Omnidirectional Proton Fluxes into a Pitch Angle Distribution*, J. Spacecraft and Rockets **27**, 350–352

Bailey, D.K.: 1959, *Abnormal ionization in the lower ionosphere associated with cosmic-ray flux enhancements*, Proc. IRE **47**, 255–266

Baker, D.N., Higbie, P.R., Hones, E.W., Jr., Belian, R.D.: 1978, *High-resolution Energetic Particle Measurements at 6.6 R_E 3. Low-energy Electron Anisotropies and Short-term Substorm Predictions*, J. Geophys. Res. **83**, 4863

Baker, D.N., Higbie, P.R., Belian, R.D., Hones, E.W., Jr., Klebesadel, R.W.: 1982, *The Los Alamos Synchronous Data Set*, The IMS Source Book, AGU

Belian R.D., Baker, D.N., Higbie, P.R., Hones, E.W., Jr.: 1978, *High-resolution energetic particle measurements at 6.6R_E. 2. High-energy proton drift echoes*, J. Geophys. Res. **83**, 4857

Bilitza, D.: 1990, *International Reference Ionosphere 1990*, NSSDC/WDC-A-R&S 90-22

Bilitza, D.: 1992, *Solar-Terrestrial Models and Application Software*, Planet. Space Sci. **40**, 541–579

Blake, J.B., Gussenhoven, M.S., Mullen, E.G., Fillius, R.W.: 1992, *Identification of an Unexpected Space Radiation Hazard*, IEEE Trans. Nucl. Sci. **39**, 1761

Brautigam, D.H., Gussenhoven, M.S., Mullen, E.G.: 1992, *Quasi-Static Model of Outer Zone Electrons*, IEEE Trans. Nucl. Sci. **39**, 1797–1803

Cain, J.C., Hendricks, S.J., Langel, R.A., Hudson, W.V.: 1967, *A Proposed Model for the International Geomagnetic Reference Field-1965*, J. Geomag. Geoelectr. **19**, 335–355

Carpenter, D.L., Anderson, R.R.: 1992, *An ISEE/Whistler Model of Equatorial Electron Density in the Magnetosphere*, J. Geophys. Res. **97**, 1097–1108

Cayton, T.E., Belian, R.D., Gary, S.P., Fritz, T.A.: 1989, *Energetic Electron Components at Geosynchronous Orbit*, Geophys. Res. Lett. **16**, 147

Chiu, Y.T., Luhmann, J.G., Ching, B.K., Boucher, D.J.: 1978, *An Equilibrium Model of Plasmaspheric Composition and Density*, The Aerospace Corporation, Los Angeles, SSL-78(3960-04)-3

Coates, A.J., Johnstone, A.D., Rodgers, D.J., Huckle, H.E.: 1990, *Meteosat P2 Technical Assistance: SEM-2 Data Processing 22 June 88 to 30 June 89. Final Report*, ESA Contract 7879/88/F/TB

CRRES System Description Handbook, Rev. E, Ball Aerospace Systems Division, Boulder, CO, 1990

Daly, E.J., Evans, H.D.R.: 1993, *Problems in Radiation Environment Models at Low Altitudes*, Memorandum ESA/ESTEC/WMA/93-067/ED

Fairfield, D.H.: 1992, *Advances in Magnetospheric Storm and Substorm Research: 1989–1991*, J. Geophys. Res. **97**, 10865

Fennell, J.F.: 1982, in: The IMS Source Book: Guide to the International Magnetosphere Study Data Analysis, Washington, DC, American Geophysical Union, p. 65–81

Fraser-Smith, A.C.: 1987, *Centered and Eccentric Geomagnetic Dipoles and Their Poles, 1600–1985*, Rev. Geophys. **25**, 1–16

Fujimoto, M., Nishida, A.: 1990, *Energization and Anisotropization of Energetic Electrons in the Earth's Radiation Belt by the Recirculation Process*, J. Geophys. Res. **95**, 4265

Gaffey, J.D. Jr., Bilitza, D.: 1994, *NASA/National Space Science Data Center Trapped Radiation Models*, J. Spacecraft and Rockets **31**, 172–176

Getselev, I.V., Gusev, A.N., Darchieva, L.A., Kabashova, N.A., Morozova, T.I., Pavlov, A.V., Panasyuk, M.I., Pugacheva, G.I., Rejzman, S.Ya., Savun, O.I., Sosnovets, E.N., Tverskaya, N.V., Timofeyev, G.A., Yushkov, B.I.: 1991, *Model of Spatial-Energetic Distribution of Charged Particles (Protons and Electrons) Fluxes in the Earth's Radiation Belts*, INP MSU Preprint MGU-91-37/241 (in Russian)

Goriainov, M.F., Dronov, A.V., Kovtykh, A.S., Sosnovets, E.N.: 1983, *Spatial, Spectral and Angular Structure of low-Altitude 30–210 keV Electron Fluxes during Magnetically Quiet Time*, Kosmicheskie Islledovaniya **21**, 609–618 (in Russian), translated in Cosmic Research **21**, 494–500

GOST 25645-138.86 and 139.86: 1986, *USSR State Standard on Earth's Radiation Belt Proton and Electron Fluxes*, Moscow (in Russian)

Grafodatsky, O.S., Islayev, Sh.N., Panasyuk, M.I., et al.: 1989, *Magnetospheric Plasma Fluxes Registration on Board of GORISONT Satellite*, Issledovaanya po geomagnetismu, aeronomii, i physike Solntsa (Geomagnetism, Aeronomy and Solar Physics Studies), Issue **86**, 99–130 (in Russian)

Gussenhoven, M.S., Mullen, E.G., Sagalyn, R.C.: 1985, *CRRES/SPACERAD Experiment Descriptions*, AFGL-TR-85-0017

Gussenhoven, M.S., Mullen E.G., Violet, M.D., Hein, C., Bass, J., Madden, D.: 1993, *CRRES High Energy Proton Flux Maps*, IEEE Trans. Nucl. Sci. **40**, 1450

Hassitt, A.: 1964, *An average atmosphere for particles trapped in the Earth's magnetic field*, University of California at San Diego

Hassitt, A.: 1965a, *The Drift Velocity of Trapped Particles*, J. Geophys. Res. **70**, 535–540

Hassitt, A.: 1965b, *Average Effect of the Atmosphere on Trapped Protons*, J. Geophys. Res. **70**, 5385–5394

Heck, F.: 1992, *Observation of Radiation Environment with CRRES Data*, ESTEC Stage Report

Hedin, A.E.: 1987, *MSIS-86 thermospheric model*, J. Geophys. Res. **92**, 4649–4662

Hedin, A.E.: 1991, *Extension of the MSIS thermosphere model into the middle and lower atmosphere*, J. Geophys. Res. **96**, 1159-1172

Hess, W.N.: 1968, *The Radiation Belt and Magnetosphere*, Blaisdell Publishing Company

Heynderickx, D.: 1995, *Comparison between methods to compensate for the secular motion of the South Atlantic Anomaly*, J. Nuclear Tracks Radiat. Meas., accepted for publication

Heynderickx, D., Beliaev, A.: 1995, *Identification of an Error in the Distribution of the NASA model AP-8 MIN*, J. Spacecraft and Rockets **32**, 190–192

Heynderickx, D., Lemaire, J., Daly, E.J.: 1995, *Historical Review of the Different Procedures Used to Compute the L Parameter*, J. Nuclear Tracks Radiat. Meas., accepted for publication

Hilton, H.H.: 1971, *L Parameter, A New Approximation*, J. Geophys. Res. **76**, 6952–6954

Hovestadt, D., Achtermann, E., Ebel, B., Haüsler, B., Pachmann, G.: 1972, *New observations of the proton population of the radiation belt between 1.5 and 104 MeV*, Earth's Magnetospheric Processes, B.M. McCormac (ed.), D. Reidel Publishing Company, Dordrecht, Holland, 115–119

Jensen, D.C., Cain, J.C.: 1962, *An Interim Geomagnetic Field*, J. Geophys. Res. **67**, 3568

Johnstone, A.D., Wrenn, G.L., Huckle, H.E., Scott, R.F.: 1985, *Meteosat-F2 Charging Monitors*, Final Report ESA Contracts 4715/81/F/CG, 5911/84/F/CG

Kamiyama, H.: 1966, *Ionization and excitation by precipitating electrons*, Rep. Ionos. Space Res. Japan **20**, 171–187

Kerns, K.J., Gussenhoven, M.S.: 1992, *CRRESRAD Documentation*, Environmental Research Papers, No. 1105, PL-TR-92-2201, Phillips Laboratory, Directorate of Geophysics

Konradi, A., Badhwar, G.D., Braby, L.A.: 1992, *Recent Space Shuttle Observations of the South Atlantic Anomaly and the Radiation Belt Models*, preprint

Lemaire, J.: 1989, *Plasma distribution models in a rotating magnetic dipole and refilling of plasmaspheric flux tubes*, Phys. Fluids **B1**, 1519–1525

Lemaire, J., Roth, M., Wisemberg, J., Domange, P., Fonteyn, D., Lesceux, J.M., Loh, G., Ferrante, G., Garres, C., Bordes, J., McKenna-Lawlor, S., Vette, J.I.: 1991, *Development Study of Improved Models of the Earth's Radiation Environment*, Final Report of TREND, ESTEC Contract No. 9011/88/NL/MAC

Lenchek, A.M., Singer, S.F.: 1962, *Geomagnetically trapped protons from cosmic-ray albedo neutrons*, J. Geophys. Res. **67**, 1263–1287

Lenchek, A.M., Singer, S.F., Wentworth, R.C.: 1961, *Geomagnetically Trapped Electrons from Cosmic Ray Albedo Neutrons*, J. Geophys. Res. **66**, 4027–4046

Lew, J.S.: 1961, *Drift rate in a dipole field*, J. Geophys. Res. **66**, 2681–2865

Lezniak, T.W., Arnoldy, R.L., Parks, G.K., Winckler, J.R.: 1968, *Measurement and Intensity of Energetic Electrons at the Equator at 6.6 R_E*, Radio Sci. **3**, 710

McIlwain, C.E.: 1961, *Coordinates for Mapping the Distribution of Magnetically Trapped Particles*, J. Geophys. Res. **66**, 3681–3691

McIlwain, C.E.: 1966, *Magnetic Coordinates*, Space Science Reviews **5**, 585–598

Mead, G.D., Fairfield, D.H.: 1975, *A Quantitative Magnetospheric Model Derived From Spacecraft Magnetometer Data*, J. Geophys. Res. **80**, 523–534

Meffert, J.D., Gussenhoven, M.S.: 1994, *CRRESPRO Documentation*, PL-TR-94-2218, Environmental Research Papers, No. 1158, Phillips Laboratory

Merrill, R.T., McElhinny, M.W.: 1983, *The Earth's Magnetic Field. Its History, Origin and Planetary Perspective*, International Geophysics Series **32**, Academic Press

Mullen, E.G., Gussenhoven, M.S.: 1991, *Results of Space Experiments: CRRES*, PLGD Internal Report

Newkirk, L.L., Walt, M.: 1964, *Longitudinal drift velocity of geomagnetically trapped particles*, J. Geophys. Res. **69**, 1759–1763

Olson, W.P.: 1969, *The Shape of the Tilted Magnetopause*, J. Geophys. Res. **74**, 5642–5651

Olson, W.P.: 1974, *A model of the Distributed Magnetospheric Currents*, J. Geophys. Res. **79**, 3731–3738

Olson, W.P., Pfitzer, K.A.: 1974, *A Quantitative Model of the Magnetospheric Magnetic Field*, J. Geophys. Res. **79**, 3739–3748

Olson, W.P., Pfitzer, K.A.: 1977, *Magnetospheric Magnetic Field Modeling*, Annual Scientific Report, AFOSR Contract No. F44620-75-C-0033, McDonnell Douglas Astronautics Company, Huntington Beach, CA

Olson, W.P., Pfitzer, K.A.: 1982, *A Dynamic Model of the Magnetospheric Magnetic and Electric Fields for July 29, 1977*, J. Geophys. Res. **87**, 5943–5948

Parker, E.N.: 1957, *Newtonian Development of the Dynamical Properties of Ionized Gases of Low Density*, Phys. Rev. **107**, 924–933

Parks, G.K.: 1991, Chapter D in *Physics of Space Plasmas*, Addison-Wesley Publishing Company

Parks, G.K., Arnoldy, R.L., Lezniak, T.W., Winckler, J.R.: 1968, *Correlated Effects of Energetic Electrons at the 6.6 R_E Equator and the Auroral Zone During Magnetospheric Substorms*, Radio Sci. **3**, 715

Pfitzer, K.A.: 1990, *Radiation Dose to Man and Hardware as a Function of Atmospheric Density in the 28.5 Degree Space Station Orbit*, MDSSC Report No. H5387 Rev A

Pfitzer, K.A.: 1991, *Improved Models of the Inner and Outer Radiation Belts*, Phillips Laboratory Scientific Report PL-TR-91-2187

Pfitzer, K.A., Olson, W.P., Mogstad, T.: 1988, *A Time Dependent, Source Driven Magnetospheric Magnetic Field Model*, EOS **69**, 426

Ray, E.C.: 1960, *On the Theory of Protons Trapped in the Earth's Magnetic Field*, J. Geophys. Res. **65**, 1125–1134

Rees, M.H.: 1963, *Auroral ionization and excitation by incident energetic electrons*, Planet. Space Sci. **11**, 1209–1218

Roberts, C.S.: 1965, *On the Relationship between the Unidirectional and Omnidirectional Flux of Trapped Particles on a Magnetic Line of Force*, J. Geophys. Res. **70**, 2517–2527

Rodgers, D.J.: 1991, *Correlation of Meteosat-3 Anomalies with Data from the Spacecraft Environment Monitor*, Internal Estec Working Paper 1620

Rodgers D.J., Johnstone, A.D.: 1995, *Statistics of the Outer Radiation Belt*, Proceedings of the Taos Workshop on the Earth's Trapped Particle Environment, G. Reeves (ed.), Taos, New Mexico, August 1994, in press

Roederer, J.G.: 1967, *On the Adiabatic Motion of Energetic Particles in a Model Magnetosphere*, J. Geophys. Res. **72**, 981–992

Roederer, J.G.: 1970, *Dynamics of Geomagnetically Trapped Radiation*, Springer-Verlag

Roederer, J.G.: 1972, *Geomagnetic Field Distortions and Their Effects on Radiation Belt Particles*, Rev. Geophys. Space Phys. **10**, 599–630

Russell, C.T.: 1971, *Geophysical Coordinate Transformations*, Cosmic Electrodynamics **2**, 184–196

Rycroft, M.J., Jones, I.R.: 1985, *Modelling the plasmasphere for the International Reference Ionosphere*, Adv. Space Res. **5**, 21–27

Rycroft, M.J., Jones, I.R.: 1987, *A suggested model for the IRI plasmaspheric distribution*, Adv. Space Res. **7**, 13–22

Savun, O.I., Yushkov, B.Yu.: 1985, *Modeling of Charged Particles Fluxes along the Trajectories of Spacecrafts in the Earth's Radiation Belts*, Vestnik Moscovskogo Universiteta, seriya Physica i Asronomiya (Moscow University Courier, Physics and Astronomy Series) **26**, 3 (in Russian)

Sawyer, D.M., Vette, J.I.: 1976, *AP-8 Trapped Proton Environment for Solar Maximum and Solar Minimum*, NSSDC/WDC-A-R&S 76-06

Singley, G.W., Vette, J.I.: 1972, *A Model Environment for Outer Zone Electrons*, NSSDC 72-13

Spjeldvik, W.N., Rothwell, P.L.: 1985, *The Radiation Belts*, Chapter 5 of Handbook of Geophysics and the Space Environment, Ed. A.S. Jura, AFGL

Tsyganenko, N.A.: 1987, *Global Quantitative Models of the Geomagnetic Field in the Cislunar Magnetosphere for Different Disturbance Levels*, Planet. Space Sci. **35**, 1347–1358

Tsyganenko, N.A.: 1989, *A Magnetospheric Magnetic Field Model with a Warped Tail Current Sheet*, Planet. Space Sci. **37**, 5–20

Tsyganenko, N.A., Usmanov, A.V.: 1982, *Determination of the Magnetospheric Current System Parameters and Development of Experimental Geomagnetic Field Models Based on Data from IMP and HEOS Satellites*, Planet. Space Sci. **30**, 985–998

Valot, P., Engelmann, J.: 1973, *Pitch Angle Distributions of Geomagnetically Trapped Protons for* $1.2 < L < 2.1$, Space Res. **XIII**, Akademie Verlag, Berlin

Vampola, A.L., Osborn, J.V., Johnson, B.M.: 1992, *CRRES Magnetic Electron Spectrometer AFGL-701-5A (MEA)*, J. of Spacecraft and Rockets **29**, 592–595

Van Allen, J.A.: 1991, *Why Radiation Belts Exist*, EOS **72**, 361

Vette, J.I.: 1977, *A Comparison of Trapped Proton Models AP8MIN and AP8MAX with Their Compressed Versions AP8MIC and AP8MAC*, NSSDC/WDC-A-R&S File No. 13489

Vette, J.I.: 1991a, *The AE-8 Trapped Electron Model Environment*, NSSDC/WDC-A-R&S 91-24

Vette, J.I.: 1991b, *The NASA/National Space Science Data Center Trapped Radiation Environment Model Program (1964–1991)*, NSSDC/WDC-A-R&S 91-29

Violet, M.D., Lynch, K., Redus, R., Riehl, K., Boughan, E., Hein, C.: 1993, *Proton Telescope (PROTEL) on the CRRES Spacecraft*, IEEE Trans. Nucl. Sci. **40**, 242

Vlasova, N.A., Knyasev, B.N., Kovtykh, A.S., Kozlov, A.G., Panasyuk, M.I., Reyzman, S.Ya., Sosnovets, E.N.: 1984, *Protons with $E > 30\,keV$ at Low Heights near Geomagnetic Equator during a Magnetically Quiet Time*, Kosmicheskie Issledovaniya **22**, 53–66 (in Russian), translated in Cosmic Research **22**, 46–58

Volkov, I.B., Dronov, A.B., Kratenko, Yu.P., et al.: 1985, *Outer Electron Belt Dynamics according Simultaneous Measurements on Board of INTERCOSMOS-19 and COSMOS-900 Satellites*, Kosmicheskiye Issledovaniya (Cosmic Researches) **23**, 642–646 (in Russian)

Williams D.J.: 1976, *SELADS; Operational Real-Time Solar Terrestrial Environment Monitoring System*, NOAA Technical Report ERL-357-SEL-37, Environmental Research Lab

Williams, D.J., Frank, C.A.: 1984, *Intense low energy ion populations at low equatorial altitudes*, J. Geophys. Res. **89**, 3903–3911

Wilson, G.R.: 1992, *Semikinetic modeling of the outflow of ionospheric plasma through the topside collisional to collisionless transition region*, J. Geophys. Res. **97**, 551–565